Time-resolved spectroscopic studies of $SrTiO_3$ photocatalysts for water splitting

Anna Andreassen Wilson

Imperial College London

Department of Chemistry

Thesis submitted for the Degree of Doctor of Philosophy

2022

Declaration of authorship

I hereby declare that the contents of this thesis is solely my own work and contribution, except where appropriate reference is made to acknowledge the contribution of others.

Anna Andreassen Wilson

October 2022

Copyright declaration

Acknowledgements

Firstly, I would like to thank and acknowledge my supervisor, James Durrant, for his guidance and support. Thank you for patiently sharing your knowledge, pushing me beyond my comfort zone and convincing me that I am producing good work when I do not believe it myself.

Thank you to all group members past and present. You make going into work a joy and from you I have learnt so much, not only from your science and expertise, but also from your kindness and generosity. A special thank you to Li and Pabitra, for always being there for everyone and everything. Thank you also to my examiners, Junwang Tang and Martyn McLachlan, for the interesting and incredibly enjoyable viva.

Thank you to my friends and family, for all that you do.

Abstract

In this thesis, the charge carrier dynamics that underpin the impressive performance of $SrTiO_3$-based photocatalysts for overall water splitting are investigated. This is primarily achieved using time-resolved transient and steady-state spectroscopic techniques. An in depth introduction into the motivation and background of this work is included in Chapter 1, whilst a detailed description of the methods employed is included in Chapter 2.

In Chapter 3, the charge carrier dynamics of $SrTiO_3$ on ps-ns timescales are characterised. In the first 10 ps after photoexcitation, charge trapping into shallow localised states is observed. This results in two distinct components, that are extracted by global analysis, and result in a slow rise and fast decay in distinct spectral regions. The bimolecular recombination that follows in $SrTiO_3$ is remarkably slow, and is quantified to reveal a bimolecular rate constant that is two magnitudes slower than that of alternative metal oxides.

In Chapters 4 and 5, the effects of flux mediated Al^{3+} doping and $RhCrO_x$ deposition on $SrTiO_3$ are explored, to identify their role in enabling high photocatalytic activities. Here, there is a focus on the steady-state charge carrier dynamics under water splitting conditions, where the performance enhancements resulting from these material modifications are observed. Al^{3+} doping suppresses recombination to enhance charge lifetimes and steady-state charge densities. $RhCrO_x$ amplifies these effects, with the influence of its deposition method on determining the balance between reactive and unreactive hole species highlighted. The optimum balance is achieved by facet selective photodeposition of $RhCrO_x$, whereby hole accumulation can be tolerated, but reactive hole species dominate and a near-unity AQY can be achieved.

Finally, $SrTiO_3$ is investigated under applied bias in Chapter 6, to gain further insights into the charge carrier dynamics of $SrTiO_3$, in addition to enabling calculation of the hole extinction coefficient and kinetics of water oxidation.

Contents

List of Figures

List of Tables

Chapter 1

Introduction

1.1 Background

1.1.1 The climate and energy crisis

The rising temperatures on earth are unprecedented, with each of the past four decades exceeding the average temperatures of any decade since 1850 (Figure 1.1a). These rising temperatures are fuelling climate breakdown, where extreme weather, environmental degradation and natural disasters threaten every corner of the world. With increased greenhouse gas (GHG) concentrations identified as the main driver of this warming, and the unequivocal link between human activities and increased GHGs, the global warming we are observing is principally the result of human activities (Figure 1.1b).[1]

The combustion of fossil fuels to obtain energy is the main source of GHGs, contributing to 76% of anthropogenic GHGs in the UK.[2] Alongside the devastating impact on the climate of GHGs released into the atmosphere, the health impacts of co-emitted pollutants, such as fine particulate matter ($PM_{2.5}$), are vast. $PM_{2.5}$ is associated with cardiovascular and respiratory diseases, and consequently $PM_{2.5}$ resulting from fossil fuel combustion is attributed to 9 million premature deaths annually, which equates to one in six deaths worldwide.[3] The overwhelming contribution of fossil fuel combustion to GHGs and poor air quality is in our control, thus it is our responsibility to make drastic changes to our lifestyles and how we sustain our energy demands.

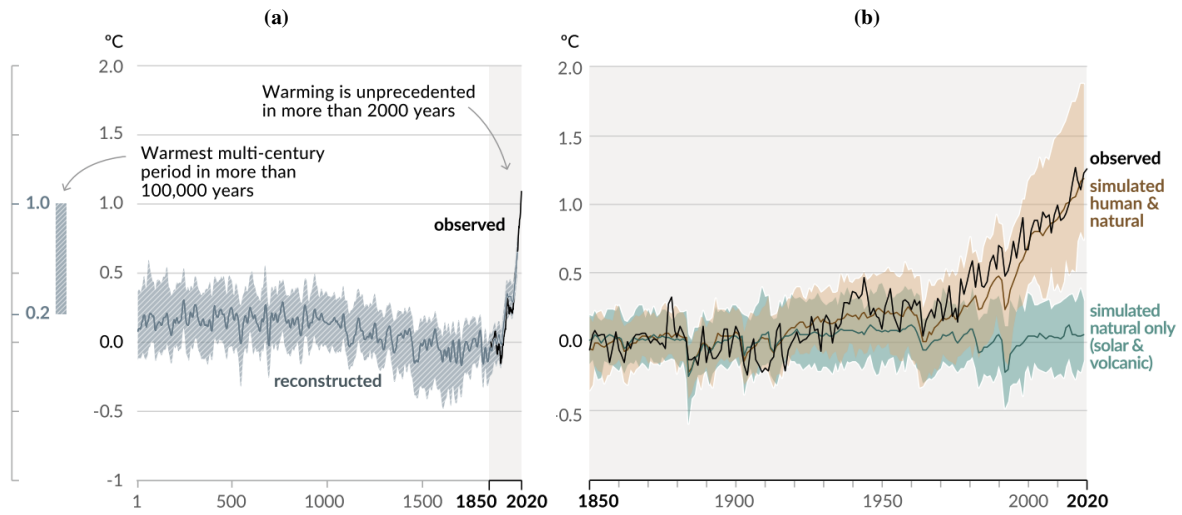

Figure 1.1: a) Changes in global surface temperature (decadal average) reconstructed from paleoclimate archives from 1850-2000 (solid grey line), compared to direct observations in temperature from 1850-2020 (solid black line). b) The change in global surface temperature from 1850-2020 observed (black line) and simulated using only human and natural factors (brown), or only natural factors (green), highlighting the dominant role of human factors in the observed temperature increase. Shaded areas around the solid lines show the very likely range of the temperature. Figure adapted from the Sixth Assessment Report by the IPCC on Climate Change.[1]

Currently, fossil fuels meet most of our energy demand, with the International Energy Agency (IEA) calculating a contribution from renewables of only 12% in 2020.[4] Sizeable increases to this contribution are vital to achieve the drastic decrease in CO_2 (the dominant GHG) emissions needed to limit global warming. Under the IEA's net zero scenario, the contribution of renewables is increased to meet 66% of demand by 2050. Even under less ambitious pathways, such as the stated policies scenario (STEPS) and the announced pledges scenario (APS), the renewable energy contribution must increase to 25% and 35% respectively.[4] The renewable energy sources expected to meet the bulk of this demand are solar, wind and bioenergy. However, these all have their respective limitations to consider. For example, ensuring the sustainability of bioenergy is complicated due to the release of CO_2 upon combustion and changes to land use threatening biodiversity and food production. Meanwhile, solar and wind energy are intermittent sources that cause sizable challenges for meeting fluctuating energy demands and achieving large scale energy storage.

1.1.2 Promise and potential of solar energy

Solar energy is of great abundance, with the estimated solar energy reaching the earths' surface in one year (3,400,400 EJ) exceeding the world's yearly energy consumption predicted for 2030

(450 EJ), by many thousands of times.[5] Solar energy can be used in solar heating, solar thermal electricity or solar photovoltaics (PV), with the latter being the most utilised technology.[5] Falling costs of solar PV in recent years have resulted in it becoming the lowest cost source of new electricity generation in most regions.[6] Despite the plentiful supply of solar energy and cost competitive electricity generation, challenges surrounding intermittency, electricity storage and decarbonising sectors that cannot be electrified remain.

The production of fuels from solar energy, termed solar fuels, addresses many of these challenges. Here, solar energy is utilised, either directly or using electricity it generates, to drive chemical transformations that store energy in the chemical bonds of fuels. In this way, during peak periods of solar energy fluxes solar fuels are produced, which can be transported and stored for months, to overcome the intermittency of solar energy and balance fluctuating energy demands. The splitting of water into hydrogen fuel and oxygen using sunlight is a simple and attractive example. In addition, carbon-based solar fuels can be produced by 'artificial photosynthesis', a process using CO_2 and water to produce fuel, similarly to the role of photosynthesis in plants. However, combustion of carbon-based fuels results in GHG emissions and frequently other pollutants such as nitrous oxides, whereas hydrogen fuel combustion burns cleanly to produce water.

1.1.3 Hydrogen economy and production routes

An attractive alternative to fossil fuels is hydrogen, a carbon-free fuel that can be combusted to release energy, or utilised in a fuel cell to generate electricity, without the release of carbon by-products or pollutants. Hydrogen fuel is one of the IEA's key pillars of decarbonisation,[4] in part due to its versatility and suitability for applications that are difficult to decarbonise by electrification, such as long haul transport and industrial processes. The widespread use of hydrogen to decarbonise a range of sectors and applications, including industry, transport, power generation and heating, is referred to as the 'hydrogen economy'.

Ambitious hydrogen strategies have been launched across the world to establish a hydrogen economy,[7] with the UK predicting that hydrogen could make up 20-35% of energy consumption by 2050.[8] These ambitious hydrogen strategies offer means to significantly reduce emissions, whilst establishing new industries and employment opportunities to replace those lost

in the fossil fuel industry. However, to ensure that the hydrogen used to meet these targets is renewable, it is important to consider how it is produced.

When considering the available routes for hydrogen production, their environmental impact, up-scalability, and cost competitiveness all need consideration. For the latter, the United States Department of Energy predicts a threshold levelised hydrogen cost for economically viable hydrogen production of \$2.00-4.00 kg^{-1}.[9] Currently, the dominant route of hydrogen production is from fossil fuels via steam methane reforming (SMR).[8] SMR uses methane, normally in the form of natural gas, and high pressure steam to produce hydrogen with CO and CO_2 by-products. Although the cost of producing hydrogen via SMR is low ($\sim$\$1.40 kg^{-1}),[9] the carbon by-products and the reliance on fossil fuel feedstocks greatly limits the sustainability.

Ideally, 'green' hydrogen is produced, whereby renewable feedstocks are used and the release of GHGs or other air pollutants is avoided. The use of solar energy to produce 'green' hydrogen as a solar fuel achieves this by using renewable energy to drive the splitting of water into hydrogen and oxygen. There are three main categories of solar-driven water splitting methods: PV coupled electrolysis (PV-EC), photoelectrochemical (PEC) and photocatalytic (PC). PV-EC is the most established route, whereby PV generated electricity drives the electrolysis of water using mature technologies, and currently achieves the highest efficiencies.[10] However, due to the coupled nature of this route and high up-scaling costs, the estimated cost of hydrogen production is \$10-12 kg^{-1},[9,11] far from the \$2.00-4.00 kg^{-1} threshold. PEC is similar to PV-EC in that water is produced electrochemically, but instead of supplying the electricity externally from the coupled PV, one or two electrodes absorb light to generate the necessary current to drive water splitting from charge illumination.[12,13] Hydrogen produced via PEC water splitting has a lower projected cost than that from PV-EC, of \$4.10-10.40 kg^{-1}.[9,14] PC hydrogen production is the simplest of the solar-driven production routes, whereby light is absorbed and used to drive overall water splitting on a single device, without any additional energy input.[15–17] PC routes offer the greatest opportunity for low-cost and up-scalable hydrogen production, with a projected cost of \$1.60-3.20 kg^{-1}.[14]

The difficult balance between achieving a low system complexity and also high efficiencies is demonstrated in Figure 1.2. For example, although PV-EC offers the highest efficiencies, the complexity is also high which limits its up-scalability and cost competitiveness. Meanwhile, the

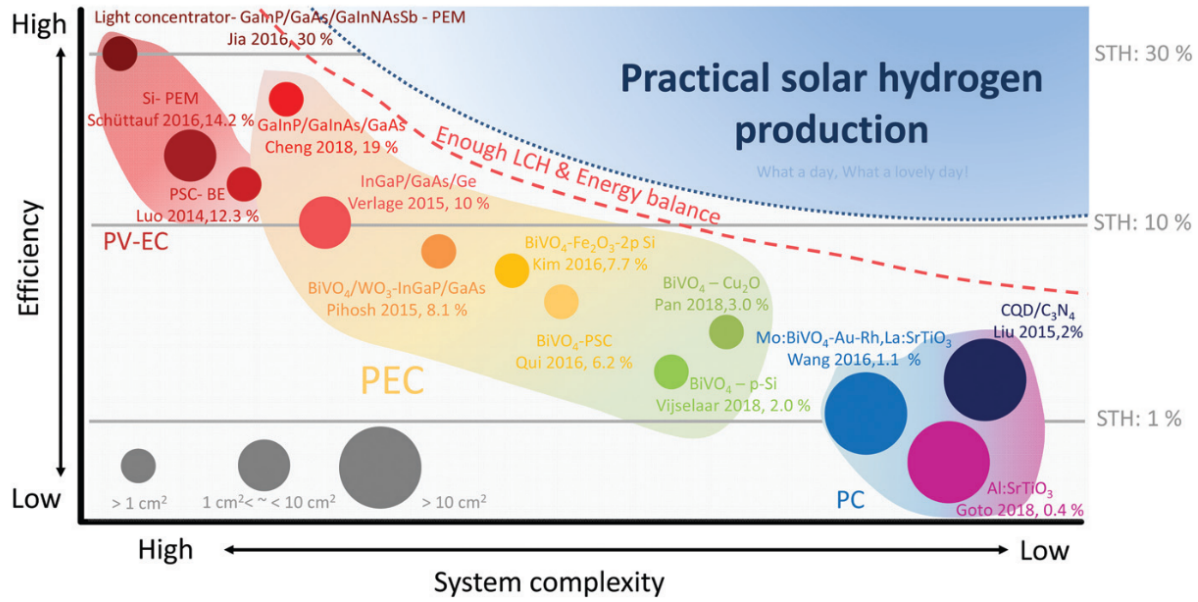

Figure 1.2: Technological map of a range of PV-EC, PEC and PC systems, mapped according to their system complexity and efficiency. The size of the points is indicative of the area of the system modules in the demonstration projects. Figure taken from a review by Kim et al.[10]

PC technologies mapped offer low complexity, and therefore good scalability and low projected costs, but they suffer from low efficiencies. Current PC water splitting systems have solar to hydrogen (STH) efficiencies that do not exceed a few percent,[18] and the low projected costs are based on an assumed STH efficiency of 10%.[14] However, they are an immature technology compared to SMR or PV-EC, so there is the potential to significantly improve upon the present efficiencies. Thus, further research into PC technologies is required to gain insights into what determines their efficiency, to facilitate the design of more efficient systems that maximise the opportunities they offer for low-cost and up-scalable renewable hydrogen production.

1.2 Photocatalytic water splitting

PC water splitting can be split into two redox processes: the hydrogen evolution reaction (HER, Equation 1.1) and oxidation evolution reaction (OER, Equation 1.2). Under standard conditions, the electrochemical potential for the overall water splitting reaction is 1.23 V (Equation 1.3), which equates to a Gibbs free energy change (ΔG) of +237 kJ per mol of hydrogen. Thus, the water splitting reaction is energetically uphill and requires an energy input to overcome this thermodynamic barrier. In PC water splitting, the absorption of light energy serves as the sole energy input. This is in contrast to PEC water splitting, where there is an additional contribution from an external electrical input.

$$HER: 4H^+ + 4e^- \rightarrow 2H_2 \qquad E^0_{red} = 0\,V_{RHE} \tag{1.1}$$

$$OER: 2H_2O + 4h^+ \rightarrow O_2 + 4H^+ \qquad E^0_{ox} = +1.23\,V_{RHE} \tag{1.2}$$

$$Overall\ reaction: 2H_2O \rightarrow 2H_2 + O_2 \qquad E^0 = +1.23\,V_{RHE} \tag{1.3}$$

1.2.1 Semiconductor photocatalysts

Fujishima and Honda were pioneering in the use of semiconductors for water splitting applications, using TiO_2 to split water in a PEC system under UV irradiation in 1972.[19] Following their discovery, Schrauzer et al. demonstrated unassisted overall water splitting, using TiO_2 powder to split water under UV irradiation with no further energy inputs required.[20] Since then, extensive research has been conducted into the use of semiconductors for water splitting, with a particular focus on metal oxides due to their low-cost, abundance, tunability and stability to photocorrosion.[21]

The sequential steps occurring in a semiconductor particle during PC water splitting are illustrated in Figure 1.3. When the semiconductor absorbs light with energy greater than or equal to its band gap, electrons are excited to the conduction band (CB) and holes are generated in the valence band (VB). These photogenerated charges are separated into free carriers and migrate

to the active sites at the reactant interfaces, whilst avoiding recombination. Reactions can occur either on the photocatalyst surface, or on deposited co-catalysts. At the reactant interfaces, the charges participate in surface redox reactions, with the holes oxidising water and the electrons reducing protons. The ability of photogenerated charges to participate in surface reactions depends on their energetic driving force, as determined by the conduction band minimum (CBM) and valence band maximum (VBM).

Overall photocatalytic water splitting (OPWS), whereby the HER and OER reactions are catalysed by a single photocatalytic system in the absence of applied bias, can be categorised as one-step and two-step photoexcitation systems.[22] In a one-step photoexcitation system (shown in Figure 1.3), the HER and OER occur on a single material (including deposited co-catalysts if present). Thus, the single photocatalytic material must possess a CBM and VBM that straddle the electrochemical potentials, in order to have sufficient driving force to simultaneously catalyse both reactions. Although one-step photoexcitation systems are the simplest method for OPWS and are the focus of this thesis, it is noted that two-step photoexcitation systems are also an interesting area of research. These two-step systems combine two semiconductor photocatalysts, where the individual components conduct either the HER or OER. In this way,

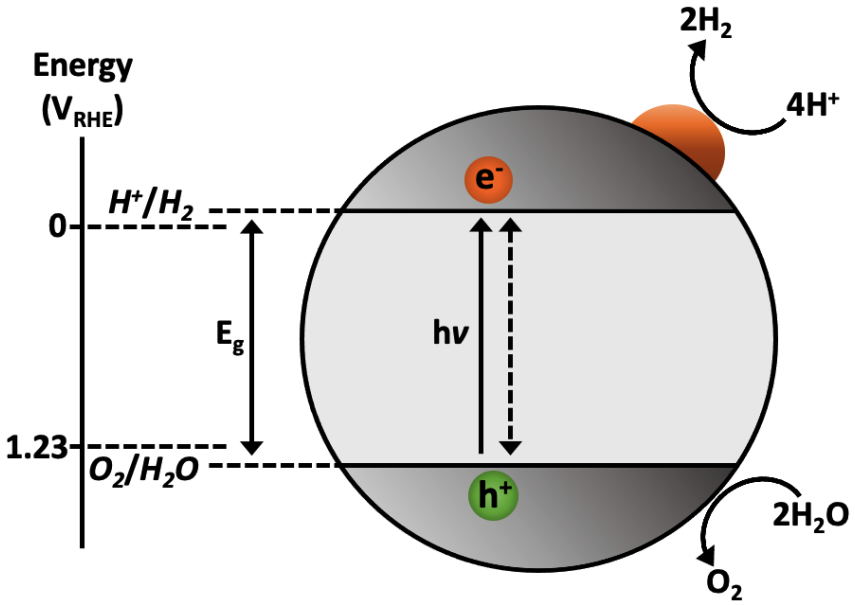

Figure 1.3: Schematic illustration of a one-step photocatalytic system conducting OPWS. Band gap excitation produces photogenerated charges (solid arrow), which must avoid recombination (dashed arrow). Here, the OER is catalysed by VB holes and the HER is catalysed by a proton reduction co-catalyst deposited on the surface of the particle. It is noted that a co-catalyst can be used for either, neither, or both of the HER and OER, depending on the system. The CBM and VBM of the photocatalyst straddle the required electrochemical potentials for the HER and OER.

the thermodynamic requirement of needing a single material that straddles the HER and OER electrochemical potentials is alleviated and visible light absorption can be enhanced. However, for each photocatalytic cycle, the number of photons that need to be absorbed is increased and there are more kinetic steps to consider, including interparticle charge transfer steps that need to be controlled to prevent backwards reactions. The fabrication of these systems is also more complex, with a redox mediator or conductive later required between the HER and OER components to shuttle the charges between them.[23–25]

1.2.2 Charge carrier dynamics of photocatalysis

The charge carrier dynamics of the photogenerated charges play a critical role in determining their efficiency. The initial step of charge separation is facile in metal oxide photocatalysts, due to their relatively high dielectric constants enabling photogenerated charge pairs to readily dissociate into free charges.[26] Following their separation, photogenerated charges must be transported to the reaction interfaces to catalyse their respective water splitting reactions, whilst avoiding recombination. The photogenerated charges can undergo recombination via a number of possible pathways, that occur across a range of timescales and are illustrated in Figure 1.4. These pathways are as follows: i) geminate recombination (fs-ps) of bound photogenerated electron-hole pairs prior to charge separation (expected to have a very small contribution in metal oxides due their high dielectric constants), ii) non-geminate/bimolecular recombination (ps-μs) of separated (free) carriers in the bulk, iii) trap-mediated recombination (ns-μs) involving photogenerated charge in a trap state, and iv) back electron-hole recombination (μs-ms) of an electron that had been extracted and a hole near to the reaction interface.[27,28]

The magnitudes of difference between the timescales of the slow interfacial water splitting reactions (μs-s) and competing processes, such as trapping (ps-μs) and recombination (fs-ms), make it challenging to ensure sufficient charge lifetimes for catalysis.[28] This challenge is intensified in the case the water oxidation reaction where four holes are required and the kinetics are especially slow (ms-s reaction timescales), resulting in it being referred to as the 'bottleneck' in photocatalytic water splitting.[29] In order to achieve sufficient lifetimes for photocatalytic water splitting, a predicted lifetime gain on the order of 10^8-10^{10} is required.[26] In photoanodes, this lifetime gain can be achieved through the application of a positive bias to drive favourable band

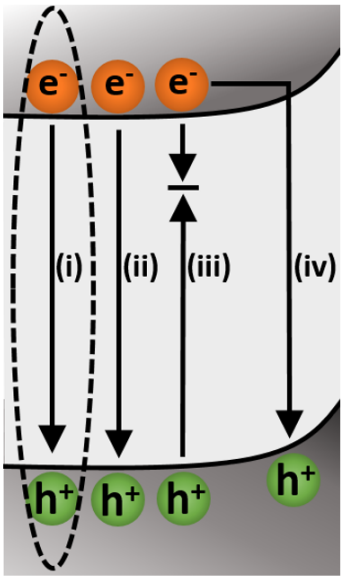

Figure 1.4: Schematic illustration of common recombination pathways following photoexcitation. These include, i) geminate recombination of bound electron-hole pairs, ii) non-geminate/bimolecular recombination of separated charges, iii) trap-mediated recombination, and iv) back electron-hole recombination.

bending. However, in photocatalysts this is not possible, and instead the intrinsic properties of the photocatalyst system under illumination must be relied upon to achieve the necessary lifetime gain.

In OPWS photocatalysts, approaches to extend lifetimes by promoting spatial charge separation include co-catalyst loading, junction formation and facet engineering.[18] In the case of co-catalyst loading and junction formation, charges are spatially separated due to their diffusion or extraction to distinct components of the photocatalyst. Meanwhile, facet engineering relies on the creation of an energy offset and internal electric field to spatially separate charge within the same photocatalyst particle.[30,31]

Charge trapping into defects is an additional approach that can spatially separate charge and extend charge lifetimes in OPWS photocatalysts, however, the balance between its potential benefits and adverse effects is complex. It is expected that charge trapping into sub-band gap states comes with an energy cost, since the energetic driving force of the charges is decreased.[26] Moreover, charge trapping can impede mobility and the trap/defect sites can serve as recombination sites,[32–34] in trap-assisted electron-hole recombination processes for example. However, charge trapping has also been shown to bring advantages by aiding charge separation and significantly extending charge lifetimes,[35] slowing recombination down to ms timescales.[28,36] Thus, whether charge trapping is advantageous for photocatalyst performance depends on the unique

nature of the defects involved, and in particular the balance between the decreased reactivity of charges and the potential to increase the overall water splitting activity due to suppressed recombination.[26] This is demonstrated in a comparison between polycrystalline $SrTiO_3$, rich in defects and deeply trapped charges, and single crystal $SrTiO_3$, low in defects and deeply trapped charges.[36] In this case, despite the lower reactivity of charges in the former, the longer lifetimes exhibited (ms vs. ns) resulted in superior photocatalytic performance.

Due to the integral role of charge carrier dynamics in determining the efficiencies of photocatalytic systems, it is interesting to investigate them using time-resolved transient spectroscopic techniques (explored in detail in Chapter 2). Through the application of such techniques, the populations and decay kinetics of photogenerated charges can be monitored and key loss processes, such as recombination and charge trapping, can be identified.

1.2.3 Photocatalyst architectures

Particulate photocatalysts for OPWS can be employed as a powder suspension in water, or immobilised onto a substrate to create photocatalyst sheets.[24,37,38] Photocatalyst sheets offer extensive practical advantages for hydrogen production, with up-scalable fabrication routes and low operational costs enabling the technology to be demonstrated on a large scale. An example of a large scale (100 m^2) pilot plant employing $SrTiO_3$-based photocatalyst sheets is shown in Figure 1.5.[39] Facile fabrication of the panel reactor units comprised of the photocatalyst sheets (Figure 1.5a) is achieved using up-scalable methods, such as screen printing or spraying techniques. When in use, the panels comprising of the photocatalyst sheets can be tilted to achieve the optimum angle for light absorption and bubble formation (Figure 1.5b).[17,37] Although a powder suspension offers the advantage of a larger particle surface area available to reactants, the advantages are limited compared to the extensive practical advantages of photocatalysts sheets. When using a powder suspension, thorough stirring of the suspension is necessary to prevent settling of the powder at the bottom, which limits the feasibility of large scale reactors and the ability to optimise the reactor angle for light absorption and bubble evolution.[17,37] Moreover, recovery of the powder from the reactor after use is a non-trivial task. The use of photocatalyst sheets largely avoids these constraints and assuming good mechanical strength and adhesion to substrate, offers comparable, or in some cases improved, performance compared to their

suspension counterparts.[25,40]

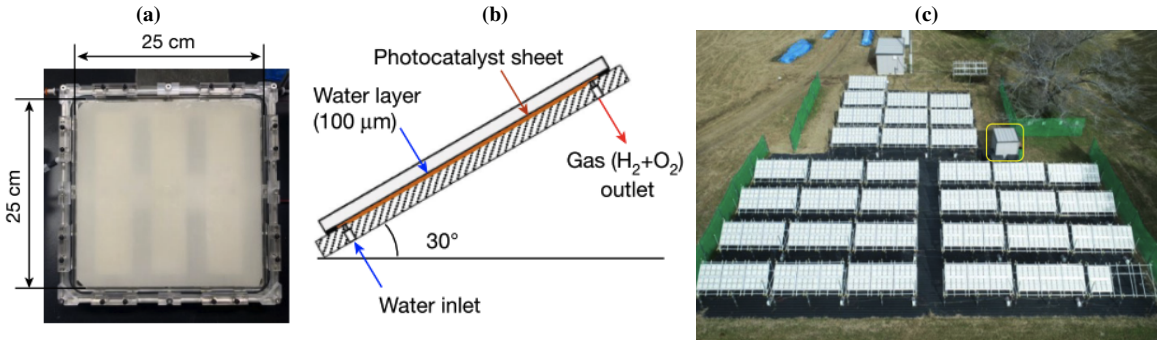

Figure 1.5: Up-scalable photocatalyst sheet design for large scale operation of $SrTiO_3$-based photocatalyst sheets. a) A 625 cm^2 panel reactor unit fabricated by a programmed spray method. b) Side-on structure of the panel reactor unit. c) 100 m^2 pilot pant demonstration, including 1600 panel reactor units and a gas separation facility (yellow box). Figure adapted from Domen and co-workers.[39]

These photocatalyst architectures for OPWS have multiple benefits over the more established PV-EC and PEC water splitting technologies. In contrast to PV-EC and PEC water splitting, there is no applied bias for OPWS, and therefore electrical contacts and electrolytes are not required. Moreover, issues regarding the build-up of large pH gradients are avoided, due to the HER and OER occurring on a single material in OPWS.[41] Thus, the simplicity of the OPWS system makes the technology an attractive option for large scale hydrogen production with low associated costs.[37,38,42]

1.2.4 Performance metrics

The efficiency of OPWS systems are evaluated using their apparent quantum yield (AQY) and STH efficiency. The AQY is the ratio of the number of photons utilised in the generation of the desired reaction product, to the number of incident photons, and is defined as:

$$AQY(\%) = \frac{n \times R}{I} \times 100 \tag{1.4}$$

Where n is the number of electrons required per mol of product, R is the number of mol of products produced and I is the number of incident photons. n is equal to two and four, for the calculation of hydrogen and oxygen evolution efficiencies respectively. Due to absorption efficiencies and migration distances being dependant on wavelength, the AQY is measured

under monochromatic irradiation. Meanwhile, the STH efficiency is a measure of the efficiency of hydrogen evolution under solar irradiation. The STH efficiency is calculated from the ratio of the energy output as hydrogen, to the energy of the incident solar irradiation, and is defined as:

$$STH(\%) = \frac{r_{H_2} \times \Delta G}{P_{sun} \times A} \times 100 \tag{1.5}$$

Wherer_{H2} is the rate of hydrogen production, ΔG is the Gibbs free energy change for the water splitting reaction under standard conditions (237 kJ mol^{-1}), P_{sun} is the incident light flux from solar irradiation and *A* is the illuminated area.

The AQY and STH are useful metrics for measuring and comparing performance, but it is important to note that stability is also an important factor to be considered, with the attractive costs of photocatalytic hydrogen production assuming a minimum system lifetime of 10 years.[10,11]

1.2.5 Previous work on overall photocatalytic water splitting

The $SrTiO_3$-based photocatalysts fabricated by Domen and co-workers are the state-of-the-art for one-step OPWS, with respect to activity, scalability and scalability. The function of this system is summarised in Figure 1.6, whereby $SrTiO_3$ is doped by Al^{3+} (Al:$SrTiO_3$) in a flux-mediated doping process, prior to the addition of a $RhCrO_x$ co-catalyst for proton reduction.[34,43] Following deposition of $RhCrO_x$ via an impregnation method (Al:$SrTiO_3$/$RhCrO_x$(IMP)), an AQY of 56% at 365 nm is achieved by the photocatalyst sheets.[37] AQYs exceeding 50% are rare for overall water splitting photocatalysts and this system is unique in achieving this efficiency whilst also exhibiting activity under solar irradiation.[18,44,45] The subsequent photodeposition of CoOOH and TiO_2 serves to increase the stability by preventing the photocorrosion of $RhCrO_x$ (Figure 1.6b), and enabling 80% of the initial activity to be maintained over a period of 1300 hours.[40] The up-scalability and stability of these photocatalysts have been demonstrated through pilot plants, including the aforementioned plant that safely and stably produced hydrogen on the 100 m^2 scale.[39] Recently, a remarkable AQY of 93% at 365 nm was achieved by selective photodeposition of $RhCrO_x$ onto the reduction facets.[38] This near-unity AQY is the highest reported to date for an OPWS system and is indicative of highly efficient preservation and

utilisation of photogenerated charges. However, it is noted that although these systems can operate under solar irradiation, they are limited by their wide band gap and low STH efficiency (0.3-0.6% under simulated sunlight illumination).[38,40]

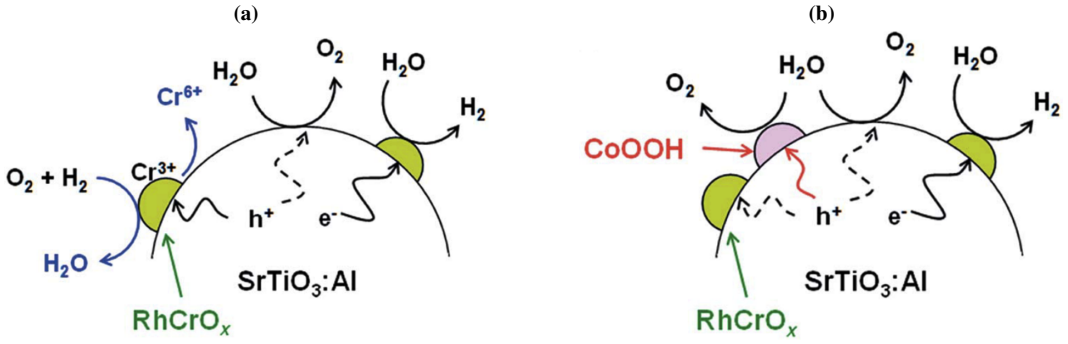

Figure 1.6: Illustrations of the $SrTiO_3$-based photocatalysts conducting OPWS. a) Al:$SrTiO_3$/$RhCrO_x$(IMP) without CoOOH, showing the desired hydrogen and oxygen evolution on the $RhCrO_x$ co-catalyst and Al:$SrTiO_3$ surface respectively. However, the oxidation of $RhCrO_x$ and subsequent dissolution of Cr is also shown, that is reported to lead to co-catalyst deactivation over time. b) Al:$SrTiO_3$/$RhCrO_x$(IMP) with CoOOH, showing the desired hydrogen and oxygen evolution as in a), but also the extraction of holes to CoOOH to prevent the deactivation of $RhCrO_x$. Although the CoOOH is shown to conduct water oxidation here, it is noted that its role remains ambiguous for this system and may solely serve to increase stability and not promote catalysis. Similarly to CoOOH, a TiO_2 overlayer can be added to further prevent catalyst deactivation. Figure taken from Domen and co-workers.[40]

As mentioned, there are few examples of photocatalysts achieving an AQY that exceeds 50% for OPWS. Beyond Al:$SrTiO_3$, these include Zn:Ga_2O_3 modified with a $RhCrO_x$ co-catalyst (71% at 254 nm)[44] and La:$NaTaO_3$ modified with a NiO co-catalyst (56% at 270 nm).[45] However, unlike Al:$SrTiO_3$/$RhCrO_x$ which does split water under solar irradiation, the band gaps of these photocatalysts are too wide to operate under such conditions. Due to the wide band gaps of the aforementioned photocatalysts achieving high AQYs, high energy incident light is required for band gap excitation and consequently there is a large energy (ΔG) loss ($\sim$2-3 eV) incurred to drive the water splitting reactions.[26] The impact of this loss is translated to low STH efficiencies below 1%.[38,40,44,46]

In order to achieve improved STH efficiencies, photocatalysts with narrower band gaps are required. The best performing photocatalysts with narrow band gaps for visible light absorption include GaN:ZnO and metal-free carbon nitride (CN_x) photocatalysts. Unfortunately, for most of these examples reports of the corresponding STH efficiency values are lacking (although due to the low AQYs they are also expected to be low). Particulate GaN:ZnO modified with a $RhCrO_x$ co-catalyst achieves an AQY of up to 17% by nanostructuring and has good

stability,[47,48] whereby activity is maintained over several months of operation.[49] Without the addition of sacrificial hole scavengers, CN_x achieves AQYs of a few percent,[50,51] which is increased to 16% at 420 nm (with a reported STH of 2%) when a junction is formed with carbon dots.[52] The AQYs of these narrow band gap materials are low and therefore the search for the ideal photocatalyst continues.

Interestingly, for the leading OPWS systems that do not require scavengers for a reasonable AQY, there are clear parallels in the modifications to the base metal oxides that are undertaken. In all cases, there is the addition of a hydrogen evolution co-catalyst and in most cases, there is metal doping to enhance the bulk properties.

1.2.6 Doping in metal oxide photocatalysts

Metal oxides can be doped extrinsically via the introduction of impurities, or by intrinsic defects such as oxygen vacancies states (V_O).[13,17,34,53] This can result in two non-exclusive categories of doping: chemical doping and electrical doping. Chemical doping refers to the introduction of a foreign atom, whilst electrical doping refers to a resulting change in conductivity (i.e. a change in the majority or minority carrier densities). Doping is frequently undertaken to improve the properties of metal oxides. For example, chemical doping can improve conductivity and overcome low carrier mobilities, by increasing the majority carrier concentration and effectively electrically doping the material.[21] This has been demonstrated through the n-type doping of $SrTiO_3$ with Nb^{5+},[54] or Ta^{5+} doping of α-Fe_2O_3.[55] Alternatively, chemical dopants can be employed to introduce states within the band gap and enhance visible light absorption, as was first demonstrated by Asahi et al. inducing the visible light absorption of TiO_2 by N doping.[56] Since then, visible light absorption has been achieved by doping with a range of transition metal cations, or non-metal cations.[13] Despite the potential benefits of doping strategies, they often result in a decrease in photocatalytic performance, due to the dopant sites serving as recombination centres and/or decreasing charge carrier mobility.[13,56]

Counter-doping strategies can be employed to passivate dopant sites that are detrimental to performance. For example, when doping $SrTiO_3$ with Rh to achieve visible light absorption, Rh^{3+} and Rh^{4+} dopant states are introduced.[57] The Rh^{3+} states just above the CB enable the visible light absorption and are photocatalytically active. However, the Rh^{4+} states result in

vacant mid-gap states that are photocatalytically inert and serve as recombination centres, consequently limiting photocatalytic performance. Passivation of the undesirable Rh^{4+} states is achieved by additional doping with La, which controls the valence state of Rh through charge compensation, such that it is fixed in the Rh^{3+} state.[58,59]

A further example of controlling a dopant that limits photocatalytic performance, is the aliovalent doping of $SrTiO_3$ with a lower valence metal cation, to suppress Ti^{3+} states that are attributed to recombination centres.[34] This was initially demonstrated for a variety of lower valence cation substitutions, such as Ga^{3+} for Ti^{4+} or Na^{+} for Sr^{2+}. Since then, aliovalent doping of $SrTiO_3$ with Al^{3+} has been optimised and employed in the state-of-the-art Al:$SrTiO_3$/$RhCrO_x$ water splitting systems developed by Domen and co-workers,[37,43] with the effects of this doping on $SrTiO_3$ being the focus of Chapter 4.

1.2.7 Co-catalyst addition

Co-catalysts loaded onto photocatalysts serve as reaction sites and improve the kinetics of the HER or OER. This is particularly useful for OPWS photocatalysts, where many light absorbers used as photocatalysts do not sufficiently catalyse both the HER and OER.[60] In addition to improving the kinetics of a given reaction, the extraction of photogenerated charges by co-catalysts can promote charge separation and transport.[22] Extracting photogenerated charges also offers improved stability, for example by extracting photogenerated holes which can otherwise oxidise photocatalyst species and lead to degradation.[49,60]

Despite the many possible advantages of using a co-catalyst, due to the HER and OER occurring within the same system and the ability of many catalysts to catalyse multiple processes, they are susceptible to catalysing backwards reactions (Figure 1.7a). Therefore, it is important to design co-catalysts that selectively catalyse the desired redox reaction and inhibit backwards reactions that would severely limit performance. In the case of proton reduction co-catalysts, which often are metals that catalyse both the HER and backwards reactions, this is often achieved through an oxide overlayer that enables the selective permeation of protons and hydrogen, but not oxygen (Figure 1.7b).[22,61]

Another consideration for co-catalysts is what their precise role is in a photocatalytic system.

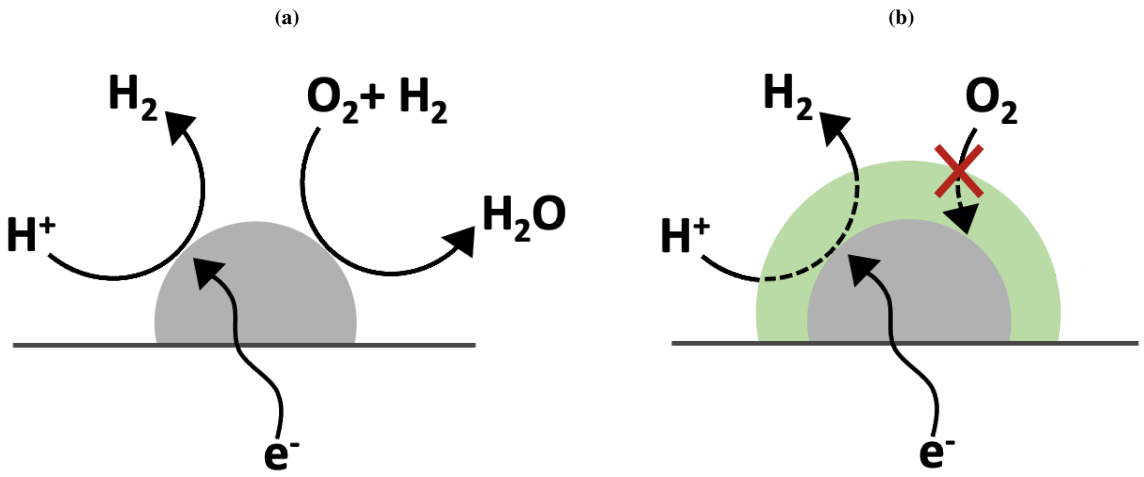

Figure 1.7: Schematic of the role of an oxide layer (light green) on the selectivity of reactions catalysed with a metal co-catalyst (grey). a) The metal co-catalyst successfully catalyses the HER, but also backwards reactions involving the HER and OER products. b) When the metal co-catalyst is coated with an oxide layer, that is selectively permeable to protons and hydrogen but not oxygen, backwards reactions involving oxygen are inhibited. The stoichiometry of reactions is ignored in this schematic for simplicity.

For example, a co-catalyst can be confused with an overlayer. This has been seen in the debated role of CoPi in improving the performance of $BiVO_4$ and α-Fe_2O_3 photoanodes,[62,63] where the effects of CoPi are regarding enhanced charge separation and suppressed recombination, rather than catalytic effects.[64,65] The role of CoOOH as a co-catalyst for the Al:$SrTiO_3$/$RhCrO_x$ photocatalyst systems investigated in Chapter 5 is also complex. In some system configurations, CoOOH prevents the photodegradation of $RhCrO_x$ and enhances stability but not photocatalytic activity (thereby serving as an overlayer),[40] whilst in others it significantly increases photocatalytic activity.[38]

1.3 In this thesis

$SrTiO_3$-based photocatalysts have been reported to achieve AQYs near to unity, with the effects of Al^{3+} doping and co-catalyst addition on enhancing performance reported in detail. However, a comprehensive understanding of the charge carrier dynamics that underpin these performance enhancements is lacking. Moreover, the key features that enable the efficient utilisation of photogenerated charges, and the resulting highest reported AQY to date, are not known. This thesis aims to address this by employing a range of time-resolved spectroscopic techniques that span ps-s timescales, and measure under steady-state conditions as well as following laser excitation. These spectroscopic techniques are coupled with material characterisation, to enable correlations to be drawn between the charge carrier dynamics and physical properties, with all methods explained in detail in Chapter 2.

To begin, the ultrafast charge carrier dynamics of $SrTiO_3$ are measured on ps-ns timescales in Chapter 3. The results of these measurements are quantified and compared to alternative metal oxides, in order to identify the unique features of $SrTiO_3$ that minimise loss processes on these fast timescales and contribute to its photocatalytic performance. Following this, the state-of-the-art photocatalysts fabricated by Domen and co-workers are investigated, primarily in the steady-state which is representative of the conditions where the performance enhancements are observed. In Chapter 4, the crucial role of the flux-mediated Al^{3+} doping and its impact on the charge carrier dynamics is investigated. Subsequently, the effects of $RhCrO_x$ deposition on Al:$SrTiO_3$ are studied in Chapter 5, and the influence of the deposition routes that result in dramatically different photocatalytic performances is explored. Finally, spectroscopic measurements of $SrTiO_3$ are undertaken under applied bias in Chapter 6, to enable additional insights into $SrTiO_3$, such as the first approximation of the water oxidation kinetics on its surface and the hole extinction coefficient.

Through the aforementioned investigations, an understanding of the key features that enable the near-unity AQY can be acquired. It is hoped that these features can be incorporated into the design of photocatalyst materials that exhibit strong visible light activity, to simultaneously achieve a high AQY and STH in the future.

Chapter 2

Methods

2.1 Materials

$SrTiO_3$ films

$SrTiO_3$ was fabricated into transmissive films on FTO coated substrates (TEC10, NSG Ltd) at the University of Liverpool. The FTO was scrubbed with Hellmanex III detergent before sequential rinsing in ultrasonic baths of deionised water and isopropyl alcohol. The $SrTiO_3$ films were deposited via radio frequency (RF) magnetron sputtering from a compound target in an AJA Orion 8 sputtering system. Films were sputtered at room temperature, in a 3 mTorr Ar atmosphere and using a power density of 2.47 W cm^{-2}. Following a 10 hour deposition time, the $SrTiO_3$ films were annealed for 30 minutes in air at 450 °C.

Particulate $SrTiO_3$, Al:$SrTiO_3$, Al:$SrTiO_3$/$RhCrO_x$(IMP) and Al:$SrTiO_3$/$RhCrO_x$(PD)

The particulate $SrTiO_3$, Al:$SrTiO_3$, Al:$SrTiO_3$/$RhCrO_x$(IMP) and Al:$SrTiO_3$/$RhCrO_x$(PD) photocatalysts were provided by the Domen group at Shinshu University. In all cases, they were provided as powders and also fabricated as photocatalyst sheets, as is detailed in the literature.[37] The photocatalyst sheets were prepared by drop casting a suspension of the given powder and SiO_2 nanoparticles (NanoTek) in distilled water onto a frosted glass plate, prior to drying on a hot plate at 50 °C for 1 hour. The SiO_2 nanoparticles served as an inorganic binder that fixed the photocatalyst to the substrate and created voids between the photocatalyst particles, to facilitate water penetration and gas evolution.[37,66]

Commercially available $SrTiO_3$ powders were used as purchased (99.9%, Wako). Al:$SrTiO_3$ was prepared by a flux-mediated doping method previously reported, that involves the dissolution and recrystalisation of the starting materials.[43] In this method, $SrTiO_3$ (99.9%, Wako), $SrCl_2$ (98.0%, Kanto) and Al_2O_3 nanopowder in a 1:10:0.02 molar ratio are mixed and ground together in an agate mortar. The mixture is heated in a covered alumina crucible at 1150 °C for 10 hours. Following heating, the powder is cooled to room temperature, washed repeatedly with distilled water and filtered under pressure using a 1 μm PTFE filter. This washing process was conducted three times in total and the resulting powder was heated in a vacuum oven at 40 °C, before briefly grinding with a pestle and mortar for 2 minutes. Due to the incorporation of Al^{3+} from the powder and the crucible, its incorporation into the bulk as well as the surface is expected and had been measured previously.[43]

$RhCrO_x$ was deposited onto the Al:$SrTiO_3$ via impregnation, following a method originally used for depositing $RhCrO_x$ onto $(Ga_{1-x}Zn_x)(N_{1-x}O_x)$.[67] Here, Al:$SrTiO_3$ powder is mixed with $Na_3RhCl_6.2H_2O$ (17.8 wt% Rh, Mitsuwa) and $Cr(NO_3)_3.9H_2O$ (98.0–103.0%, Kanto) in distilled water. The mixture is evaporated over a warm water bath with constant stirring until dry and the resulting powder is calcined in air at 350 °C for 1 hour. The method for photodepositing $RhCrO_x$ also followed that reported previously.[38,68] An aqueous solution of $Na_3RhCl_6.2H_2O$ (Wako) was added to a suspension of Al:$SrTiO_3$ in distilled water, under constant stirring and irradiation from a Xe lamp (300W full arc) for 10 minutes. Without exchanging the solvent, an aqueous solution of K_2CrO_4 (Kanto) was subsequently added, under irradiation and stirring for 5 minutes. The concentrations of Rh and Cr in their respective solutions were both 2 mg ml^{-1}.

Comparison materials

The ultrafast TAS results on the $SrTiO_3$ films are compared to other metal oxides (TiO_2, $BiVO_4$ and α-Fe_2O_3), as well as methylammonium lead iodide ($MAPbI_3$). The dense and mesoporous anatase TiO_2 films were fabricated following a method reported previously by Sachs et al.[27] The dense films were prepared by atmospheric pressure chemical vapour deposition (APCVD). The precursor solution was prepared by reacting $TiCl_4$ and ethyl acetate at 500 °C in a cold-walled reactor. In the reactor, the quartz substrate was heated on a graphite block at 500 °C. N_2 was used as an inert carrier gas to transfer the precursor vapours into and through the reactor. Preparation of the mesoporous films on quartz followed a sol-gel processes, using a paste comprised

of 15 nm TiO_2 particles, before hydrothermal treatment of the films. In a furnace, the films were dried in air at 100 °C and cooled to room temperature.

The dense $BiVO_4$ films were fabricated by a sol-gel process reported previously by Selim et al.[69] Here, a sol-gel mixture was prepared by dissolving bismuth nitrate pentahydrate in acetic acid, vanadyl acetyl acetone and acetyl acetone. The sol-gel mixture was spin coated onto FTO substrates, with calcining at 450 °C for 10 minutes between layers, and calcining at 450 °C for 5 hours when the desired thickness was achieved to yield dense films.

The preparation of α-Fe_2O_3 was based on a previously reported method by Tang et al.,[70] also using a sol-gel method. Briefly, the sol-gel mixture of $FeCl_2.4H_2O$, citric acid and ascorbic acid dissolved in N_2 saturated ethanol was heated at 60 °C for 5-6 hours. DMF was added to the resulting solution as a drying control reagent and the solution was stirred for 30 minutes. The solution was then spin coated onto quartz substrates, prior to annealing at 300 °C for 50 minutes. The second layer was subsequently deposited and the films were again annealed at 300 °C for 50 minutes. A further annealing step at 450 °C for 3 hours was conducted to produce α-Fe_2O_3.

$MAPbI_3$ was prepared on indium-doped tin oxide (ITO) coated glass substrates, following a method reported in the literature.[71–73] The ITO substrate was cleaned in acetone, isopropanol and deionised water for 10 minutes, prior to being dried under N_2 flow and treated with O_2 plasma. A 1:1 ratio of 1.5 M lead iodide (PbI_2, 99.99%, Alfa Aesar) and methylammonium iodide (MAI, Dyesol, 99.99%) was dissolved in a mixture of N,N-dimethylmethanamide (DMF) and dimethyl sulfoxide (DMSO) (9:1.1 volume ratio). The mixture was stirred for 1 hour at 50 °C to dissolve precursors and then passed through a 0.45 μm PTFE filter. The resulting solution was dropped onto the ITO substrate and spun at 4000 rpm for 30 s, with 0.5 mL diethyl ether added at 7 s. The substrates were annealed on a hot plate at 1000 °C for 15 minutes.

2.2 Materials characterisation

2.2.1 XRD, SEM, TEM and XPS

X-ray diffraction (XRD) patterns were obtained from 20 to 80 $2\theta°$, using Bruker D2 phaser with parallel beam optics, equipped with a PSD LinxEye silicon strip detector and using Cu Kα radiation (40 kV and 40 mA). Diffraction patterns were compared to standards from the Inorganic Crystal Structure Database (ICSD). Scanning electron microscopy (SEM) images were taken using a Leo Gemini 1525 Field Emission Gun scanning electron microscope (FEG SEM). Prior to imaging, samples were coated with a 15 nm Cr layer. High resolution transmission electron microscopy (HR-TEM) was applied for more detailed imaging and investigation of the crystal structure, using the Joel TEM 2100 Plus. X-ray photoelectron spectroscopy (XPS) was conducted using a Thermo K-Alpha spectrometer with a monochromated Al Kα radiation source. Survey scans were taken from 0-1350 at intervals of 0.1 eV. Peaks were calibrated to the adventitious C 1s peak at 284.5 eV. Avantage software (Thermo Scientific v.5.9925) was used for peak fitting and analysis.

2.2.2 UV-Vis spectroscopy

The steady-state optical absorption was measured using a UV-Vis spectrometer (Shimadzu 2600) fitted with an integrating sphere (Shimadzu ISR-2600Plus). As a reference, a barium sulfate plate with 100% reflectance was used. Absorbance (%Abs) was calculated from the as measured reflectance (%R) and transmittance (%T) using Equation 2.1:

$$Abs(\%) = 100 - T(\%) - R(\%) \tag{2.1}$$

Reflectance data was converted into dimensionless units proportional to absorbance using the Kubelka-Munk function:

$$f(R) = \frac{(1-R)^2}{2R} \tag{2.2}$$

Where *R* is the diffuse reflectance measured. Tauc plots of $(\alpha hv)^{1/n}$ vs. hv, where α is the absorption coefficient and *n* is a value determined by the nature of the band gap (2 for the indirect allowed transition of $SrTiO_3$), were used to approximate the optical band gap using the following equation:

$$(\alpha hv)^{1/n} = B(hv - E_g) \tag{2.3}$$

Where B is a constant and *f(R)* is substituted for α.

2.2.3 Photoelectrochemical characterisation

Photoelectrochemical (PEC) measurements were conducted in a home-made PEEK cell with 0.5 cm^2 quartz windows. PEC measurements on the $SrTiO_3$ photoanodes in this thesis employed front-side illumination, a Pt mesh counter electrode and Ag/AgCl in saturated KCl solution as the reference electrode. The electrodes were submerged in an aqueous electrolyte solution of 0.1 NaOH (pH 13). Voltage was applied via an Autolab potentiostat (PGSTAT 12) controlled by Nova 1.11 software. Linear sweep voltammetry (LSV) to obtain current-voltage (J-V) curves was measured under chopped light conditions, using illumination from a 365 nm LED at $\sim$2.7 mW cm^{-2} to simulate the photon flux expected from 1 sun AM1.5G irradiation. The applied bias was converted from $V_{Ag/AgCl}$ to V_{RHE} using the Nernst equation:

$$V_{RHE} = V_{Ag/AgCl} + 0.0591 + pH + V^0_{Ag/AgCl} \tag{2.4}$$

Where $V^0_{Ag/AgCl}$ is the standard potential (+0.197 V) of the Ag/AgCl in saturated KCl solution reference electrode.

2.3 Methods

2.3.1 Transient absorption spectroscopy

Transient absorption spectroscopy (TAS) is a time resolved pump-probe technique used to monitor the charge carrier dynamics of photogenerated species, thus it is a very useful tool for studying photocatalytic systems. The technique is based upon the pioneering work by Lord Porter on the use of flash photolysis to study short-lived free radical species.[74] In a typical TAS experiment, a semiconducting sample is photoexcited with an intense light pulse (the 'pump'), usually with sufficient energy for band gap excitation. The photogenerated species (electrons and holes) generated are monitored by a continuous second light source (the 'probe'), that is time-delayed with respect to the pump. The technique relies on the photogenerated species having specific spectral absorptions, which modulate the transmission, or reflectance, of light and therefore the optical density (OD) that reaches the photodiode detector. In this way, changes to the OD measured (ΔOD) as a function of time are used to track photogenerated species and their corresponding charge carrier dynamics, including their generation, lifetimes and participation in processes such as trapping, recombination and catalysis.

Calculating transient absorption changes

The OD measured by the photodiode can be defined using the Beer-Lambert Law and the following equation:

$$OD_{(\lambda,t)} = -log(T_{(\lambda,t)}) = -log(\frac{I_{(\lambda,t)}}{I_{(\lambda,i)}}) = \epsilon_{\lambda}.c_t.l \tag{2.5}$$

Where ϵ_{λ} is the molar extinction coefficient of the absorbing species at the given wavelength (λ), c_t is the concentration of the transient species at time (t), and l is the optical pathway length. $T(\lambda,t)$ is the transmittance of light through the sample at a given wavelength as a function of time. $I(\lambda,t)$ and $I(\lambda,i)$ are the intensities of the transmitted and incident light respectively.

A change in optical density, ΔOD, due to photoexcitation from the laser 'pump' pulse is calculated by finding the difference in OD before and after the excitation:

$$\Delta OD_{(\lambda,t)} = OD_{(\lambda,t)} - OD_{(\lambda,t_0)} \tag{2.6}$$

Where *OD(λ,t)* and *OD(λ,t_0)* correspond to the optical density at time *t* and prior to photoexcitation respectively, and are both probed at a given λ.

Using Equation 2.5, Equation 2.6 can be rewritten as:

$$\Delta OD_{(\lambda,t)} = -log(\frac{I_{(\lambda,t)}}{I_{(\lambda,i)}}) + log(\frac{I_{(\lambda,t_0)}}{I_{(\lambda,i)}}) = -log(\frac{I_{(\lambda,t)}}{I_{(\lambda,t_0)}}) \tag{2.7}$$

Where *I(λ,t)* is the transmitted light intensity at time *t* and *I(λ,t_0)* is the transmitted light intensity prior to photoexcitation. Since *I(λ,t)* is equal to the sum of *I(λ,t_0)* and Δ*I(λ,t)*, Equation 2.7 can be expressed as:

$$\Delta OD_{(\lambda,t)} = -log(\frac{I_{(\lambda,t_0)} + \Delta I_{(\lambda,t)}}{I_{(\lambda,t_0)}}) = -log(1 + \frac{\Delta I_{(\lambda,t)}}{I_{(\lambda,t_0)}}) \tag{2.8}$$

The change in transmitted light intensity, Δ*I(λ,t)*, at the photodiode detector is proportional to the change in voltage, Δ*V(λ,t)*, measured across the photodiode. Therefore, Equation 2.8 can be rewritten as:

$$\Delta OD_{(\lambda,t)} = -log(1 + \frac{\Delta V_{(\lambda,t)}}{V_{(\lambda,t_0)}}) \approx -\frac{1}{2.303}.ln(1 + \frac{\Delta V_{(\lambda,t)}}{V_{(\lambda,t_0)}}) \tag{2.9}$$

Following the conversion to a natural logarithm in Equation 2.9, the Taylor series can be applied where for small *x* values ln(1+*x*) $\approx$ *x* (noting that the changes in voltage are typically small and on the order of 10^{-2}):

$$\Delta OD_{(\lambda,t)} \approx -\frac{1}{2.303}.\frac{\Delta V_{(\lambda,t)}}{V_{(\lambda,t_0)}} \tag{2.10}$$

Wilkinson and co-workers identified the need to monitor the transient species in materials with a highly scattering nature, such as powdered semiconductors, due to their role in technological advances.[75,76] As such, they developed diffuse reflectance flash photolysis, whereby the photodiode detects the fractional change in reflected light, $\Delta R_{(\lambda,t)}$, rather than transmitted light. Thus, instead of referring to the voltage change measured by the photodiode as ΔOD, the %Abs can be is used instead and is defined in this case as:

$$\%Abs = 1 - R_{(\lambda,t)} = \frac{R_{(\lambda,t_0)} - R_{(\lambda,t)}}{R_{(\lambda,t_0)}} = \Delta R_{(\lambda,t)} \tag{2.11}$$

Decreases in diffuse reflectance, and therefore increases in %Abs, were shown by Wilkinson and co-workers to be linearly proportional to the concentration of the probed species where the concentration of transient species is low (as we assume for our DRTS measurements).[77] Whilst this enables insights into the densities of photogenerated species under different conditions, for highly scattering samples it is not possible to reliably make comparisons between different materials with different light scattering properties.

Contributions to the optical signal

The optical signal (ΔOD or % Abs) that results from photoexcitation can have contributions from different photophysical processes and can be observed as:

a) A positive signal corresponding to a transient absorption, due to a new absorption band that results from the photoexcited state

b) A negative signal corresponding to a transient bleach, due to the depopulation of the ground state absorption or stimulated emission

It is noted that a combination of these contributions can be observed in a single spectrum.

Microsecond transient spectroscopy

Transient spectroscopy on μs-s timescales was conducted using a home-built set-up illustrated in Figure 2.1. Depending on the optical properties of the samples, this system can be operated in transmission (μs-TAS) or diffuse reflectance (DRTS) mode. For the transmissive $SrTiO_3$ investigated in Chapter 3 and 6, μs-TAS was employed. Meanwhile, DRTS was employed for the highly scattering and opaque $SrTiO_3$-based photocatalysts investigated in Chapters 4 and 5. In all cases, reagents are bubbled with N_2 for 15 minutes prior to the measurement, unless otherwise stated. The third harmonic of a Nd:YAG laser (OPOTEK Opolette 355 II with a 7 ns pulse width) was used as the excitation source. The second and third harmonic crystals were tuned for a 355 nm output which was guided through a liquid light guide (0.5 cm diameter) onto the sample. The laser repetition rate and laser intensity (determined by the Q-switch delay) was modulated using the hand held controller. The probe light source was a 100 W Bentham IL1 quartz tungsten halogen lamp connected to a Bentham 605 power supply. When probing in the visible region, the probe light was followed by an IR filter (H_2O, 5 cm path length) to prevent sample heating. The transmitted or reflected light from the sample was directed and focused, using lenses and mirrors, through long pass filters (Thorlabs), a motorised colour wheel (Thorlabs) and a monochromator (Oriel 4 Cornerstone 130). The light was focused onto a visible or IR silicon photodiode detector (Hamamatsu S3071). The output from the photodiode collected on μs-ms timescales was electronically amplified (Costronics) and recorded by an oscilloscope (Tektronics TDS 2012B), whilst data on ms-s timescales was recorded by the DAQ card ((National Instruments, NI USB-6211). A home-built LabView software was used for data acquisition and processing. Measurements were undertaken with the sample in a quartz cuvette, or in a PEC cell connected to a potentiostat (analogously to in the PEC measurements) when applying constant bias.

Ultrafast transient absorption spectroscopy

Ultrafast TAS was employed to measure the charge carrier dynamics on ps-ns timescales, using a commercially available set-up illustrated in Figure 2.2. The set-up used a regeneratively amplified Ti:sapphire laser system (Solstice, Spectra-Physics) together with a broadband pump-probe spectrometer (HELIOS, ultrafast systems), that produced 800 nm laser pulses with a 92 fs width and 1 kHz repetition rate. The resulting pulse is split into a pump and probe pulse by

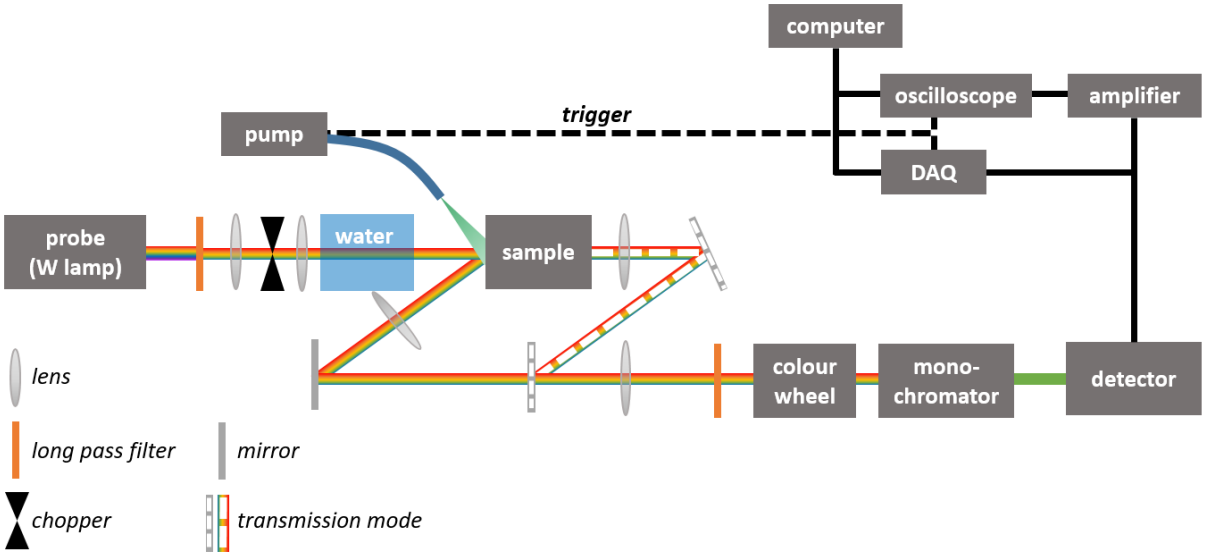

Figure 2.1: Schematic representation of the transient spectroscopy set-up used to measure scattering or transmissive samples on μs-s timescales. The dashed light and mirrors are present in transmission mode only.

a semi-transparent mirror. It is noted here that instead of a continuous illumination source, a second laser pulse is used as the probe for enhanced time resolution. For the pump pulse, a portion of the 800 nm laser output is directed through an optical parametric amplifier (TOPAS Prime, Spectra-Physics) and a frequency mixer (NirUVis, Light Conversion) to tune the pump to the desired wavelength. Neutral density filters control the pump intensity that is measured with a 500 μm diameter aperture. Meanwhile, the probe portion is sent through a motorized a delay stage which changes the beam path length to result in delays of up to $\sim$6 ns relative to the pump beam. Next, the probe is focussed onto a Ti:sapphire crystal to produce a white light continuum that can probe either the full wavelength range of the visible (450-800 nm) or NIR (800-1400 nm) continuum. Using a semi-transparent mirror, the resulting continuum beam is split into two, where one is directed onto the sample for probing, whilst the other is reflected and serves as a reference to improve the signal to noise ratio. The resulting continuum beams are focussed onto separate spectrometers for detection (Si or InGaAs sensors). The probe and pump beams are focussed onto a single spot on the sample so that they overlap. A motorised chopper operating at 500 Hz blocks alternate pump pulses, so that the excited and unexcited states are probed and the absorption difference can be calculated. Multiple scans are taken for each measurement (3-10, depending on the signal size and quality) and they are averaged before analysis. Surface Xplorer software is used for initial data processing, including cropping, background subtraction and a chirp correction. A chirp correction is necessary due to the wavelength dependence of the temporal overlap of the pump and probe (time zero, t_0).

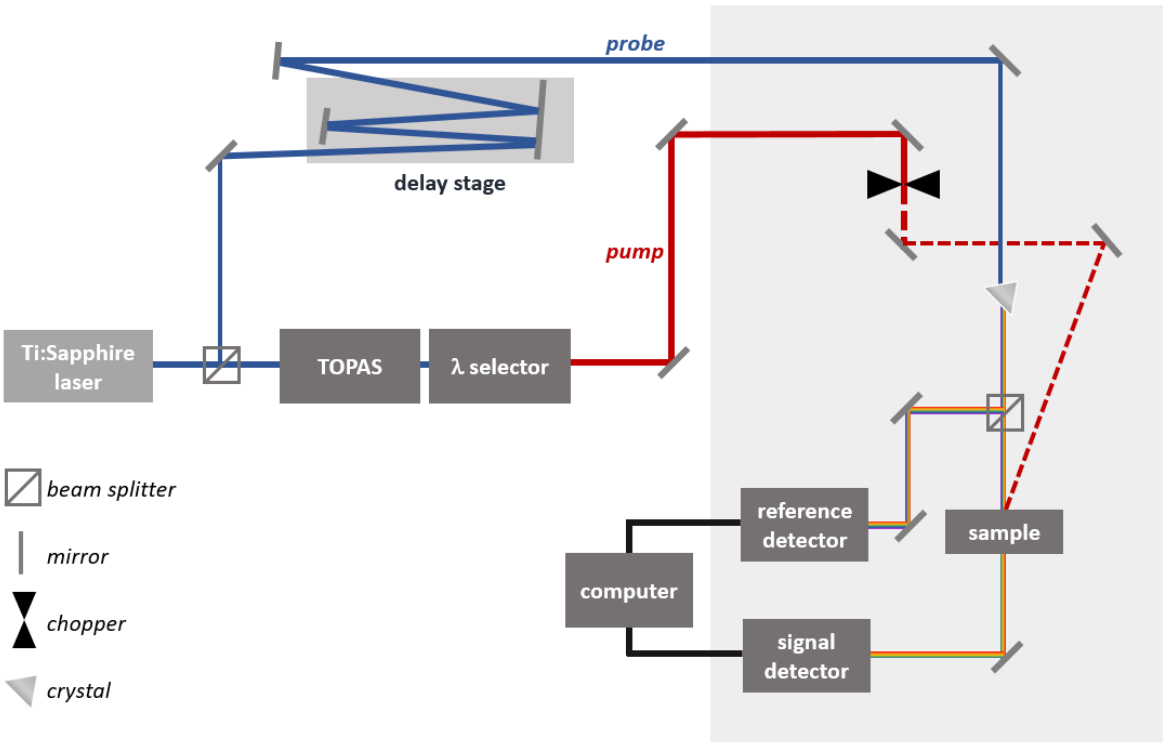

Figure 2.2: Schematic representation of the ultrafast TAS set up used to measure transmissive samples on ps-ns timescales.

2.3.2 Photoinduced absorption spectroscopy

Photoinduced absorption spectroscopy (PIAS) is a pump-probe technique that measures charge carrier dynamics under steady-state continuous illumination conditions, that are more comparable to working photocatalyst conditions than those in transient spectroscopy. The accumulation and decay of the charges under these PIAS conditions are probed over long timescales, up to 10's of seconds. The set-up is analogous to that in in microsecond transient spectroscopy, however, instead of using short laser pulses to excite the sample and serve as the probe source, continuous excitation from a 365 nm LED is used instead. The LED is connected to a power supply (QL564P, Thurlby Thandar Instruments) to control the light intensity, and a MOSFET transistor (STF8NM50N, STMicroelectronics) to generate light pulses of a defined length (usually 8 s). In this case, data from the DAQ was recorded and data from the oscilloscope is not required.

The kinetic trace from a typical PIAS measurement is illustrated in Figure 2.3. When the LED is turned on, photogenerated species rapidly accumulate and result in a steep increase in the

optical signal (a). Over time a steady-state is achieved (b), as the rate of charge generation is balanced by the rate of consumption, comprising of reaction and recombination rates. This manifests in a plateauing of the PIAS signal. The amplitude of the optical signal that is reached serves as an indication of the charge density present in the steady-state, however, it also has contributions from the charge lifetime. When the LED is turned off, the signal decays as charge consumption dominates (c).

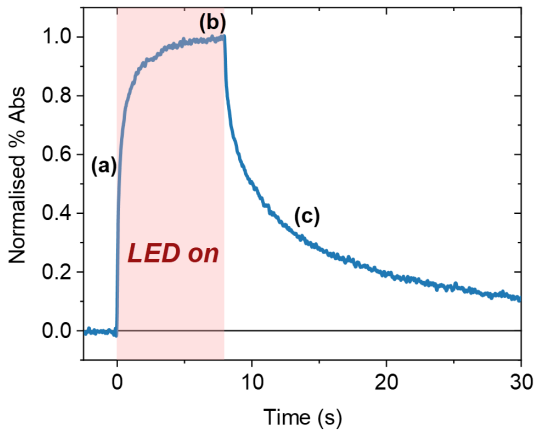

Figure 2.3: Example PIAS trace, highlighting the rise and plateau of the signal during 8 seconds of having the LED on, followed by a decay in the signal following turning the LED off.

2.3.3 Transient photocurrent measurements

Transient photocurrent (TPC) measurements were undertaken using the same experimental set-up as for microsecond transient spectroscopy measurements under applied bias, but with a change in the time base recorded by the oscilloscope and the probe light blocked. Following laser excitation and an induced trigger signal measured by the photodiode, the photogenerated TPC was obtained by measuring the voltage change with the oscilloscope from 10 μs to 0.1 s. In this measurement, data from the DAQ is not required.

2.3.4 Spectroelectrochemistry

Spectroelectrochemical (SEC) measurements were undertaken on $RhCrO_x$ films on FTO substrate. The measurements were undertaken in a three electrode system in an electrolyte solution of 0.1 M Na_2SO_4, with a Pt mesh counter electrode and Ag/AgCl in saturated KCl solution as the reference electrode. A Vertex potentiostat was used to control the voltage and measure the current. A stabilised 10 mW tungsten-halogen light source from Thorlabs (SLS201L) was used

with a collimating add-on (SLS201C). The light emitted from the lamp was transmitted through the sample and collected using a 1 cm diameter liquid light guide (Edmund optics). Light transmitted to the spectrograph was columnated and refocused using two 5 cm planoconvex lenses (Edmund) to match the optical components of the spectroscope (Kymera 193i, Andor) and CCD camera (iDus 420A-BEX2-DD, Andor). The detector was maintained at -80 °C during the measurements to optimise the signal to noise ratio. Measurements were undertaken in potentiostat mode and following a 10 s equilibrium time at each potential, the optical spectra was measured. A custom-built LabView software was used for data acquisition and 30 averages of the spectra were taken at each potential before moving onto the next potential, with each average taking $\sim$30 ms. At each potential, the current and spectra were measured simultaneously.

2.3.5 Global analysis

Global analysis was conducted on the ultrafast TAS results obtained in Chapter 3. The components contributing to the NIR spectral region were extracted using non-negative matrix factorisation (NMF), which was performed using the freely available sci-kit learn Python package. The data of interest contained only transient photoinduced absorption signals giving a positive contribution to the ΔOD, thus making NMF an appropriate technique to use in this case. The data was fitted from 0.5 ps and the datasets were cropped for a wavelength range of 890-1345 nm, due to the signal to noise ratio of the data outside of this range being too large for reliable analysis, especially for that measured at lower excitation intensities. The NMF kinetics were analysed and fit using the Python package LMFIT: Non-Linear Least Squares Minimisation and Curve-Fitting for Python. In the data analysed there was a clear fast decaying component and a growing component manifesting as a rise in ΔOD. The hypothesis wanting to be tested was whether the rise could be fitted as a component that was proportional to the component exhibiting a fast decay. In order to ensure confidence in the extracted components, the algorithm was run 50 times for each data set, starting from different random starting points for optimisation ('seeds') for each iteration. The spectra and kinetics obtained for each run was reproducible, with only small differences observed for different seeds.

2.3.6 Calculation of extinction coefficient

The correlation between hole absorbance and surface hole density is used to extract the extinction coefficient (ϵ_{h^+}) of holes, following a method previously used in our group.[78–80] The hole absorbance was obtained from the change in optical density, ΔOD, probed at 500 nm under a positive applied bias (assumed to correspond predominantly to holes), measured by μs-TAS measurements. The surface hole density was obtained from the cumulative charge extracted in TPC measurements, assuming that every photogenerated electron extracted resulted in one surface hole. This assumption was made based on a sufficiently positive bias being applied (1.3 V_{RHE} herein), such that back electron-hole recombination is assumed to be turned off. The charge extracted was converted to surface hole density ($|h^+|$) using Equation 2.12:

$$|h^+| = \frac{C}{(e \times A_v \times V)} \tag{2.12}$$

Where *C* is the total charge extracted, *e* is the elementary charge (1.60 x 10^{-19} C), A_v is Avogadro's number (6.02 x 10^{23} mol) and *V* is the volume investigated (PEC cell window size (cm^2) x film thickness (cm)). The gradient of the linear fit on the plot of hole absorbance vs. $|h^+|$ was subsequently used to extract the ϵ_{h^+} of holes from the Beer-Lambert Law:

$$A = \epsilon_{h^+} \times c \times l \tag{2.13}$$

Where *A* and *c* are taken as the hole absorbance and surface hole density respectively, and *l* is the sample thickness.

2.3.7 Relative quantum yield of hole generation

The quantum yield (QY) of holes probed in PIAS measurements is approximated by calculating the ratio between the holes generated to the absorbed photon flux multiplied by the charge lifetime, as shown in Equation 2.14:

$$QY = \frac{number\,of\,photogenerated\,holes}{absorbed\,photon\,flux \times t_{50\%}} \times 100 \tag{2.14}$$

Here, the molar photon flux absorbed is calculated from the incident 365 nm LED photon flux and the steady-state absorbance at 365 nm, whilst the population of holes generated is calculated using the optical signal amplitude and the ϵ_{h^+} of $SrTiO_3$. It is recognised that the ϵ_{h^+} can be used to quantify hole populations from the optical hole signal measured in transmission mode. However, due to the scattering nature of the $SrTiO_3$-based photocatalyst materials where the QY is calculated, diffuse reflectance mode is employed. Therefore, the resulting QY values are not as percentages and can only be compared as relative QY (RQY) values to the other $SrTiO_3$-based materials, that all exhibit similar steady-state optical properties. To obtain the RQY values for each $SrTiO_3$-based photocatalyst, the calculated QY values are divided by the highest value achieved (corresponding to the fast phase of Al:$SrTiO_3$/$RhCrO_x$(IMP)). For comparison purposes, RQY values for all of the $SrTiO_3$-based photocatalysts are calculated using the PIAS results obtained using 60% of 1 sun illumination intensity, as Al:$SrTiO_3$/$RhCrO_x$(PD) cannot be measured at higher intensities without bubble formation hindering the optical measurement.

2.3.8 Kinetic analyses

A combination of steady-state PIAS and TPC measurements can be used to approximate the kinetics of water oxidation on the photoanode surface, using the rate law analysis method. For this analysis, a sufficiently positive bias is applied (1.3 V_{RHE} herein), such that the contribution of back electron-hole recombination can be assumed to be negligible and therefore neglected in the analysis. Under these conditions, the rate of change of the surface hole density can be expressed as:

$$\frac{dp_s}{dt} = J_{holes} - k_{wo}.p_s^{\beta} \tag{2.15}$$

Where p_s is the surface hole density, J_{holes} is the flux of holes to the surface, k_{wo} is the rate of water oxidation and β is the reaction order. Under steady-state conditions, the rate of change of the surface hole density is assumed to be zero and the flow of electrons to the external circuit (i.e. the photocurrent) is equal to the flux of holes to the surface. Therefore:

$$\frac{dp_s}{dt} = J_{holes} - k_{wo}.p_s^{\beta} = 0 \tag{2.16}$$

$$J_{holes} = k_{wo}.p_s^{\beta} = J_{photo} \tag{2.17}$$

Where J_{photo} is the photocurrent. The kinetic parameters can be extracted when plotting this relationship on a log-log scale, where J_{photo} increases linearly with p_s:

$$log(J_{photo}) = log(k_{wo}.p_s^{\beta}) = log(k_{wo}) + \beta log(p_s) \tag{2.18}$$

The reaction order, β, represents the number of holes that need to accumulate to overcome the rate determining step (RDS) of water oxidation.

Under the same measurement conditions as the rate law analysis, the turnover frequency (TOF) and the reaction time constant (τ), where hole species are the oxidising equivalent, can be calculated using the following equations:

$$TOF(s^{-1}) = \frac{number\ of\ electrons \times s^{-1}}{[oxidising\ equivalent]} \tag{2.19}$$

$$\tau(s) = \frac{[oxidising\ equivalent]}{number\ of\ electrons \times s^{-1}} \tag{2.20}$$

Chapter 3

Ultrafast charge carrier dynamics of $SrTiO_3$

In this chapter, the charge carrier dynamics of $SrTiO_3$ are investigated on ps-ns timescales using ultrafast TAS. In this way, the fast recombination processes immediately following photoexcitation, that can significantly influence the resulting photocatalytic activity are investigated. Most notably, quantification of the bimolecular rate constant of $SrTiO_3$ reveals remarkably slow bimolecular recombination compared to alternative metal oxides. Due to an unremarkable intrinsic doping density calculated, alternative explanations for the slow bimolecular recombination are explored, such as the high dielectric constant and charge screening effects of $SrTiO_3$. In addition, the evolution of the spectrum is investigated through global analysis, to assign a fast decaying component to the localisation of charges into shallow states, which manifests as a slow rise in the optical signal observed elsewhere in the spectrum. These results provide a novel insight into how the charge carrier dynamics of $SrTiO_3$ compare to alternative materials and aid explanation of its suitability in water splitting applications.

3.1 Introduction

$SrTiO_3$ is a central component of several state-of-the-art systems for overall photocatalytic water splitting, OPWS. This includes the Al:$SrTiO_3$/$RhCrO_x$ system explored in Chapters 4 and 5, as well as scalable Z-scheme photocatalysts ($SrTiO_3$:La,Rh/Au/$BiVO_4$:Mo).[24,38,40] Efficient utilisation of photogenerated charges is demonstrated by these systems, in particular by Al:$SrTiO_3$/$RhCrO_x$ which achieves a near-unity AQY. In order to achieve this, recombination pathways must be suppressed such that there is efficient preservation and utilisation of the photogenerated charges for catalysing water splitting reactions. The charge carrier dynamics of metal oxides at early times (ps-ns) are dominated by fast recombination processes, including bimolecular (non-geminate) recombination of free charges in the bulk and monomolecular trap-mediated recombination.[26,28,81,82] Given the imbalance between these fast recombination processes and the slower timescales of the interfacial water splitting reactions (μs-s),[28] materials that can suppress fast recombination processes and extend charge carrier lifetimes are essential to achieve high water splitting activities. Since $SrTiO_3$-based photocatalysts can achieve high water splitting activities without the application of applied bias or scavengers, their intrinsic properties are responsible for achieving the necessary lifetime gain for the slow interfacial water splitting reactions.

Despite the promising reports of $SrTiO_3$-based materials in OPWS applications, the charge carrier dynamics of photogenerated charges in $SrTiO_3$ on fast timescales, where significant losses to the yield of photogenerated charges occurs, are not fully understood. To my knowledge, most previous studies focus on slower (μs-s) timescales,[83–85] or are limited to tracking transient radical species and reaction intermediates.[86] Meanwhile, the single previous study employing TAS to investigate the ultrafast charge carrier dynamics of $SrTiO_3$ is limited to investigating a single probe wavelength and does not quantify or compare the fast charge carrier dynamics to alternative materials.[87] These previous studies are all in agreement regarding their identification of photogenerated species that have decay kinetics on ns timescales. However, a comprehensive investigation into the ultrafast charge carrier dynamics of $SrTiO_3$ is lacking, whereby a range of intensities and wavelengths are measured and put into context, by quantifying photophysical properties and comparing to alternative materials.

In this chapter, ultrafast TAS is employed to measure the charge carrier dynamics of $SrTiO_3$ on ps-ns timescales. Due to the ultrafast TAS set-up operating solely in transmission mode and the opaque, scattering nature of the Al:$SrTiO_3$/$RhCrO_x$ investigated in the following chapters, an alternative $SrTiO_3$ film is studied in this chapter. The spectrum is measured in both the visible and NIR regions, and the decay kinetics are measured across this full spectral region from ps-ns timescales and under a range of excitation intensities, to gain a comprehensive insight into the fast charge carrier dynamics of $SrTiO_3$. Global analysis is conducted to extract distinct spectral components and explore the relationship between them. In addition, the bimolecular rate constant and doping densities of $SrTiO_3$ are calculated to gain a quantitative insight into its properties. The decay kinetics and the results of these calculations for $SrTiO_3$ are compared to other metal oxides (TiO_2, $BiVO_4$ and α-Fe_2O_3), in addition to the highly efficient and dominant perovskite in solar cell research, $MAPbI_3$.[88–90] Through these comparisons, the key features of $SrTiO_3$ that make it well suited to OPWS are explored.

3.2 Experimental methods

The $SrTiO_3$ investigated in this chapter is fabricated by RF sputtering at the University of Liverpool (with contributions from Dr Azim Mumtaz, Dr Troy Manning and Thomas Shalvey). The resulting $SrTiO_3$ films on FTO substrate are thin ($\sim$700 nm) polycrystalline films that are transmissive, making them well-suited for the ultrafast TAS set-up operating exclusively in transmission mode. These films are characterised in this chapter using XRD, SEM, AFM, UV-Vis and XPS analysis. Their charge carrier dynamics are predominantly investigated by ultrafast TAS on ps-ns timescales, in inert Ar conditions and employing 355 nm band gap excitation in all cases.

Global analysis of the ultrafast TAS results on $SrTiO_3$ was conducted by Lucy Hart (Imperial College London). Comparisons are made to other metal oxides, namely TiO_2, $BiVO_4$ and α-Fe_2O_3, in addition to $MAPbI_3$. The calculations and analysis conducted in this chapter uses the ultrafast TAS results obtained by others on these additional materials. The results on TiO_2, $BiVO_4$ and α-Fe_2O_3 were obtained by Dr Michael Sachs and the results on $MAPbI_3$ by Weidong Xu (both obtained when at Imperial College London). Comparisons to these alternative materials uses results obtained by employing band gap excitation, inert conditions and similar photogenerated charge densities as far as was possible.

3.3 Results

3.3.1 Physical characterisation

The morphology of the RF sputtered $SrTiO_3$ films was imaged by SEM and AFM. Side-on SEM images show a dense film with a consistent thickness of approximately 700 nm throughout (Figure 3.1a). The surface morphology measured by AFM comprised of a relatively smooth surface with a roughness factor of 1.1 (Figure A.1). The crystallinity of the $SrTiO_3$ films was analysed by XRD, with diffraction patterns of $SrTiO_3$ and the FTO substrate present (Figure 3.1b). The chemical composition of the surface was analysed by XPS, to reveal a small population of Ti^{3+} states of 4% (Figure 3.1c), with some population of Ti^{3+} states expected for $SrTiO_3$.[34,91] The valence band XPS structure is analogous to the particulate $SrTiO_3$ photocatalyst material investigated in the following chapter, with a Fermi level (E_F) lying approximately 2 eV above the valence band (Figure A.2). Further XPS analysis, including the C 1s, O 1s and Sr 3d core lines are included in Figure A.2 for completeness. From the ground state absorption spectrum measured by UV-Vis (Figure A.3), the transmissive properties of the film are evident, making the films suitable for measurements with the ultrafast TAS set-up. An optical band gap between 3.3 eV and 3.4 eV was calculated from a Tauc plot (Figure 3.1d), a larger band gap than the $\sim$3.2 eV typically reported for $SrTiO_3$.[34,92,93] However, a larger band gap is typical of thin and crystalline $SrTiO_3$ films fabricated by sputtering,[94,95] and has been explained by different degrees of stress distorting the bands to differing extents.[94] Oscillations are observed in the spectra (Figures A.3 and 3.1d), that are attributed to Fabry-Perot interference fringes that can be observed in thin and uniformly smooth films.[82,96] These oscillations complicate data interpretation and reduce the accuracy of the band gap estimation from the Tauc plot, so the calculated band gap should be taken as an approximation.

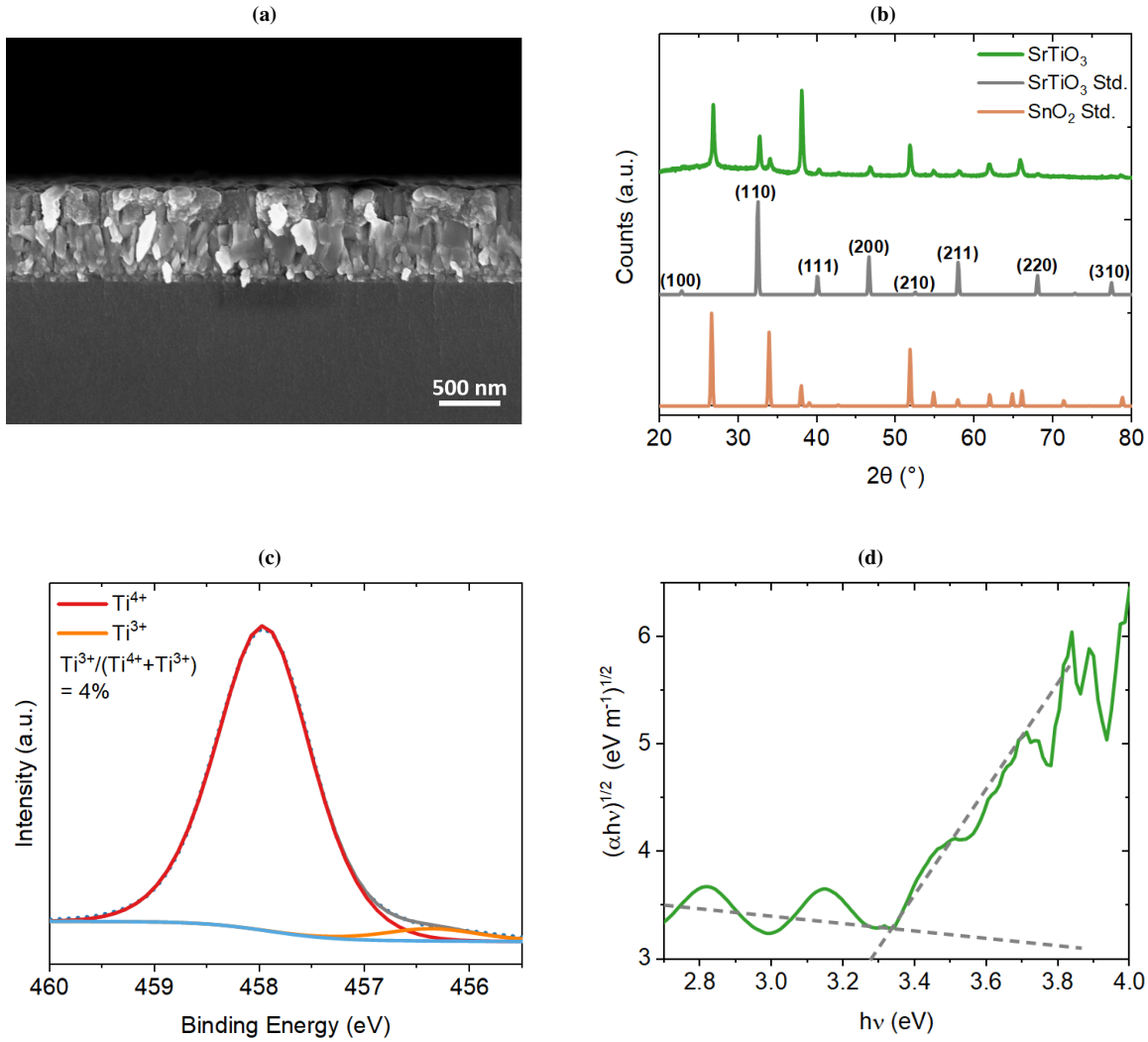

Figure 3.1: a) Side-on SEM of the $SrTiO_3$ films, showing a dense film with an average thickness of 700 nm. b) XRD diffraction pattern of the $SrTiO_3$ film on FTO, compared to standard $SrTiO_3$ (ICDS collection no: 23076) and SnO_2 (ICDS collection no: 9163) diffraction patterns. c) XPS Ti 2p core line spectra, fitted for the Ti $2p_{3/2}$ peak and showing a relative Ti^{3+} contribution of 4%. d) Tauc plot giving an estimated indirect band gap of 3.3-3.4 eV.

3.3.2 Charge carrier dynamics on ps-ns timescales

Ultrafast TAS measurements were used to investigate the charge carrier dynamics of $SrTiO_3$ at early times (ps-ns) following photoexcitation. The resulting TAS spectrum is comprised of two main features, in the visible and NIR regions (Figure 3.2a). Features in the visible and NIR regions are assigned to holes and electrons respectively,[27,84,85,97,98] in agreement with the spectral assignments made for the particulate $SrTiO_3$ in Chapter 4. The relative amplitudes of these NIR and visible features vary between different $SrTiO_3$ materials, as they are sensitive to the fabrication route and defects,[84,85] in addition to optical interference in the transmission of

the field, as was previously observed in dense TiO_2 films.[27]

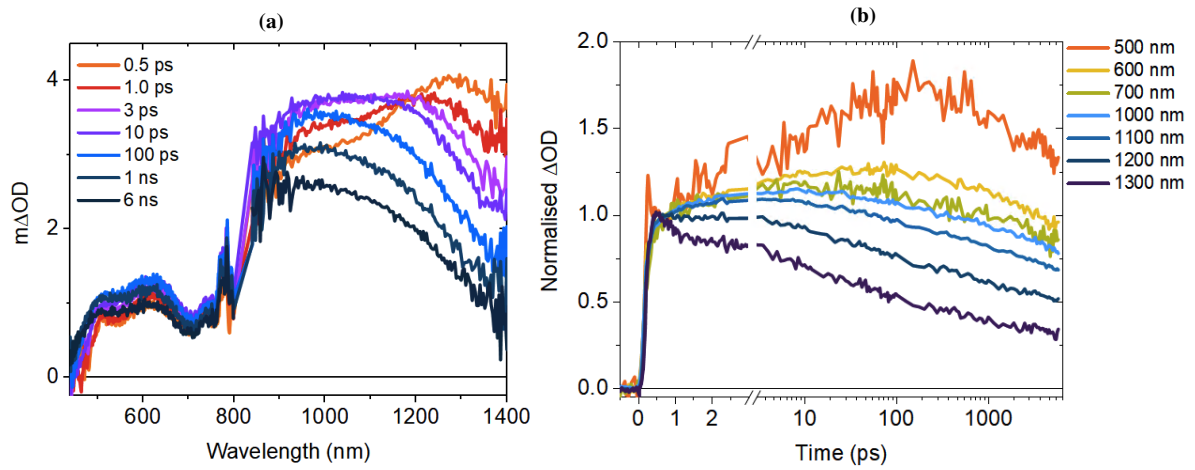

Figure 3.2: Ultrafast TAS measurements of $SrTiO_3$ in Ar, measured using a laser excitation intensity of 0.22 mJ cm^{-2}. a) Spectrum measured across the visible and NIR regions. b) Comparison of the decay kinetics probed at different wavelengths across the spectrum.

The decay kinetics exhibit a strong dependence on probe wavelength (Figure 3.2b) and consequently the spectral shape evolves over time (Figure 3.2a). With decreasing probe wavelengths, an increasingly slow rise in the optical signal is observed over 10-100 ps timescales. For probe wavelengths above 1100 nm, there is no rise in the signal observed and faster decay kinetics are observed immediately following photoexcitation. The contributions of the fast decay process and the slow rise to the spectrum, and the relationship between them, are investigated by global analysis.

The global analysis is conducted on decays probed in the NIR from 900-1350 nm, across a range of excitation intensities. Two components are extracted through the deconvolution of this spectral region (Figure 3.3a), which are consistent across the range of intensities measured (Figure A.4). Component 1 is dominant at probe wavelengths above 1100 nm (Figure 3.3a and corresponds to a fast decay process that is largely intensity independent (Figure 3.3b), suggesting that it predominantly corresponds to a monomolecular localisation or decay process.[27] Some deviation from a pure monomolecular decay process is observed, likely due to a small intensity dependent contribution. Meanwhile, component 2 dominates at probe wavelengths below 1100 nm (Figure 3.3a) and exhibits a slow rise typical of charge localisation, followed by an intensity dependent decay (Figure 3.3d). Interestingly, in the first 10 ps component 2 appears to grow as component 1 decays (Figure 3.3c). As a result, the rise of component 2 over the first 10 ps can be fitted using the following relationship between the increasing optical density of component

2 (ΔOD_2) and the decreasing optical density of component 1 (ΔOD_1):

$$\frac{d(\Delta OD_2)}{dt} = -B\frac{d(\Delta OD_1)}{dt} \tag{3.1}$$

Where B is a constant (0.15) that can be fitted globally for the intensities analysed (Figure A.4). The relationship between these components highlights the correlation between the fast decay of component 1 and the rise of component 2. More explicitly, this suggests that the fast decay of component 1 is due to the localisation of charge carriers, which manifests in the rise of component 2 that corresponds to these localised species. The consequence of the localisation process is observed in the as-measured ultrafast kinetics and spectra (Figure 3.2), in the fast decay and slow rise of the signal observed for probe wavelengths above and below 1100 nm respectively, and the resulting evolution of the spectrum with time.

Turning now to the intensity dependence of the as-measured $SrTiO_3$ decay kinetics illustrated in Figures 3.4a and A.5. At high probe wavelengths above 1100 nm, such as 1300 nm, the intensity dependence of the decay kinetics is very small (Figure A.5) and in agreement with the largely intensity independent decays of component 1 that dominate in this spectral region (Figure 3.3b). This suggests that the fast decays, attributed to charge localisation, correspond to an intensity independent pseudo first order process.[27] Meanwhile, following the initial rise, strongly intensity dependent decays are observed for the rest of the spectrum below 1100 nm. This is in agreement with the intensity dependent decays of component 2 after charge localisation and is indicative of a bimolecular recombination and/or trap filling processes.[99–101] For a bimolecular process, the corresponding decays can be fit by power laws with a linear gradient on a log-log plot, where $\Delta OD \propto t^{-\alpha}$.[100] The exponent, α, is dependent on the energetic distribution of localised states within the band gap. For an 'ideal' bimolecular process, the exponent is equal to 1. Meanwhile, exponents less than 1 are indicative of dispersive bimolecular recombination kinetics, that are frequently observed in metal oxides and commonly result from trapping/de-trapping mediated recombination via a distribution of mid-gap states.[102,103] The exponent values for the as measured bimolecular decays of $SrTiO_3$ (probed from 1100 nm and below) are between 0.12-0.14 (Figure A.6), suggesting highly dispersive bimolecular decay kinetics.

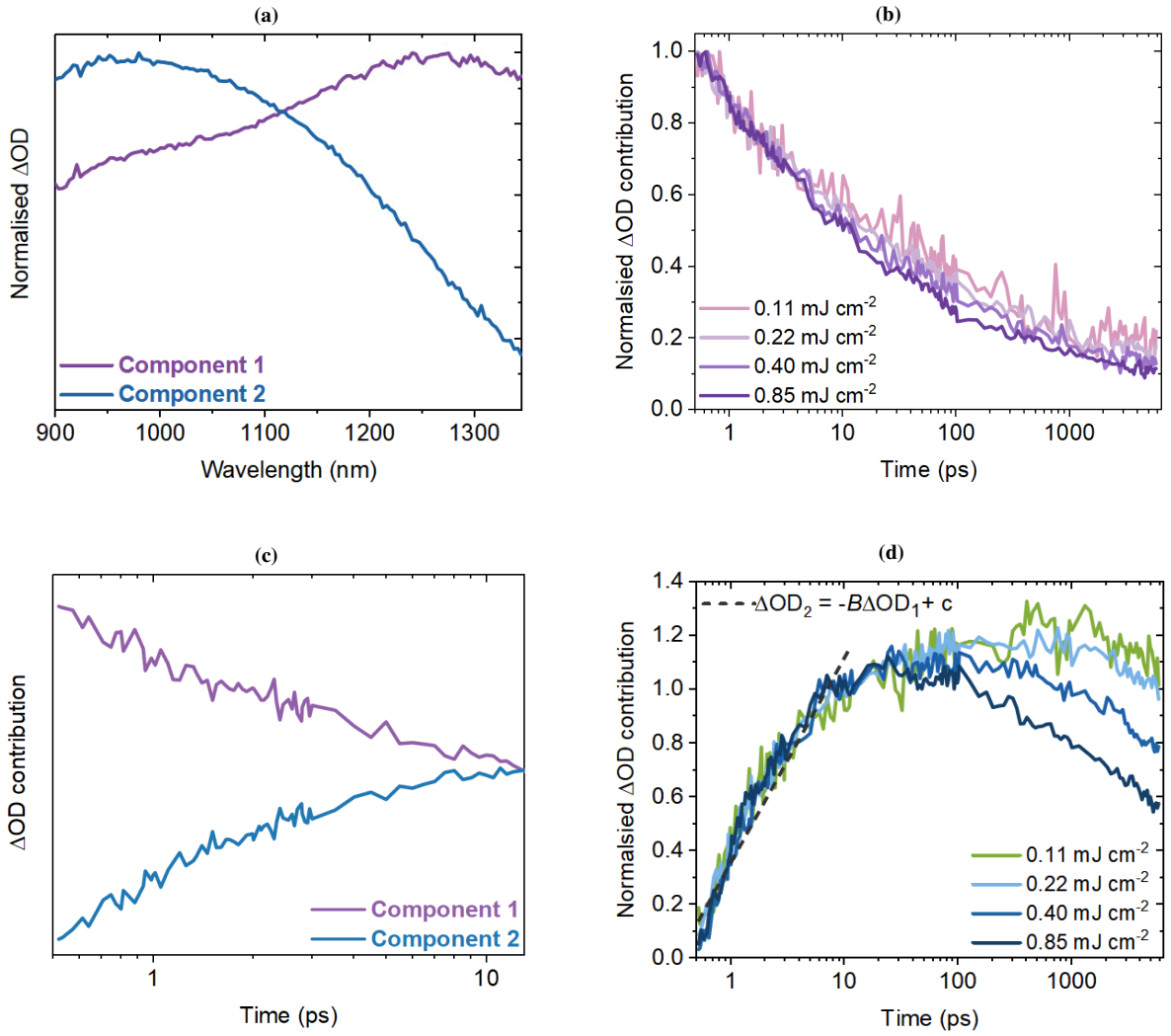

Figure 3.3: Global analysis of the ultrafast TAS decays of $SrTiO_3$. a) Deconvolution of the NIR region between 900 nm and 1350 nm to extract two components. b) Normalised kinetics of component 1 at a range of excitation intensities. c) Comparison of the kinetics of component 1 and 2 in the first 10 ps. d) Normalised kinetics of component 2 at a range of excitation intensities, with the dashed lines corresponding to the fitted kinetics as a function of ΔOD_1 (at 0.40 mJ cm^{-2}).

The bimolecular decays of $SrTiO_3$ are compared to other metal oxides (ensuring comparisons are made in the intensity dependent region and with comparable photogenerated charge densities), to reveal considerably slower bimolecular recombination kinetics and longer lifetimes in $SrTiO_3$ (Figure 3.4b). The slow bimolecular recombination of $SrTiO_3$ compared to other metal oxides is quantified by calculating their bimolecular rate constants, using the charge lifetimes ($t_{50\%}$) at a given excitation intensity, with the results shown in Table 3.1. The intensity dependent kinetics and parameters used for the calculations are shown in Figure A.7 and Table A.1 respectively. The bimolecular rate constant of 10^{-11} cm^3 s^{-1} for $SrTiO_3$ is at least two magnitudes lower than the other metal oxides, with a value of 10^{-9} cm^3 s^{-1} calculated for anatase

TiO_2 (dense or mesoporous) and $BiVO_4$. It is evident that the calculated bimolecular rate constants correspond to the differences in decay kinetics exhibited in Figure 3.4b. For example, with the similar decay kinetics and $t_{50\%}$ lifetimes of TiO_2 and $BiVO_4$, they have a calculated bimolecular rate constant that is of the same order of magnitude. It is noted here that fast non-bimolecular recombination processes occur on sub-ps timescales in α-Fe_2O_3. However, when normalising from 0.5 ps as has been done previously for α-Fe_2O_3,[102] the calculated bimolecular rate constant remains on the order of 10^{-8} cm^3 s^{-1}.

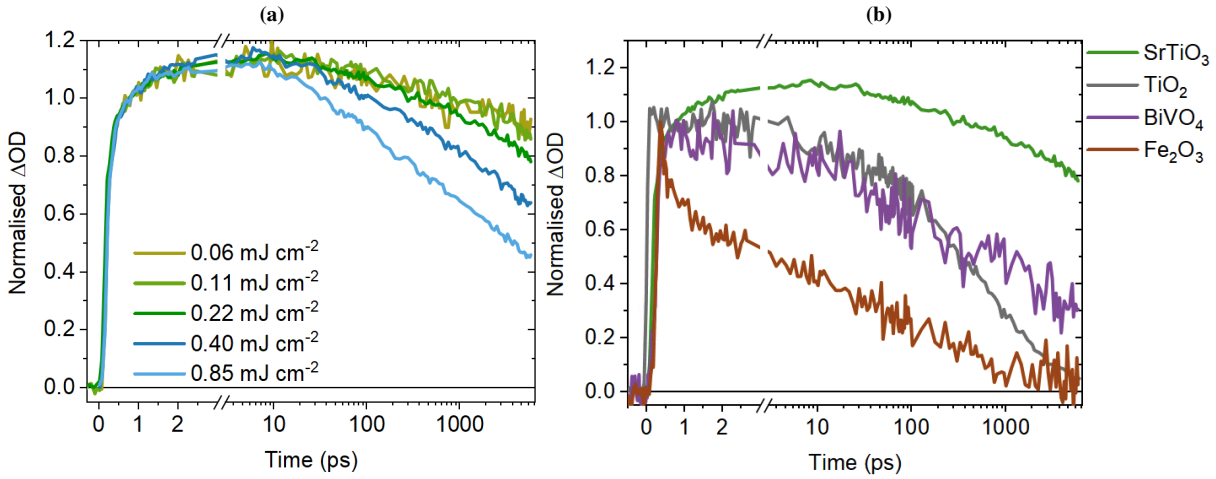

Figure 3.4: Intensity dependence of the ultrafast TAS decays of $SrTiO_3$ in Ar, probed at 1000 nm. b) Comparison of the decay kinetics of $SrTiO_3$ to other metal oxides in Ar, at photogenerated charge densities on the order of 10^{18} cm^{-3}.

Table 3.1: Calculated bimolecular rate constant (κ_2) of $SrTiO_3$, TiO_2 anatase, $BiVO_4$ and α-Fe_2O_3, using their intensity dependent ultrafast TAS decays.

	Rate constant κ_2 (cm^3 s^{-1})
$SrTiO_3$	10^{-11}
TiO_2 anatase	10^{-9}
$BiVO_4$ anatase	10^{-9}
α-Fe_2O_3 anatase	10^{-8}

In addition to the bimolecular rate constant, the intrinsic doping density was calculated from the intensity dependent decays measured by ultrafast TAS at 1000 nm and illustrated in Figure 3.4a. Here, the threshold excitation intensity from which intensity dependence is observed is converted into a photogenerated charge density, using the absorbance at the 355 nm excitation wavelength and the photon energy (Table A.2). At photogenerated charge densities below the

intrinsic doping density, photogenerated charge carriers predominantly recombine with the intrinsic charge carriers and intensity independent pseudo first order recombination is observed. At higher photogenerated charge densities that exceed the intrinsic doping density, photogenerated electrons and holes predominantly recombine with each other via intensity dependent bimolecular recombination. Therefore, the photogenerated charge density beyond which intensity dependent decays are observed can be taken as an approximation of the intrinsic doping density. The intrinsic doping density calculated herein can have contributions from the electronic doping density (e.g. the majority carrier density) and the chemical doping density from defects or trap states that can mediate bimolecular recombination. For metal oxides such as $SrTiO_3$, the latter is typically due to the presence of V_O that can serve as traps or dopants, depending on their occupancy.[83,104–106] The intrinsic doping density calculated for $SrTiO_3$ (10^{18} cm^{-3}) is in the range of that calculated herein (Table A.2) and reported for anatase TiO_2 and $BiVO_4$ (10^{16}-10^{19} cm^{-3}),[103,107] in addition to α-Fe_2O_3 (10^{17}-10^{20} cm^{-3}).[108,109]

3.4 Discussion

This chapter investigates the charge carrier dynamics of $SrTiO_3$ films on fast timescales immediately following photoexcitation. Whilst a handful of previous studies investigated the charge carrier dynamics of photogenerated charges in $SrTiO_3$ from μs timescales (and a single study does so on ps-ns timescales), a comprehensive understanding and analysis of the fast kinetic processes in $SrTiO_3$ was lacking prior to this investigation.

There is an intriguing evolution of the ultrafast TAS spectrum of $SrTiO_3$ with time, due to a slow rise in signals probed at wavelengths below 1200 nm. Through global analysis, two components are extracted from the spectrum and the slow rise (component 2) is correlated to the intensity independent decays observed immediately following excitation at higher probe wavelengths (component 1). The component spectra and the fitting of component 2 as a function of component 1 could be applied across all intensities measured (Figure A.4), strengthening the reliability of the results. Overall, this supports the model of a monomolecular localisation process, whereby the decay of component 1 corresponds to charges localising into the states corresponding to component 2. Due to the bimolecular recombination observed at later times in component 2, the fitting could only be reliably extended to 10 ps.[110,111] It is difficult to determine for certain whether the charge localisation observed corresponds to charge trapping or polaron formation.[21,97,100] A slow rise due to charge trapping of free carriers has been reported to occur in $SrTiO_3$ in 20 ps,[112] and into shallow trap states in TiO_2 in 10 ps. However, the timescales of polaron formation reported in metal oxides (0.1-1 ps) are significantly faster than the rise corresponding to localisation processes observed herein (10-100 ps),[97,113] If assuming that the localisation corresponds to charge trapping, the bimolecular recombination of these charges at later times suggests that it is into shallow trap states, with shallowly trapped electrons observed $\sim$0.3 eV below the CB in $SrTiO_3$.[84,85,112]

The charge localisation into these shallow states within the first 10 ps and their subsequent bimolecular recombination on ns timescales is illustrated in Figure 3.5. The bimolecular decay kinetics of $SrTiO_3$ are slow and generally do not approach a complete decay over the 6 ns measured, which is largely expected from the slow decay kinetics of $SrTiO_3$ reported previously.[86,87] For example, Kanemitsu and co-workers measured the decay dynamics of $SrTiO_3$ using photo-

luminescence (PL) and TAS (albeit at a single probe wavelength of 800 nm) and reported decays on ns timescales for high photogenerated charge carrier densities (10^{19}-10^{20} cm^{-3}), which were attributed to recombination.[87] The hole lifetimes measured in this chapter, at the highest laser intensities to give the most comparable photogenerated carrier densities of 7 x 10^{18} cm^{-3}, are also on ns timescales. Additionally, Cuk and co-workers used *in situ* ultrafast infrared spectroscopy to track the decay of a transient Ti-O• radical species in n-$SrTiO_3$ (attributed to a reactive site for photogenerated holes), and reported lifetimes on ns timescales at photogenerated carrier densities on the order of 1 x 10^{19} cm^{-3}.[86] However, in contrast to to Cuk and co-workers who attributed their ns decays to the reaction of holes, the ns decays observed herein are attributed to bimolecular recombination. The discrepency between the reaction timescales suggested from the lifetimes of the radical species and the results obtained in this thesis are explored in more detail in Chapter 6.

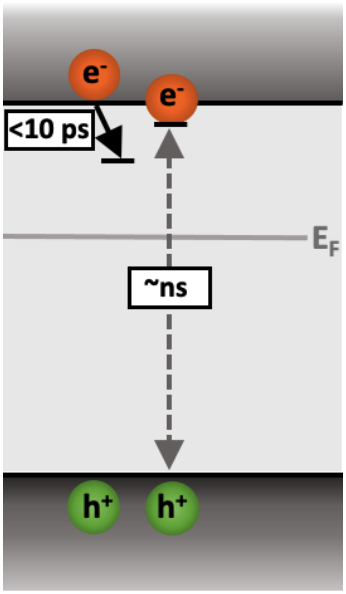

Figure 3.5: Schematic illustration of the charge localisation and bimolecular recombination processes observed in $SrTiO_3$. The timescales of these processes measured by ultrafast TAS are included in the white boxes.

Through demonstration of intensity dependent decay kinetics, bimolecular recombination is identified as the dominant recombination pathway in $SrTiO_3$. When comparing the bimolecular decay kinetics of $SrTiO_3$ to other metal oxides commonly employed in photocatalytic applications, it is immediately evident that $SrTiO_3$ exhibits remarkably slower decay kinetics and longer lifetimes. This observation is quantified by calculating and comparing their bimolecular rate constants. The result of this analysis is striking, with the bimolecular rate constant of $SrTiO_3$ (10^{-11} cm^3 s^{-1}) being at least two magnitudes lower than the other metal oxides. As significant losses to the yield of photogenerated charges in metal oxides can occur via fast re-

combination processes,[102] such as bimolecular recombination, the greatly suppressed bimolecular recombination rate will maximise the yield of photogenerated charges available to catalyse interfacial water splitting reactions.

The low degree of bimolecular recombination in $SrTiO_3$ observed herein is supported by the previous study on ultrafast $SrTiO_3$ kinetics by Kanemitsu and co-workers.[87] In this study, fitting of the transient decay using three parameters identified a negligible contribution of the parameter corresponding to bimolecular and non-radiative Auger recombination combined (compared to the other two parameters attributed to single carrier trapping and band-to-band Auger recombination). However, the contribution of bimolecular recombination was not quantified or compared to other materials in this case. The intrinsic doping density of $SrTiO_3$ (10^{18} cm^{-3}) is not notable and is equivalent to other metal oxides. Therefore, this is ruled out as a cause of the low bimolecular rate constant. A possible explanation for the low bimolecular rate constant of $SrTiO_3$ is its high dielectric constant. As the dielectric constant of a semiconductor increases, the Coulomb interactions are screened and the probability of photogenerated charges recombining is decreased due to a diminished capture radius.[114] Consequently, an increase in dielectric constant can decrease bimolecular recombination rates and increase lifetimes, as has been observed in perovskite and organic photovoltaics.[82,114–117] The dielectric constant of $SrTiO_3$ ($\sim$300)[118–121] is significantly higher than that of anatase TiO_2 (13-45),[122] rutile TiO_2 (70-170),[122,123] $BiVO_4$ (32-86)[124–126] and α-Fe_2O_3 (18-26).[127,128] Therefore, increased dielectric screening effects in $SrTiO_3$ may play a key role in suppressing recombination, thus offering an explanation for the lower bimolecular rate constant observed.

Turning now to comparing $SrTiO_3$ to $MAPbI_3$, a material that is typically employed in photovoltaic applications, rather than photocatalytic, but shares the perovskite crystal structure of $SrTiO_3$. Interestingly, their bimolecular decay kinetics are very similar (Figure 3.6) and accordingly so are their bimolecular rate constants, with literature reports for $MAPbI_3$ in the range of 10^{-11}-10^{-10} cm^3 s^{-1} (compared to the 10^{-11} cm^3 s^{-1} calculated for $SrTiO_3$).[82,129–131] Although there are a multitude of differences between $SrTiO_3$ and $MAPbI_3$, with both materials employed in state-of-the-art devices for their respective applications, it is interesting to note their similarities. They share their perovskite structure and compared to their counterparts, they exhibit characteristically long lifetimes and slow bimolecular recombination, in addition to notably high dielectric constants and charge screening effects. These latter effects are recognised

as an influential factor in photovoltaic performance,[88,114,115,117] but are often overlooked in photocatalysts despite the important role they can play.

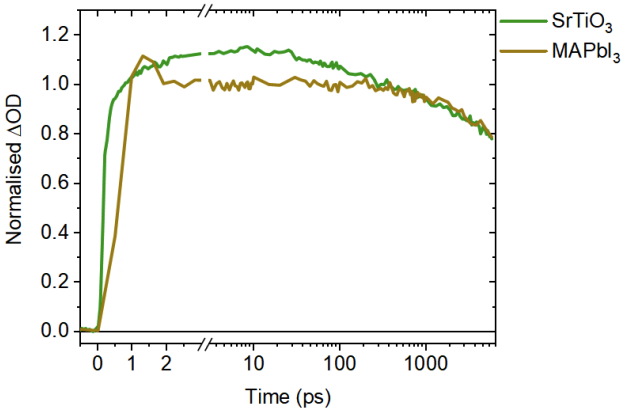

Figure 3.6: Comparison of the ultrafast TAS decay kinetics in Ar of $SrTiO_3$ and $MAPbI_3$.

The intrinsic doping density calculated from ultrafast TAS measurements (10^{18} cm^{-3}) can have contributions from the electrical doping density and chemical dopants that can mediate bimolecular recombination. For comparison, the chemical doping density at the surface from V_O can also be calculated, using the contribution of Ti^{3+} states measured by XPS and assuming that each V_O results in two Ti^{3+} states. This yields a chemical doping density of 10^{20} cm^{-3}, that is close to the doping density of WO_3 ($\sim 10^{20}$-10^{22})[132,133] which is widely recognised for its large doping density resulting from V_O. The large chemical doping density of $SrTiO_3$ is indicative of a high density of occupied V_O states present as Ti^{3+}. This suggests that the V_O states are sufficiently deep such that the E_F lies near the top of their distribution, to enable their high electron occupancy. The difference between the intrinsic doping density and chemical doping density calculated can be rationalised by the different doping types they consider. The intrinsic doping density calculated from ultrafast TAS measurements can have contributions from the electrical doping density and shallow chemical dopants that can mediate bimolecular recombination. Therefore, it is unlikely to account for the deep V_O dopants responsible for the calculation of the chemical doping density from V_O. Meanwhile, it is not unusual to observe higher chemical doping densities than intrinsic electrical doping densities, as activation of deep chemical dopant sites is often required for charge carriers to be released from these sites to subsequently contribute to conductivity and the electrical doping density.[21]

The morphology of the $SrTiO_3$ investigated in this chapter differs from that investigated in the particulate $SrTiO_3$ employed in the OPWS systems, explored in the following chapters of this thesis and in the literature.[24,43] However, properties such as their chemical composition and de-

cay kinetics on μs-s timescales are shown to be analogous, and the bimolecular rate constant is generally an intrinsic property that does not depend appreciably on metal oxide morphology. For example, the bimolecular recombination characteristics of a given TiO_2 polymorph (e.g. anatase) has previously been shown to not differ significantly between the dense and mesoporous morphologies.[27] This is further demonstrated herein by the equivalent bimolecular rate constants calculated for the dense and mesoporous morphologies of anatase TiO_2 (Table A.1). With this in mind, the observations in this chapter can somewhat be extended to what one can expect to observe for $SrTiO_3$ in general.

3.5 Conclusion

In this chapter, the fast (ps-ns) charge carrier dynamics of $SrTiO_3$ are investigated in detail by ultrafast TAS, with the aim of exploring how these properties underpin its suitability for OPWS applications. To the best of my knowledge, this is the first study to date that comprehensively measures and quantifies the properties of $SrTiO_3$ on these timescales, and compares them to those of other metal oxides commonly employed in photocatalytic applications. Under the conditions measured, dispersive bimolecular recombination was identified as the dominant decay pathway for $SrTiO_3$, suggesting that despite the slow decay kinetics significant disorder and trapping is present. Compared to the bimolecular decays of other metal oxides, those of $SrTiO_3$ are remarkably slow. Quantification of this observation, by way of calculating the bimolecular rate constant, reveals a bimolecular rate constant of $SrTiO_3$ that is at least two magnitudes slower than the alternative metal oxides. Appreciable losses to the yield of photogenerated charges typically occurs via fast processes such as bimolecular recombination. Therefore, a lower bimolecular recombination rate can facilitate higher yields of photogenerated charges for the slower timescales of interfacial water splitting reactions, and therefore enhance OPWS performance. The intrinsic doping density of $SrTiO_3$, determined from the intensity dependence of the decay kinetics, is in the range of that calculated and reported for other metal oxides, thus is unlikely to be responsible for the slower bimolecular recombination observed. However, the difference between the intrinsic and chemical doping density calculation was interesting and highlights the importance of defining what is meant by doping density. An alternative explanation explored for the slow bimolecular recombination is the very high dielectric constant of $SrTiO_3$, which can increase charge screening effects and subsequently suppress bimolecular recombination. Interestingly, the bimolecular recombination characteristics of $SrTiO_3$ bear more similarity to $MAPbI_3$ than the other metal oxides, with both $SrTiO_3$ and $MAPbI_3$ being perovskite structures with strong charge screening effects and slow bimolecular recombination.

Considering the above, it would be interesting to investigate further metal oxides that simultaneously exhibit low bimolecular recombination rates and high dielectric constants, in order to consolidate and explore the correlation between these two properties and their influence on photocatalytic performance. Even though the bimolecular rate constant is largely an intrinsic property, it would be useful to calculate it from the intensity dependent decays of an alternative

$SrTiO_3$ material. This would enable confirmation that the remarkably slow bimolecular rate constant observed in this work does indeed extend to $SrTiO_3$ in general. Assuming that the slow bimolecular recombination of $SrTiO_3$ is largely an intrinsic property, the results presented in this chapter indicate that it is a key property of $SrTiO_3$ that enables it to support high activities in photocatalytic systems. With this in mind, the properties of $SrTiO_3$ that likely contribute to the slow bimolecular recombination, including its high dielectric constant and perovskite structure (that also facilitates modifications due to its chemical flexibility), should be considered in the future design of photocatalysts for OPWS applications.

Chapter 4

The influence of Al^{3+} doping on the physical properties and charge carrier dynamics of $SrTiO_3$

The intrinsic properties of $SrTiO_3$ that facilitate long charge carrier lifetimes and make it an attractive base material for overall photocatalytic water splitting, OPWS, were highlighted in Chapter 3. However, Al^{3+} doping of $SrTiO_3$ via a flux mediated doping process is required to achieve the state-of-the-art OPWS performance of Al:$SrTiO_3$/$RhCrO_x$ photocatalysts. In this chapter, the physical properties and charge carrier dynamics of the exact $SrTiO_3$ and Al:$SrTiO_3$ utilised by Domen and co-workers in their photocatalysts are studied. Al^{3+} doping modifies the physical properties of $SrTiO_3$, primarily by suppressing Ti^{3+} recombination centres and introducing a faceted morphology. Following these modifications, suppressed recombination on μs-s timescales is observed and higher steady-state charge densities are achieved. These advantageous features are attributed to enhanced charge separation, resulting from the introduction of an internal electric field in the faceted structure, and suppressed Ti^{3+} states. Through these investigations, the key effects of Al^{3+} doping that contribute to its critical role in the OPWS photocatalysts are explored.

4.1 Introduction

The quantum efficiency of a photocatalyst is limited by recombination, with defects often offering recombination sites,[32] as was introduced in Chapter 1. In $SrTiO_3$, such defects can take the form of Ti^{3+} states that are associated with recombination centres.[34] The formation of these defects is described in Equations 4.1 and 4.2, using the Kröger-Vink notation.[91,134] These Ti^{3+} states are believed to be formed by the dissociation of Ti-O bonds at the lattice surface, resulting in the release of oxygen and the subsequent generation of V_O and free elections (Equation 4.1).[34] In the sub-stoichiometric $SrTiO_3$ that results, the free electrons reduce Ti^{4+} to sub-band gap Ti^{3+} states, in order to maintain charge neutrality (Equation 4.2). It is desirable to minimise these limiting defects and improve crystallinity, to promote charge migration and sufficient charge lifetimes for catalysing interfacial water splitting reactions. This can be achieved by exploiting the chemical flexibility of the $SrTiO_3$ perovskite structure through aliovalent doping.

Aliovalent doping of $SrTiO_3$ with a cation of lower valence than Ti^{4+} but similar ionic radii, such as Al^{3+}, has been shown to decrease the concentration of Ti^{3+} by charge compensating for the V_O and by substituting Ti^{4+} states (Equation 4.3).[34,91] In previous work by Domen and co-workers, Al:$SrTiO_3$ was prepared using a flux-mediated doping process (described in detail in Chapter 2) that introduces Al^{3+} ions and facilitates the growth of particles with improved crystallinity.[43] Following the doping procedure, they report a change in morphology from a cubic to truncated cubic structure, and crucially, a dramatically improved OPWS performance of Al:$SrTiO_3$ compared to pristine $SrTiO_3$ (when a $RhCrO_x$ proton reduction co-catalyst has been added via impregnation in both cases).[43] The Al:$SrTiO_3$ prepared in this way is the central building block for the state-of-the-art OPWS photocatalysts fabricated by Domen and co-workers, that achieve a near-unity AQY when modified with co-catalysts.

$$O_O^X \rightarrow V_O^{\bullet\bullet} + \frac{1}{2}O_2 + 2e^{'} \tag{4.1}$$

$$2e^{'} + 2Ti_{Ti}^X \rightarrow 2Ti_{Ti}^{'} \tag{4.2}$$

$$Al_2O_3 + 2Ti_{Ti}^X \rightarrow 2Al_{Ti}^{'} + V_O^{\bullet\bullet} + 2TiO_2 \tag{4.3}$$

The optimisation of the flux-mediated doping process has been investigated in detail in prior work.[43] However, the role of Al^{3+} doping on the *in situ* charge carrier dynamics of $SrTiO_3$ and how this can aid explanation of the improved OPWS performance, remains relatively unexplored. A previous study by Yamakata et. al., on the photocatalysts fabricated by Domen and co-workers, used TAS in the visible to near-IR range to explore the effects of Al^{3+} doping on the charge carrier dynamics.[84] Peaks at 500 nm and 800 nm in the TAS spectra were observed in $SrTiO_3$ and Al:$SrTiO_3$ and attributed to trapped charge carriers, which exhibited enhanced lifetimes in Al:$SrTiO_3$. This study was limited by the application of TAS exclusively on sub-μs timescales and under gaseous conditions, that are unlikely to be representative of water splitting conditions.

Osterloh and co-workers used XPS, surface photovoltage spectroscopy (SPS) and density functional theory (DFT) calculations to study the effects of Al^{3+} doping on $SrTiO_3$.[91] Through XPS and DFT calculations, they measured the suppression of Ti^{3+} states and a subsequent E_F shift towards the VB in Al:$SrTiO_3$. Meanwhile, they assigned their SPS results to increased electron diffusion lengths and decreased hole trapping in Al:$SrTiO_3$, although neither of these features are measured directly or under photocatalytic water splitting conditions. Since Osterloh and co-workers fabricated their $SrTiO_3$ and Al:$SrTiO_3$ in-house, using a different method to that of Domen and co-workers, their results cannot be directly applied to the photocatalysts that are the focus of this chapter. For example, there is a fundamental difference in the physical properties including the optical absorption, with the brown colour of the Al:$SrTiO_3$ fabricated by Osterloh and co-workers differing from the white Al:$SrTiO_3$ fabricated by Domen and co-workers and studied herein.

In this chapter, the $SrTiO_3$ and Al:$SrTiO_3$ produced by Domen and co-workers is characterised in detail, through the use of techniques including SEM, XRD and XPS. After establishing the effects of Al^{3+} doping on the physical properties of $SrTiO_3$, the charge carrier dynamics of Al:$SrTiO_3$ are investigated and compared to $SrTiO_3$ using DRTS and PIAS. Using these time-resolved techniques, they are investigated *in situ* to understand the impact of Al^{3+} doping on the charge carrier dynamics of photogenerated charges relevant to water splitting.

4.2 Experimental methods

The Domen group at Shinshu University in Japan (specifically Prof. Kazunari Domen, Prof. Takashi Hisatomi and Prof. Tsuyoshi Takata) are acknowledged for fabricating and providing the $SrTiO_3$ and Al:$SrTiO_3$ photocatalysts investigated in this chapter. The $SrTiO_3$ was as-purchased from Wako chemicals and the Al:$SrTiO_3$ was prepared by their flux-mediated Al^{3+} doping method described in Chapter 2.[43] Photocatalyst sheets from these powders were prepared on quartz with SiO_2 nanoparticles, in order to facilitate water filtration into the material and gas evolution, as reported previously.[37]

Materials are characterised by XRD, SEM, UV-Vis and XPS. Apart from the XPS, this characterisation was largely confirming what had been reported previously.[37,38,40,43] The charge carrier dynamics investigated by PIAS and DRTS are both conducted in diffuse reflectance mode due to the scattering nature of the samples, with detailed descriptions of these techniques included in Chapter 2. These time-resolved spectroscopic measurements are conducted in H_2O and reagents are degassed with N_2, unless otherwise stated. When employing scavengers, pure 2-propanol and 0.1 M $Na_2S_2O_8$ are used as hole and electron scavengers respectively. Due to the scattering nature of these samples, it is not possible to measure them using the ultrafast TAS set-up which operates exclusively in transmission mode. In DRTS, the excitation fluence from the 355 nm laser is $\sim$400 μJ cm^{-2}, apart from in intensity dependence measurements. Whilst in PIAS, the excitation intensity from the 365 nm LED is $\sim$2.7 mW cm^{-2}, to simulate the photon flux expected to be absorbed under 1 sun AM1.5G illumination, apart from in intensity dependence measurements. The quantum yield, QY, of photogenerated holes measured under steady-state PIAS conditions (calculated using the ratio between the moles of photogenerated holes to the moles of photons absorbed multiplied by the $t_{50\%}$ lifetimes, as explained in Section 2.3.7) is discussed as a relative quantum yield, termed RQY. This is due to the scattering nature of the samples, meaning that absolute determination of the moles of photogenerated holes is not possible, so the RQY values can only be compared relative to the other $SrTiO_3$-based photocatalysts investigated in this thesis.

Preliminary hard X-ray photoelectron spectroscopy (HAXPES) work was conducted by Dr Anna Regoutz and Dr Curran Kalha (University College London) at the Petra III synchrotron in

Hamburg, Germany. Dr Benjamin Moss (Imperial College London) assisted with the XPS.

4.3 Results

4.3.1 Physical characterisation

XRD diffraction patterns were obtained for the powder form of the photocatalysts, to clearly see the spectral features due to the photocatalyst components, and not the SiO_2 nanoparticles or quartz substrate present in the sheets. The XRD data are shown in Figure 4.1, with the corresponding full width at half maximum (FWHM) of the {110} diffraction peak in (Table 4.1). The spectra obtained agree well with that expected for $SrTiO_3$, of the pure cubic or truncated cubic structures.[135] For both compositions, peaks are assigned solely to $SrTiO_3$, with no peaks from aluminium or other species observed. The decrease in the FWHM of the {110} peak following Al^{3+} doping, from 0.17 to 0.13 (Table 4.1), suggests decreased strain of the crystals and increased crystallinity,[43,84] or alternatively a decreased crystallite size.[94]

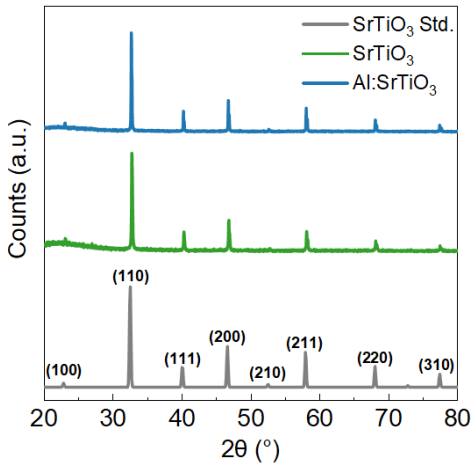

Figure 4.1: XRD diffraction pattern of $SrTiO_3$ and Al:$SrTiO_3$ powders compared to an $SrTiO_3$ standard (ICDS collection no: 9163).

Table 4.1: FWHM of the dominant {110} XRD peak of $SrTiO_3$ and Al:$SrTiO_3$.

	FWHM {110}
$SrTiO_3$	0.17
Al:$SrTiO_3$	0.13

SEM imaging was conducted to compare the morphology of the photocatalysts. The $SrTiO_3$ is

predominantly cubic particles of varying shapes and sizes, ranging from 150-500 nm in diameter (Figure 4.2a). Al:$SrTiO_3$ particles are slightly larger, with 200-800 nm diameters (Figure 4.2b). The dominant morphology of Al:$SrTiO_3$ is a faceted truncated cubic structure, the equilibrium crystal shape of $SrTiO_3$ that minimises the energy of the exposed facets.[43,136] The flat facets are assigned to {100} facets, whilst the curved edge facets are not clearly defined but are predominantly in the [110] direction and are referred to as the {110} facets herein for simplicity.[38,136] It is the energy difference between the {100} and {110} facets that results in an internal electric field and enables the facet selective photodeposition of co-catalysts achieved in prior work.[38]

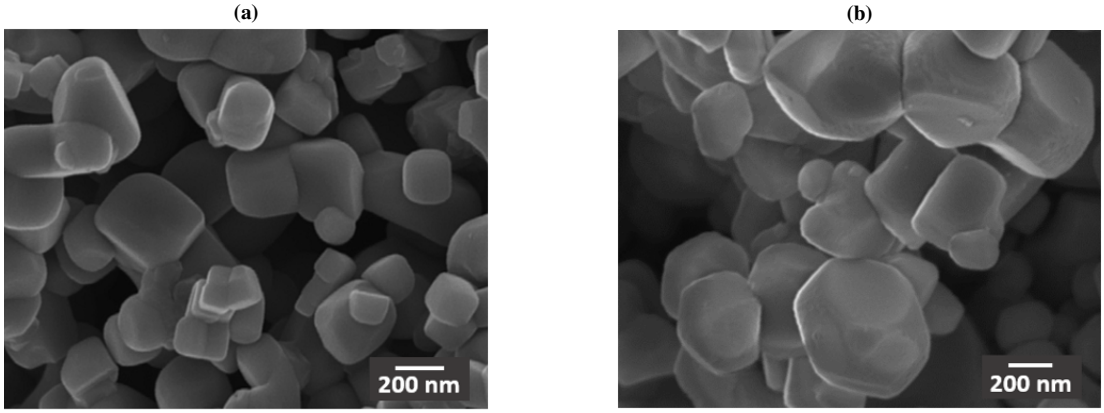

Figure 4.2: SEM image of a) $SrTiO_3$, and b) Al:$SrTiO_3$.

The surface chemical compositions of the photocatalysts were determined by XPS. Core line spectra of Ti $2p_{3/2}$ (Figure 4.3a and 4.3b) are included in this section, with additional spectra included in Figures A.8 and A.9 for reference. In the Ti $2p_{3/2}$ spectrum of $SrTiO_3$ the majority of states are assigned to Ti^{4+}, but with a relative contribution of Ti^{3+} of 3%. This is expected due to the typically non-stoichiometric nature of $SrTiO_3$ resulting in Ti^{3+} formation and is similar to the 4% Ti^{3+} contribution measured for the $SrTiO_3$ in Chapter 3. Successful introduction of Al^{3+} ($\sim$5 at%) is confirmed by the presence of a peak at 74.0 eV in the Al 2p spectra, agreeing with the 74.1 eV expected for Al^{3+}.[137] In Al:$SrTiO_3$, the Ti^{3+} states are completely suppressed within the resolution of the measurement ($\sim$1% at%), in line with the aims and expected role of Al^{3+} doping.[34,43] Although XPS is a surface measurement,[138,139] previous work on these materials by Domen and co-workers has measured Al in the bulk of Al:$SrTiO_3$ following their flux mediated doping procedure, by Inductively Coupled Plasma Optical Emission spectroscopy (ICP-OES).[43]

Alongside the core line spectra, valence XPS spectra were measured to approximate the VB position (E_{VB}) relative to the E_F (0 eV on the binding energy scale). The structure of the VB

XPS spectra for $SrTiO_3$ and Al:$SrTiO_3$ are analogous and a E_F position ~2 eV above the VB is estimated for each (Figure 4.3c). The stability of the VB position relative to the E_F suggests that the E_F does not shift. The absence of a significant shift in either the O 1s or Ti 2p core binding energies supports a stable E_F position (Figure 4.3d), given E_{BE} = E_F - E_i (where E_{BE} and E_i correspond to the binding and initial energy of the electron respectively).[59]

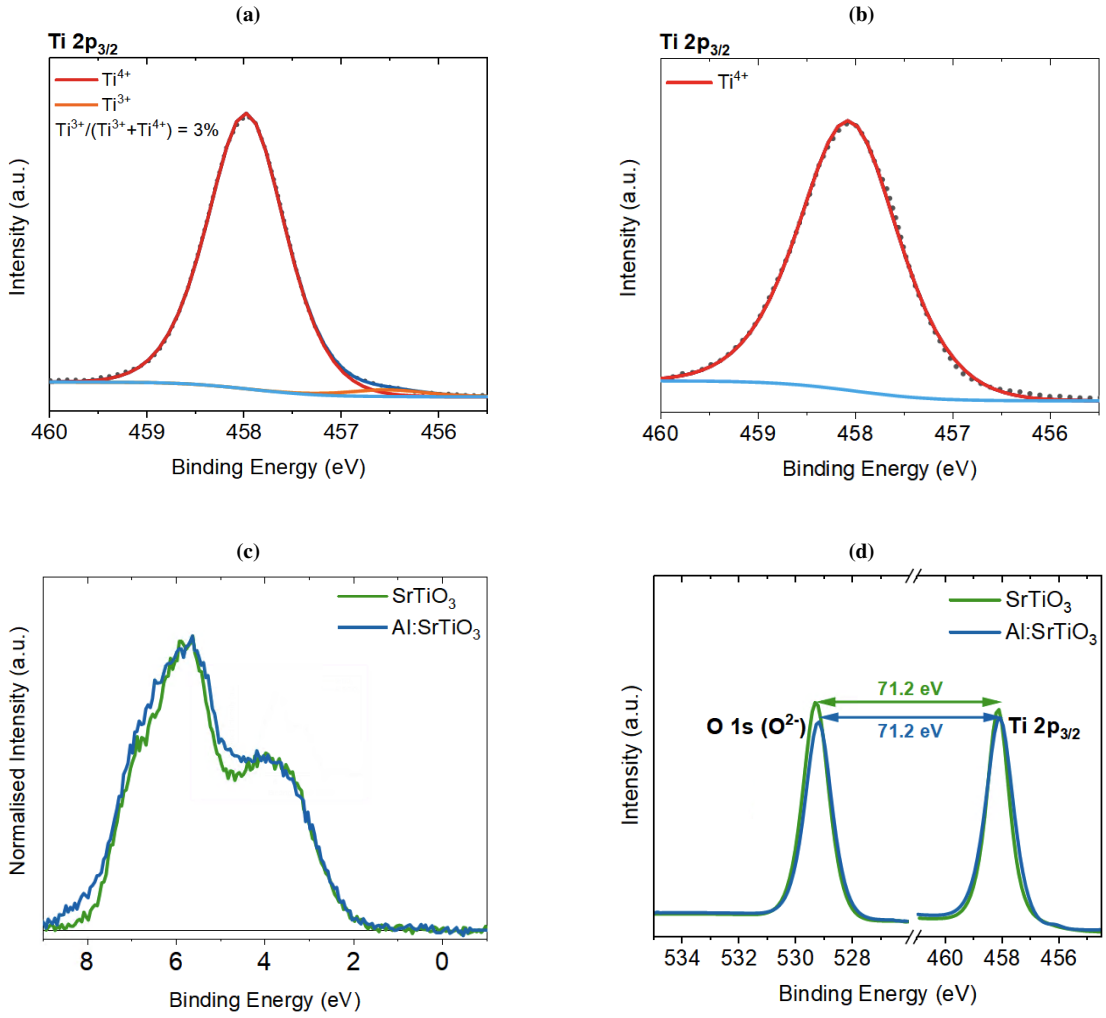

Figure 4.3: XPS Ti $2p_{3/2}$ core line spectra of a) $SrTiO_3$, and b) Al:$SrTiO_3$. c) Normalised valence XPS spectra of $SrTiO_3$ and Al:$SrTiO_3$. d) Comparison of the XPS core lines of Ti $2p_{3/2}$ and O 1s (O^{2-}), showing very negligible shifts of the peaks following Al^{3+} doping and a constant binding energy difference of 71.2 eV.

Steady-state optical absorption measured by UV-Vis spectroscopy identified equivalent properties of $SrTiO_3$ and Al:$SrTiO_3$ (Figure 4.4a). There is a marginal tail absorption towards the NIR in all compositions, but this is likely the result of increased scattering and is inconsequential to light absorption affecting the yield of photogenerated charges and performance. In both cases, an indirect band gap of 3.25 eV nm was identified from Tauc plots (Figures 4.4b and 4.4c) and is consistent with what is expected for bulk $SrTiO_3$ (~3.2).[34,92,93]

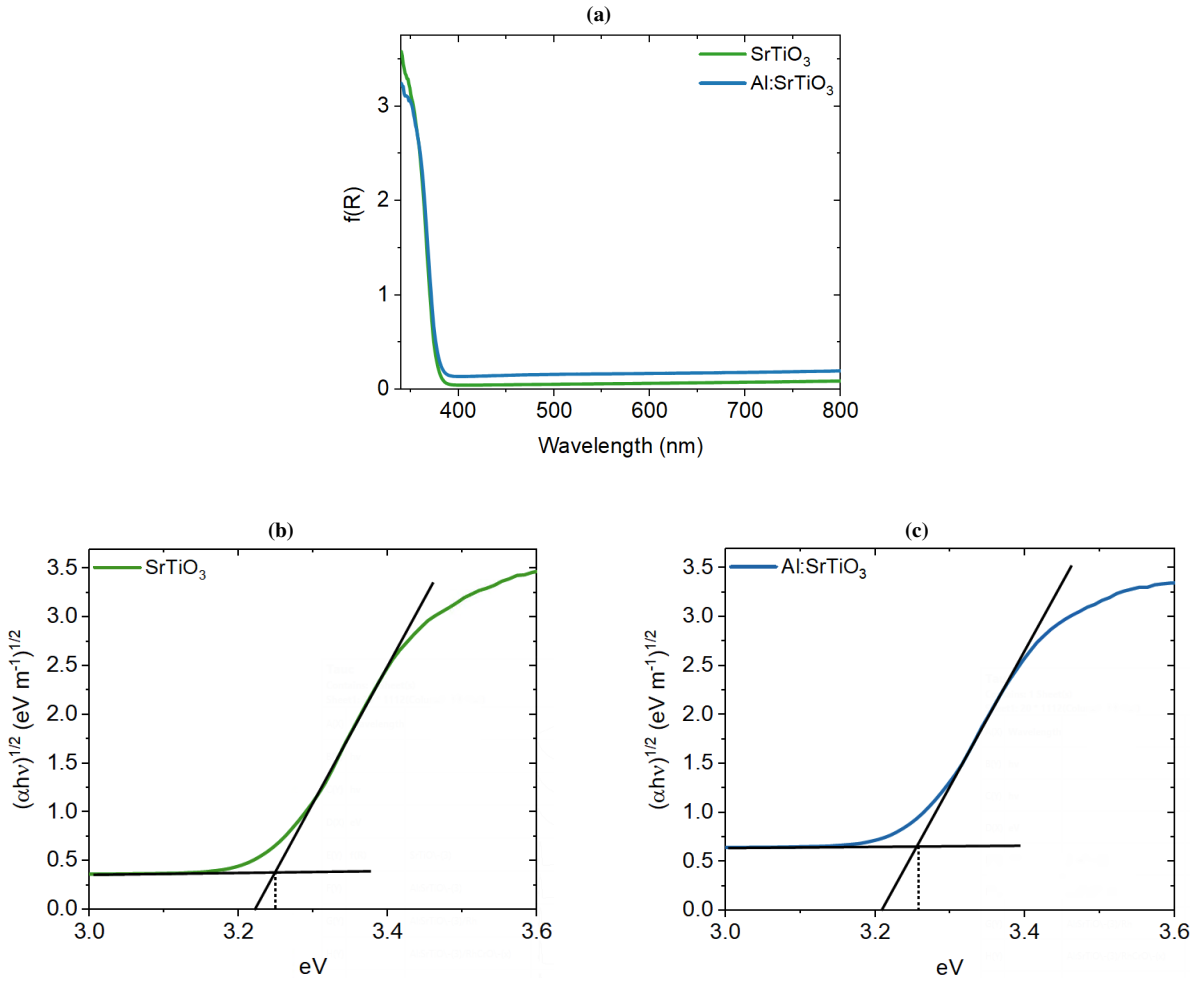

Figure 4.4: a) Ground state optical absorption measured by UV-Vis, and reported using the Kubelka-Munk function f(R), for $SrTiO_3$ and Al:$SrTiO_3$. Tauc plots from optical data obtained by UV-Vis spectroscopy to obtain the indirect band gaps of b) $SrTiO_3$ (E_g = 3.25 eV) and c) Al:$SrTiO_3$ (E_g = 3.25 eV)

4.3.2 Steady-state charge carrier dynamics

The impact of Al^{3+} doping on the steady-state charge carrier dynamics was investigated by PIAS, in H_2O and using a LED excitation intensity corresponding to 1 sun illumination, unless otherwise stated. The spectra of $SrTiO_3$ and Al:$SrTiO_3$ are dominated by <600 nm probe wavelengths, whilst at increasing probe wavelengths the signal decreases consistently (Figure 4.5a). Although signals <600 nm dominate for $SrTiO_3$ and Al:$SrTiO_3$, the relative amplitude of the signals at longer wavelengths are suppressed in Al:$SrTiO_3$ compared to in $SrTiO_3$, as has also been seen in the literature on earlier timescales measured by TAS.[85] On average, a three-fold increase in PIA amplitude is observed across the spectrum upon Al^{3+} doping (Figure 4.5a). Given the commensurate UV-Vis absorption properties (Figure 4.4) and the large magnitude

of this increase, this is indicative of an increase in the steady-state charge density under PIAS conditions and suppressed recombination prior to the measurement timescales.

The steady-state charge density (i.e. the population of species probed by PIAS) has contributions from the lifetime of the PIAS signal and the yield of charge generation. The lifetimes of the probed species in $SrTiO_3$ and Al:$SrTiO_3$ are analogous (Figure 4.5b inset). Thus, an increase in the RQY of charge generation in Al:$SrTiO_3$ is responsible for the increased population. The RQY of hole generation is three times greater for Al:$SrTiO_3$ compared to $SrTiO_3$ (0.9 vs. 0.3, Table 4.2), suggesting more efficient conversion of absorbed photons to photogenerated charges that persist under steady-state conditions and on ms-s timescales.

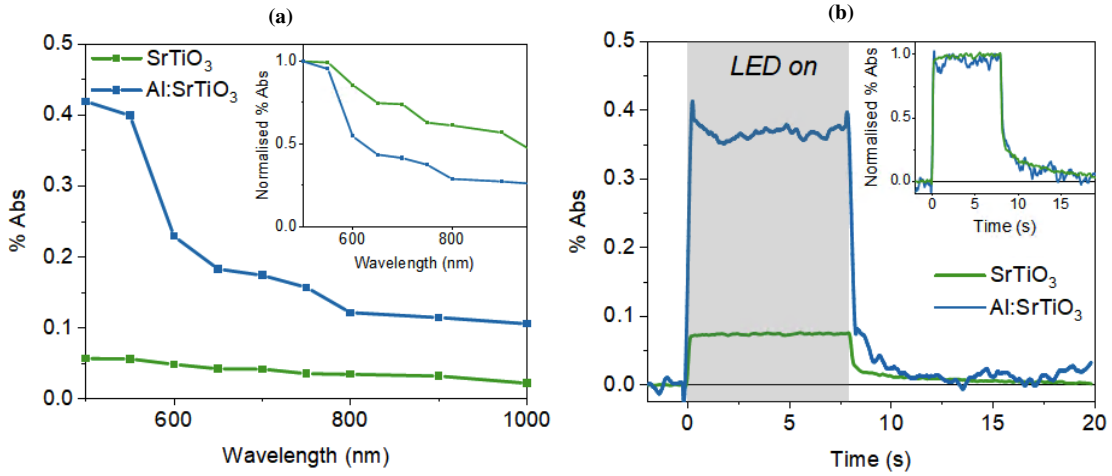

Figure 4.5: a) Comparison of the PIAS spectra in H_2O of $SrTiO_3$ and Al:$SrTiO_3$ as measured, with normalised spectra compared in the inset. b) Comparison of the PIAS kinetics of $SrTiO_3$ and Al:$SrTiO_3$ in H_2O and probed at 500 nm, with normalised kinetics compared in the inset.

The effects of scavengers on the spectral shape were investigated to determine the spectral signature of holes and electrons. Under anaerobic hole scavenging conditions (2-propanol), the spectral shape of $SrTiO_3$ changes dramatically, such that the early NIR signals increase and dominate the spectrum, whilst the <600 nm feature is absent (Figures 4.6a and A.10). This suggests that the broad early NIR absorption corresponds to electrons, whilst holes are probed <600 nm, in good agreement with spectral assignments from previous spectroscopic studies on $SrTiO_3$.[84,85] This is supported by the decrease in the early NIR contribution in $Na_2S_2O_8$ electron scavenger (Figure A.10) which also suggests that electrons are probed in this region, although the effect is small. The overall impact of the scavengers is analogous for Al:$SrTiO_3$ (Figures 4.6 and A.11) and thus the spectral assignments are unchanged following Al^{3+} doping. With this

Table 4.2: Comparison of the RQYs of hole generation calculated for $SrTiO_3$ and Al:$SrTiO_3$ at 60% of 1 sun illumination intensity. The RQY is calculated by dividing the calculated QY by the highest QY reported of the $SrTiO_3$-based photocatalysts.

	Amplitude (%Abs)	$t_{50\%}$ (s)	RQY
$SrTiO_3$	0.1	0.14	0.3
Al:$SrTiO_3$	0.3	0.13	0.9

in mind, the decreased contribution of the early NIR signals to the spectrum in Al:$SrTiO_3$ compared to $SrTiO_3$ (Figure 4.5), suggests a decreased prevalence of electrons probed in the former and is perhaps due to the suppression of Ti^{3+} donor states (with the impact of this on charge carrier dynamics explored in more detail in Section 4.3.3 and 4.4). The extent of the changes observed under scavenging conditions, in particular in 2-propanol, is decreased in Al:$SrTiO_3$. This could be due to Al^{3+} doping altering surface defects by changing the surface composition and morphology, as surface defects have previously been correlated to changes in the reactivity of $SrTiO_3$-based materials towards scavengers.[83–85] The main difference observed in the hole scavenging effects is the reduced dominance of the <600 nm hole signals, suggesting that these surface changes decrease the reactivity of hole species towards the scavenger. Alternatively, there could be an increased mixture of electron and hole contributions in each spectral region.[84,85]

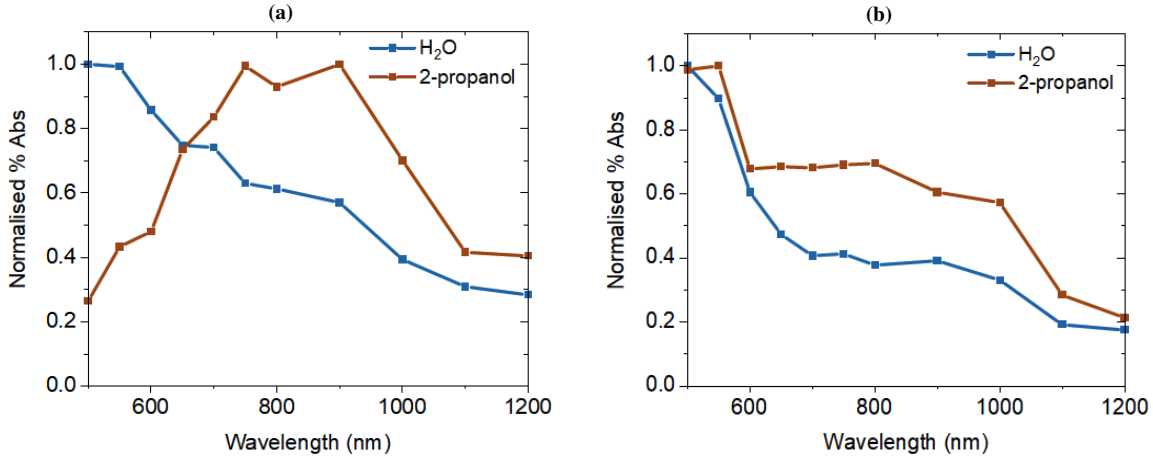

Figure 4.6: Effect of 2-propanol hole scavenger on the normalised PIAS spectrum, compared to in H_2O for a) $SrTiO_3$, and b) Al:$SrTiO_3$.

PIAS measurements were undertaken under continuous BG illumination from an additional 365 nm LED, simulating the effects of continuous illumination conditions experienced during device operation. Here, BG illumination can fill states prior to the PIAS measurement, resulting

in a decrease in the optical signals attributed to these filled states. Under BG illumination, the early NIR region of $SrTiO_3$ and Al:$SrTiO_3$ is largely unchanged (Figure A.12), whilst at lower wavelengths (corresponding to holes) the signal amplitude is suppressed considerably. This suggests that BG illumination predominantly fills hole states prior to the PIAS measurement.

The intensity dependence of the steady-state charge carrier dynamics and the dominant decay processes were investigated by varying the LED excitation intensities in PIAS. In $SrTiO_3$ and Al:$SrTiO_3$, the optical signals increase with increasing intensity, until they plateau (Figure 4.7). The increase in optical signal is assigned to increased charge generation at higher intensities and therefore an increase in the charge densities achieved in the steady-state. When the signal amplitude plateaus, the rate of charge consumption balances the rate of charge generation, and there is a saturation in the steady-state charge density. This is attributed to non-linear processes dominating at higher photogenerated charge densities, such as bimolecular recombination and/or trap filling processes.[99–101] Upon turning the light off, a fast initial decay is observed. In $SrTiO_3$, the rate of this initial decay is independent of excitation intensity (Figure 4.7a). This is typical for a monomolecular decay pathway where one charge is in excess, such as pseudo first order recombination of the majority carrier (electrons in the case of n-type $SrTiO_3$).[27] In contrast, the initial decay in Al:$SrTiO_3$ accelerates with increasing intensity (Figure 4.7b), which is a common observation for the decay of reactive charges in metal oxides,[78–80] and is due to increased rates of charge consumption with increasing excitation intensity. Given the low water splitting activity of Al:$SrTiO_3$, this is primarily attributed to increased recombination rates.

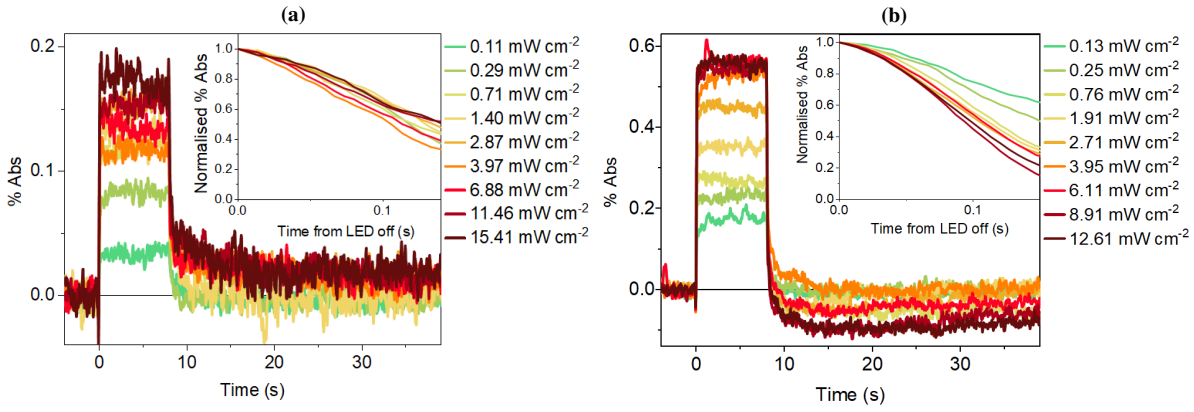

Figure 4.7: Intensity dependence of the PIAS traces probed at 500 nm in H_2O, with insets showing the normalised decay kinetics of the PIAS signal following light-off, for a) $SrTiO_3$, and b) Al:$SrTiO_3$.

Through the above PIAS studies, it is evident that Al^{3+} doping enables higher charge densities

and RQYs to be achieved under steady-state conditions, applicable to those of water splitting. In Al:$SrTiO_3$, lower intrinsic doping densities are implied by the change from intensity independent pseudo first-order monomolecular decays in $SrTiO_3$, to intensity dependent decays in Al:$SrTiO_3$. These results are consistent with the role of Al^{3+} doping in enhancing the morphology and passivating Ti^{3+} donor states that serve as recombination centres.

4.3.3 Charge carrier dynamics on μs-s timescales

The charge carrier dynamics of $SrTiO_3$ and Al:$SrTiO_3$ on earlier (μs-s) timescales were investigated by DRTS, to extend the investigation of charge carrier dynamics beyond the steady-state conditions and slower (ms-s) timescales of PIAS. Despite the different morphology of these $SrTiO_3$ particles to the dense $SrTiO_3$ films investigated in Chapter 3, they have a similar chemical composition and decay kinetics on μs-s timescales (Figure A.13). In $SrTiO_3$ and Al:$SrTiO_3$, the DRTS spectrum measured at 10 μs comprises of two main features: a broad feature in the early NIR and an increase in signal amplitude below 600 nm (Figure 4.8a). The feature in the NIR is unique to the DRTS spectra of these materials and is not present in PIAS. However, due to the faster decays in the NIR, over time the DRTS spectra evolve to resemble a shape that is more akin to the PIAS spectra (Figure A.14). Despite the similar spectral features of $SrTiO_3$ and Al:$SrTiO_3$, Al:$SrTiO_3$ exhibits a higher signal amplitude and decelerated decays across the spectrum (Figure 4.8). For example, the charge lifetimes ($t_{50\%}$) are increased by an order of magnitude following Al^{3+} doping, increasing from 0.4-3 ms and 0.03-0.2 ms, at 500 nm and 800 nm respectively.

In $SrTiO_3$ and Al:$SrTiO_3$, there is a distinct change in the DRTS decay kinetics for the spectral features probed below and from 600 nm (Figure 4.9), whereby slower kinetics are observed at wavelengths below 600 nm. The decays are complex and apart from the 800 nm $SrTiO_3$ decay they cannot be fit simply by power laws. However, they can be fit reasonably well by two stretched exponentials (Figure A.15), that are typically associated with dispersive recombination due to a distribution of trap states and multiple trapping events.[100,140] Spectral assignments from the PIAS studies and literature TAS investigations, assign species probed below and from 600 nm to holes and electrons respectively.[27,84,85,97,98] Unfortunately, scavenger studies in DRTS were inconclusive (Figures A.16 and A.17), as has previously been observed and attributed to

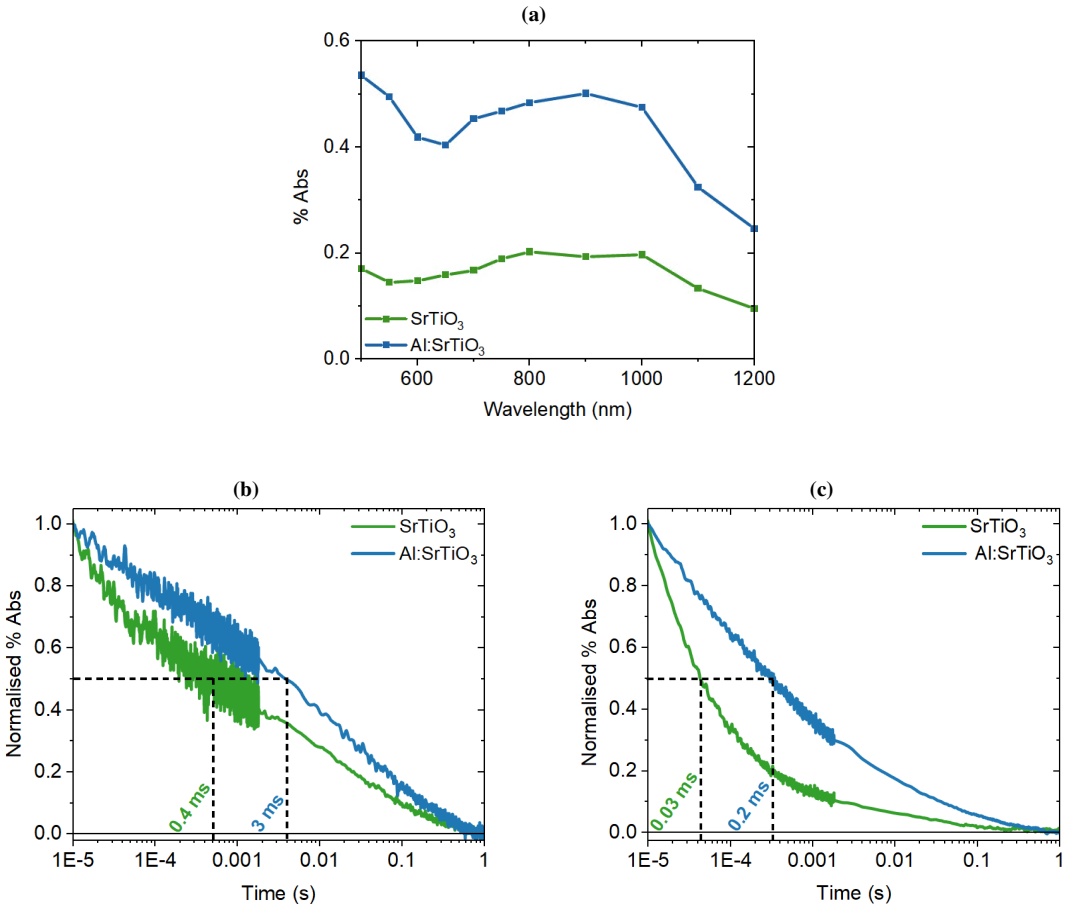

Figure 4.8: Comparison of the DRTS spectra of $SrTiO_3$ and Al:$SrTiO_3$ at 10 μs in H_2O. Comparison of the decay kinetics and $t_{50\%}$ times in H_2O of $SrTiO_3$ and Al:$SrTiO_3$, probed at b) 500 nm, and c) 800 nm.

low reactivity of the probed charges towards the scavengers.[36,83] Nevertheless, the distinct decay kinetics observed for holes and electrons suggests that they do not simply correspond to the recombination of the species probed. Instead, an additional decay pathway that extends the lifetimes of holes is present.

Following initial DRTS studies, measurements were undertaken under continuous BG illumination to further investigate the origins of the two decay pathways observed (below and from 600 nm). Interestingly, under BG illumination analogous decay kinetics are observed across the spectrum for $SrTiO_3$, with an absence of the slower decays observed at probe wavelengths <600 nm (Figure 4.10a). This implies that these slower hole decays are due to trapped hole states which are filled by BG illumination prior to the laser excitation, in agreement with the filling of hole states by BG illumination in PIAS (Figure A.12). In Al:$SrTiO_3$, the slower decay component is also absent under BG illumination (Figure 4.10b). However, instead of identical kinetics being observed across the spectrum, a small degree of bleaching on ms timescales is

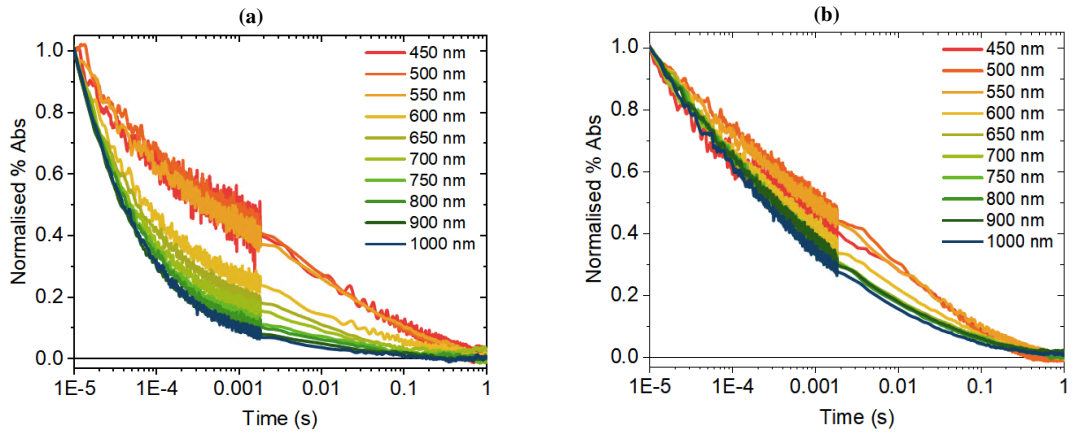

Figure 4.9: Normalised DRTS kinetics in H_2O for a) $SrTiO_3$, and b) Al:$SrTiO_3$.

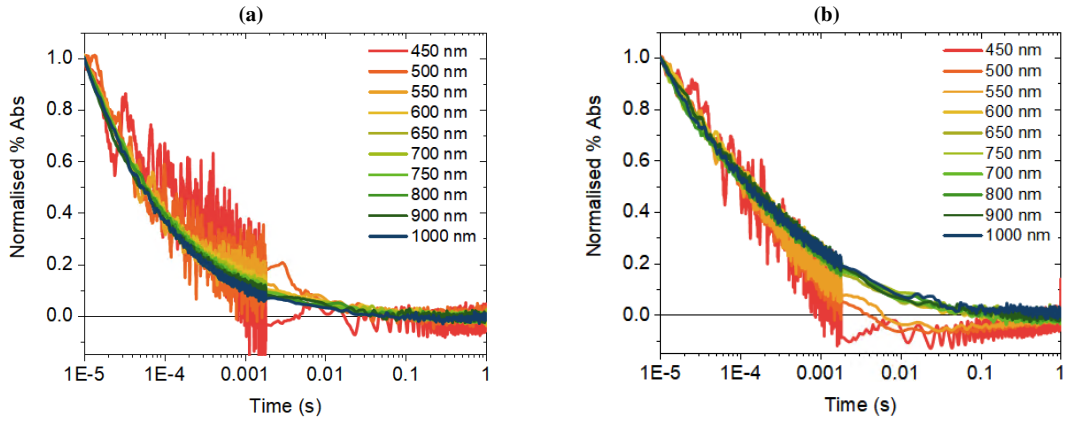

Figure 4.10: Normalised DRTS kinetics in H_2O under continuous BG illumination for a) $SrTiO_3$, and b) Al:$SrTiO_3$.

observed for <600 nm probe wavelengths. This bleaching is rationalised by electrons trapping into the V_O which are indirectly introduced by Al^{3+} doping. Similar observations of bleaching resulting from charge trapping into V_O has been reported for other metal oxide systems, such as $BiVO_4$ and WO_3.[104,105]

In PIAS, a change in intrinsic doping density following Al^{3+} doping is insinuated by the change from intensity independent to dependent decays. This is also observed in the intensity dependence of the DRTS decays. In $SrTiO_3$, the normalised DRTS decay kinetics are independent of excitation intensity at 500 nm and 800 nm (Figure 4.11a and A.18a). This is characteristic of a monomolecular decay process where the majority carrier is in excess, such as pseudo first order recombination,[27] and is in agreement with the intensity independent decays of $SrTiO_3$ observed in PIAS. In contrast, the decay kinetics of Al:$SrTiO_3$ probed at 500 nm accelerate slightly with

increasing intensity (Figure 4.7b), whilst the 800 nm decay kinetics remain intensity independent (Figure A.18). This dependence of hole decays on excitation intensity was also observed in the PIAS decay kinetics of Al:$SrTiO_3$ (Figure 4.7b). However, the degree of dependence is smaller than what is expected for a bimolecular recombination process and instead is consistent with a trap-filling model whereby a large majority of traps have been filled,[101,111] and therefore their influence on recombination kinetics is negligible.

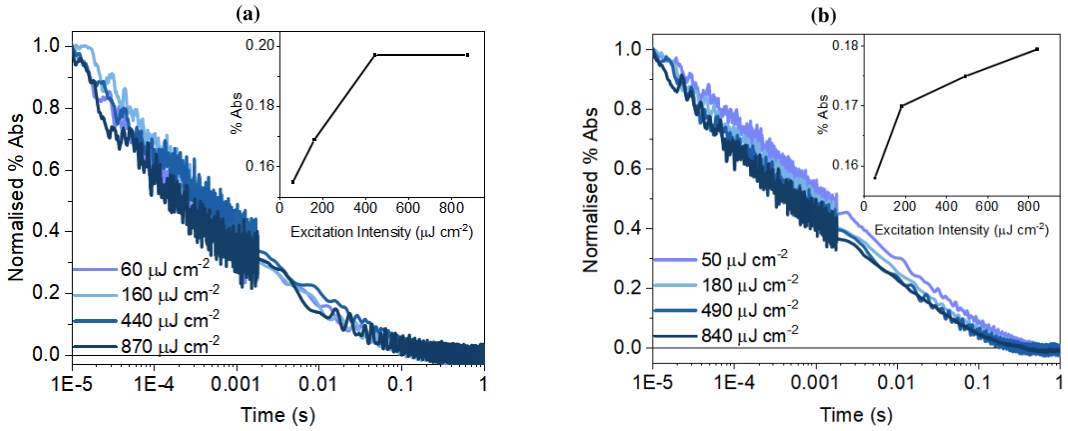

Figure 4.11: Normalised intensity dependence of DRTS kinetics probed at 500 nm in H_2O, with as measured kinetics in the inset, for a) $SrTiO_3$, and b) Al:$SrTiO_3$.

These DTRS investigations comparing $SrTiO_3$ and Al:$SrTiO_3$ expand on and support the PIAS results. In PIAS, higher steady-state charge densities are observed in Al:$SrTiO_3$ and attributed to suppressed recombination on timescales prior to the PIAS measurement. This is supported by the slower DRTS decays observed for Al:$SrTiO_3$, that represent suppressed recombination kinetics on μs-s timescales following photoexcitation. Two distinct kinetic regimes are observed for DRTS decays probed below and from 600 nm, with notably slower decay kinetics observed below 600 nm. The slower decays kinetics are attributed to trapped hole species by investigating the effects of BG illumination, in line with the effects of BG illumination predominantly filling hole states in PIAS. Lastly, following Al^{3+} doping a higher degree of dependence of the decay kinetics on excitation intensity is observed in PIAS and DRTS. This is indicative of a decrease in the intrinsic doping density, perhaps due to the suppression of Ti^{3+} states serving as electron donors.

4.4 Discussion

The changes to the physical characteristics of $SrTiO_3$ following Al^{3+} doping play a critical role in supporting higher charge densities and extending charge lifetimes. Firstly, Al^{3+} doping suppresses Ti^{3+} states measured by XPS, that are attributed to recombination centres and electron donor states in $SrTiO_3$.[34] Secondly, the morphology of the $SrTiO_3$ particles is transformed from a cubic to truncated cubic structure (Figure 4.2). The truncated cubic structure, with an internal electric field between the {100} and {110} facets of differing energies, is integral for the facet selective photodeposition of co-catalysts that enables the near-unity AQY (explored in detail in Chapter 5).[38] In addition to transforming the morphology, Al^{3+} doping increases the crystallinity (as is expected for the flux-mediated process).[43] A higher degree of crystallinity can promote successful migration of photogenerated charges to the reaction sites, for example by decreasing defects that promote recombination.[22,141]

The above effects of Al^{3+} doping on $SrTiO_3$ are summarised in Figure 4.12, with the impacts of these effects on the charge carrier dynamics explained as follows. In $SrTiO_3$ (Figure 4.12a), there is a significant density of electrons in relatively deep Ti^{3+} states, with the E_F close to the top of their energy distribution (as calculated and discussed in Chapter 3). A combination of the significant population of sub-band gap Ti^{3+} states and the absence of a significant internal electric field, increases opportunities for charge trapping (sub-ms) and recombination, via the Ti^{3+} trap states or of free charges. In DRTS, recombination on the timescale of $\sim$0.05 ms is observed, in addition to the occurrence of hole trapping extending hole lifetimes. In Al:$SrTiO_3$ (Figure 4.12b), the Ti^{3+} states are suppressed and an electric field between distinct oxidation and reduction facets drives charge separation. Consequently, recombination is slowed by four times ($\sim$0.2 ms) and hole trapping further enhances lifetimes. Thus, under steady-state conditions higher charge densities can be achieved, as observed in the increased signal amplitude in PIAS.

The three-fold increase in the steady-state charge density measured in PIAS for Al:$SrTiO_3$ (Figure 4.5a) is beneficial for maintaining sufficient charge lifetimes and populations for interfacial water splitting reactions, in particular for the kinetically slow and multi-hole water oxidation reaction.[79,106,107] The increased steady-state charge density is attributed to the increase in the RQY (0.3 to 0.9) of hole generation in Al:$SrTiO_3$. This is indicative of a higher efficiency for

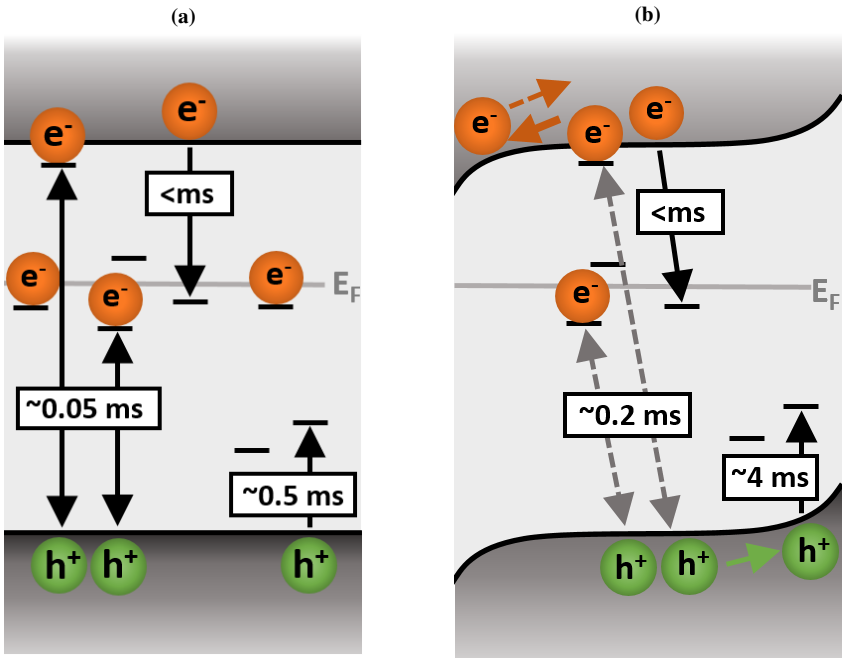

Figure 4.12: Schematic illustration of the recombination and trapping processes in a) $SrTiO_3$, and b) Al:$SrTiO_3$. Timescales in white boxes are that of recombination and trapping processes. Electron trapping into Ti^{3+} states is assumed to occur on sub-ms timescales, prior to the subsequent recombination that is observed, due to the correlation between the two.

the generation of holes that persist under steady-state PIAS conditions and is supported by the suppressed recombination observed in DRTS, prior to the PIAS timescales. Due to the minimal change in the UV-Vis absorption properties, these changes are solely attributed to the changes to the aforementioned enhancements achieved by Al^{3+} doping, rather than changes to the ground state absorption.

Although the steady-state charge densities and DRTS lifetimes are enhanced in Al:$SrTiO_3$, both $SrTiO_3$ and Al:$SrTiO_3$ exhibit significant PIAS signals. These are rare observations for metal oxides without the application of a positive bias to drive charge separation and enhance lifetimes.[21,79,107,142] This suggests that $SrTiO_3$ and Al:$SrTiO_3$ exhibit intrinsically good charge separation capabilities, which is important for their use as a base material of photocatalysts employed in OPWS.

Al^{3+} doping and the associated suppression of Ti^{3+} states has further effects on the charge carrier dynamics, beyond the dramatic increase in steady-state charge density and DRTS charge lifetimes (Figure 4.5 and 4.8). For example, following Al^{3+} doping a change from a monomolecular to a more bimolecular type decay pathway is observed in the intensity dependence of the

PIAS and DRTS decays. The intensity independent monomolecular kinetics in $SrTiO_3$ are attributed to Ti^{3+} states resulting in a higher electron density and pseudo first order recombination. However, $SrTiO_3$ is not a notably intrinsic material, with similar intrinsic doping densities to other metal oxides including anatase TiO_2 (see Chapter 3). Meanwhile, the Ti^{3+} states in Al:$SrTiO_3$ are suppressed and subsequently there is a change from an intensity independent monomolecular decay pathway to a decay pathway with a degree of intensity dependence.

Whilst the increase in crystallinity and suppressed Ti^{3+} states are expected results of flux-mediated Al^{3+} doping,[34,43] the stable E_F position differs from what is observed in the XPS studies of $SrTiO_3$ and Al:$SrTiO_3$ conducted by Osterloh and co-workers.[91] DFT calculations estimate that Ti^{3+} states resulting from V_O are situated 0.6-1.3 eV below the CB.[91,143,144] Assuming the Ti^{3+} are situated in a similar sub-band gap position in the $SrTiO_3$ investigated herein, their suppression could decrease the n-type character and cause a downward shift in the E_F. Osterloh and co-workers report a downward E_F shift following their Al^{3+} doping procedure, due to a downward shift of the O 1s and Ti 2p peaks of $\sim$0.5 eV, which is supported by a concurrent decrease in the E_{VB} position relative to the E_F measured by valence XPS. However, in this chapter a constant E_F position in the $SrTiO_3$ and Al:$SrTiO_3$ studied is demonstrated by the stable O 1s and Ti 2p positions, in addition to an unchanged E_{VB} position relative to the E_F illustrated by the valence XPS. The discrepancies between Osterloh's work and this work are rationalised by the differing source of $SrTiO_3$ and method of flux-mediated doping (producing a different coloured Al:$SrTiO_3$ to that investigated herein), with both proven to impact the morphology and defects.[84,85] For example, the $SrTiO_3$ investigated herein has a lower initial proportion of Ti^{3+} states (3% vs. 27%), which can limit the impact of their suppression on the E_F position. A possible explanation for the stability of the E_F in the materials studied in this chapter is that the E_F could be pinned to the V_O, which remain present and unchanged in their position following Al^{3+} doping. An alternative explanation is that the Ti^{3+} defects arising from V_O are predominantly at the $SrTiO_3$ surface, with preferential formation of V_O at the surface rather than inside the crystallites reported previously.[145] Therefore, the Ti^{3+} states in $SrTiO_3$ are readily observed in the surface sensitive XPS core line spectrum. Meanwhile, the E_F is a bulk property which may not be affected to a measurable extent by the small changes to the Ti^{3+} concentration at the surface.

The time-resolved spectroscopic techniques employed in this chapter bear similarities regarding

their utilisation of band gap excitation and pump-probe nature. Despite this, there are differences in the species and processes they predominantly probe. The continuous LED pulses and measurement timescales of several of seconds in PIAS results in longer-lived charges dominating this steady-state measurement. In contrast, DRTS employs short, high intensity laser pulses that probe transient charge densities at short μs-s timescales following photoexcitation. Thus, processes with faster recombination rates can be observed in DRTS but are likely to decay prior to the PIAS measurement timescales. The result of these differences is evident in the differing spectral shapes of $SrTiO_3$ and Al:$SrTiO_3$ obtained by PIAS and DRTS. A prevalent feature in the NIR is observed exclusively in the DRTS spectra measured at 10 μs. This feature corresponds to faster decays than those probed at lower wavelengths, so that the DRTS spectrum evolves with time to more closely resemble the PIAS spectral shape (Figure A.14), where the early NIR feature is diminished and the <600 nm signals dominate. Further consequences of the differences in the measurement conditions are observed in the differing impacts of scavengers in PIAS and DRTS, and in the following chapter exploring the effects of $RhCrO_x$ on charge carrier dynamics.

4.5 Conclusion

The effects of flux mediated Al^{3+} doping on the physical characteristics of $SrTiO_3$ are investigated in this chapter and related to changes to the charge carrier dynamics, both in the steady-state and following laser excitation. Whilst initial characterisation of these compositions has been conducted in previous work,[37,38,43] *in situ* spectroscopic studies using PAIS and DRTS, and detailed XPS analysis of these exact components of the Al:$SrTiO_3$/$RhCrO_x$ photocatalysts, had not been conducted.

In summary, the compositional flexibility of the perovskite $SrTiO_3$ structure can be effectively exploited via flux-mediated Al^{3+} doping. Consequently, Ti^{3+} states that can serve as recombination centres are suppressed, whilst the crystallinity and morphology is enhanced. A resulting electric field to drive charge separation is proposed and is explored in more detail in the next chapter. For the first time, the advantageous effects of these material changes on the steady-state and *in situ* charge carrier dynamics are demonstrated. On μs-s timescales following photoexcitation, recombination is suppressed in Al:$SrTiO_3$. Subsequently, the RQY of charges in the steady-state is increased to result in a three-fold increase in the steady-state charge density obtained. Thus, under these conditions that are representative of those in OPWS, the population of charges that can be utilised in slow interfacial water splitting reactions is increased. In both $SrTiO_3$ and Al:$SrTiO_3$, decay kinetics in DRTS are not simply due to recombination of the probed species. Instead, slower decays are observed for hole species and attributed to hole trapping. With the extended lifetimes of photogenerated charges in Al:$SrTiO_3$ in mind, Al^{3+} doping addresses the challenges of OPWS, and specifically the kinetically slow water oxidation reaction, by extending the lifetimes of photogenerated charges rather than increasing their reactivity.

The stable E_F position measured following Al^{3+} doping is somewhat unexpected and controversial. To further explore why the E_F does not shift, further investigations into the energy of the Ti^{3+} states and their depth distribution in the particles are necessary. Preliminary HAXPES studies indicate that the Ti^{3+} states are predominantly at the surface of $SrTiO_3$. However, further measurements to confirm this and compare to Al:$SrTiO_3$ are required.

Although Al^{3+} doping is a key step in fabricating the final photocatalyst compositions, it requires the addition of a $RhCrO_x$ co-catalyst. With the role of Al^{3+} established in this chapter, the results of further investigations into the effects of $RhCrO_x$ on the physical properties and charge carrier dynamics in Chaper 5 can be deconvoluted from those of Al^{3+} doping.

Chapter 5

Role of $RhCrO_x$ and its deposition route on facilitating the state-of-the-art performance of $Al:SrTiO_3/RhCrO_x$

This chapter follows on from the investigation of the role of flux-mediated Al^{3+} doping on $SrTiO_3$ in Chapter 4, and investigates the effect of $RhCrO_x$ co-catalyst addition on the $Al:SrTiO_3$ system. $RhCrO_x$ deposition plays a critical role in enabling impressive performance for overall photocatalytic water splitting, OPWS, with impregnation and photodeposition of $RhCrO_x$ achieving AQYs of 56% and 93% respectively. Thus, the effects of the two distinct deposition methods, on the physical properties and charge carrier dynamics of $Al:SrTiO_3$, are investigated and compared in this chapter to determine the role of the $RhCrO_x$ co-catalyst and its deposition route. This is primarily investigated under steady-state conditions in PIAS, representative of the OPWS conditions where the dramatic performance differences are reported. Through these investigations, it is evident that in all cases $RhCrO_x$ suppresses recombination and facilitates charge accumulation, to enable a population of extremely long-lived charges. However, the importance of selectively depositing $RhCrO_x$ onto reduction facets is highlighted, to ensure that the reactivity of holes is maximised and that hole trapping into unreactive states is prevented.

5.1 Introduction

Single-step particulate OPWS systems, where both light absorption and photocatalysis occurs on a single particulate material, offers a straight-forward and up-scalable route for hydrogen production.[14,22,38,146] However, when employing such systems, hydrogen and oxygen are evolved from the same particle in close proximity to each other. Thus, backwards reactions of evolved hydrogen and oxygen can significantly limit the photocatalytic activity of these systems. To prevent the extent to which these backwards reactions limit photocatalytic activity, a co-catalyst that catalyses the desired forward reactions and blocks backward reactions can be deposited at the surface. Noble metals (e.g. Rh, Pd and Pt) are typically good hydrogen evolution catalysts, however, they also facilitate the backwards reaction of evolved oxygen and hydrogen.[67] This is overcome by the addition of a transition metal oxide, such as Cr_2O_3, to the noble metal, that catalyses proton reduction but inhibits the backwards reactions.[67,147]

An example of such a co-catalyst is a mixed rhodium chromium oxide, $RhCrO_x$, co-catalyst, developed by Domen and co-workers to successfully enhance the photocatalytic activity of GaN:ZnO.[61,67,68,147,148] The proposed function of this photocatalyst is threefold: the Rh extracts electrons from the bulk photocatalyst, Rh and Cr_2O_3 components catalyse proton reduction, and Cr_2O_3 prevents backwards reactions.[67,147] $RhCrO_x$ can be deposited randomly on the photocatalyst surface via impregnation to yield a mixed oxide structure,[43,67] or selectively onto specific facets via photodeposition to result in a core-shell structure.[38,61,68]

In addition to the increased risk of backwards reactions, the close proximity of oxidation and reduction sites in photocatalyst particles can promote recombination of photogenerated charges, prior to their participation in the desired photocatalytic reactions. One way to avoid this is to have distinct facets for the oxidation and reduction reactions. Previously, this has been achieved by using $SrTiO_3$ and $BiVO_4$ with anisotropic facets,[30,149–151] and more recently by Domen and co-workers using Al:$SrTiO_3$.[38] In these cases, distinct facets served as photo-oxidation and photo-reduction sites, as demonstrated by the facet selective photodeposition of co-catalysts.

$RhCrO_x$ has been deposited onto the Al:$SrTiO_3$ introduced in Chapter 4 (Al:$SrTiO_3$/$RhCrO_x$), to achieve state-of-the-art photocatalyst performance. With the $RhCrO_x$ co-catalyst deposited

onto the powders via impregnation, Al:$SrTiO_3$/$RhCrO_x$(IMP), an AQY of 56% at 365 nm is achieved.[37] AQYs exceeding 50% are rare for overall water splitting photocatalysts, and this system is unique in achieving this efficiency whilst also exhibiting visible light activity.[18,44,45] Upon modification with CoOOH stability is enhanced, with initial activity maintained for over 72 hours, compared to an activity drop of a third prior to CoOOH addition.[40] The up-scalability of this photocatalyst has been demonstrated by the production of meter scale panels and a pilot plant that safely and stably produced hydrogen on the 100 m^2 scale.[39]

More recently, a remarkable increase in photocatalytic performance was achieved by depositing $RhCrO_x$ via photodeposition, Al:$SrTiO_3$/$RhCrO_x$(PD), with a near-unity AQY of 93% reported at 365 nm.[38] In order to achieve such an impressive AQY, almost all photogenerated charges must successfully avoid recombination, diffuse to active sites and participate in the water splitting reactions. This was attributed to the spatial separation of the oxidation and reduction sites, arising as a result of an internal electric field between the oxidation and reduction facets, that enabled the facet selective photodeposition of co-catalysts.

Whilst the state-of-the-art performance of these Al:$SrTiO_3$/$RhCrO_x$ photocatalytic systems has been extensively investigated, the underlying mechanisms that enable efficient operation, without external bias or scavengers, remains largely unknown. Moreover, a detailed comparison of the physical properties and charge carrier dynamics in Al:$SrTiO_3$/$RhCrO_x$(IMP) and Al:-$SrTiO_3$/$RhCrO_x$(PD) is yet to be conducted. In fact, there are no previous studies investigating the charge carrier dynamics in either of these materials.

In this chapter, the effects of $RhCrO_x$ deposition via impregnation and photodeposition are investigated and compared, to reveal the mechanisms underpinning the state-of-the-art AQYs and the influence of the deposition route on activity. To this end, the physical properties of Al:$SrTiO_3$/$RhCrO_x$(IMP) and Al:$SrTiO_3$/$RhCrO_x$(PD) are characterised, in order to reveal any material differences at play prior to an in-depth *in situ* investigation of their charge carrier dynamics. For investigating the charge carrier dynamics, PIAS and DRTS are employed under a range of conditions. There is a focus on PIAS due to the more informative results obtained and its ability to probe charge carrier dynamics under steady-state conditions, that are more relevant to the operational conditions where the performance differences are observed. The results presented in this chapter on Al:$SrTiO_3$/$RhCrO_x$(IMP) and Al:$SrTiO_3$/$RhCrO_x$(PD) are

compared to each other, as well as to the $SrTiO_3$ and Al:$SrTiO_3$ investigated Chapter 4, in order to explore the influence of $RhCrO_x$ addition, as well as the deposition route.

5.2 Experimental methods

This chapter investigates the effects of $RhCrO_x$ deposition, via impregnation or photodeposition, on the Al:$SrTiO_3$ investigated in Chapter 4. Similarly to $SrTiO_3$ and Al:$SrTiO_3$, $RhCrO_x$ deposition was conducted by the Domen group at Shinshu University in Japan (specifically by Prof. Kazunari Domen, Prof. Takashi Hisatomi and Prof. Tsuyoshi Takata). The $RhCrO_x$ was deposited onto Al:$SrTiO_3$ via impregnation or photodeposition following methods reported previously,[38,43,67,68] and explained in detail in Chapter 2. Photocatalyst sheets of Al:$SrTiO_3$/-$RhCrO_x$(IMP) and Al:$SrTiO_3$/$RhCrO_x$(PD) were prepared in the same way as those of $SrTiO_3$ and Al:$SrTiO_3$, on quartz substrates and with the addition on SiO_2 nanoparticles. The methods followed in this chapter for physical characterisation and investigating the charge carrier dynamics are analogous to those used for $SrTiO_3$ and Al:$SrTiO_3$ in Chapter 4, to enable reliable comparisons to be made from the results. SEC measurements on $RhCrO_x$ are undertaken by Dr Benjamin Moss (Imperial College London) and use films fabricated by the Domen group. Apart from the XPS, the physical characterisation is largely confirming what has been reported previously. Also previously reported, but not measured in this thesis, is the photocatalytic performance of the materials, with AQYs of 56% and 93% at 365 nm reported for Al:$SrTiO_3$/-$RhCrO_x$(IMP) and Al:$SrTiO_3$/$RhCrO_x$(PD) respectively (the AQY of the Al:$SrTiO_3$ used for comparison is negligible). To the best of my knowledge, the spectroscopic investigations on Al:$SrTiO_3$/$RhCrO_x$(IMP) and Al:$SrTiO_3$/$RhCrO_x$(PD) are all the first of their kind to date.

5.3 Results

5.3.1 Physical characterisation

Prior to investigating the effects of $RhCrO_x$ deposition via impregnation and photodeposition on charge carrier dynamics, the effects on the physical properties were investigated. Compared to Al:$SrTiO_3$, the bulk particle morphology is maintained but the presence of additional particles on the Al:$SrTiO_3$/$RhCrO_x$(IMP) and Al:$SrTiO_3$/$RhCrO_x$(PD) surfaces is evident in SEM (Figure 5.1). The size and distribution of these additional particles, attributed to $RhCrO_x$, is highly dependent on the deposition route. In Al:$SrTiO_3$/$RhCrO_x$(IMP), there is a random and sporadic distribution of $RhCrO_x$ particles (20-50 nm) on Al:$SrTiO_3$, with no $RhCrO_x$ visible on a portion of Al:$SrTiO_3$ particles (Figure 5.1a). Meanwhile, in Al:$SrTiO_3$/$RhCrO_x$(PD), there is a comparatively uniform distribution of smaller $RhCrO_x$ particles (15-30 nm) deposited exclusively onto the flat facets of Al:$SrTiO_3$ (Figure 5.1b). This is in agreement with the selective deposition of $RhCrO_x$ onto the {100} reduction facets when using the photodeposition method.[38]

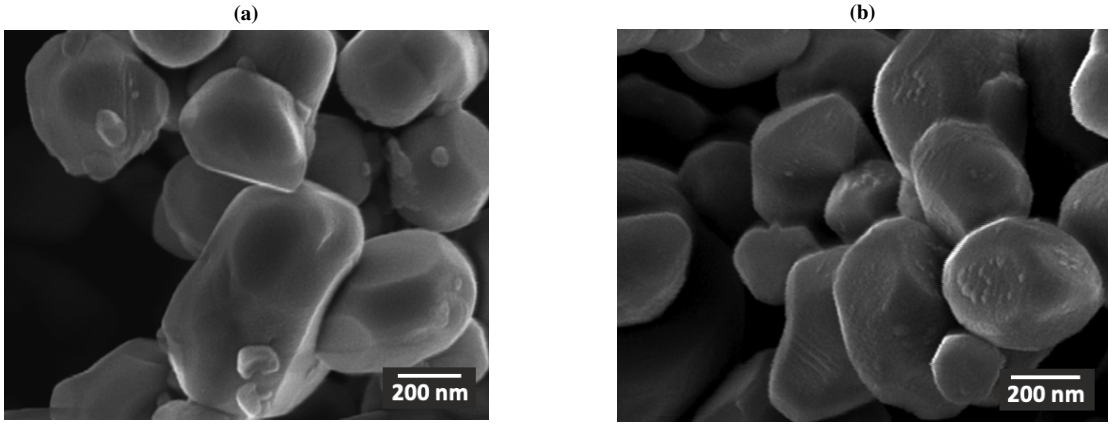

Figure 5.1: SEM images of a) Al:$SrTiO_3$/$RhCrO_x$(IMP), and b) Al:$SrTiO_3$/$RhCrO_x$(PD)

XPS analysis confirms the presence of Rh and reveals the dependence of the dominant oxidation state on the deposition route of $RhCrO_x$. The Rh 3d spectra of Al:$SrTiO_3$/$RhCrO_x$(IMP) is dominated by oxidised Rh species (Figure 5.2a), with peaks at 308.4 eV and 309.3 eV attributed to Rh^{3+} and Rh^{4+} respectively.[152,153] Meanwhile, the metallic Rh peak at 308.3 eV has a comparatively smaller contribution (atomic weight percent (Rh^0/(Rh^0+Rh^{3+}+Rh^{4+})) = 24%).[152–154] In contrast, the Rh 3d spectra in Al:$SrTiO_3$/$RhCrO_x$(PD) has a more even contribution from

the different oxidation states (Figure 5.2b), with a greater contribution of metallic Rh (atomic weight percent ($Rh^0/(Rh^0+Rh^{3+}+Rh^{4+})$) = 36%) compared to in Al:$SrTiO_3$/$RhCrO_x$(IMP). This is rationalised by the nature of the photodeposition method, whereby photogenerated electrons reduce Rh during the deposition and consequently metallic Rh has a large presence in the resulting $RhCrO_x$. In contrast, the impregnation method is recognised to predominantly yield Rh oxide species.[67,155]

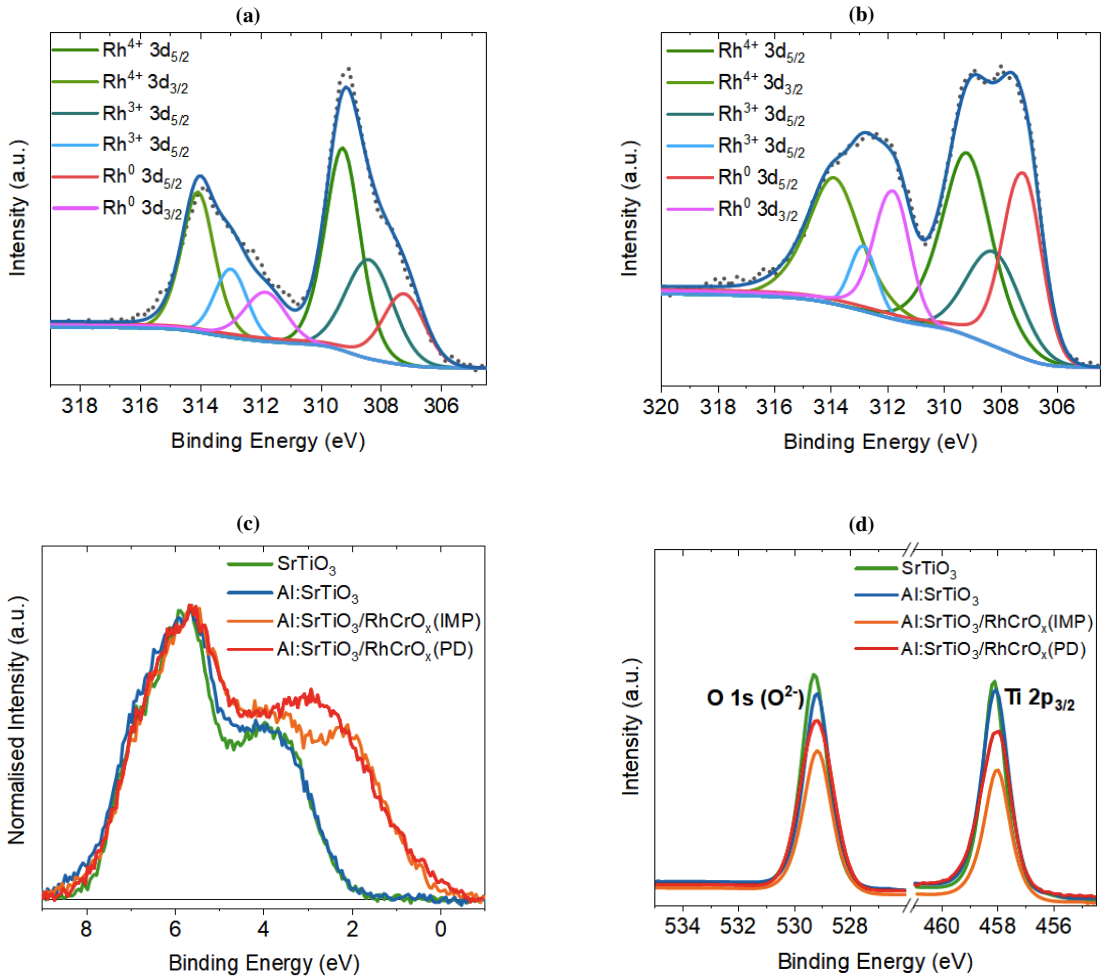

Figure 5.2: XPS Rh 3d spectra for a) Al:$SrTiO_3$/$RhCrO_x$(IMP) and b) Al:$SrTiO_3$/$RhCrO_x$(PD). c) Valence XPS spectra of $SrTiO_3$, Al:$SrTiO_3$, Al:$SrTiO_3$/$RhCrO_x$(IMP) and Al:$SrTiO_3$/$RhCrO_x$(PD). d) Comparison of the XPS core lines of the O 1s (O^{2-}) and Ti $2p_{3/2}$ peaks of $SrTiO_3$, Al:$SrTiO_3$, Al:$SrTiO_3$/$RhCrO_x$(IMP) and Al:$SrTiO_3$/$RhCrO_x$(PD). Negligible downward shifts in energy the O 1s and Ti $2p_{3/2}$ peaks are measured following Al^{3+} doping (-0.04 eV) and $RhCrO_x$ deposition by impregnation (-0.08 eV) or photodeposition (-0.10 eV), maintaining a 71.2 eV binding energy difference between the peaks.

The position and shape of the Al:$SrTiO_3$ valence XPS structure is maintained following $RhCrO_x$ deposition (Figure 5.2c). In addition to the bulk Al:$SrTiO_3$ structure in the valence XPS spectra, the introduction of states extending from the VB to just beyond the E_F is observed for Al:$SrTiO_3$/$RhCrO_x$(IMP) and Al:$SrTiO_3$/$RhCrO_x$(PD). However, a negligible shift in both the O

1s or Ti 2p core line binding energies (Figure 5.2d) is observed, which suggests a stable E_F position, given E_{BE} = E_F - E_i (where E_{BE} and E_i correspond to the binding and initial energy of the electron respectively).[59] Together, this suggests that the E_F position continues to be stable following $RhCrO_x$ deposition.

As expected for a surface modification, no changes to the crystallinity of the bulk Al:$SrTiO_3$ particles are observed in Al:$SrTiO_3$/$RhCrO_x$(IMP) or Al:$SrTiO_3$/$RhCrO_x$(PD) (Figure A.19). In addition, the steady-state UV-Vis absorption spectra and calculated band gaps are consistent for all compositions measured (Figures 5.3 and 4.4). Therefore, these particular properties do not account for the changes to photocatalytic performance that result from $RhCrO_x$ and depend on its deposition route.

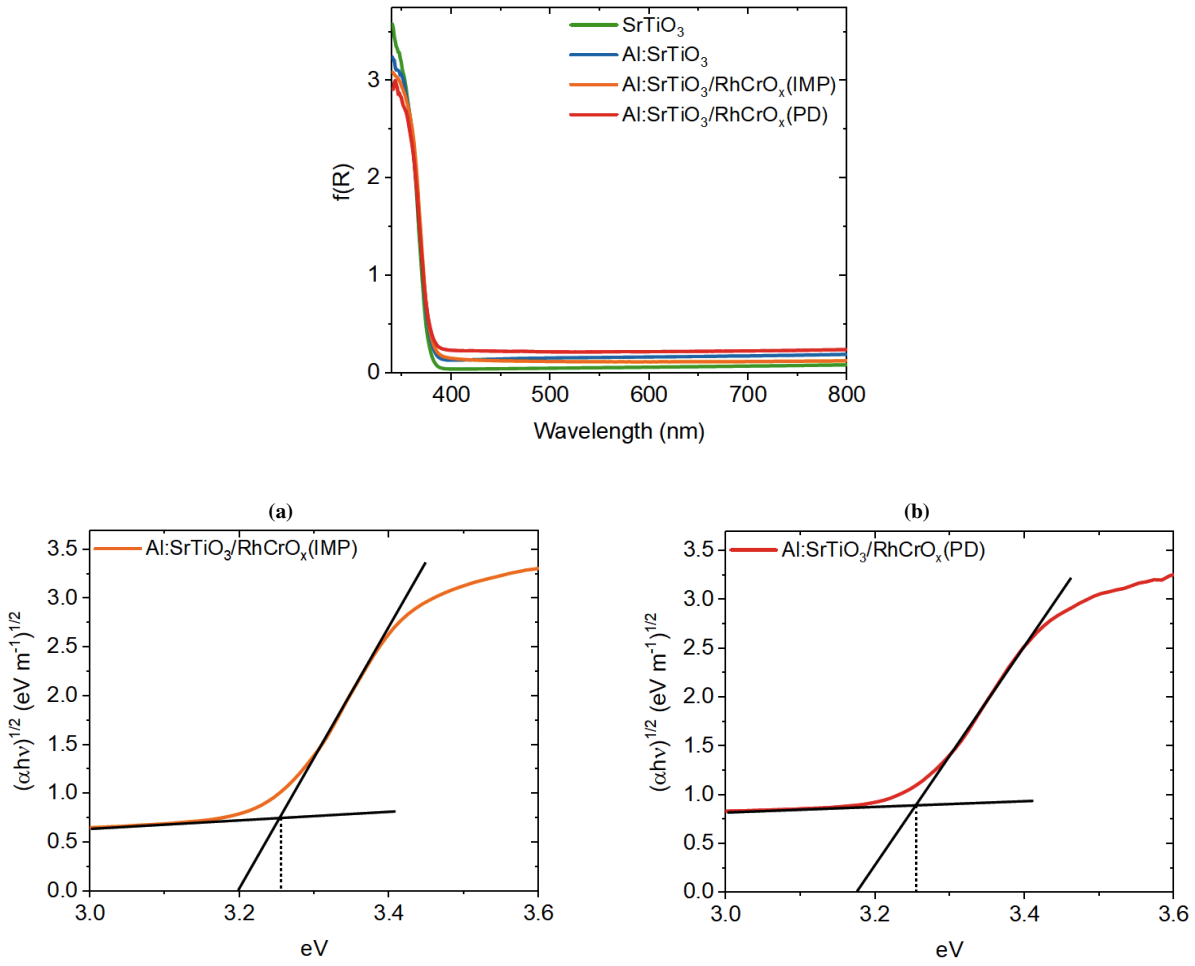

Figure 5.3: a) Ground state optical absorption measured by UV-Vis, and reported using the Kubelka-Munk function f(R), for $SrTiO_3$, Al:$SrTiO_3$, Al:$SrTiO_3$/$RhCrO_x$(IMP) and Al:$SrTiO_3$/$RhCrO_x$(PD). Tauc plots from optical data obtained by UV-Vis spectroscopy to obtain the indirect band gaps of a) Al:$SrTiO_3$/$RhCrO_x$(IMP) (E_g = 3.25 eV) and d) Al:$SrTiO_3$/$RhCrO_x$(PD) (E_g = 3.25 eV).

5.3.2 Steady-state charge carrier dynamics

Al:$SrTiO_3$/$RhCrO_x$(IMP) and Al:$SrTiO_3$/$RhCrO_x$(PD) are investigated by PIAS, to determine the differences in steady-state charge carrier dynamics on the slow (ms-s) timescales of water oxidation. Several PIAS decays in this section are analysed by splitting the decay into a fast phase, which corresponds to the decay immediately following light-off, and a slow phase, which corresponds to the decays from 1 s after light-off. Scavenger studies are undertaken to identify the species probed, whilst the impact of excitation intensity and BG illumination was used to further investigate the nature of the slow phase and its relation to photocatalytic performance. Given the dramatic differences in lifetimes observed in this chapter, it is important to note here that the amplitude of the PIAS signal, and the population of probed charge species it represents, has contributions from their lifetimes and steady-state yields. Therefore, it does not scale linearly with either of these properties. The RQY of holes in Al:$SrTiO_3$/$RhCrO_x$(IMP) and Al:$SrTiO_3$/$RhCrO_x$(PD) is calculated for the hole species that result in the fast and slow decay phases, as they exhibit distinct decay kinetics that cannot be fitted to a single component and instead are fitted to two components (Figure A.21). This is in contrast to the single RQY calculated for $SrTiO_3$ and Al:$SrTiO_3$, which do not exhibit the slow phase.

Effect of $RhCrO_x$ deposition *via* impregnation on the steady-state charge carrier dynamics

Following the deposition of $RhCrO_x$ via impregnation, there is approximately a fourfold increase in signal amplitude across the spectrum compared to Al:$SrTiO_3$ (Figure 5.4a), representing an increase in the population of charges present in the steady-state. The effect of $RhCrO_x$ impregnation on the decay kinetics is striking. Al:$SrTiO_3$/$RhCrO_x$(IMP) exhibits extremely slow decay kinetics, with charges persisting for 10s of seconds and exhibiting lifetimes an order of magnitude longer than Al:$SrTiO_3$ (Figure 5.4b, $t_{50\%}$ = $\sim$0.13 s vs. $\sim$2 s for Al:$SrTiO_3$ and Al:$SrTiO_3$/$RhCrO_x$(IMP) respectively). The dominant slow decay phase that persists for 10s of seconds in Al:$SrTiO_3$/$RhCrO_x$(IMP) is indicative of very slow recombination, likely due to spatial charge separation following electron extraction to $RhCrO_x$ and/or charge trapping extending charge lifetimes.[28,36] The RQY calculated for the fast phase of Al:$SrTiO_3$/$RhCrO_x$(IMP) of 1, is very similar to that calculated for Al:$SrTiO_3$ (0.9, Table 5.1). Thus, the large increase in hole population is primarily attributed to the remarkably long charge lifetimes, rather than

an increase in the RQY of steady-state holes. It is noted that despite the low RQY of the slow phase in Al:$SrTiO_3$/$RhCrO_x$(IMP) (0.15), it dominates the PIAS (Figure 5.4b), due to the PIAS signal amplitude being determined by both the yield and lifetimes of the photogenerated species probed.

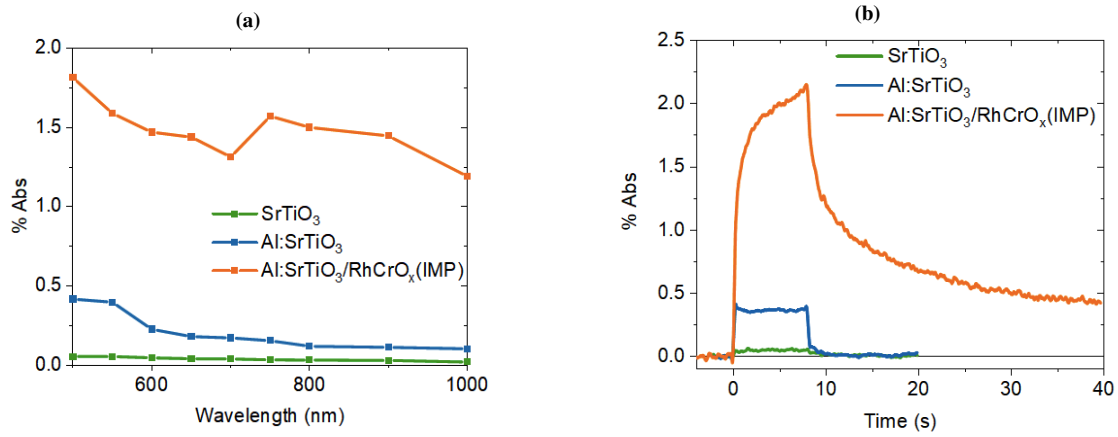

Figure 5.4: a) PIAS spectra, and b) PIAS kinetics probed at 500 nm, of $SrTiO_3$, Al:$SrTiO_3$ and Al:$SrTiO_3$/-$RhCrO_x$(IMP) measured in H_2O

Table 5.1: Comparison of the RQYs of hole generation calculated for $SrTiO_3$, Al:$SrTiO_3$ and Al:$SrTiO_3$/$RhCrO_x$-(IMP).

	Amplitude (%Abs)	$t_{50\%}$ (s)	RQY
$SrTiO_3$	0.1	0.14	0.3
Al:$SrTiO_3$	0.3	0.13	0.9
Al:$SrTiO_3$/$RhCrO_x$(IMP) *fast*	0.4	0.14	1.0
Al:$SrTiO_3$/$RhCrO_x$(IMP) *slow*	0.8	2.2	0.15

In 2-propanol hole scavenger, there is a significant and equivalent decrease in the signal amplitude across the Al:$SrTiO_3$/$RhCrO_x$(IMP) spectrum (Figure 5.5), resulting in the assignment of holes as the dominant species probed across the full wavelength range. This is in contrast to Al:$SrTiO_3$ and $SrTiO_3$, where holes are predominantly observed at low (<600 nm) wavelengths and suggests that in Al:$SrTiO_3$/$RhCrO_x$(IMP) electrons no longer dominate at longer wavelengths. This is rationalised by the faster timescales expected for electron transfer to $RhCrO_x$ (sub-μs)[35] and proton reduction (μs-ms),[156,157] compared to the PIAS measurement. It is noted here that electrons in $RhCrO_x$ appear to be optically inactive, as indicated by the lack of a significant or characteristic spectrum in SEC characterisation (Figure A.20).

Across the spectrum, the fast phase accelerates in hole scavenger (Figures 5.6c and 5.6d LHS), leading to the assignment of this phase to reactive hole species. Meanwhile, the slow phase

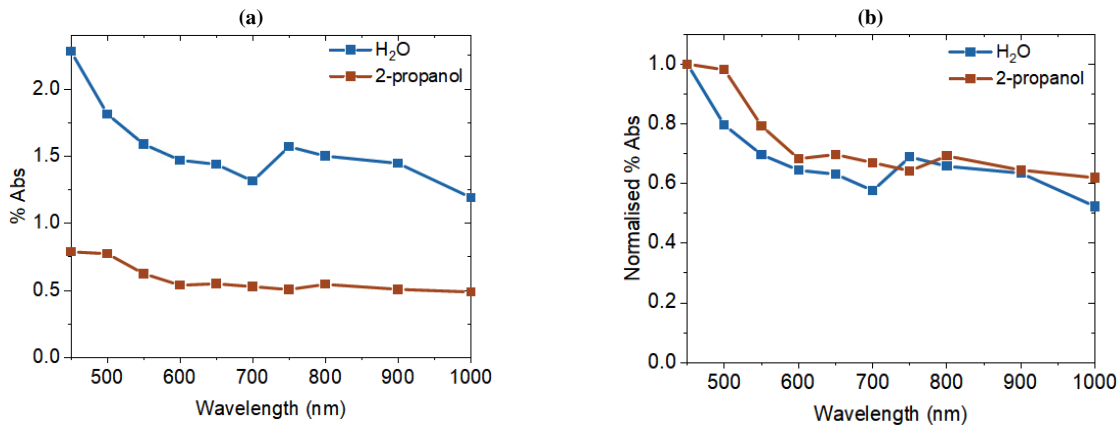

Figure 5.5: PIAS spectrum of Al:$SrTiO_3$/$RhCrO_x$(IMP) in H_2O and 2-propanol, a) as measured, and b) normalised to the maximum PIAS amplitude.

amplitude is suppressed, but the kinetics are largely unchanged (Figures 5.6c and 5.6d RHS). This suggests that their yield is decreased by the transfer of holes on earlier timescales but that they are not reactive hole species themselves, likely due to being trapped species.[27,35]

Interestingly, under aerobic hole scavenger conditions, whereby oxygen can serve as an electron scavenger, the slow decay phase is accelerated in the early NIR (Figure 5.6d RHS). This identifies a small, long-lived electron contribution to the slow phase, that reacts with oxygen and is attributed to a small population of trapped electrons that are not extracted to $RhCrO_x$. Meanwhile, at lower wavelengths there is not a significant effect of oxygen (Figure 5.6c), thus we are likely only probing hole species in this region.

To summarise, under steady-state PIAS conditions Al:$SrTiO_3$/$RhCrO_x$(IMP) exhibits an increased optical signal across the spectrum compared to Al:$SrTiO_3$. This does not appear to be due to an increase in the RQY of reactive holes under PIAS conditions (as their RQY is similar to the RQY of Al:$SrTiO_3$), so is instead due to an increase in hole lifetime. These hole species dominate across the entire spectrum in Al:$SrTiO_3$/$RhCrO_x$(IMP). This is attributed to electron extraction to $RhCrO_x$ occurring prior to the PIAS measurement, where they form optically invisible states and no longer contribute to the spectrum. The decay of these hole species exhibits a fast phase corresponding to reactive species, in addition to the introduction of a slow phase that corresponds to long-lived and unreactive holes.

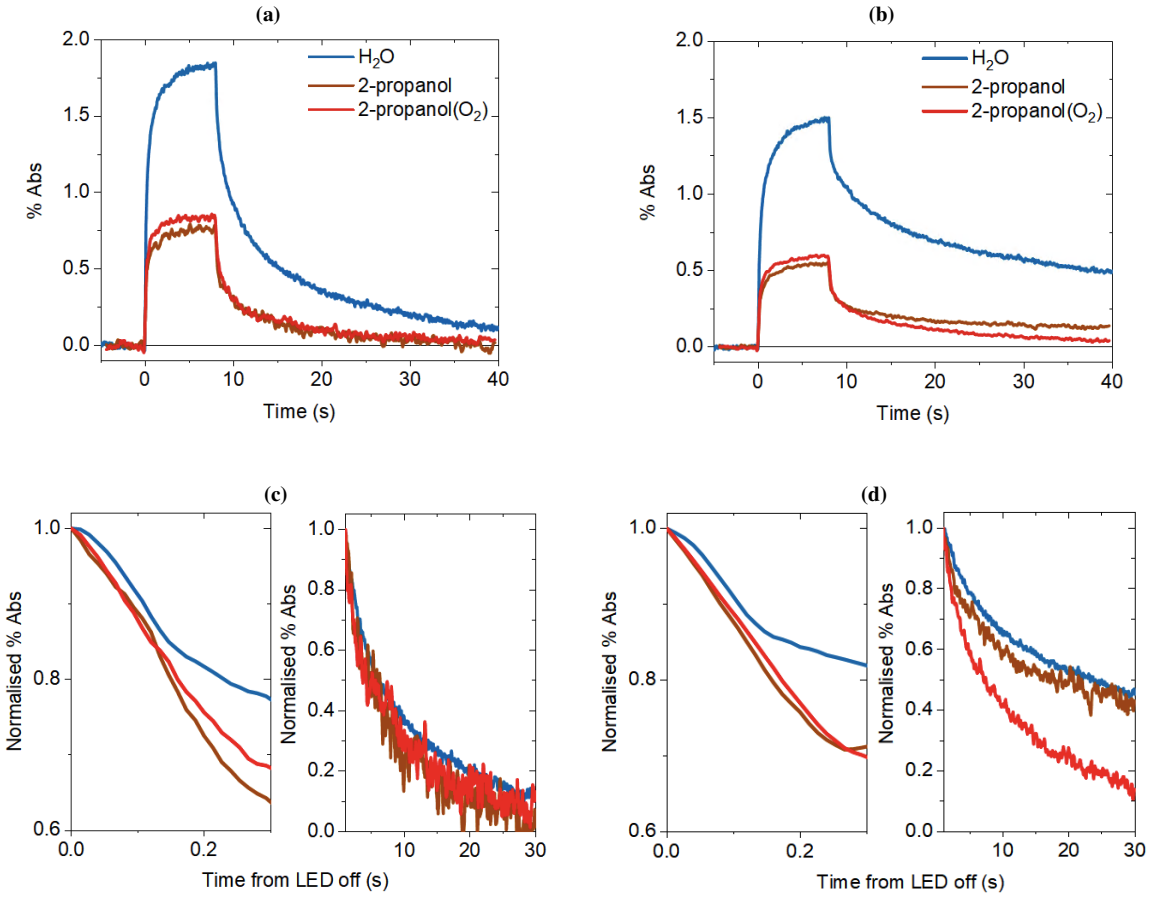

Figure 5.6: Comparison of PIAS kinetics of Al:$SrTiO_3$/$RhCrO_x$(IMP) in anaerobic H_2O and 2-propanol compared to aerobic 2-propanol(O_2). Full kinetic traces probed at, a) 500 nm, and b) 800 nm. Normalised fast (LHS) and slow (RHS) phase kinetics, probed at c) 500 nm, and d) 800 nm.

Effect of $RhCrO_x$ deposition via photodeposition on the steady-state charge carrier dynamics

Turning now to Al:$SrTiO_3$/$RhCrO_x$(PD), where measurements were undertaken using an LED intensity that simulates the photon flux absorbed under 60% of 1 sun illumination, instead of the standard 1 sun illumination typically used. Under 1 sun illumination, the very high rate of bubble formation from the Al:$SrTiO_3$/$RhCrO_x$(PD) surface (supported by the near-unity AQY reported)[38] caused optical interference that impaired the measurement. Consequently, the intensity was lowered to 60% of 1 sun where bubble formation was more manageable. When directly comparing Al:$SrTiO_3$/$RhCrO_x$(PD) to Al:$SrTiO_3$/$RhCrO_x$(IMP), PIAS measurements on both photocatalysts were undertaken under 60% of 1 sun illumination.

The Al:$SrTiO_3$/$RhCrO_x$(PD) spectrum differs from Al:$SrTiO_3$/$RhCrO_x$(IMP), due to lower sig-

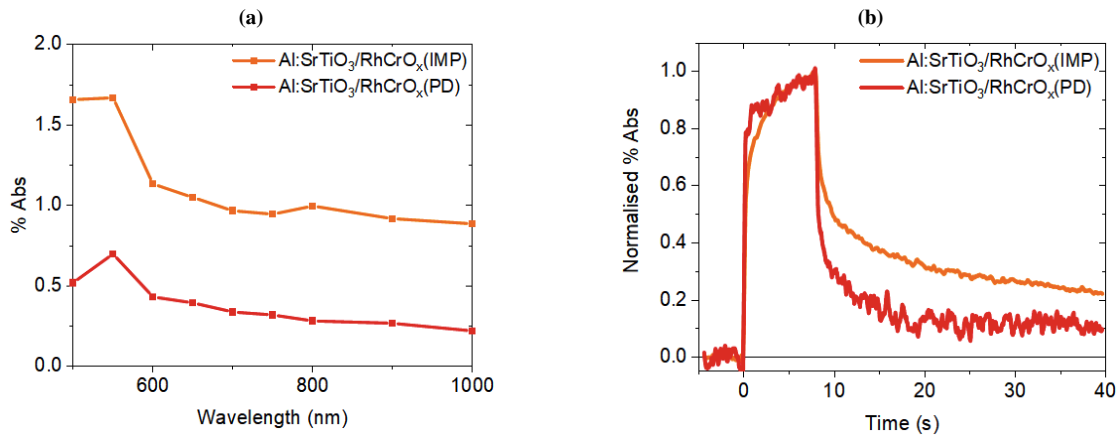

Figure 5.7: A comparison of the a) PIAS spectra, and b) PIAS kinetics probed at 500 nm, of Al:$SrTiO_3$/$RhCrO_x$-(IMP) Al:$SrTiO_3$/$RhCrO_x$(PD) measured in H_2O and with 60% of 1 sun illumination intensity.

Table 5.2: Comparison of the RQYs of hole generation calculated for $SrTiO_3$, Al:$SrTiO_3$, Al:$SrTiO_3$/$RhCrO_x$-(IMP) and Al:$SrTiO_3$/$RhCrO_x$(PD).

	Amplitude (%Abs)	$t_{50\%}$ (s)	RQY
$SrTiO_3$	0.1	0.14	0.3
Al:$SrTiO_3$	0.3	0.13	0.9
Al:$SrTiO_3$/$RhCrO_x$(IMP) *fast*	0.4	0.14	1.0
Al:$SrTiO_3$/$RhCrO_x$(IMP) *slow*	0.8	2.2	0.15
Al:$SrTiO_3$/$RhCrO_x$(PD) *fast*	0.3	0.13	0.6
Al:$SrTiO_3$/$RhCrO_x$(PD) *slow*	0.3	1.5	0.04

nal amplitudes across the spectrum and a peak at 550 nm (Figure 5.7a). Due to the equivalent UV-Vis absorption spectra of all the $SrTiO_3$-based photocatalyst compositions (Figure 5.3), the lower signal amplitude in Al:$SrTiO_3$/$RhCrO_x$(PD) is attributed to faster reaction of charges, occurring prior to the PIAS measurement. Despite these differences, the spectral assignments of Al:$SrTiO_3$/$RhCrO_x$(PD) are consistent with that of Al:$SrTiO_3$/$RhCrO_x$(IMP). In Al:$SrTiO_3$/-$RhCrO_x$(PD), hole scavenger also decreases the signal amplitude to an equivalent extent across the spectrum (Figure 5.8) and accelerates the fast decay phase (Figure 5.9c and 5.9d LHS), in addition to accelerating the slow decay phase in the early NIR under aerobic conditions (Figure 5.9d RHS).

Compared to Al:$SrTiO_3$/$RhCrO_x$(IMP), the decay kinetics of Al:$SrTiO_3$/$RhCrO_x$(PD) are dominated by the fast decay phase (Figure 5.7b), whilst the slow phase is less prominent. This is demonstrated by the slow phase RQYs being 15% and 7% of the fast phase RQYs, of Al:$SrTiO_3$/$RhCrO_x$(IMP) and Al:$SrTiO_3$/$RhCrO_x$(PD) respectively. Moreover, the slow phase

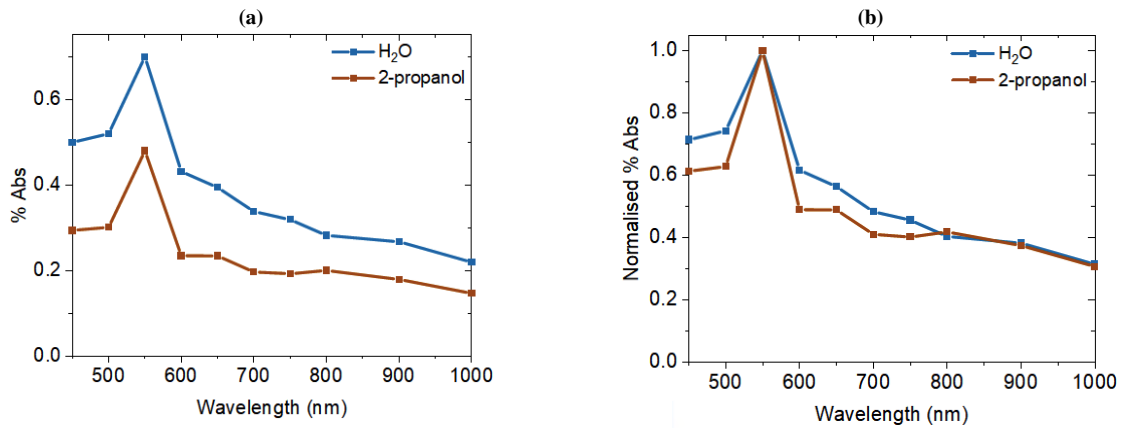

Figure 5.8: PIAS spectrum of Al:$SrTiO_3$/$RhCrO_x$(PD) in H_2O and 2-propanol, a) as measured, and b) normalised to the maximum PIAS amplitude.

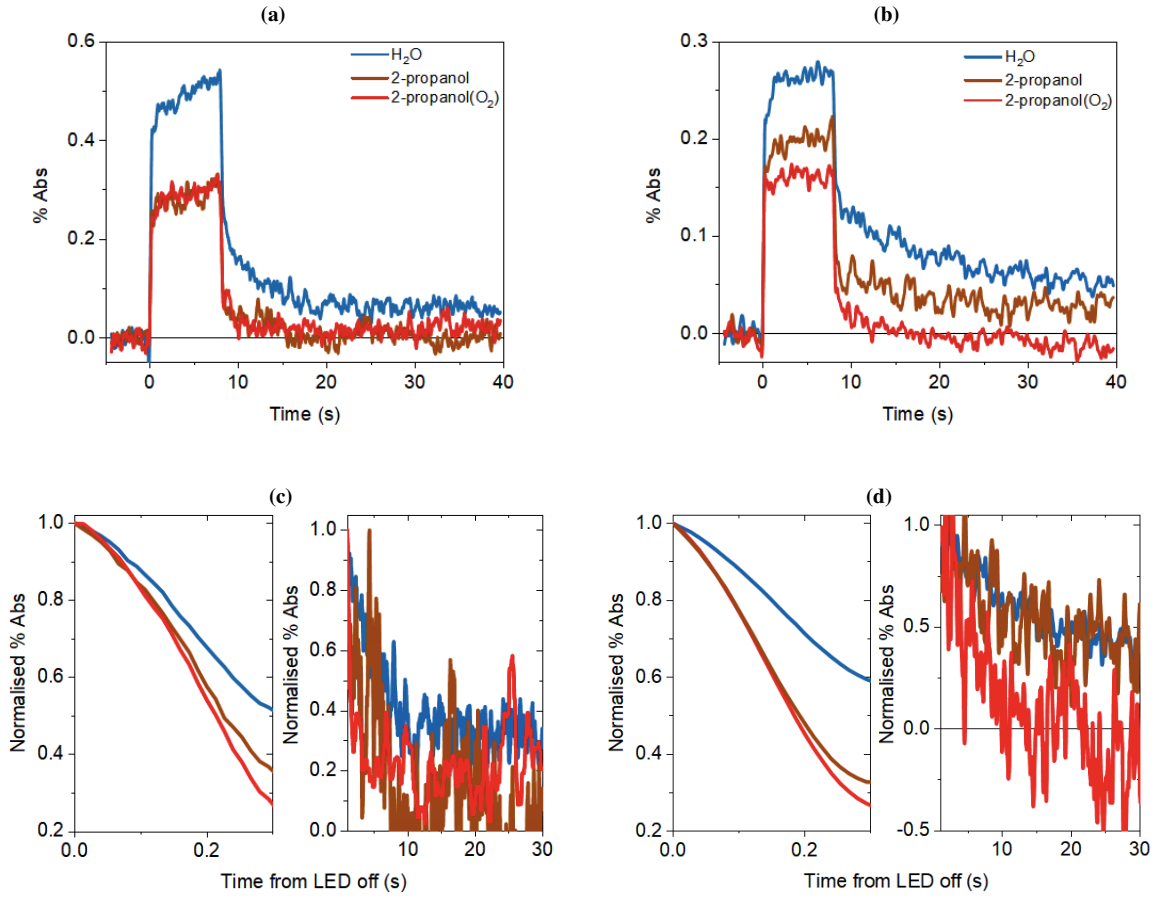

Figure 5.9: Comparison of PIAS kinetics of Al:$SrTiO_3$/$RhCrO_x$(PD) in anaerobic H_2O and 2-propanol compared to aerobic 2-propanol(O_2). Full kinetic traces probed at, a) 500 nm, and b) 800 nm. Normalised fast (LHS) and slow (RHS) phase kinetics, probed at c) 500 nm, and d) 800 nm.

RQY of Al:$SrTiO_3$/$RhCrO_x$(IMP) is likely to be an underestimate. This is due to the full amplitude of its slow phase decay being underestimated, as it is evident that it continues to decay significantly beyond the timescale of the measurement. Together, this is indicative of a lower

prevalence of unreactive trapped holes (corresponding to the slow phase) compared to mobile hole species (corresponding to the fast phase) in Al:$SrTiO_3$/$RhCrO_x$(PD). Given the demonstration of the reactivity of the fast phase towards hole scavenger (Figure 5.9c and 5.9d LHS) and the notably higher AQY of Al:$SrTiO_3$/$RhCrO_x$(PD) compared to Al:$SrTiO_3$/$RhCrO_x$(IMP) (93% vs. 56% at 365 nm), the larger contribution from the fast phase decay in the former is primarily attributed to increased reactivity of the hole species probed.

It is evident from the above comparisons that apart from the spectral assignments, the steady-state charge carrier dynamics of Al:$SrTiO_3$/$RhCrO_x$(PD) and Al:$SrTiO_3$/$RhCrO_x$(IMP) are dramatically different. Even though hole species in both compositions undergo a reactive fast phase decay and an unreactive slow phase, the prevalence of each differs greatly. In Al:$SrTiO_3$/$RhCrO_x$-(PD), the fast phase is more dominant, with a suppressed contribution of immobile and trapped holes compared to Al:$SrTiO_3$/$RhCrO_x$(IMP). This is indicative of higher hole reactivity and aids explanation of the enhanced water splitting performance of Al:$SrTiO_3$/$RhCrO_x$(PD).

Identification of deeply trapped hole species

The intensity dependence of the PIAS signals is investigated for Al:$SrTiO_3$/$RhCrO_x$(IMP) and Al:$SrTiO_3$/$RhCrO_x$(PD), to gain an insight into the differing distribution of states in these compositions that correspond to the fast and slow decay phases. In both compositions, the PIAS signal increases with increasing excitation intensity, due to increased charge generation out-competing recombination, until the signal saturates (Figure 5.10a and 5.10b). This was observed for Al:$SrTiO_3$ in Chapter 4 and is attributed to non-linear processes dominating at higher photogenerated charge densities, such as bimolecular recombination and/or trap filling processes.[99–101] Also observed in Al:$SrTiO_3$, is the acceleration of the fast phase decay with increasing excitation intensity (Figure 5.10c and 5.10d LHS), attributed to a non-linear increase in the rate of charge consumption with increasing charge densities.[80,158,159] The amplitude of the fast phase in Al:$SrTiO_3$/$RhCrO_x$(PD) is over two times larger than in Al:$SrTiO_3$/$RhCrO_x$(IMP) (Figure 5.10c and 5.10d LHS). This is in agreement with the doubling of the fast phase RQY and highlights the greater proportion of reactive hole species in this composition.

Turning now to the slow phase, which exhibits opposing dependencies on excitation intensity for Al:$SrTiO_3$/$RhCrO_x$(IMP) and Al:$SrTiO_3$/$RhCrO_x$(PD) (Figure 5.10c and 5.10d RHS). In Al:-$SrTiO_3$/$RhCrO_x$(IMP), the slow phase decelerates with increasing excitation intensity (Figure

5.10c RHS). This inverse dependence suggests that holes access and saturate increasingly deep trap states with increasing excitation energies and photogenerated hole densities. The opposing dependencies of the fast and slow phases on excitation intensity in Al:$SrTiO_3$/$RhCrO_x$-(IMP) implies that holes access and occupy states with a wide energy distribution under illumination conditions. Even though the slow phase is still present in Al:$SrTiO_3$/$RhCrO_x$(PD), it is less dominant and an inverse dependence on excitation intensity, assigned to filling increasingly deep trap states, is not observed (Figure 5.10d RHS). This suggests that in Al:$SrTiO_3$/$RhCrO_x$-(PD), holes are not accessing and trapping into such deep and unreactive hole states.

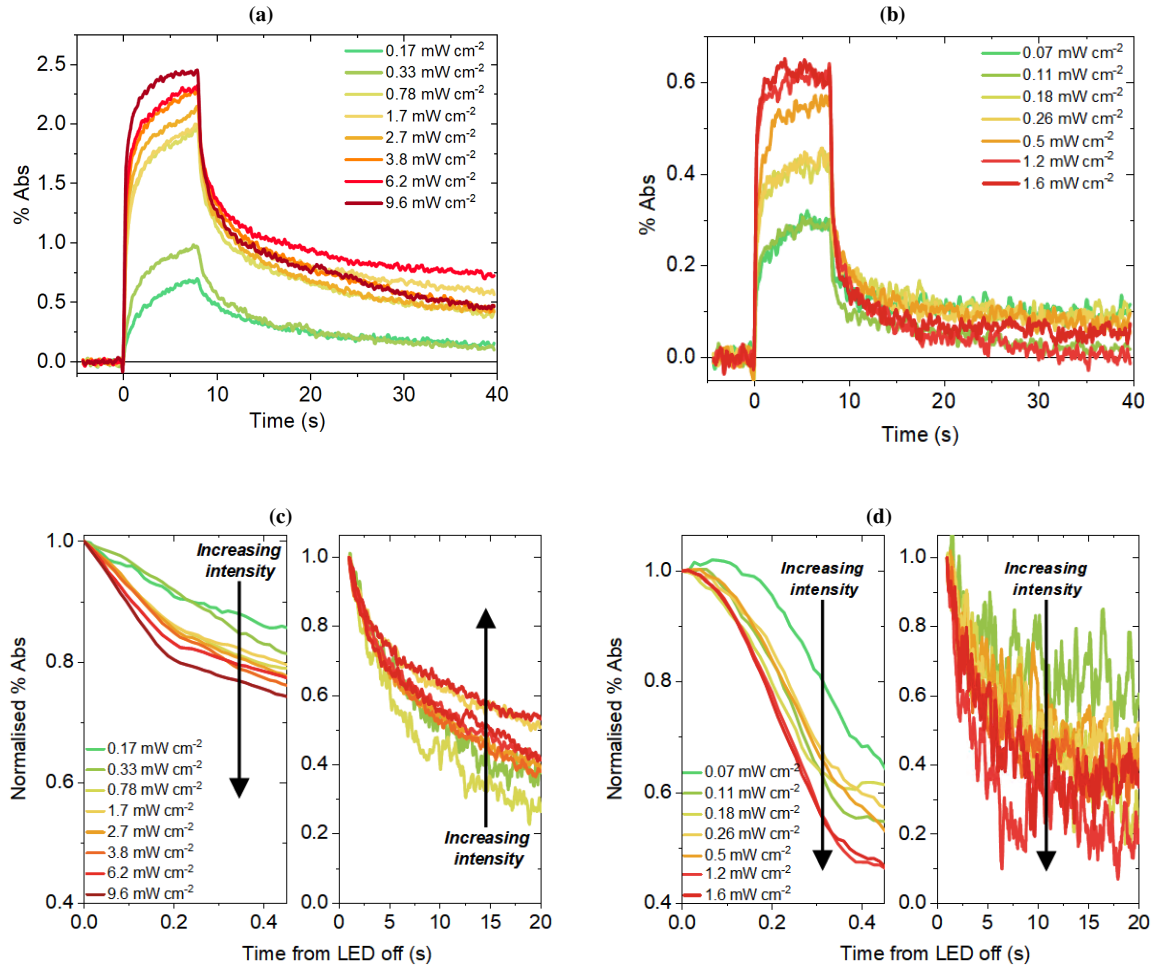

Figure 5.10: PIAS dependence on excitation intensity in H_2O for a) Al:$SrTiO_3$/$RhCrO_x$(IMP), and b) Al:$SrTiO_3$/-$RhCrO_x$(PD). dependence of the fast (LHS) and slow (RHS) phase decays on excitation intensity in H_2O for c) Al:$SrTiO_3$/$RhCrO_x$(IMP), and d) Al:$SrTiO_3$/$RhCrO_x$(PD)

To further understand the relationship between the fast reactive phase and the slow unreactive phase, PIAS measurements were taken under continuous BG illumination. Under BG illumination, there is a decrease in signal amplitude of almost 50% across the spectrum of Al:-$SrTiO_3$/$RhCrO_x$(IMP) (Figure 5.11a). This is attributed to prior excitation by BG illumination

filling hole states that would otherwise be probed in PIAS, and was also observed for $SrTiO_3$ and Al:$SrTiO_3$ in Chapter 4. Therefore, the uniform decrease in signal amplitude across the spectrum is unsurprising, given that holes are probed across the full spectrum of Al:$SrTiO_3$/-$RhCrO_x$(IMP) (Figure 5.5). Alongside the decrease in signal amplitude, the fast phase accelerates increases in dominance under BG illumination (in line with the intensity dependence), whilst the amplitude of the slow phase is suppressed (Figure 5.11c). This suggests the filling and passivation of deeply trapped hole states by BG illumination, such that a greater proportion of photogenerated holes in PIAS occupy reactive and shallow states that are responsible for the fast phase.

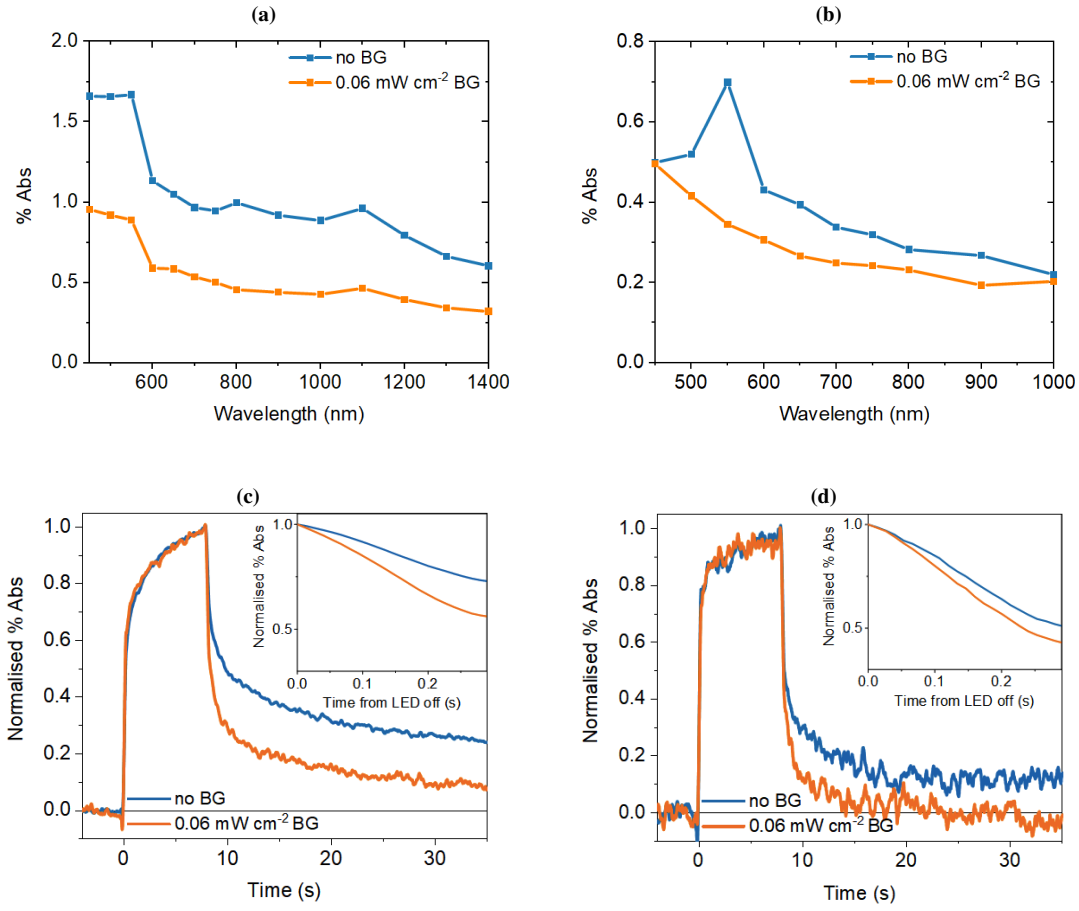

Figure 5.11: Impact of continuous BG illumination (from a 365 nm LED at 0.06 mW cm^{-2}) on the PIAS in H_2O. The impact of continuous BG illumination on the spectrum of a) Al:$SrTiO_3$/$RhCrO_x$(IMP), and b) Al:$SrTiO_3$/-$RhCrO_x$(PD), and on the normalised hole decay kinetics with the impact on the fast phase shown in the inset, for c) Al:$SrTiO_3$/$RhCrO_x$(IMP), and d) Al:$SrTiO_3$/$RhCrO_x$(PD).

As the fast phase is already dominant in Al:$SrTiO_3$/$RhCrO_x$(PD) prior to applying BG illumination, the impact of BG illumination is diminished (Figure 5.11b and 5.11d). The overall impact remains, whereby the signal amplitude is suppressed across the spectrum and the fast

phase decay is accelerated (whilst the slow phase is suppressed). However, compared to Al:-$SrTiO_3$/$RhCrO_x$(PD) these effects are small. Interestingly, the 550 nm peak in the Al:$SrTiO_3$/-$RhCrO_x$(PD) spectrum is eradicated under BG illumination, suggesting that it is due to a hole state that is filled under these conditions.

Through these PIAS investigations, the impact of $RhCrO_x$ deposition and its deposition route on the steady-state charge carrier dynamics is explored. The results provide useful insights into slow hole trapping and water oxidation processes. This includes the extensive hole trapping into unreactive and deep states in Al:$SrTiO_3$/$RhCrO_x$(IMP), that is suppressed in Al:$SrTiO_3$/-$RhCrO_x$(PD) where a higher prevalence of reactive hole species is observed. In order to investigate the consequences of these observations and recombination processes on earlier (μs-s) timescales DRTS is employed, with the results outlined in the following section.

5.3.3 Charge carrier dynamics on μs-s timescales

Al:$SrTiO_3$/$RhCrO_x$(IMP) and Al:$SrTiO_3$/$RhCrO_x$(PD) were investigated by DRTS, to compare the charge carrier dynamics measured at μs-s timescales following laser excitation to that measured for Al:$SrTiO_3$ and $SrTiO_3$, and also to those measured under steady-state PIAS conditions. Similarly to the case of $SrTiO_3$ and Al:$SrTiO_3$, there is a clear change in the DRTS decay kinetics probed above and below ~600 nm for Al:$SrTiO_3$/$RhCrO_x$(IMP) and Al:$SrTiO_3$/-$RhCrO_x$(PD) (Figure 5.12). Inconclusive scavenger studies in DRTS (Figure A.22 and A.23) result in the spectral assignments from PIAS and literature TAS investigations being used instead.[27,84,85,97,98] Using these assignments, the species probed below and from 600 nm are assigned to holes and electrons respectively. The kinetics are complex and cannot be fit to a simple power law or exponential decay. Nevertheless, they can be fit reasonably by two stretched exponentials (Figure A.24), similarly to Al:$SrTiO_3$ and indicative of dispersive recombination.[100,140] The stretched exponential fits comprise of a faster and slower component, which is not unlike the two component (fast and slow phase) PIAS decays. Overall, the stretching components are greater for the fits at 500 nm than 800 nm, which corresponds to the slower decays observed at 500 nm and extended hole lifetimes due to trapping that are expected from PIAS. In addition to the stretched exponential decays, there is a small bleach at later times (from 0.1 s) observed at the lowest probe wavelengths, assigned to electron trapping into V_O after the initial electron

extraction to $RhCrO_x$.[104,105]

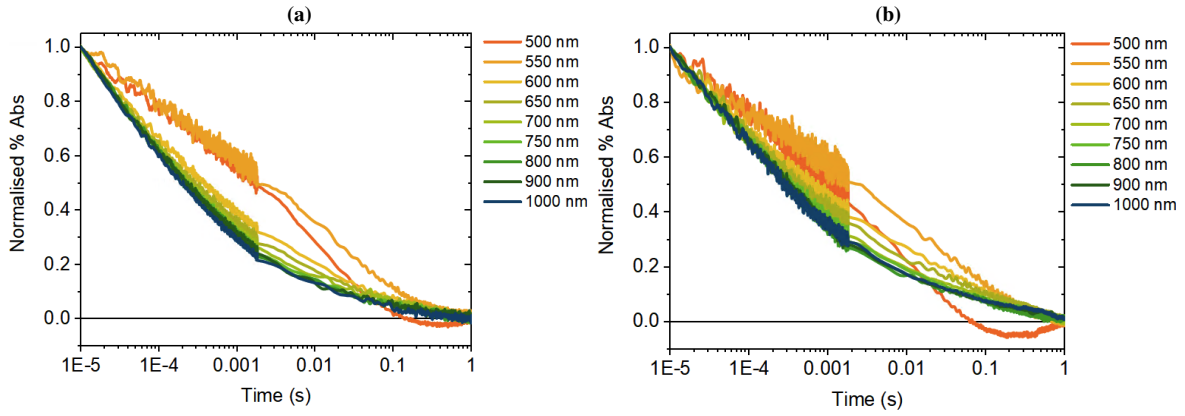

Figure 5.12: Normalised DRTS kinetics in H_2O, for a) Al:$SrTiO_3$/$RhCrO_x$(IMP), and b) Al:$SrTiO_3$/$RhCrO_x$(PD).

In PIAS, the initial fast phase decays accelerated with increasing excitation intensities for all compositions and there was a slow phase observed that indicated the presence of trapped hole species. These observations are confirmed and explored further by intensity dependent DRTS measurements. The hole decays of Al:$SrTiO_3$/$RhCrO_x$(IMP) and Al:$SrTiO_3$/$RhCrO_x$-(PD), probed at 500 nm in DRTS, accelerate with increasing excitation intensity (Figure 5.13) in agreement with the fast phase hole decays in PIAS. The degree of the kinetic dependence is smaller than is expected for a typical bimolecular decay process (as was also observed in Al:$SrTiO_3$ in Chapter 4)[33,102,142,160] and there is a non-linear increase in signal amplitude with excitation intensity (Figure 5.13, insets). As explained in more detail in Chapter 4, this is indicative of a trap-filling model.[111] Thus, the intensity dependence of the decays in both the PIAS and DRTS of Al:$SrTiO_3$/$RhCrO_x$(IMP) and Al:$SrTiO_3$/$RhCrO_x$(PD) suggests the presence of trap states that influence the kinetics.

Under BG illumination, the filling of hole states and an acceleration in their kinetics is observed for Al:$SrTiO_3$/$RhCrO_x$(IMP) and Al:$SrTiO_3$/$RhCrO_x$(PD). As holes and electrons are probed in different spectral regions in DRTS, the filling of hole states manifests as a decrease in amplitude at probe wavelengths <600 nm that are assigned to hole species (Figures 5.14a and 5.14b). This is in agreement with the filling of hole states by BG illumination in PIAS, where due to holes being probed at all wavelengths the amplitude decreases across the full PIAS spectrum. Meanwhile, the acceleration in hole decay kinetics under BG illumination, expected from what was observed in PIAS, is also observed in DRTS (FigureS 5.14c and 5.14d). The hole decay kinetics are accelerated in DRTS such that they no longer exhibit a slower decay compared to

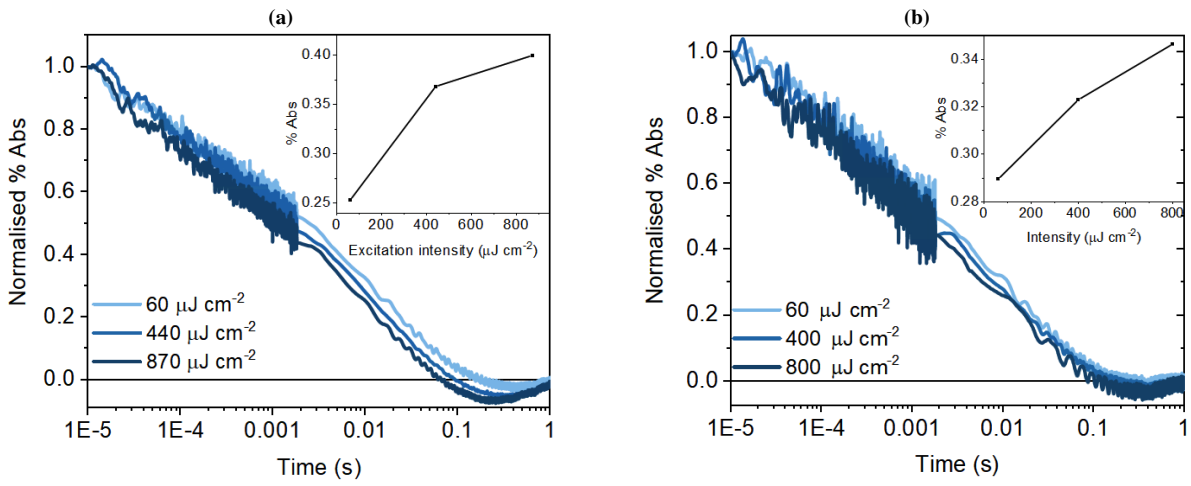

Figure 5.13: Intensity dependent DRTS kinetics H_2O, with the dependence of the signal amplitude on intensity showed in the insets. Probed at 500 nm, for a) Al:$SrTiO_3$/$RhCrO_x$(IMP), and b) Al:$SrTiO_3$/$RhCrO_x$(PD). A small degree of intensity dependence is observed regarding an acceleration of decay kinetics with increasing excitation intensity. The signal amplitude increases with increasing excitation intensity and begins to plateau at higher intensities.

the electrons. In addition, under BG illumination bleaching at later times is amplified compared to in $SrTiO_3$ and Al:$SrTiO_3$, tentatively attributed to electron trapping into states vacant of electrons from prior electron extraction to $RhCrO_x$.

Despite the above parallels between what is observed in PIAS and DRTS, there are also some notable differences. Primarily, the dramatically different decay kinetics of Al:$SrTiO_3$ following $RhCrO_x$ deposition observed in PIAS are not observed in the DRTS decay kinetics displayed in Figure 5.15. As discussed in Chapter 4, Al^{3+} doping slows down the DTRS kinetics compared to $SrTiO_3$. However, the deposition of $RhCrO_x$ does not significantly impact the DRTS kinetics and the kinetics probed at 800 nm for Al:$SrTiO_3$/$RhCrO_x$(IMP) and Al:$SrTiO_3$/-$RhCrO_x$(PD) are unchanged compared to Al:$SrTiO_3$ (Figure 5.15b). The 500 nm kinetics are relatively unchanged at early times, until ~0.1 ms when the decays of Al:$SrTiO_3$/$RhCrO_x$(IMP) and Al:$SrTiO_3$/$RhCrO_x$(PD) accelerate due to the small degree of bleaching from 0.1 ms (Figure 5.15a). Moreover, the notable differences in the impact of BG illumination on Al:$SrTiO_3$/-$RhCrO_x$(IMP) and Al:$SrTiO_3$/$RhCrO_x$(PD) in PIAS are not translated to DRTS. In PIAS, BG illumination had more significant effects on Al:$SrTiO_3$/$RhCrO_x$(IMP), due to increased filling of deep hole trap states that would otherwise be filled and observed in the PIAS measurement. In μs-TAS, differences in hole trapping into these deep states are not observed.

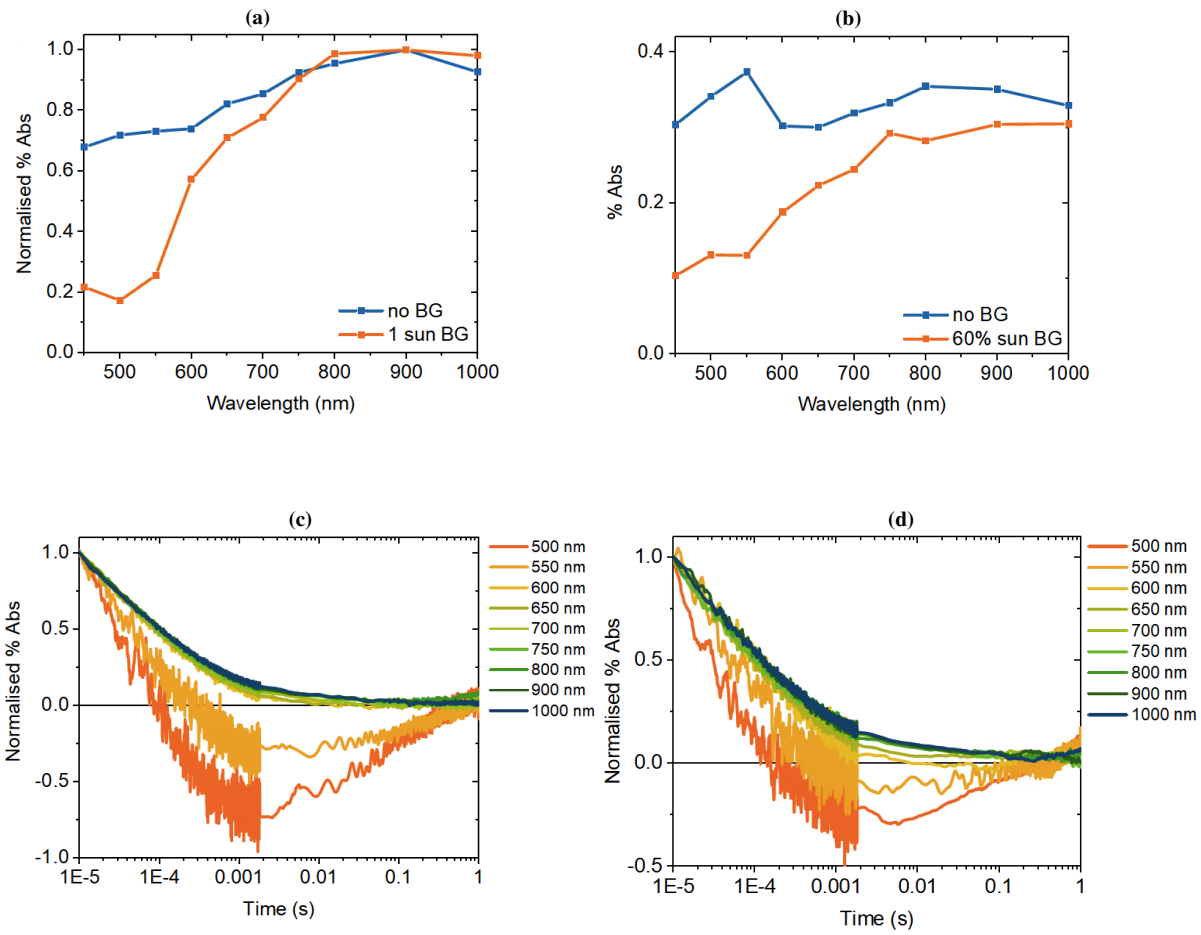

Figure 5.14: DRTS spectrum in H_2O without and with continuous BG illumination and normalised at 10 μs, for a) Al:$SrTiO_3$/$RhCrO_x$(IMP), and b) Al:$SrTiO_3$/$RhCrO_x$(PD). DRTS decay kinetics under continuous BG illumination, for c) Al:$SrTiO_3$/$RhCrO_x$(IMP), and d) Al:$SrTiO_3$/$RhCrO_x$(PD).

When considering the differences in the results obtained by PIAS and DRTS it is important to consider the different timescales measured and excitation conditions employed. PIAS employs continuous illumination and measures in the steady-state, whilst DRTS employs high intensity laser pulses and measures at earlier timescales. Therefore, PIAS can effectively measure slow processes that occur during or following steady-state conditions, whilst DRTS can measure the laser induced populations and recombination kinetics of photogenerated species. With these differences in mind, the results reported reveal that $RhCrO_x$ deposition does not affect the laser induced recombination or charge separation capabilities observed under DRTS conditions. However, under the steady-state conditions and longer timescales of PIAS, the effects of $RhCrO_x$ on slow charge trapping and decay processes can be observed.

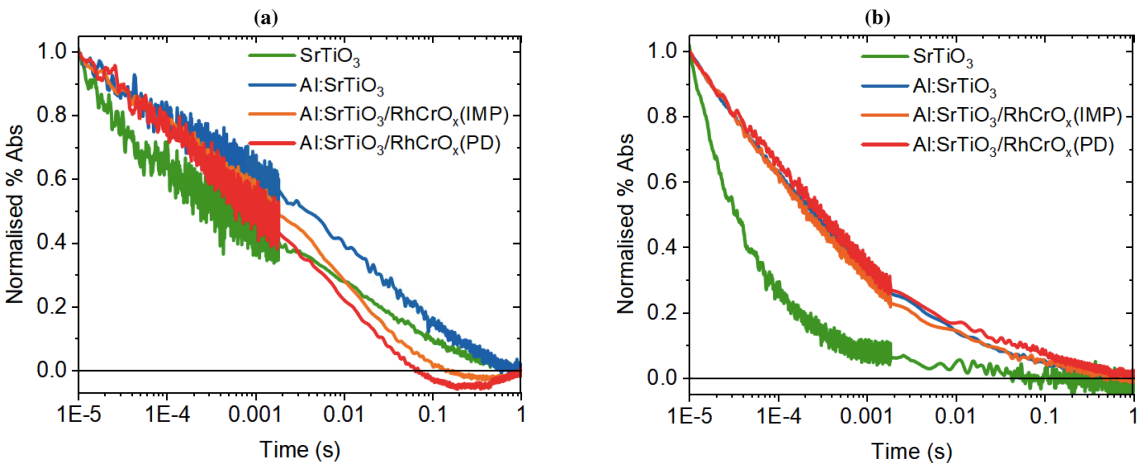

Figure 5.15: A comparison of the DRTS decay kinetics in H_2O for $SrTiO_3$, Al:$SrTiO_3$, Al:$SrTiO_3$/$RhCrO_x$(IMP), and Al:$SrTiO_3$/$RhCrO_x$(PD), a) probed at 500 nm, and b) probed at 800 nm.

5.4 Discussion

The addition of $RhCrO_x$ is integral for the state-of-the-art performance of Al:$SrTiO_3$/$RhCrO_x$-(IMP) and Al:$SrTiO_3$/$RhCrO_x$(PD). It serves to extract electrons and catalyse proton reduction, offering the opportunity to spatially separate charge and extend hole lifetimes as a result. This is demonstrated in Al:$SrTiO_3$/$RhCrO_x$(IMP) and Al:$SrTiO_3$/$RhCrO_x$(PD), by the hole species dominating the full PIAS spectra (with the dominant electron contribution at longer wavelengths in Al:$SrTiO_3$ no longer present) and the presence of a slow phase that is absent in $SrTiO_3$ and Al:$SrTiO_3$. Despite these similarities, dramatically different photocatalytic activity is observed for Al:$SrTiO_3$/$RhCrO_x$(IMP) and Al:$SrTiO_3$/$RhCrO_x$(PD), with reported AQYs of 56% and 93% at 365 nm respectively.[37,38] The two deposition routes give rise to different distributions of the $RhCrO_x$ co-catalyst, with $RhCrO_x$ randomly distributed in Al:$SrTiO_3$/$RhCrO_x$(IMP), in contrast to it being selectively deposited onto reduction facets in Al:$SrTiO_3$/$RhCrO_x$(PD). The consequences of this can be seen in the different steady-state charge carrier dynamics observed in PIAS, that are explored in detail in this chapter and the focus of this discussion.

5.4.1 Influence of $RhCrO_x$ deposition route on steady-state charge carrier dynamics

In Al:$SrTiO_3$/$RhCrO_x$(IMP), the steady-state hole populations measured by PIAS are greatly increased compared to Al:$SrTiO_3$, due to the significant increase in lifetimes, rather than an increase in hole RQY. The similar RQYs of reactive hole species measured under PIAS conditions suggests that in this composition, the primary role of the $RhCrO_x$ co-catalyst is not increasing charge separation on timescales prior to the PIAS measurement. Instead, the $RhCrO_x$ can improve photocatalytic activity by other means, for example by extracting electrons such that backwards reactions on the Al:$SrTiO_3$ surface are suppressed. In any case, with the high steady-state hole populations, a significant charge imbalance under illumination is expected to result from the accumulation of holes in Al:$SrTiO_3$ regions that neighbour the $RhCrO_x$ co-catalyst extracting electrons. Instead of a concurrent increase in recombination being observed with hole accumulation, as is commonly observed in metal oxides,[12,161,162] holes are remarkably long-lived and a slow decay phase persists for 10s of seconds. Although a fast reactive decay coexists with the slow decay phase, the latter is correlated to deeply trapped hole states that appear unreactive and are therefore expected to limit the photocatalytic activity.

The fast decay phase of hole species in Al:$SrTiO_3$/$RhCrO_x$(PD) is more prominent compared to in Al:$SrTiO_3$/$RhCrO_x$(IMP). Due to this phase corresponding to reactive species, this is indicative of higher yields of reactive hole species that can contribute to water splitting activity. Al:-$SrTiO_3$/$RhCrO_x$(PD) maintains the ability to accommodate long-lived holes, as demonstrated by a slow phase contribution that remains present. However, this contribution is greatly suppressed compared to Al:$SrTiO_3$/$RhCrO_x$(IMP), meaning that a lower proportion of holes reside in unreactive hole trap states that are unable to contribute to water splitting activity.

A proposed hypothesis for the enhanced hole reactivity in Al:$SrTiO_3$/$RhCrO_x$(PD), compared to in Al:$SrTiO_3$/$RhCrO_x$(IMP), is illustrated in Figure 5.16. In Al:$SrTiO_3$/$RhCrO_x$(IMP), $RhCrO_x$ is distributed randomly across both oxidation and reduction facets (Figure 5.1a). When the $RhCrO_x$ proton reduction co-catalyst is located on oxidation facets, the reaction of holes is inhibited and there is extensive opportunity for them to access and accumulate in deeply trapped hole states (Figure 5.16a). This limits the population of holes residing in mobile and reactive

hole states, and instead results in a significant population of unreactive and deeply trapped holes that limit photocatalytic activity. In Al:$SrTiO_3$/$RhCrO_x$(PD), $RhCrO_x$ is exclusively on the reduction facets and absent from the oxidation facets, enabling holes to transfer to the reactant solution uninhibited by $RhCrO_x$ (Figure 5.16b). Thus, holes exhibit increased reactivity and participation in the water oxidation reaction, and therefore have less opportunity to accumulate in deeply trapped hole states.

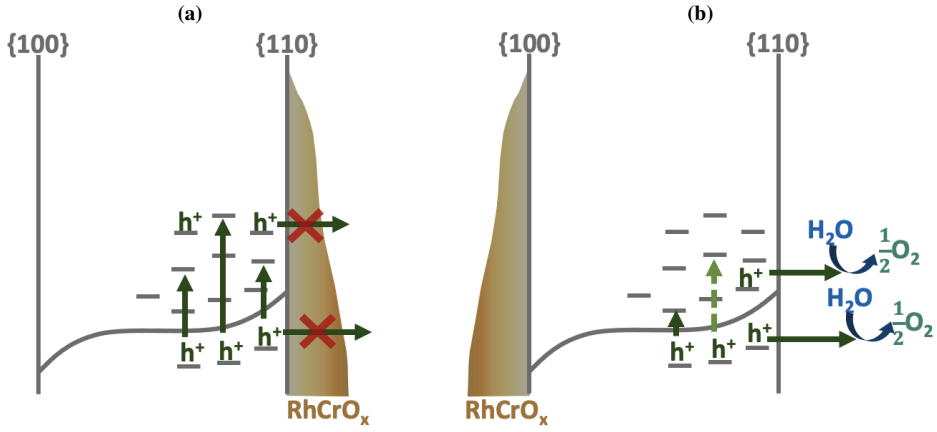

Figure 5.16: Schematic illustration of the effect of the $RhCrO_x$ deposition route on hole trapping. a) In Al:-$SrTiO_3$/$RhCrO_x$(IMP), $RhCrO_x$ is unselectively deposited across all facets, including the {110} oxidation facet, where it inhibits the interfacial transfer of holes to H_2O and their utilisation in catalytic reactions. b) In Al:$SrTiO_3$/-$RhCrO_x$(PD), $RhCrO_x$ is selectively deposited onto the {100} reduction facets, so that the holes at the oxidation facets can transfer across the interface and oxidise H_2O uninhibited.

It is noted that the higher proportion of metallic Rh in Al:$SrTiO_3$/$RhCrO_x$(PD) could also play a role in the higher photocatalytic activity observed, as metallic Rh is the optimum oxidation state for catalysing the proton reduction reaction.[61] However, under illumination the dominant Rh oxidation states in Al:$SrTiO_3$/$RhCrO_x$(IMP) may change and result in a greater proportion of metallic Rh, perhaps contributing to the induction period required for this composition to achieve the final water splitting activity.[163] Unfortunately, correlating the dominant Rh oxidation states to photocatalyst performance and charge carrier dynamics is beyond the scope of this work.

5.4.2 The origins of long-lived charges in photocatalysts

In Al:$SrTiO_3$/$RhCrO_x$(IMP) and Al:$SrTiO_3$/$RhCrO_x$(PD), the combined effects of several factors facilitate the charge accumulation and long-lived charges observed. Primarily, efficient and seemingly irreversible electron extraction to $RhCrO_x$ spatially separates holes and electrons to

suppress their recombination, but the intrinsic properties of $SrTiO_3$ and the role of Al^{3+} doping also play a key role. $SrTiO_3$ has a dielectric constant ($\sim$300)[118–121] that is much higher than other metal oxides commonly employed in photocatalytic applications (a property of $SrTiO_3$ explored in more detail in Chapter 3),[122,124–126] which increases the screening of charge pairs and reduces the probability of them recombining. Flux mediated Al^{3+} doping further minimises recombination (as demonstrated in Chapter 3) due to the suppression of Ti^{3+} recombination centres and enhanced morphology.[34,43] This enhanced morphology manifests in the energy offset and electric field between the oxidation and reduction facets of the Al:$SrTiO_3$ crystals, which facilitates the spatial separation of charges and enables the selective deposition of $RhCrO_x$ onto reduction facets in Al:$SrTiO_3$/$RhCrO_x$(PD).[38]

PIAS investigations of several other photocatalyst systems reveal long-lived charges, but in each case the mechanisms that underpin their lifetimes and accumulation are different. For the hydrogen evolution system comprised of GaN:ZnO modified with $RhCrO_x$, this is achieved by the energy offset between the GaN and ZnO domains, in combination with electron extraction to $RhCrO_x$.[35] However, in most other cases an external driver such as scavengers or applied bias is required to observe accumulated and long-lived species. For example, in carbon nitride based systems scavengers are required,[33,164] whilst for photoanode systems the application of applied bias is needed to drive the necessary lifetime gain.[21] Regardless of the different classes of photocatalyst material and mechanisms underpinning their ability to achieve long-lived species, it is noteworthy that they are frequently observed in operational photocatalytic water splitting systems studied by PIAS.[35,59,165] Thus, the ability to sustain these long-lived species appears to be an integral feature of water splitting photocatalyst systems.

5.4.3 The impact of accumulated and long-lived charges on photocatalytic performance

In the photocatalysts investigated in this chapter, charge accumulation and lifetimes measured by PIAS increase simultaneously. This is a rare feature for photocatalytic materials, where in addition to decreasing reactivity, charge trapping and accumulation can serve to increase recombination.[32,33,160–162] Such adverse effects are observed in cyanamide surface functionalised carbon nitride ($^{NCN}CN_x$) photocatalysts, where electron trapping and accumulation in-

creases recombination losses and limits the efficiency of hydrogen production.[33,160] Meanwhile, in photoanodes employed in PEC water oxidation, hole accumulation frequently results in increased back electron-hole recombination that kinetically competes with water oxidation and limits the efficiency.[32,161,162] The ability of the $SrTiO_3$-based photocatalysts observed herein, to avoid these adverse effects and accumulate charge without detriment to recombination rates, is important for sustaining sufficient hole densities for the kinetically slow multi-hole water oxidation reaction (and for enabling reasonably good function of Al:$SrTiO_3$/$RhCrO_x$(IMP) despite the low reactivity of the hole species).

The ability to accumulate high charge densities without an increase in recombination is attributed to charge screening effects and efficient spatial charge separation on long timescales. The spatial charge separation in Al:$SrTiO_3$/$RhCrO_x$(IMP) and Al:$SrTiO_3$/$RhCrO_x$(PD) primarily results from electron extraction to $RhCrO_x$, with added effects from the internal electric field between facets. Meanwhile, in organic heterojunctions for photocatalytic hydrogen evolution, accumulated and long-lived species are correlated to higher photocatalytic efficiencies, and attributed to efficient spatial charge separation resulting from the phase segregated morphology.[165] In the case of these $SrTiO_3$-based systems, the large dielectric constant of $SrTiO_3$ is responsible for the high degree of charge screening. Interestingly, ionic carbon nitrides based on poly(heptazine imides) (PHI) exhibit charge accumulation without detriment to recombination.[164] This is attributed to the screening of accumulated negative charge by the positive cations, a phenomenon that is not possible in non-ionic carbon nitrides where charge accumulation is of detriment to recombination and performance.[33] A further example is in perovskite solar cells, where deep charge trapping and a high dielectric constant enables charge accumulation to occur simultaneously with a decrease in recombination rates.[82,166]

Even when accumulated charges in photocatalysts are long-lived and do not result in a measurable increase in recombination, their typically trapped nature results in a loss in reactivity,[35,160,164] as is the recognised trade-off between lifetime gain and energetic driving force.[26] In Al:$SrTiO_3$/-$RhCrO_x$(IMP), the population of trapped hole states with poor reactivity can be suppressed by decreasing opportunities for hole trapping (achieved by the facet selective photodeposition in Al:$SrTiO_3$/$RhCrO_x$(PD)), or alternatively by BG illumination. This is demonstrated by the intensity dependence and BG illumination PIAS measurements in this chapter, and supports a recent study by Domen and co-workers into the oxygen evolution kinetics of Al:$SrTiO_3$/$RhCrO_x$-

(IMP).[163] In their study, a slow initial rate of oxygen evolution increased under illumination until a steady-state was achieved after several seconds. This led to a proposed two-state model of oxygen evolution, where microscopic regions are converted from an inactive to active state under illumination. The *in situ* spectroscopic studies in this chapter provide novel evidence for such explanations and demonstrate the link between suppressing or passivating unreactive hole states and achieving faster reaction kinetics.

5.4.4 Overall photocatalyst function

The overall functions and factors facilitating the state-of-the-art performance of Al:$SrTiO_3$/-$RhCrO_x$(PD) are summarised in Figure 5.17. The desirable attributes of this system builds on that achieved by Al^{3+} doping as explored in Chapter 4, which included recombination kinetics that were four times slower than $SrTiO_3$. This was achieved in part by suppressing Ti^{3+} states, such that their role in charge trapping and facilitating electron-hole recombination is minimised. In addition, the resulting electric field between oxidation and reduction facets, that is required for the facet selective $RhCrO_x$ photodeposition, drives charge separation. In Al:-$SrTiO_3$/$RhCrO_x$(PD), these attributes are combined with fast electron extraction to $RhCrO_x$ selectively deposited onto the reduction facets. Once electrons are successfully extracted to $RhCrO_x$, they reduce protons to evolve hydrogen and do not participate in backwards reactions, on the Al:$SrTiO_3$ surface for example. As electron extraction to $RhCrO_x$ appears to occur prior to PIAS measurements, and proton reduction on $RhCrO_x$ is also reported to be fast,[35,156,157] short sub-ms lifetimes of electrons in the bulk Al:$SrTiO_3$ regions are assumed. Finally, as the oxidation facets are free from $RhCrO_x$, holes participate in water oxidation catalysis uninhibited and exhibit high reactivity. Although deep hole trapping is less prevalent in Al:$SrTiO_3$/$RhCrO_x$(PD) compared to Al:$SrTiO_3$/$RhCrO_x$(IMP), a degree of hole trapping does still occur. Nevertheless, the population of hole species in these states is lower in Al:$SrTiO_3$/$RhCrO_x$(PD). Moreover, due to efficient electron extraction to $RhCrO_x$ and good charge separation in the photocatalyst, they are not correlated to an increase in recombination (as indicated by their corresponding lifetimes of seconds).

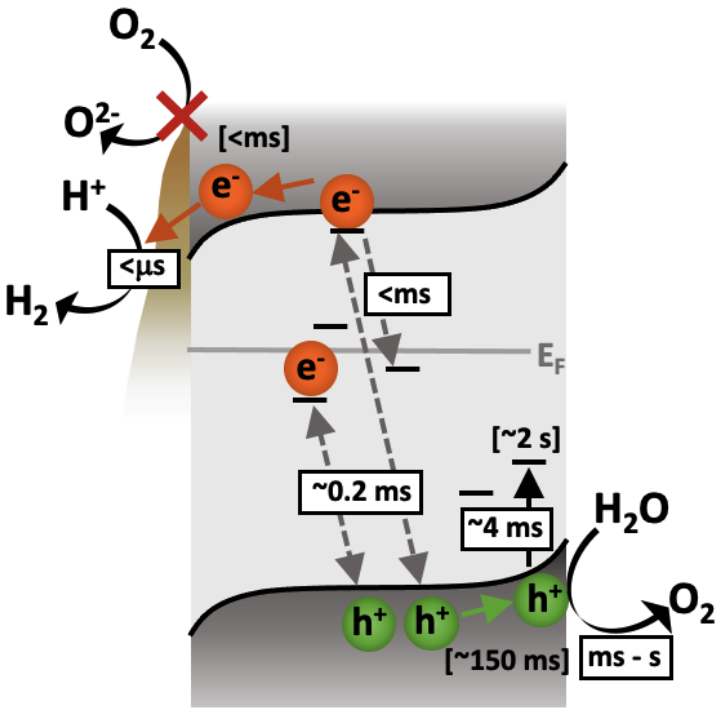

Figure 5.17: Schematic illustration of the overall function of the high performing Al:$SrTiO_3$/$RhCrO_x$(PD) photocatalyst for OPWS. Timescales in white boxes are that of recombination, trapping and extraction processes. Meanwhile, timescales in square brackets indicate the lifetimes of species.

5.5 Conclusion

In this chapter, the steady-state charge carrier dynamics of Al:$SrTiO_3$/$RhCrO_x$(IMP) and Al:-$SrTiO_3$/$RhCrO_x$(PD) are investigated and compared to each other, $SrTiO_3$ and Al:$SrTiO_3$, for the first time. Through the use of *in situ* spectroscopic measurements, these investigations explore the influence of $RhCrO_x$ and its deposition route on charge carrier dynamics relevant to photocatalytic performance, and identify reasons for the state-of-the-art near-unity AQY of Al:$SrTiO_3$/$RhCrO_x$(PD).

Building on the enhancement to charge densities and lifetimes observed following Al^{3+} doping, $RhCrO_x$ deposition via impregnation or photodeposition further enhances these features, due to electron extraction to $RhCrO_x$ and the resulting spatial separation of charges. Although accumulated and trapped hole species are prevalent in these systems, particularly in Al:$SrTiO_3$/-$RhCrO_x$(IMP), a concurrent increase in recombination is not observed and instead a slow phase persists for 10s of seconds. The slow rate of water oxidation compared to proton reduction, and the need to acquire multiple holes at the reactant site, frequently leads to hole accumulation in water splitting systems. Thus, the ability to tolerate charge accumulation, demonstrated by the photocatalysts investigated in this chapter, is an important feature of water splitting systems in general. However, it is especially important in single-step OPWS, where the holes and electrons reside and react in the same particles. Despite the accumulated species not resulting in increased recombination (due to the multitude of properties and modifications discussed that facilitate charge separation and suppress recombination), these charges are assigned to trapped hole species that are unreactive and limit photocatalytic activity.

This work identifies the importance of striking a balance between accommodating accumulated and long-lived species for the kinetically slow multi-hole water oxidation reaction, and obtaining charges with good reactivity. This is demonstrated by Al:$SrTiO_3$/$RhCrO_x$(IMP) being able to accumulate large amounts of charge without detriment to recombination, but exhibiting a significantly lower AQY than Al:$SrTiO_3$/$RhCrO_x$(PD) (56% vs. 93% at 365 nm). In Al:$SrTiO_3$/$RhCrO_x$(PD), the ability to accumulate charge without detriment to recombination is maintained. However, there is a markedly increased contribution from reactive hole species, together with a decrease in deeply trapped holes that are unreactive. As a result, higher photocat-

alytic activities are achieved. Thus, the population of reactive hole species should be maximised and the extent of the long-lived species arising from deep hole trapping should be moderated, to ensure that they do not significantly limit photocatalytic activity.

Different morphologies result from $RhCrO_x$ deposited via impregnation and photodeposition, yielding mixed oxide and core-shell structures respectively.[38,43,61,67,68] In addition, a higher proportion of metallic Rh in Al:$SrTiO_3$/$RhCrO_x$(PD) is identified in this work. Future work exploring the effects of such properties on the charge carrier dynamics and photocatalytic performance could give useful insights into how to optimise the $RhCrO_x$ co-catalyst. An additional direction for future work is regarding the role of CoOOH in the final photocatalyst systems fabricated by Domen and co-workers.[37,38,40] It is not clear from the literature what the role of CoOOH is, due to it solely improving stability and not the photocatalytic activity of Al:$SrTiO_3$/$RhCrO_x$(IMP), but increasing the photocatalytic activity of Al:$SrTiO_3$/$RhCrO_x$(PD). Thus, exploring the effects of CoOOH on the charge carrier dynamics of these photocatalysts would offer the potential to gain new and important insights into its precise role.

In order for OPWS photocatalysts to be a commercially viable and competitive technology, they need to achieve a good STH efficiency (5-10%).[9,17,18] To achieve this, photocatalysts that combine a high AQY with good visible light absorption are required. However, at present there are no known photocatalysts that successfully combine these properties. To obtain such materials, the insights from this chapter regarding what enables Al:$SrTiO_3$/$RhCrO_x$(PD) to achieve a near-unity AQY can be incorporated into the design of photocatalysts with enhanced visible light absorption. These include tolerance to charge accumulation and utilising an internal electric field to enable selective co-catalyst deposition and the separation of oxidation and reduction sites.

Chapter 6

$SrTiO_3$ under applied bias – charge carrier dynamics and water oxidation kinetics

In this final results chapter, $SrTiO_3$ is investigated under applied bias. Although the central interest in $SrTiO_3$ of this thesis is not due to its photoanode performance, the application of applied bias can offer invaluable insights into the properties and kinetics of the charge carriers probed in spectroscopic measurements. Under applied bias, confident spectral assignments under TAS conditions are made for $SrTiO_3$, whilst the first known calculation of the hole extinction coefficient and rate law analysis of water oxidation are conducted. The intrinsically good charge separation properties of $SrTiO_3$ are further explored, in addition to the influence of Ti^{3+} states on electron transport.

6.1 Introduction

The focus of this thesis is on $SrTiO_3$-based materials employed in overall photocatalytic water splitting, OPWS, without an applied bias to drive photocatalysis. Despite this, the investigation of $SrTiO_3$ under applied bias can still yield useful insights that are relevant for its use in OPWS. With this in mind, the aim of this chapter is to better understand the fundamental charge carrier dynamics and photophysical properties of $SrTiO_3$, through the application of applied bias to a $SrTiO_3$ photoanode.

Previous work investigating $SrTiO_3$ under applied bias has focused on the photoanode performance of $SrTiO_3$, rather than its spectroscopic or photophysical properties. The photocurrent response of photoanodes comprised only of $SrTiO_3$ is poor and typically requires Nb doping to enhance the conductivity and photocurrent.[54,167] Following optimisation of Nb doping, the photocurrents reported are in the range of $\sim$0.1 mA cm^{-2}. These photocurrents are not notable and a magnitude lower than the 3-6 mA cm^{-2} that can be achieved by photoanodes comprised of alternative metal oxides, such as $BiVO_4$, TiO_2, WO_3 or α-Fe_2O_3.[168–172] With this in mind, most research and interest in $SrTiO_3$ for water splitting surrounds its photocatalytic applications, rather than its PEC properties.[24,37,38,40,91]

Under PEC conditions, it is interesting to go beyond measuring photoanode performance and use the applied bias to acquire insights into $SrTiO_3$ that would not be possible under OPWS conditions. For example, the effects of bias induced band bending on charge separation and lifetimes can be investigated. Using the influence of applied bias on such properties, spectral assignments can be made that do not rely on the reactivities towards sacrificial scavenging agents.[79,106,107] This is achieved by monitoring the dependence of the optical signal and decay kinetics on the applied bias. For a photoanode, a positive bias drives electron extraction to the back contact and holes towards the surface. Therefore, with increasingly positive applied bias hole populations and lifetimes are enhanced, with the opposite true of electrons. Thus, optical signals that increase in amplitude and have decelerating decay kinetics with increasingly positive bias are assigned to holes, and vice versa for electrons.

Additionally, under applied bias intrinsic properties such as the hole extinction coefficient (a

measure of how strongly a species absorbs light at a given wavelength) can be calculated.[158,173] The hole extinction coefficient of $SrTiO_3$ is not known, and in fact is not widely reported for metal oxides employed in photocatalytic applications in general. Without knowledge of extinction coefficients, the potential of spectroscopic methods to quantify charge populations and charge generation yields is limited.[101,174] Finally, rate law analyses can be conducted, to gain an insight into the water oxidation kinetics occurring on the $SrTiO_3$ surface and specifically the hole accumulation required to achieve the RDS.[78–80,157,175,176] The analysis is conducted under applied bias, where the rate of water oxidation can be correlated to the steady-state surface hole density. The theory and method of the rate law analysis is explained in detail in Chapter 2.

In this chapter, the ability to undertake spectroscopic measurements on $SrTiO_3$ under applied bias is exploited. The aim of this is to gain novel insights into $SrTiO_3$ that can support the investigations of this thesis and future work. Spectral assignments in μs-TAS are made from the bias dependence of the signal amplitudes and decay kinetics. With this confirmed hole assignment, the hole extinction coefficient is calculated to facilitate the quantification of hole species in the spectroscopic studies undertaken throughout this thesis. Lastly, a rate law analysis on $SrTiO_3$ is conducted to gain a novel insight into the water oxidation kinetics at the surface.

6.2 Experimental methods

The $SrTiO_3$ photoanodes investigated in this chapter are identical to the $SrTiO_3$ thin films on FTO, that are provided by the University of Liverpool and the focus of Chapter 3. The results from the physical characterisation of these films are therefore included in Chapter 3. All PEC and spectroscopic measurements in this chapter are undertaken in 0.1 M NaOH (pH 13) electrolyte solution, with a detailed description of the PEC set-up included in Chapter 2. Transient spectroscopic techniques (PIAS and μs-TAS) are conducted in transmission mode, due to the transmissive nature of the $SrTiO_3$ films. All μs-TAS measurements employ an excitation intensity of 400 μJ cm^{-2}.

6.3 Results

6.3.1 Photoelectrochemical characterisation

The J-V response of $SrTiO_3$ was recorded under chopped light conditions to ensure that it exhibits photocurrent generation (Figure 6.1). The onset potential for photocurrent generation is $\sim$0.4 V_{RHE}, in good agreement with what has been observed previously for unmodified $SrTiO_3$.[54] With increasingly positive applied bias, the photocurrent increases and reaches 7 μA cm^{-2} at 1.23 V_{RHE}. It is acknowledged that this is a low photocurrent, but that unmodified $SrTiO_3$ is not a popular photoanode material recognised to give large photocurrents.[54,167] Improved photocurrents are only achieved through modifying the composition of $SrTiO_3$, for example by Nb doping to improve electrical conductivity ($\sim$0.1 mA cm^{-2} at 1.23 V_{RHE}).[54,167]

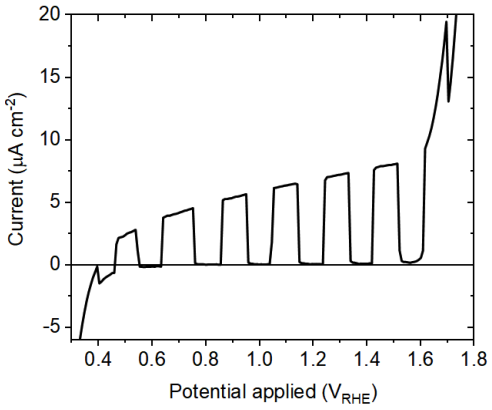

Figure 6.1: Chopped light J-V response of $SrTiO_3$, measured using illumination from a 365 nm LED at 1 sun illumination intensity ($\sim$2.7 mW cm^{-2}).

6.3.2 Charge carrier dynamics on μs timescales

The charge carrier dynamics of the films were primarily investigated by μs-TAS. The decay kinetics exhibited a strong dependence on wavelength (Figure 6.2a), with a characteristic change in decay kinetics at $\sim$600 nm, as was also observed for the $SrTiO_3$-based particulate photocatalysts in Chapters 4 and 5. The spectrum at 10 μs is also characteristic of $SrTiO_3$ and is dominated by signals probed below 600 nm, with a weaker feature in the early NIR (Figure 6.2b). This is in good agreement with the features observed in the literature,[84] and also the fea-

tures present in Chapter 4. However, compared to the particulate $SrTiO_3$ in Chapter 4, the early NIR feature observed here is less dominant. A change in spectral shape between $SrTiO_3$ materials fabricated by different routes is expected, due to the spectral features being very sensitive to defects and surface contaminants, which are likely to differ between fabrication routes.[84]

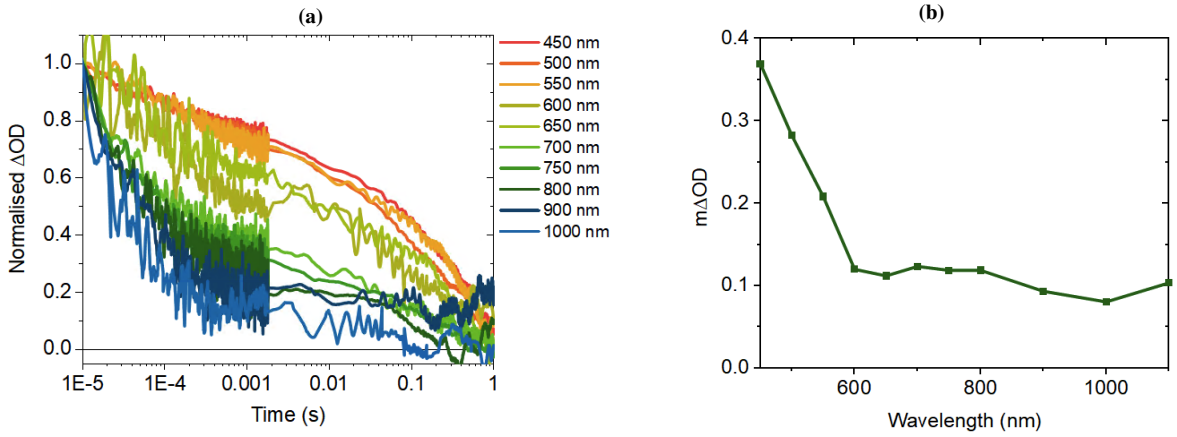

Figure 6.2: μs-TAS measurements of $SrTiO_3$ in NaOH using a laser excitation intensity of 400 μJ cm^{-2}. a) Normalised decay kinetics measured across the range of probe wavelengths. b) μs-TAS spectrum measured at 10 μs.

The bias dependence of the TAS decays in the two decay regions (at 500 nm and 800 nm) are compared in Figure 6.3, to enable spectral assignments of electron and hole species. At 500 nm, the signal amplitudes increase and the decay kinetics decelerate with increasingly positive applied bias (Figure 6.3a). This is characteristic of hole species being probed, whereby with increasingly positive bias electron extraction is increased and therefore so are hole lifetimes. Thus, the signals at 500 nm and the corresponding region probed below 600 nm are assigned to hole species. In contrast, at 800 nm (Figure 6.3b) the signal amplitudes decrease and the decays accelerate with increasingly positive bias. Using the same logic as for the hole assignment at 500 nm, the signals probed at 800 nm and the corresponding region probed from 600 nm are assigned to electron species. These assignments are in agreement with the literature and the results of the PIAS scavenger studies in Chapter 4.[83,84]

6.3.3 Calculation of extinction coefficient

The hole extinction coefficient, ϵ_{h^+}, is calculated using the relationship between hole absorbance and surface hole density at a range of excitation intensities, following a method used previously in our group.[79,80,159] This method uses the Beer-Lambert Law, whereby the absorbance and

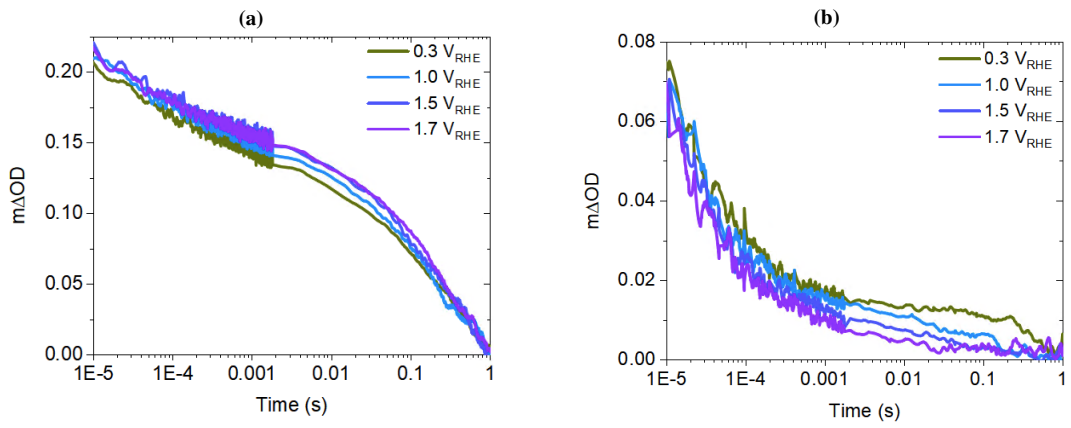

Figure 6.3: Bias dependence of $SrTiO_3$ μs-TAS decays in NaOH, a) probed at 500 nm, and b) probed at 800 nm

concentration components are taken as the hole absorbance and the surface hole density respectively. Further details of this method and the calculations undertaken are included in Chapter 2. In this case, the hole absorbance is obtained from the ΔOD probed at 500 nm in μs-TAS, as this wavelength is assigned to hole species. Meanwhile, the surface hole density is calculated from the cumulative charge extracted, assuming that every electron extracted results in one surface hole. This assumption is made due to sufficiently positive bias (1.3 V_{RHE}) being applied, such that back electron-hole recombination is assumed to be turned off.

The charge extraction properties as a function of laser excitation intensity are obtained by TPC measurements. The peak of charge extraction occurs around 0.1 ms (Figure 6.4a), with the cumulative charge extracted as a function of time obtained by integrating the TPC (Figure 6.4b). The cumulative charge extracted corresponds well to the rate of the 800 nm electron decay observed in μs-TAS (Figure 6.3b). This rate of charge extraction is reasonably fast and analogous to that observed for $BiVO_4$.[105] The amount of charge extracted increases with excitation intensity until it begins to saturate at high laser intensities ($\sim$620 μJ cm^{-2}). The ΔOD of the hole species measured by μs-TAS exhibits the same trend, whereby the ΔOD increases in amplitude with increasing excitation intensity until it begins to saturate at $\sim$620 μJ cm^{-2} (Figure 6.4c). Thus, a linear correlation between the optical hole signal and surface hole density is observed (Figure 6.4d), with the gradient of the linear fit used to extract the ϵ_{h^+} using the Beer-Lambert Law equation. Using this method, the calculated value for ϵ_{h^+} in $SrTiO_3$ is 2200 ± 100 M^{-1} cm^{-1}, in the range of that reported for dense anatase TiO_2 (2000-2930 M^{-1} cm^{-1}).[79,173] However, it is noted that the linear fit does not extrapolate to zero, suggesting that there is a small degree of overlap between the electron and hole absorption at 500 nm.

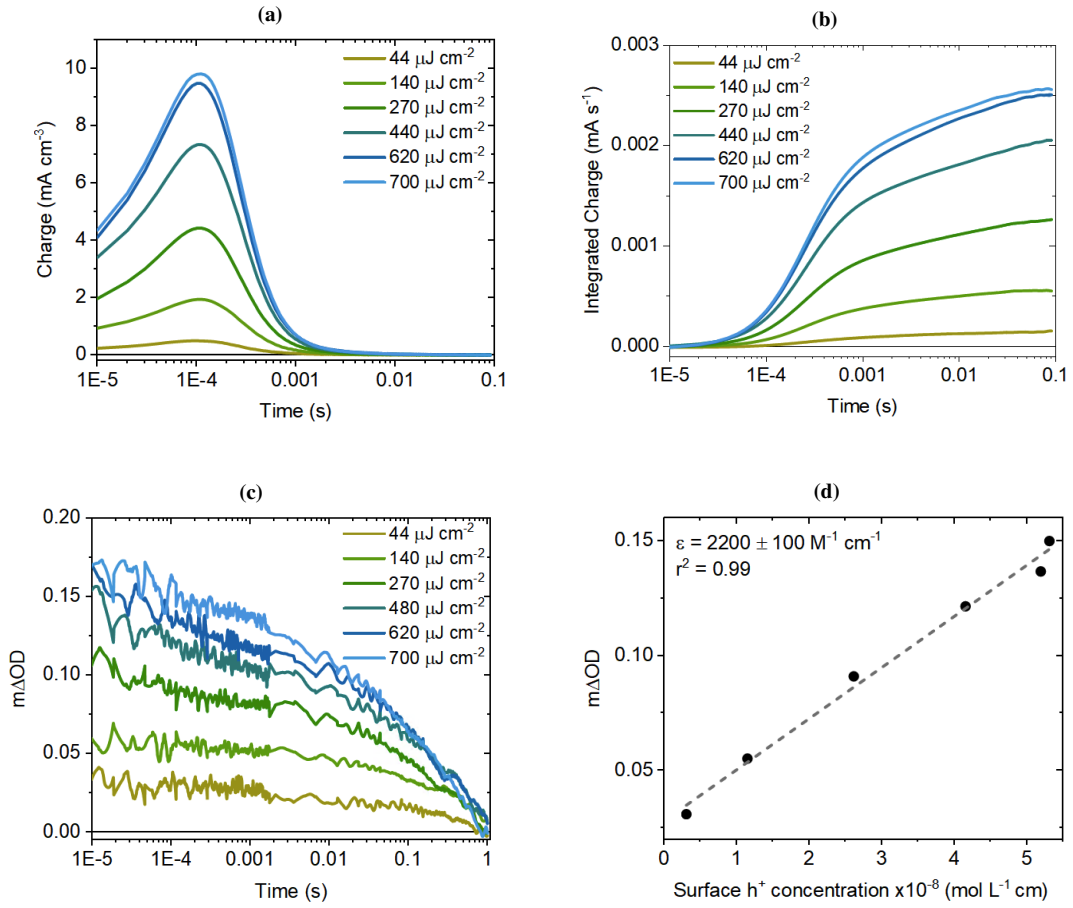

Figure 6.4: Measurements undertaken under an applied bias of 1.3 V_{RHE} and with increasing laser excitation intensities for the calculation of the ϵ_{h^+}. a) TPC measured as the charge extracted as a function of time following laser excitation. b) The integrated charge extracted from the TPC in a). c) μs-TAS decays probed at 500 nm. d) Plot of the hole absorbance measured by μs-TAS vs. the surface hole density calculated from the charge extracted, with the ϵ_{h^+} obtained from the gradient of the linear fit.

6.3.4 Kinetics of water oxidation

A rate law analysis is conducted to investigate the water oxidation kinetics on the $SrTiO_3$ surface, by correlating the rate of water oxidation to the surface hole density. In this way, the degree of hole accumulation required to achieve the RDS is determined. Similarly to the calculation of ϵ_{h^+}, a sufficiently positive bias (1.3 V_{RHE}) is applied so that it can be assumed that back electron-hole recombination is switched off and the only extraction pathway for surface holes is to the electrolyte. Thus, the amplitude of the PIAS signal corresponds to the surface hole density, whilst the TPC corresponds to the hole flux to the electrolyte (i.e. the rate of reaction).

At a range of excitation intensities from a 365 nm LED, the steady-state TPC was measured

simultaneously with the steady-state optical hole signal from PIAS (Figures 6.5a and 6.5b). With increasing excitation intensities, the PIAS signal increases until it begins to plateau. This is attributed to hole densities increasing, until the flux of holes to the surface is balanced by the flux of holes to the electrolyte. Meanwhile, the TPC signals do not exhibit a plateau, indicating a continuous increase in the electrons extracted with the increasing excitation intensities applied. This is commonly observed in metal oxides and suggests that the rate of electron extraction is faster than the rate of hole accumulation and decay.[79,80,175] Negative TPC spikes upon light-off are characteristic of back electron-hole recombination processes in photoanodes.[107,161] The absence of this feature under these conditions suggests that such recombination processes are not significant and the PIAS decays are due to hole transfer to the electrolyte.

The steady-state optical hole signal is converted to a surface hole density using the calculated extinction coefficient of 2200 M^{-1} cm^{-1}. The gradient of two for the logarithmic plot of the steady-state photocurrent vs. the steady state hole density is indicative of a second order reaction (Figure 6.5c). This suggests that the accumulation of two holes (or oxidising equivalents) is required to achieve the RDS of water oxidation.

The TOF of the hole species in the $SrTiO_3$ photoanodes and their reaction time constant, τ, were also calculated using the relationship between the hole flux to the surface and the surface hole density (Figure A.26). The calculated TOF values (<1 s^{-1}) are small and significantly lower than that reported for other metal oxides, with values of $\sim$20 s^{-1}, 14 s^{-1} and 1-5 s^{-1} reported for TiO_2 anatase, $BiVO_4$ and α-Fe_2O_3 respectively.[78,79,106] Thus, the τ is larger than expected and even at the highest hole densities only reaches 1 s.

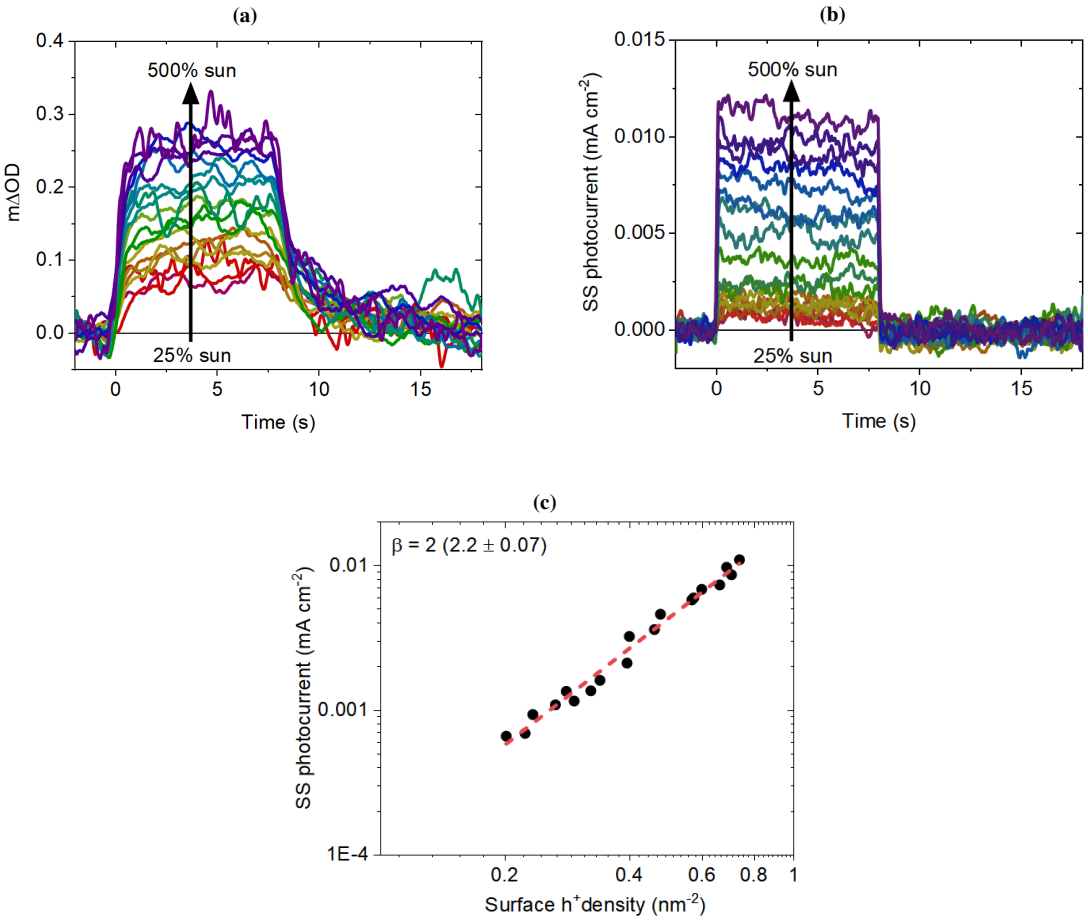

Figure 6.5: Measurements undertaken under an applied bias of 1.3 V_{RHE} and with increasing LED excitation intensities for the rate law analysis. a) PIAS traces probed at 500 nm. b) Steady-state TPC measurements. d) Rate law analysis plot of the steady-state photocurrent (obtained from the TPC in b)) measured simultaneously with the steady-state optical hole signal (obtained from the PIAS in a)). The steady-state optical hole signal was converted into a surface h^+ density using the calculated extinction coefficient of 2200 M^{-1} cm^{-1}. The gradient of two for the linear fit suggests a second order reaction with respect to the hole density.

6.4 Discussion

On μs-s timescales, distinct kinetic regimes are observed for probe wavelengths below and from 600 nm, as is characteristic for all the $SrTiO_3$-based materials investigated in this thesis. In Chapters 4 and 5, DRTS studies employing hole and electron scavengers were inconclusive. Therefore, spectral assignments for these distinct kinetic regimes were made from PIAS scavenger studies and the literature. The ability to investigate the bias dependence of the μs-TAS in this chapter, enables confirmation of the previously assumed spectral assignments under these conditions, whereby probe wavelengths below and from 600 nm correspond to holes and electrons respectively.

The bias dependence of the signal amplitudes and decay kinetics which facilitate the above spectral assignments is clear, but the dependence is small compared to what is frequently observed for photoanodes.[79,106,107,142] This can be attributed to the small photocurrent response, or alternatively, intrinsically good charge separation properties in $SrTiO_3$ that enable long-lived charges independently of the applied bias. Possible reasons for intrinsically good charge separation properties of $SrTiO_3$ include the high dielectric constant screening charge (as discussed in Chapter 3) and a wide space charge layer.[21] A wide space charge layer has previously been reported for $SrTiO_3$ with a similar intrinsic doping density to the $SrTiO_3$ measured herein (10^{18} cm^{-3}),[54] as calculated in Chapter 3. Regardless of the origins, intrinsically good charge separation in $SrTiO_3$ that does not require an applied bias is a key feature for $SrTiO_3$ photocatalysts for OPWS.

Despite the good charge separation demonstrated by the aforementioned decay kinetics, and a reasonably fast rate of electron extraction that peaks at 0.1 ms, a low photocurrent is observed. A proposed explanation for this observation is that a significant population of electrons reside in deep states that are immobile and subsequently limit the electrons that can be extracted as photocurrent, but have little impact on the extraction rate. This explanation is supported by the high prevalence of deep V_O states that manifest as Ti^{3+} states when occupied by an electron. This is discussed in Chapter 3, whereby the density of these Ti^{3+} states was notably high, at 10^{20} cm^{-3}. Therefore, electron trapping into these immobile states is likely to limit the mobile electron population that contribute to the photocurrent.

Interestingly, the $SrTiO_3$ studied herein has a Ti^{3+} donor density that is close to that of the charge density of WO_3 ($\sim 10^{20}$-10^{22}),[132,133] which is recognised to have a high doping density from V_O states. However, WO_3 exhibits electron extraction times that are an order of magnitude slower than that observed for $SrTiO_3$.[32] In WO_3, electrons are reported to trap into shallow V_O states to form W^{5+}.[98] Consequently, the high prevalence of W^{5+} states limits the rate of charge extraction, through the slow trapping-detrapping electron transport mechanism that results.[177] In contrast, the deep V_O in $SrTiO_3$ is proposed to result in deep and immobile Ti^{3+} states, that limit their influence on the rate of charge extraction.

The aforementioned charge carrier dynamics on μs-s timescales and photoelectrochemical properties under positive applied bias are summarised in Figure 6.6. Here, sufficiently positive

applied bias leads to the assumption that back electron-hole recombination is turned off. Recombination between holes and electrons trapped as Ti^{3+} states occurs and the timescales are analogous to that observed in the absence of applied bias (Chapter 4), due to the low degree of bias dependence of the decay kinetics. Electron extraction is fast ($\sim$0.1 ms) but the photocurrent is limited by the large prevalence of Ti^{3+} sites in the absence of Al^{3+} doping, which trap electrons into immobile states on sub-ms timescales that compete with charge extraction.

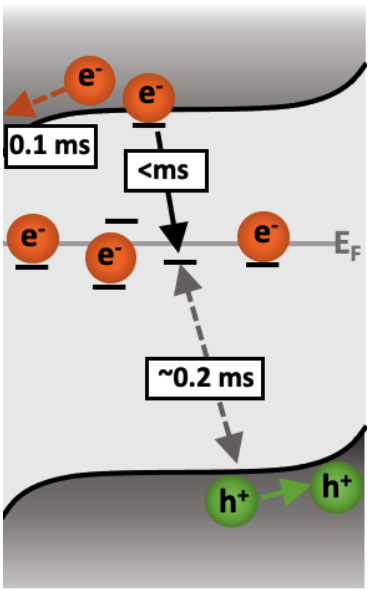

Figure 6.6: Schematic illustration of the operation of the $SrTiO_3$ photoanode on μs-s timescales and under a positive applied bias, where back electron-hole recombination is assumed to be turned off. Timescales in white boxes are that of recombination, trapping and electron extraction processes, as indicated by μs-TAS and TPC measurements. Electron trapping into Ti^{3+} states is assumed to occur on sub-ms timescales prior to the subsequent recombination that is observed, due to the correlation between the two.

In addition to spectral assignments, applied bias facilitated the approximation of the ϵ_{h^+} in $SrTiO_3$. A clear linear correlation was achieved between the hole absorbance and surface hole density, as desired for the extraction of the ϵ_{h^+}. The value of 2200 ± 100 M^{-1} cm^{-1} obtained is the first known report of a ϵ_{h^+} value for $SrTiO_3$, so cannot be compared to literature values for the same materials. However, compared to the ϵ_{h^+} range reported for TiO_2 of 2000-2930 M^{-1} cm^{-1},[79,173] the value calculated for $SrTiO_3$ appears to be very reasonable. The calculation of the extinction coefficient relies on the assumption that under the positive bias applied, back electron-hole recombination is turned off, such that every photogenerated electron extracted results in one surface hole. Despite the reasonable value and low associated error calculated for the ϵ_{h^+}, it is acknowledged that due to the low photocurrent response there is uncertainty surrounding this assumption.

In the subsequent rate law analysis, the calculated ϵ_{h^+} facilitated the conversion of the steady-state optical hole signal to a surface hole density. In this way, the correlation between the steady-state photocurrent and the surface hole density could successfully be analysed. Using this method, a reaction order of two for the water oxidation reaction was obtained, which is within the range of one to three that is typically reported for metal oxide photoanodes.[78–80] Similarly to the calculated ϵ_{h^+}, the value obtained is reasonable, but the low photocurrent response weakens assumptions regarding back electron-hole recombination being turned off and each photogenerated electron extracted resulting in one surface hole.

The calculated TOF (<1 s^{-1}) and τ (1-5 s) values suggest a slower reaction of holes in $SrTiO_3$ than that indicated by the consumption of reactive holes species, measured by the PIAS studies throughout this thesis ($\sim$0.1 s). This discrepancy is rationalised by the use of the photocurrent to calculate the TOF and τ values. The poor photocurrent response of the $SrTiO_3$ photoanode, due to a significant population of photogenerated electrons trapping into Ti^{3+} states, leads to an underestimate of the TOF and overestimate of the τ.

Previously, interfacial transfer of photogenerated holes in $SrTiO_3$ to form intermediate species was reported by Cuk and co-workers to occur on ps timescales.[86] This is notably faster than the consumption of any reactive hole species reported in this thesis (even under the application of positive applied bias) and corresponds more closely to the timescales of bimolecular recombination reported in Chapter 3. Using ultrafast *in situ* infrared spectroscopy, Cuk and co-workers monitor the formation of Ti-O• radicals at the surface, that are proposed to trap hole species and are correlated to oxygen evolution. A central difference to the transient spectroscopic techniques employed herein, is that the infrared spectroscopy monitors the dynamics of radical species at the surface, rather than directly probing the photogenerated species in $SrTiO_3$. It is therefore not possible to be certain that the infrared spectroscopy is detecting changes that directly result from the photogenerated species within $SrTiO_3$, that are monitored in this thesis.

6.5 Conclusion

In this chapter, the first known TAS studies on $SrTiO_3$ are conducted under applied bias. The impact of applied bias on the decay kinetics is much smaller than what is typically expected for metal oxides. Thus, the ability to generate long-lived charges that are not highly dependent on an applied bias is demonstrated. This is an exceedingly useful feature for photocatalytic materials employed in OPWS, where there is no applied bias to drive charge separation. Despite the small degree of dependence on applied bias, the dependence observed enabled previously assumed spectral assignments of $SrTiO_3$ on μs-s timescales to be confirmed, and the previously unknown ϵ_{h^+} to be calculated. The ϵ_{h^+} is used in this chapter for the rate law analysis and for the calculation of the RQYs of steady-state hole generation in Chapters 4 and 5. It is expected that the ϵ_{h^+} can be used extensively for future investigations on $SrTiO_3$, in the quantification of hole populations from optical signals. The rate law analysis conducted in this chapter, yielding a reaction order of two, is the first attempt of a kinetic analysis of this kind on $SrTiO_3$ and supports the requirement of hole accumulation at the reaction sites. The rate law analysis could be improved upon in future by using a $SrTiO_3$ photoanode that exhibits an improved photocurrent response, which in this case was limited by electron trapping into deep and immobile states, in addition to an experimental set-up that enables a larger range of photocurrent densities to be measured. The former could be achieved by optimising the morphology, for example by nanostructuring, or by passivating the deep electron traps that limit the photocurrent that can be extracted. Beyond the analysis of the water oxidation kinetics of $SrTiO_3$, it would be interesting to investigate the corresponding mechanism and reaction intermediates of the water oxidation reaction in future work, as this was beyond the scope of this work and the methods employed.

Chapter 7

Concluding remarks

7.1 Summary

The central objective of this thesis was to investigate the charge carrier dynamics of $SrTiO_3$, with the aim of uncovering what underpins the state-of-the-art performance of $SrTiO_3$-based photocatalytic systems for overall photocatalytic water splitting, OPWS. To this end, time-resolved spectroscopic techniques were employed across the timescales of charge generation and fast recombination processes (ps-ns), to the slow timescales of water oxidation (ms-s). Moreover, both transient and steady-state spectroscopic measurements under operational conditions were employed, to gain a comprehensive insight into the charge carrier dynamics that can be expected under water splitting conditions. In this way, the charge carrier dynamics underpinning the highly efficient charge generation, separation and utilisation of photogenerated charges in Al:$SrTiO_3$/$RhCrO_x$(PD) can be determined, to explain the near-unity AQY achieved by the system.

In Chapter 3, the charge carrier dynamics of $SrTiO_3$ immediately following photoexcitation are investigated on ps-ns timescales. The results of this investigation are used to calculate the bimolecular rate constant and intrinsic doping density, with comparisons made to alternative photocatalytic metal oxides for the first time. ln the first 10 ps after photoexcitation, charge localisation into shallow states is observed. Consequently, a slow rise and fast decay is observed in distinct spectral regions, with the deconvolution and correlation of these spectral components achieved by global analysis. Following charge localisation, the bimolecular decay kinetics are slow compared to alternative metal oxides (TiO_2, $BiVO_4$ and α-Fe_2O_3), with a bimolecular

rate constant of $SrTiO_3$ that is at least two magnitudes slower than the other metal oxides. The remarkably slow bimolecular rate constant of $SrTiO_3$ (10^{-11} cm^3 s^{-1}) is invaluable for its use in photocatalytic water splitting, whereby fast loss processes of photogenerated charges (such as via bimolecular recombination) must be suppressed, in order to maximise the yields of photogenerated charges available to catalyse the comparatively slow interfacial water splitting reactions. The intrinsic doping density calculated for $SrTiO_3$ (10^{18} cm^{-3}) is within the range of that expected and calculated for the alternative metal oxides, and therefore does not provide explanation for the slow bimolecular recombination. Alternatively, the notably high dielectric constant of $SrTiO_3$ is explored as a contributing factor, due to its recognised ability to screen charge. Whilst the intrinsic doping density calculated from ultrafast TAS is not notably high, there is a very high density of Ti^{3+} defect states (10^{20} cm^{-3}), associated with V_O occupied with an electron. Thus, these states are assigned to deep states with an energy distribution that is predominantly below the E_F.

Despite the promising properties of $SrTiO_3$ identified in Chapter 3, to achieve high photocatalytic activities, modifications by way of flux mediated Al^{3+} doping and $RhCrO_x$ addition are required to obtain the state-of-the-art Al:$SrTiO_3$/$RhCrO_x$ systems. The influence of these modifications on performance have been studied in detail. However, their effects on charge carrier dynamics, particularly under operational conditions, remained largely unexplored prior to this thesis.

In Chapter 4, the role of flux mediated Al^{3+} doping on enhancing the properties of $SrTiO_3$ for OPWS was explored. Here, the chemical flexibility of the $SrTiO_3$ perovskite structure is exploited, to successfully suppress the deep Ti^{3+} defect states that are associated with recombination and reduced photocatalytic performance. In addition to suppressing these undesirable Ti^{3+} states, Al^{3+} doping transforms the morphology of the cubic $SrTiO_3$ particles, to yield Al:$SrTiO_3$ particles with a faceted structure. These faceted particles are proposed to comprise of distinct oxidation and reduction facets, with an electric field between them to facilitate the spatial separation of photogenerated charges and the facet selective photodeposition of $RhCrO_x$ explored in Chapter 5. The advantageous effects of these material changes are evident in the suppressed recombination on μs-s timescales in Al:$SrTiO_3$. Interestingly, on these timescales both $SrTiO_3$ and Al:$SrTiO_3$ exhibit distinct decay kinetics for photogenerated electron and hole species, whereby hole trapping extends hole lifetimes. Following the suppressed recombination

in Al:$SrTiO_3$, the efficiency of generating steady-state holes is increased and higher yields of photogenerated charges are available for the slow interfacial water splitting reactions. Thus, the primary role of Al^{3+} doping in addressing the kinetic challenges of photocatalytic water splitting, is to enhance the yields and lifetimes of photogenerated charges, rather than increasing their reactivity.

With the role of Al^{3+} doping established, the effects of the $RhCrO_x$ proton reduction co-catalyst and the influence of its deposition route are investigated in Chapter 5. Due to the faceted morphology introduced by Al^{3+} doping, facet selective photodeposition of $RhCrO_x$ onto the reduction facets was observed. Meanwhile, impregnation of $RhCrO_x$ resulted in a random distribution of the co-catalyst across all facets. In both cases, the ability to accumulate high steady-state charge densities, without a concurrent increase in recombination, is observed and attributed to the combined effects of slow bimolecular recombination in $SrTiO_3$, Al^{3+} doping, and electron extraction to $RhCrO_x$. The ability to tolerate accumulated charge is valuable for the slow and multi-hole water oxidation reaction. However, the long-lived species persisting for 10s of seconds are attributed to deeply trapped and unreactive hole species. Therefore, they must be modulated to ensure that reactive hole species contributing to water splitting activity are dominant. The differing balance of reactive and unreactive hole species in Al:$SrTiO_3$/$RhCrO_x$(IMP) and Al:$SrTiO_3$/$RhCrO_x$(PD) offers explanation for the dramatically different photocatalytic activities, whereby they achieve AQYs of 56% and 93% respectively. In Al:$SrTiO_3$/$RhCrO_x$(IMP), a high prevalence of deep hole trapping is observed, that is the proposed result of the blocking of oxidation sites following the unselective impregnation of $RhCrO_x$ across all facets. By selectively photodepositing $RhCrO_x$ onto reduction facets in Al:$SrTiO_3$/$RhCrO_x$(PD), the oxidation sites are uninhibited, hole reactivity is enhanced, and opportunities for deep hole trapping are decreased. Thus, reactive hole species dominate in Al:$SrTiO_3$/$RhCrO_x$(PD) and enable the dramatic increase in photocatalytic activity that is highlighted by the near-unity AQY.

In Chapter 6, spectroscopic studies of $SrTiO_3$ under applied bias provide novel and interesting insights into properties of $SrTiO_3$ that are relevant to its use in photocatalysis. For example, the ability of $SrTiO_3$ to achieve long-lived charges independently of applied bias was demonstrated, and is a valuable feature for photocatalysts where applied bias cannot be used to drive charge separation. In addition, the first known calculation of the hole extinction coefficient, ϵ_{h^+}, of $SrTiO_3$ was achieved in this chapter. Knowledge of the ϵ_{h^+} enabled the hole density

to be calculated from the optical signal for the kinetic analyses in this chapter and the RQY calculations in Chapters 4 and 5. It is also expected to be useful in future work, for quantifying hole populations in spectroscopic investigations.

7.2 Future work

As is expected for scientific research, many avenues for future research arose in the process of achieving the aims of this thesis. In Chapter 3, the high dielectric constant of $SrTiO_3$ is proposed and explored as an explanation for the remarkably slow bimolecular recombination observed, compared to alternative metal oxides with much lower dielectric constants. Further investigations explicitly exploring the relationship between the dielectric constant and the rate of bimolecular recombination in metal oxides are required to confirm the role of the dielectric constant in $SrTiO_3$ and in metal oxide photocatalysts in general. In Chapter 4, the effects of Al^{3+} doping on the morphology and charge carrier dynamics of $SrTiO_3$ are in agreement with what was expected for the flux mediated procedure and corresponding improvements to the photocatalytic properties. However, the E_F shift that is expected to correspond to the suppression of sub-band gap Ti^{3+} states, is not observed. Several explanations for this discrepancy are briefly explored in the thesis, but additional investigations into the depth and energy distributions of the Ti^{3+} states in $SrTiO_3$ are required to provide a robust explanation. The notable effects of the $RhCrO_x$ co-catalyst, and the role of selectively depositing $RhCrO_x$ onto reduction facets was explored in detail in Chapter 5, but the effects of CoOOH on the charge carrier dynamics remains to be explored. Investigating the effects of CoOOH would enable clarification of its somewhat ambiguous role as either a co-catalyst or overlayer. Finally, much of the investigations in Chapter 6 employing an applied bias relied on the assumption that under a sufficiently positive applied bias, back electron-hole recombination is turned off. Undertaking these investigations with a $SrTiO_3$ photoanode that exhibits an improved photocurrent response would increase the reliability of this assumption. With an improved photoanode, the rate law analysis could be expanded upon, by employing a set-up that enables the dependence of the reaction order under a wider range of intensities to be measured.

More broadly, the insights gained in this thesis, regarding the multitude of factors that enable a near-unity AQY, can be applied to the development of photocatalysts that exhibit strong visible light absorption. In this way, photocatalysts that also achieve a high STH efficiency can be obtained, and the potential of photocatalytic water splitting to produce sustainable hydrogen in an up-scalable and competitive manner can be achieved.

References

(1) IPCC, *Assessment Report 6 Climate Change 2021: The Physical Science Basis*, tech. rep., 2021.

(2) National Statistics, *Department for Business, Energy & Industrial Strategy*, 2020, 47.

(3) K. Vohra, A. Vodonos, J. Schwartz, E. A. Marais, M. P. Sulprizio and L. J. Mickley, *Environmental Research*, 2021, **195**, 110754.

(4) IEA, *Net Zero by 2050: A Roadmap for the Global Energy Sector*, tech. rep., 2021, p. 224.

(5) World Energy Council, *World Energy Council 2013 World Energy Resources: Solar*, 2013, 1–28.

(6) IEA, *World Energy Outlook 2021 - revised version October 2021*, tech. rep., 2021.

(7) IEA, *The Future of Hydrogen*, tech. rep. June, 2019.

(8) HM Government, *UK hydrogen strategy*, 2021, vol. 85, p. 17.

(9) M. R. Shaner, H. A. Atwater, N. S. Lewis and E. W. McFarland, *Energy and Environmental Science*, 2016, **9**, 2354–2371.

(10) J. H. Kim, D. Hansora, P. Sharma, J. W. Jang and J. S. Lee, *Chemical Society Reviews*, 2019, **48**, 1908–1971.

(11) K. Sivula, *Journal of Physical Chemistry Letters*, 2015, **6**, 975–976.

(12) C. Jiang, S. J. Moniz, A. Wang, T. Zhang and J. Tang, *Chemical Society Reviews*, 2017, **46**, 4645–4660.

(13) J. Li and N. Wu, *Catalysis Science and Technology*, 2015, **5**, 1360–1384.

(14) B. A. Pinaud, J. D. Benck, L. C. Seitz, A. J. Forman, Z. Chen, T. G. Deutsch, B. D. James, K. N. Baum, G. N. Baum, S. Ardo, H. Wang, E. Miller and T. F. Jaramillo, *Energy and Environmental Science*, 2013, **6**, 1983–2002.

(15) H. Wu, H. L. Tan, C. Y. Toe, J. Scott, L. Wang, R. Amal and Y. H. Ng, *Advanced Materials*, 2019, **1904717**, 1–21.

(16) T. Hisatomi, J. Kubota and K. Domen, *Chemical Society Reviews*, 2014, **43**, 7520–7535.

(17) T. Takata and K. Domen, *ACS Energy Letters*, 2019, **4**, 542–549.

(18) Q. Wang and K. Domen, *Chemical Reviews*, 2020, **120**, 919–985.

(19) A. Fujishima and K. Honda, *Nature*, 1972, **238**, 37–38.

(20) G. N. Schrauzer and T. D. Guth, *Journal of the American Chemical Society*, 1977, **99**, 7189–7193.

(21) S. Corby, R. R. Rao, L. Steier and J. R. Durrant, *Nature Reviews Materials*, 2021, **6**, 1136–1155.

(22) S. Chen, T. Takata and K. Domen, *Nature Reviews Materials*, 2017, **2**, 1–17.

(23) Q. Wang, Y. Li, T. Hisatomi, M. Nakabayashi, N. Shibata, J. Kubota and K. Domen, *Journal of Catalysis*, 2015, **328**, 308–315.

(24) Q. Wang, T. Hisatomi, Q. Jia, H. Tokudome, M. Zhong, C. Wang, Z. Pan, T. Takata, M. Nakabayashi, N. Shibata, Y. Li, I. D. Sharp, A. Kudo, T. Yamada and K. Domen, *Nature Materials*, 2016, **15**, 611–615.

(25) Q. Wang, T. Hisatomi, Y. Suzuki, Z. Pan, J. Seo, M. Katayama, T. Minegishi, H. Nishiyama, T. Takata, K. Seki, A. Kudo, T. Yamada and K. Domen, *Journal of the American Chemical Society*, 2017, **139**, 1675–1683.

(26) R. Godin and J. R. Durrant, *Chemical Society Reviews*, 2021, **50**, 13372–13409.

(27) M. Sachs, E. Pastor, A. Kafizas and J. R. Durrant, *Journal of Physical Chemistry Letters*, 2016, **7**, 3742–3746.

(28) R. Godin, A. Kafizas and J. R. Durrant, *Current Opinion in Electrochemistry*, 2017, **2**, 136–143.

(29) H. Dau, C. Limberg, T. Reier, M. Risch, S. Roggan and P. Strasser, *ChemCatChem*, 2010, **2**, 724–761.

(30) L. Mu, Y. Zhao, A. Li, S. Wang, Z. Wang, J. Yang, Y. Wang, T. Liu, R. Chen, J. Zhu, F. Fan, R. Li and C. Li, *Energy and Environmental Science*, 2016, **9**, 2463–2469.

(31) D. Li, R. Chen, P. Wang, Z. Li, J. Zhu, F. Fan, J. Shi and C. Li, *ChemCatChem*, 2019, **11**, 3763–3769.

(32) S. Corby, L. Francàs, S. Selim, M. Sachs, C. Blackman, A. Kafizas and J. R. Durrant, *Journal of the American Chemical Society*, 2018, **140**, 1616816177.

(33) W. Yang, R. Godin, H. Kasap, B. Moss, Y. Dong, S. A. Hillman, L. Steier, E. Reisner and J. R. Durrant, *Journal of the American Chemical Society*, 2019, **141**, 11219–11229.

(34) T. Takata and K. Domen, *Journal of Physical Chemistry C*, 2009, **113**, 19386–19388.

(35) R. Godin, T. Hisatomi, K. Domen and J. R. Durrant, *Chemical Science*, 2018, **9**, 7546–7555.

(36) A. Yamakata, M. Kawaguchi, N. Nishimura, T. Minegishi, J. Kubota and K. Domen, *Journal of Physical Chemistry C*, 2014, **118**, 23897–23906.

(37) Y. Goto, T. Hisatomi, Q. Wang, T. Higashi, K. Ishikiriyama, T. Maeda, Y. Sakata, S. Okunaka, H. Tokudome, M. Katayama, S. Akiyama, H. Nishiyama, Y. Inoue, T. Takewaki, T. Setoyama, T. Minegishi, T. Takata, T. Yamada and K. Domen, *Joule*, 2018, **2**, 509–520.

(38) T. Takata, J. Jiang, Y. Sakata, M. Nakabayashi, N. Shibata, V. Nandal, K. Seki, T. Hisatomi and K. Domen, *Nature*, 2020, **581**, 411–414.

(39) H. Nishiyama, T. Yamada, M. Nakabayashi, Y. Maehara, M. Yamaguchi, Y. Kuromiya, Y. Nagatsuma, H. Tokudome, S. Akiyama, T. Watanabe, R. Narushima, S. Okunaka, N. Shibata, T. Takata, T. Hisatomi and K. Domen, *Nature*, 2021, **598**, 304–307.

(40) T. Minegishi, H. Nishiyama, T. Hisatomi, M. Yoshida, H. Lyu, M. Katayama, K. Domen, Y. Goto, K. Asakura, Y. Sakata, T. Yamada, T. Higashi and T. Takata, *Chemical Science*, 2019, **10**, 3196–3201.

(41) K. Takanabe, *ACS Catalysis*, 2017, **7**, 8006–8022.

(42) T. Hisatomi and K. Domen, *Nature Catalysis*, 2019, **2**, 387–399.

(43) Y. Ham, T. Hisatomi, Y. Goto, Y. Moriya, Y. Sakata, A. Yamakata, J. Kubota and K. Domen, *J. Mater. Chem. A*, 2016, **4**, 3027–3033.

(44) Y. Sakata, T. Hayashi, R. Yasunaga, N. Yanaga and H. Imamura, *Chemical Communications*, 2015, **51**, 12935–12938.

(45) H. Kato, K. Asakura and A. Kudo, *Journal of the American Chemical Society*, 2003, **125**, 3082–3089.

(46) H. Kato, M. Kobayashi, M. Hara and M. Kakihana, *Catalysis Science and Technology*, 2013, **3**, 1733–1738.

(47) K. Maeda and K. Domen, *Journal of Physical Chemistry Letters*, 2010, **1**, 2655–2661.

(48) Y. Li, L. Zhu, Y. Yang, H. Song, Z. Lou, Y. Guo and Z. Ye, *Small*, 2015, **11**, 871–876.

(49) T. Ohno, L. Bai, T. Hisatomi, K. Maeda and K. Domen, *Journal of the American Chemical Society*, 2012, **134**, 8254–8259.

(50) J. Zhang, X. Suo, X. Liu, B. Liu, Y. Xue, L. Mu and H. Shi, *Materials Letters*, 2016, **184**, 25–28.

(51) X. Chen, R. Shi, Q. Chen, Z. Zhang, W. Jiang, Y. Zhu and T. Zhang, *Nano Energy*, 2019, **59**, 644–650.

(52) J. Liu, Y. Liu, N. Liu, Y. Han, X. Zhang, H. Huang, Y. Lifshitz, S. T. Lee, J. Zhong and Z. Kang, *Science*, 2015, **347**, 970–974.

(53) A. Kudo, R. Niishiro, A. Iwase and H. Kato, *Chemical Physics*, 2007, **339**, 104–110.

(54) S. Kawasaki, R. Takahashi and M. Lippmaa, *Journal of Physical Chemistry C*, 2019, **123**, 15551–15556.

(55) H. Zhang, D. Li, W. J. Byun, X. Wang, T. J. Shin, H. Y. Jeong, H. Han, C. Li and J. S. Lee, *Nature Communications*, 2020, **11**, 1–11.

(56) R. Asahi, T. Morikawa, T. Ohwaki, K. Aoki and Y. Taga, *Science*, 2001, **293**, 269–271.

(57) S. Kawasaki, K. Akagi, K. Nakatsuji, S. Yamamoto, I. Matsuda, Y. Harada, J. Yoshinobu, F. Komori, R. Takahashi, M. Lippmaa, C. Sakai, H. Niwa, M. Oshima, K. Iwashina and A. Kudo, *Journal of Physical Chemistry C*, 2012, **116**, 24445–24448.

(58) B. Modak and S. K. Ghosh, *Journal of Physical Chemistry B*, 2015, **119**, 11089–11098.

(59) B. Moss, Q. Wang, K. T. Butler, R. Grau-Crespo, S. Selim, A. Regoutz, T. Hisatomi, R. Godin, D. J. Payne, A. Kafizas, K. Domen, L. Steier and J. R. Durrant, *Nature Materials*, 2021, **20**, 511–517.

(60) J. Yang, D. Wang, H. Han and C. Li, *Accounts of Chemical Research*, 2013, **46**, 1900–1909.

(61) M. Yoshida, K. Takanabe, K. Maeda, A. Ishikawa, J. Kubota, Y. Sakata, Y. Ikezawa and K. Domen, *Journal of Physical Chemistry C*, 2009, **113**, 10151–10157.

(62) D. K. Zhong and D. R. Gamelin, *Journal of the American Chemical Society*, 2010, **132**, 4202–4207.

(63) F. F. Abdi, L. Han, A. H. Smets, M. Zeman, B. Dam and R. Van De Krol, *Nature Communications*, 2013, **4**, 1–7.

(64) Y. Ma, F. Le Formal, A. Kafizas, S. R. Pendlebury and J. R. Durrant, *Journal of Materials Chemistry A*, 2015, **3**, 20649–20657.

(65) M. Barroso, A. J. Cowan, S. R. Pendlebury, M. Grätzel, D. R. Klug and J. R. Durrant, *Journal of the American Chemical Society*, 2011, **133**, 14868–14871.

(66) A. Xiong, G. Ma, K. Maeda, T. Takata, T. Hisatomi, T. Setoyama, J. Kubota and K. Domen, *Catalysis Science and Technology*, 2014, **4**, 325–328.

(67) K. Maeda, K. Teramura, H. Masuda, T. Takata, N. Saito, Y. Inoue and K. Domen, *Journal of Physical Chemistry B*, 2006, **110**, 13107–13112.

(68) K. Maeda, K. Teramura, D. Lu, N. Saito, Y. Inoue and K. Domen, *Journal of Physical Chemistry C*, 2007, **111**, 7554–7560.

(69) S. Selim, L. Francàs, M. García-Tecedor, S. Corby, C. Blackman, S. Gimenez, J. R. Durrant and A. Kafizas, *Chemical Science*, 2019, **10**, 2643–2652.

(70) N. J. Tang, W. Zhong, H. Y. Jiang, X. L. Wu, W. Liu and Y. W. Du, *Journal of Magnetism and Magnetic Materials*, 2004, **282**, 92–95.

(71) T. Du, W. Xu, S. Xu, S. R. Ratnasingham, C. T. Lin, J. Kim, J. Briscoe, M. A. McLachlan and J. R. Durrant, *Journal of Materials Chemistry C*, 2020, **8**, 12648–12655.

(72) T. J. MacDonald, A. J. Clancy, W. Xu, Z. Jiang, C. T. Lin, L. Mohan, T. Du, D. D. Tune, L. Lanzetta, G. Min, T. Webb, A. Ashoka, R. Pandya, V. Tileli, M. A. McLachlan, J. R. Durrant, S. A. Haque and C. A. Howard, *Journal of the American Chemical Society*, 2021, **143**, 21549–21559.

(73) T. Du, W. Xu, M. Daboczi, J. Kim, S. Xu, C. T. Lin, H. Kang, K. Lee, M. J. Heeney, J. S. Kim, J. R. Durrant and M. A. McLachlan, *Journal of Materials Chemistry A*, 2019, **7**, 18971–18979.

(74) G. Porter, *Science*, 1968, **160**, 1299–1307.

(75) F. Wilkinson, *Journal of Photochemistry*, 1986, **17**, 52.

(76) F. Wilkinson and D. R. Worrall, *Proceedings of the Indian Academy of Sciences - Chemical Sciences*, 1992, **104**, 287–298.

(77) R. W. Kessler and F. Wilkinson, *The Life and Scientific Legacy of George Porter*, 2006, 421–432.

(78) Y. Ma, C. A. Mesa, E. Pastor, A. Kafizas, L. Francàs, F. Le Formal, S. R. Pendlebury and J. R. Durrant, *ACS Energy Letters*, 2016, **1**, 618–623.

(79) A. Kafizas, Y. Ma, E. Pastor, S. R. Pendlebury, C. Mesa, L. Francàs, F. Le Formal, N. Noor, M. Ling, C. Sotelo-Vazquez, C. J. Carmalt, I. P. Parkin and J. R. Durrant, *ACS Catalysis*, 2017, **7**, 4896–4903.

(80) F. Le Formal, E. Pastor, S. D. Tilley, C. A. Mesa, S. R. Pendlebury, M. Grätzel and J. R. Durrant, *Journal of the American Chemical Society*, 2015, **137**, 6629–6637.

(81) E. V. Peán, S. Dimitrov, C. S. De Castro and M. L. Davies, *Physical Chemistry Chemical Physics*, 2020, **22**, 28345–28358.

(82) C. L. Davies, M. R. Filip, J. B. Patel, T. W. Crothers, C. Verdi, A. D. Wright, R. L. Milot, F. Giustino, M. B. Johnston and L. M. Herz, *Nature Communications*, 2018, **9**, 1–9.

(83) J. J. M. Vequizo, S. Nishioka, J. Hyodo, Y. Yamazaki, K. Maeda and A. Yamakata, *Journal of Materials Chemistry A*, 2019, **7**, 26139–26146.

(84) A. Yamakata, J. J. M. Vequizo and M. Kawaguchi, *Journal of Physical Chemistry C*, 2015, **119**, 1880–1885.

(85) A. Yamakata, H. Yeilin, M. Kawaguchi, T. Hisatomi, J. Kubota, Y. Sakata and K. Domen, *Journal of Photochemistry and Photobiology A: Chemistry*, 2015, **313**, 168–175.

(86) D. M. Herlihy, M. M. Waegele, X. Chen, C. D. Pemmaraju, D. Prendergast and T. Cuk, *Nature Chemistry*, 2016, **8**, 549–555.

(87) Y. Yamada, H. Yasuda, T. Tayagaki and Y. Kanemitsu, *Applied Physics Letters*, 2009, **95**, 121112.

(88) J. Y. Kim, J. W. Lee, H. S. Jung, H. Shin and N. G. Park, *Chemical Reviews*, 2020, **120**, 7867–7918.

(89) N. J. Jeon, H. Na, E. H. Jung, T. Y. Yang, Y. G. Lee, G. Kim, H. W. Shin, S. Il Seok, J. Lee and J. Seo, *Nature Energy*, 2018, **3**, 682–689.

(90) X. Zheng, B. Chen, J. Dai, Y. Fang, Y. Bai, Y. Lin, H. Wei, X. C. Zeng and J. Huang, *Nature Energy*, 2017, **2**, 1–9.

(91) Z. Zhao, R. V. Goncalves, S. K. Barman, E. J. Willard, E. Byle, R. Perry, Z. Wu, M. N. Huda, A. J. Moulé and F. E. Osterloh, *Energy and Environmental Science*, 2019, **12**, 1385–1395.

(92) D. Kan, T. Terashima, R. Kanda, A. Masuno, K. Tanaka, S. Chu, H. Kan, A. Ishizumi, Y. Kanemitsu, Y. Shimakawa and M. Takano, *Nature Materials*, 2005, **4**, 816–819.

(93) Y. Yamada and Y. Kanemitsu, *Physical Review B - Condensed Matter and Materials Physics*, 2010, **82**, 1–4.

(94) J. H. Ma, Z. M. Huang, X. J. Meng, S. J. Liu, X. D. Zhang, J. L. Sun, J. Q. Xue, J. H. Chu and J. Li, *Journal of Applied Physics*, 2006, **99**, 033515.

(95) D. Xu, Y. Yuan, H. Zhu, L. Cheng, C. Liu, J. Su, X. Zhang, H. Zhang, X. Zhang and J. Li, *Materials*, 2019, **12**, 138.

(96) Z. Chen, H. N. Dinh and E. Miller, *Photoelectrochemical Water Splitting*, 2013, pp. 49–62.

(97) E. Pastor, J. S. Park, L. Steier, S. Kim, M. Grätzel, J. R. Durrant, A. Walsh and A. A. Bakulin, *Nature Communications*, 2019, **10**, 1–7.

(98) M. Sachs, J. S. Park, E. Pastor, A. Kafizas, A. A. Wilson, L. Francàs, S. Gul, M. Ling, C. Blackman, J. Yano, A. Walsh and J. R. Durrant, *Chemical Science*, 2019, **10**, 5667–5677.

(99) H. L. Tan, F. F. Abdi and Y. H. Ng, *Chemical Society Reviews*, 2019, **48**, 1255–1271.

(100) J. Nelson and R. E. Chandler, *Coordination Chemistry Reviews*, 2004, **248**, 1181–1194.

(101) T. M. Clarke, F. C. Jamieson and J. R. Durrant, *Journal of Physical Chemistry C*, 2009, **113**, 20934–20941.

(102) S. R. Pendlebury, X. Wang, F. L. Formal, M. Cornuz, A. Kafizas, S. D. Tilley, M. Grätzel, J. R. Durrant and F. Formal, *Journal of American Chemical Society*, 2014, **136**, 9854–9857.

(103) A. Kafizas, X. Wang, S. R. Pendlebury, P. Barnes, M. Ling, C. Sotelo-Vazquez, R. Quesada-Cabrera, C. Li, I. P. Parkin and J. R. Durrant, *Journal of Physical Chemistry A*, 2016, **120**, 715–723.

(104) S. Corby, E. Pastor, Y. Dong, X. Zheng, L. Francàs, M. Sachs, S. Selim, A. Kafizas, A. A. Bakulin and J. R. Durrant, *The Journal of Physical Chemistry Letters*, 2019, **10**, 5395–5401.

(105) S. Selim, E. Pastor, M. García-Tecedor, M. R. Morris, L. Francàs, M. Sachs, B. Moss, S. Corby, C. A. Mesa, S. Gimenez, A. Kafizas, A. A. Bakulin and J. R. Durrant, *Journal of the American Chemical Society*, 2019, **141**, 18791–18798.

(106) M. Barroso, S. R. Pendlebury, A. J. Cowan and J. R. Durrant, *Chemical Science*, 2013, **4**, 2724–2734.

(107) Y. Ma, S. R. Pendlebury, A. Reynal, F. Le Formal and J. R. Durrant, *Chemical Science*, 2014, **5**, 2964–2973.

(108) Z. Luo, C. Li, S. Liu, T. Wang and J. Gong, *Chemical Science*, 2016, **8**, 91–100.

(109) Y. Liang, C. S. Enache and R. Van De Krol, *International Journal of Photoenergy*, 2008, **2008**, 739864.

(110) Y. Tamaki, A. Furube, R. Katoh, M. Murai, K. Hara, H. Arakawa and M. Tachiya, *Comptes Rendus Chimie*, 2006, **9**, 268–274.

(111) J. Tang, J. R. Durrant and D. R. Klug, *Journal of the American Chemical Society*, 2008, **130**, 13885–13891.

(112) K. Kato, A. Yamakata and A. Yamakata, *Journal of Physical Chemistry C*, 2020, **124**, 11057–11063.

(113) J. S. Pelli Cresi, L. Di Mario, D. Catone, F. Martelli, A. Paladini, S. Turchini, S. D'Addato, P. Luches and P. O'Keeffe, *Journal of Physical Chemistry Letters*, 2020, **11**, 5686–5691.

(114) R. Su, Z. Xu, J. Wu, D. Luo, Q. Hu, W. Yang, X. Yang, R. Zhang, H. Yu, T. P. Russell, Q. Gong, W. Zhang and R. Zhu, *Nature Communications*, 2021, **12**, DOI: 10.1038/s41467-021-22783-z.

(115) Z. Fu, X. Zhang, H. Zhang, Y. Li, H. Zhou and Y. Zhang, *Chinese Journal of Chemistry*, 2021, **39**, 381–390.

(116) S. Shao, M. Abdu-Aguye, L. Qiu, L. H. Lai, J. Liu, S. Adjokatse, F. Jahani, M. E. Kamminga, G. H. Ten Brink, T. T. Palstra, B. J. Kooi, J. C. Hummelen and M. Antonietta Loi, *Energy and Environmental Science*, 2016, **9**, 2444–2452.

(117) G. Zhang, T. M. Clarke and A. J. Mozer, *Journal of Physical Chemistry C*, 2016, **120**, 7033–7043.

(118) N. F. Muhamad, R. A. Maulat Osman, M. S. Idris and M. N. Mohd Yasin, *EPJ Web of Conferences*, 2017, **162**, 2–5.

(119) B. Pongthippitak, P. Wongtha, P. Reabroy, P. Kunsuwan and S. Thountom, *Journal of Physics: Conference Series*, 2018, **1144**, 012162.

(120) M. Marques, L. K. Teles, V. Anjos, L. M. Scolfaro, J. R. Leite, V. N. Freire, G. A. Farias and E. F. Da Silva, *Applied Physics Letters*, 2003, **82**, 3074–3076.

(121) R. M. Doughty, B. Hodges, J. Dominguez, R. Han, Z. Zhao, S. Assavachin and F. E. Osterloh, *Journal of Physical Chemistry C*, 2020, **124**, 18426–18435.

(122) M. Dou and C. Persson, *Journal of Applied Physics*, 2013, **113**, 083703.

(123) R. A. Parker, *Physical Review*, 1961, **124**, 1719–1722.

(124) S. Sarkar and K. K. Chattopadhyay, *Physica E: Low-Dimensional Systems and Nanostructures*, 2012, **44**, 1742–1746.

(125) K. H. Ye, X. Yu, Z. Qiu, Y. Zhu, X. Lu and Y. Zhang, *RSC Advances*, 2015, **5**, 34152–34156.

(126) D. K. Zhong, S. Choi and D. R. Gamelin, *Journal of the American Chemical Society*, 2011, **133**, 18370–18377.

(127) R. A. Lunt, A. J. Jackson and A. Walsh, *Chemical Physics Letters*, 2013, **586**, 67–69.

(128) O. Madelung, U. Rössler and M. Schulz, in *Non-Tetrahedrally Bonded Binary Compounds II, Landolt-Börnstein - Group III Condensed Matter*, Springer-Verlag Berlin Heidelberg, 2000, ch. Hematite (.

(129) L. M. Pazos-Outón, T. P. Xiao and E. Yablonovitch, *Journal of Physical Chemistry Letters*, 2018, **9**, 1703–1711.

(130) J. G. Labram and M. L. Chabinyc, *Journal of Applied Physics*, 2017, **122**, 065501.

(131) C. Wehrenfennig, G. E. Eperon, M. B. Johnston, H. J. Snaith and L. M. Herz, *Advanced Materials*, 2014, **26**, 1584–1589.

(132) X. Liu, F. Wang and Q. Wang, *Physical Chemistry Chemical Physics*, 2012, **14**, 7894.

(133) M. Regragui, V. Jousseaume, M. Addou, A. Outzourhit, J. C. Bernéde and B. El Idrissi, *Thin Solid Films*, 2001, **397**, 238–243.

(134) F. A. Kröger and H. J. Vink, *Solid State Physics - Advances in Research and Applications*, 1956, **3**, 307–435.

(135) P. L. Hsieh, G. Naresh, Y. S. Huang, C. W. Tsao, Y. J. Hsu, L. J. Chen and M. H. Huang, *Journal of Physical Chemistry C*, 2019, **123**, 13664–13671.

(136) T. Sano, D. M. Saylor and G. S. Rohrer, *Journal of the American Ceramic Society*, 2003, **86**, 1933–1939.

(137) J. Rotole and P. Sherwood, 1998, **5**, 10–17.

(138) R. Escobar Galindo, R. Gago, D. Duday and C. Palacio, *Analytical and Bioanalytical Chemistry*, 2010, **396**, 2725–2740.

(139) C. V. Cushman, S. Chatterjee, G. H. Major, N. J. Smith, A. Roberts and M. R. Linford, *Vacuum Technology & Coating*, 2016, 2–9.

(140) J. N. Clifford, E. Palomares, M. K. Nazeeruddin, M. Grätzel, J. Nelson, X. Li, N. J. Long and J. R. Durrant, *Journal of the American Chemical Society*, 2004, **126**, 5225–5233.

(141) A. Kudo and Y. Miseki, *Chemical Society Reviews*, 2009, **38**, 253–278.

(142) S. R. Pendlebury, A. J. Cowan, M. Barroso, K. Sivula, J. Ye, M. Grätzel, D. R. Klug, J. Tang and J. R. Durrant, *Energy and Environmental Science*, 2012, **5**, 6304–6312.

(143) C. Mitra, C. Lin, J. Robertson and A. A. Demkov, *Physical Review B - Condensed Matter and Materials Physics*, 2012, **86**, 1–8.

(144) A. Al-Zubi, G. Bihlmayer and S. Blügel, *Crystals*, 2019, **9**, 580–590.

(145) L. L. Rusevich, M. Tyunina, E. A. Kotomin, N. Nepomniashchaia and A. Dejneka, *Scientific Reports*, 2021, **11**, 1–8.

(146) Y. Wang, X. Liu, X. Han, R. Godin, J. Chen, W. Zhou, C. Jiang, J. F. Thompson, K. B. Mustafa, S. A. Shevlin, J. R. Durrant, Z. Guo and J. Tang, *Nature communications*, 2020, **11**, 2531.

(147) K. Maeda, K. Teramura, D. Lu, N. Saito, Y. Inoue and K. Domen, *Angewandte Chemie - International Edition*, 2006, **45**, 7806–7809.

(148) Y. Lee, K. Teramura, M. Hara and K. Domen, *Chemistry of Materials*, 2007, **19**, 2120–2127.

(149) Y. Li and K. Yang, *Energy and Environmental Science*, 2019, **12**, 2233–2243.

(150) Y. Qi, J. Zhang, Y. Kong, Y. Zhao, S. Chen, D. Li, W. Liu, Y. Chen, T. Xie, J. Cui, C. Li, K. Domen and F. Zhang, *Nature Communications*, 2022, **13**, 1–9.

(151) J. Li, Y. Liu, Z. Zhu, G. Zhang, T. Zou, Z. Zou, S. Zhang, D. Zeng and C. Xie, *Scientific Reports*, 2013, **3**, 2–7.

(152) Z. Weng-Sieh, R. Gronsky and A. T. Bell, *Journal of Catalysis*, 1997, **170**, 62–74.

(153) M. Kurnatowska, M. E. Schuster, W. Mista and L. Kepinski, *ChemCatChem*, 2014, **6**, 3125–3131.

(154) C. Fadley and D. Shirley, *Journal of Research of the National Bureau of Standards Section A: Physics and Chemistry*, 1970, **74A**, 543.

(155) K. Maeda, K. Teramura, D. Lu, T. Takata, N. Saito, Y. Inoue and K. Domen, *Journal of Physical Chemistry B*, 2006, **110**, 13753–13758.

(156) A. Yamakata, T. A. Ishibashi and H. Onishi, *Journal of Physical Chemistry B*, 2001, **105**, 7258–7262.

(157) E. Pastor, F. Le Formal, M. T. Mayer, S. D. Tilley, L. Francàs, C. A. Mesa, M. Grätzel and J. R. Durrant, *Nature Communications*, 2017, **8**, 14280.

(158) A. Kafizas, L. Francàs, C. Sotelo-Vazquez, M. Ling, Y. Li, E. Glover, L. McCafferty, C. Blackman, J. Darr and I. Parkin, *The Journal of Physical Chemistry C*, 2017, **121**, 5983–5993.

(159) Y. Ma, A. Kafizas, S. R. Pendlebury, F. Le Formal and J. R. Durrant, *Advanced Functional Materials*, 2016, **26**, 4951–4960.

(160) R. Godin, Y. Wang, M. A. Zwijnenburg, J. Tang and J. R. Durrant, *Journal of the American Chemical Society*, 2017, **139**, 5216–5224.

(161) F. Le Formal, S. R. Pendlebury, M. Cornuz, S. D. Tilley, M. Grätzel and J. R. Durrant, *Journal of the American Chemical Society*, 2014, **136**, 2564–2574.

(162) T. W. Kim and K. S. Choi, *Science*, 2014, **343**, 881–886.

(163) T. Kosaka, Y. Teduka, T. Ogura, Y. Zhou, T. Hisatomi, H. Nishiyama, K. Domen, Y. Takahashi and H. Onishi, *ACS Catalysis*, 2020, **10**, 13159–13164.

(164) C. Adler, S. Selim, I. Krivtsov, C. Li, D. Mitoraj, B. Dietzek, J. R. Durrant and R. Beranek, *Advanced Functional Materials*, 2021, **31**, DOI: 10.1002/adfm.202105369.

(165) J. Kosco, S. Gonzalez-Carrero, C. T. Howells, T. Fei, Y. Dong, R. Sougrat, G. T. Harrison, Y. Firdaus, R. Sheelamanthula, B. Purushothaman, F. Moruzzi, W. Xu, L. Zhao, A. Basu, S. De Wolf, T. D. Anthopoulos, J. R. Durrant and I. McCulloch, *Nature Energy*, 2022, **7**, 340–351.

(166) S. Feldmann, S. Macpherson, S. P. Senanayak, M. Abdi-Jalebi, J. P. Rivett, G. Nan, G. D. Tainter, T. A. Doherty, K. Frohna, E. Ringe, R. H. Friend, H. Sirringhaus, M. Saliba, D. Beljonne, S. D. Stranks and F. Deschler, *Nature Photonics*, 2020, **14**, 123–128.

(167) A. N. Pinheiro, E. G. Firmiano, A. C. Rabelo, C. J. Dalmaschio and E. R. Leite, *RSC Advances*, 2014, **4**, 2029–2036.

(168) T. W. Kim, Y. Ping, G. A. Galli and K. S. Choi, *Nature Communications*, 2015, **6**, 1–10.

(169) J. Y. Kim, G. Magesh, D. H. Youn, J. W. Jang, J. Kubota, K. Domen and J. S. Lee, *Scientific Reports*, 2013, **3**, 1–8.

(170) J. K. Kim, K. Shin, S. M. Cho, T. W. Lee and J. H. Park, *Energy and Environmental Science*, 2011, **4**, 1465–1470.

(171) J. S. Yang, W. P. Liao and J. J. Wu, *ACS Applied Materials and Interfaces*, 2013, **5**, 7425–7431.

(172) Z. Wang, X. Huang and X. Wang, *Catalysis Today*, 2019, **335**, 31–38.

(173) A. J. Cowan, W. Leng, P. R. Barnes, D. R. Klug and J. R. Durrant, *Physical Chemistry Chemical Physics*, 2013, **15**, 8772–8778.

(174) C. Li, E. Hofmeister, I. Krivtsov, D. Mitoraj, C. Adler, R. Beranek and B. Dietzek, *ChemSusChem*, 2021, **14**, 1728–1736.

(175) L. Francàs, C. A. Mesa, E. Pastor, F. Le Formal and J. R. Durrant, in *RSC Energy and Environment Series*, 2018, ch. 5, pp. 128–162.

(176) L. Francàs, S. Corby, S. Selim, D. Lee, C. A. Mesa, R. Godin, E. Pastor, I. E. Stephens, K. S. Choi and J. R. Durrant, *Nature Communications*, 2019, **10**, 1–10.

(177) S. Corby, L. Francás, A. Kafizas, J. R. Durrant, L. Francàs, A. Kafizas and J. R. Durrant, *Chemical Science*, 2020, **11**, 2907–2914.

Appendix A

Appendix: Supporting Figures

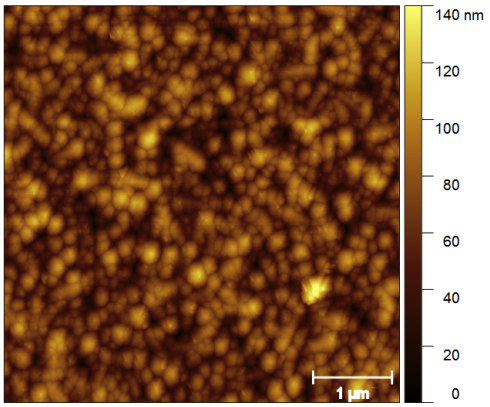

Figure A.1: 2D AFM image of the $SrTiO_3$ surface. The surface is relatively smooth with a roughness factor of 1.1, calculated by dividing the actual surface area (27.3 μm^2) by the projected surface area (25.0 μm^2).

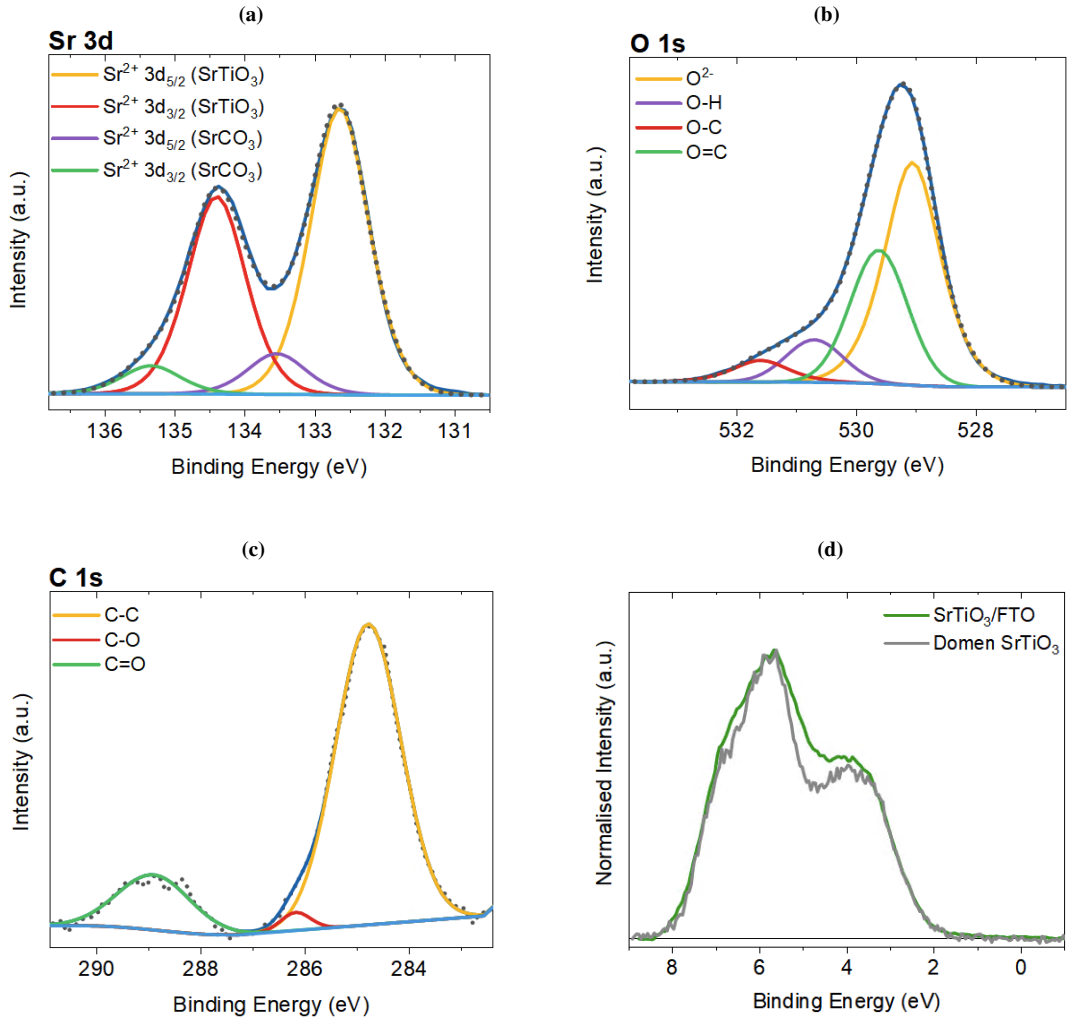

Figure A.2: XPS core line spectra corresponding to the $SrTiO_3$ film on FTO for a) Sr 3d, b) O 1s, c) C 1s, and d) the valence XPS spectrum compared to the $SrTiO_3$ used in the photocatalysts fabricated by Domen and co-workers.

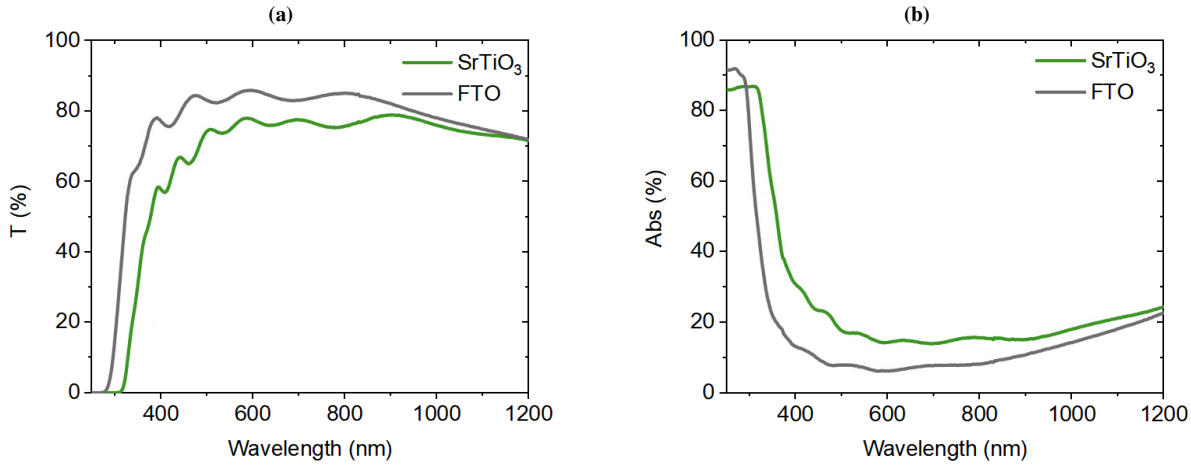

Figure A.3: Steady-state spectra of $SrTiO_3$ compared to FTO, a) as the transmittance, and b) the absorbance.

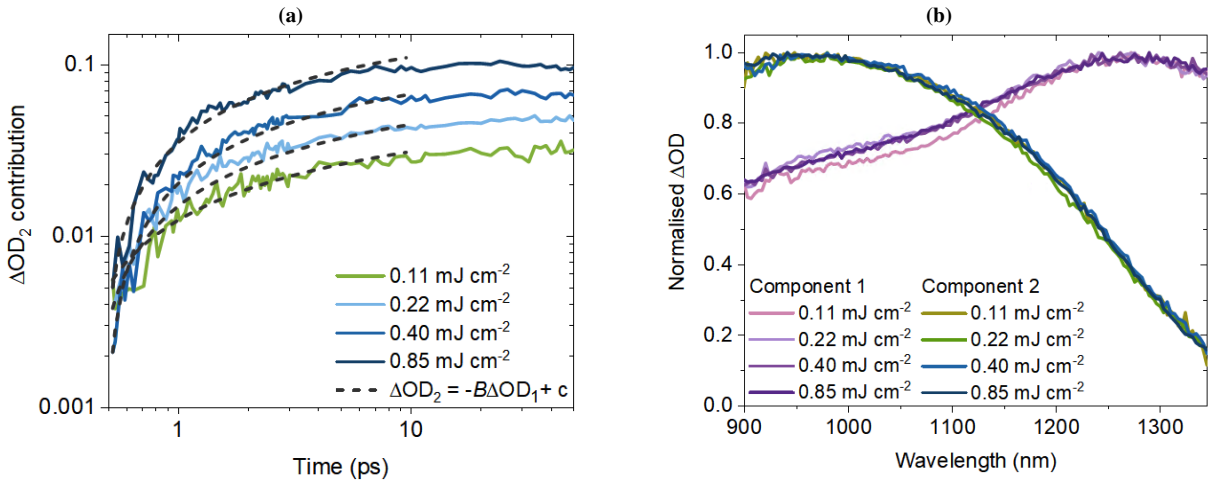

Figure A.4: Global analysis results at a range of excitation intensities. a) Fitting of component 2 across a range of excitation intensities. b) Spectra of components 1 and 2 across a range of excitation intensities.

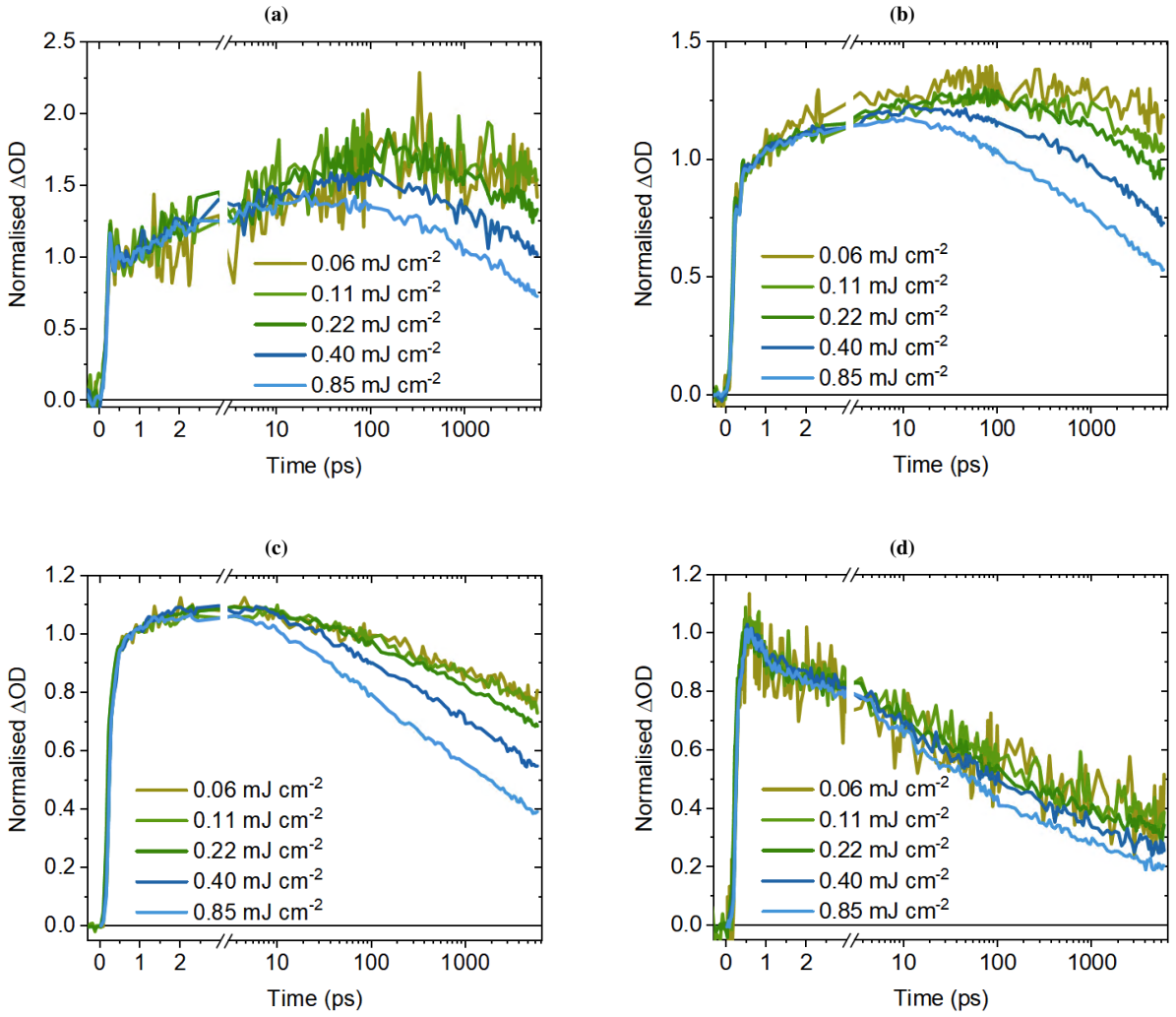

Figure A.5: Intensity dependence of ultrafast $SrTiO_3$ TAS decays, probed at a) 500 nm, b) 600 nm, c) 1100 nm, and d) 1300 nm.

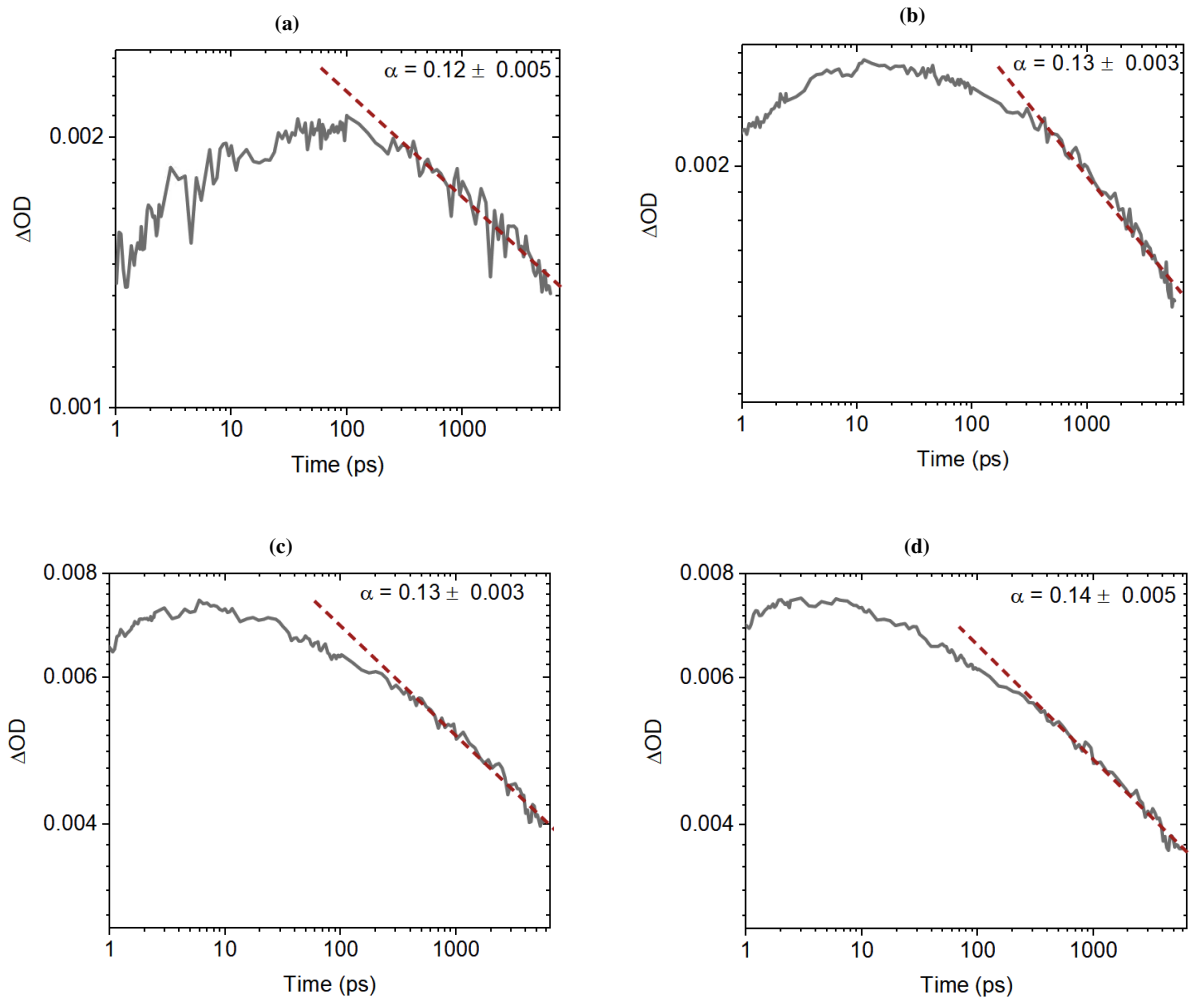

Figure A.6: Ultrafast TAS decay kinetics measured at 0.4 mJ cm^{-2} fitted to a power law decay, where $\Delta OD \propto t^{-\alpha}$, for probe wavelengths of a) 500 nm, b) 600 nm, c) 1000 nm, and d) 1100 nm.

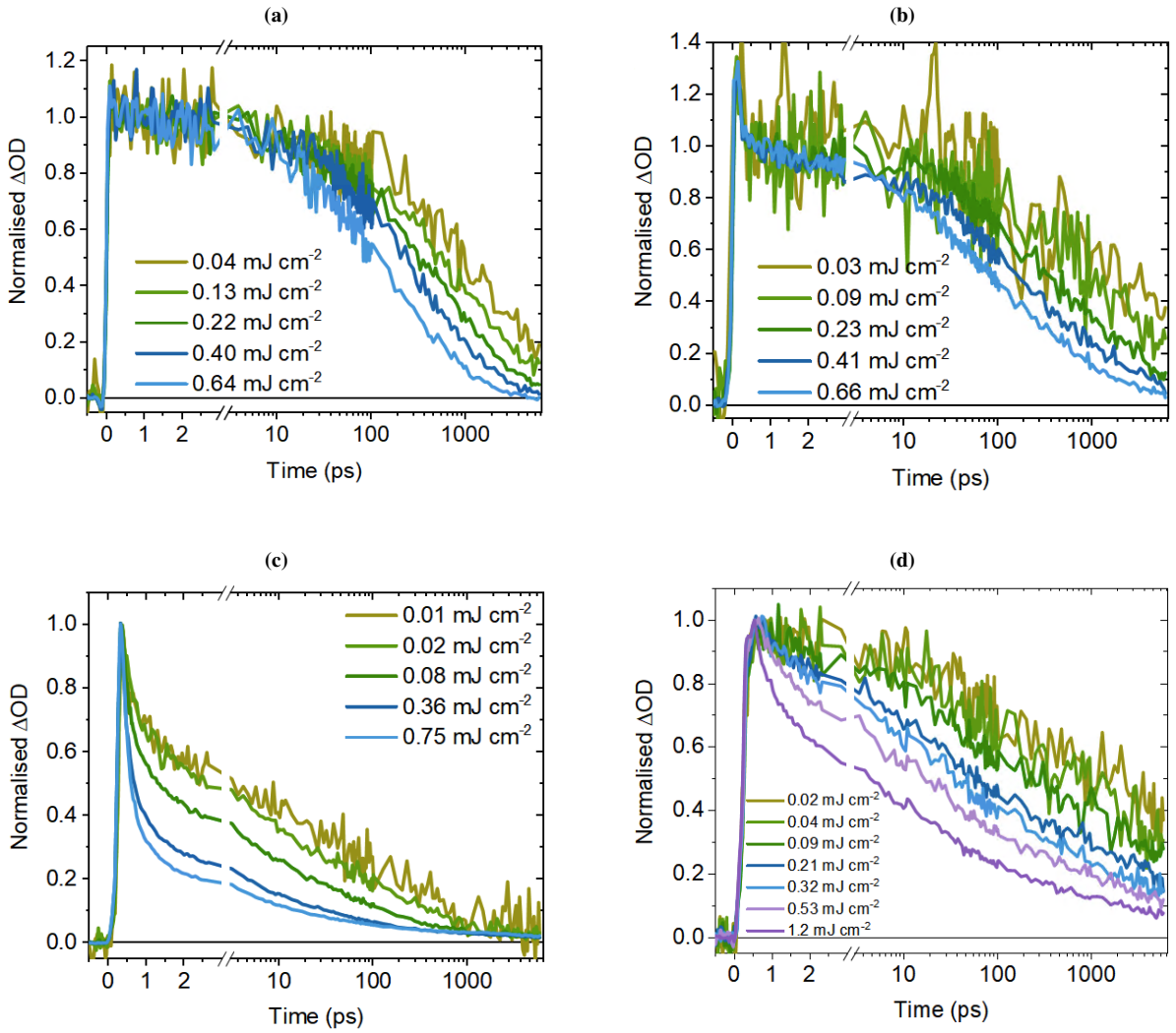

Figure A.7: Intensity dependence of ultrafast TAS decays of a) TiO_2 dense anatase (355 nm ex., 1000 nm probe), b) TiO_2 mesoporous anatase (355 nm ex., 1000 nm probe), c) α-Fe_2O_3 (400 nm ex., 750 nm probe), and d) $BiVO_4$ (440 nm ex., 700 nm probe).

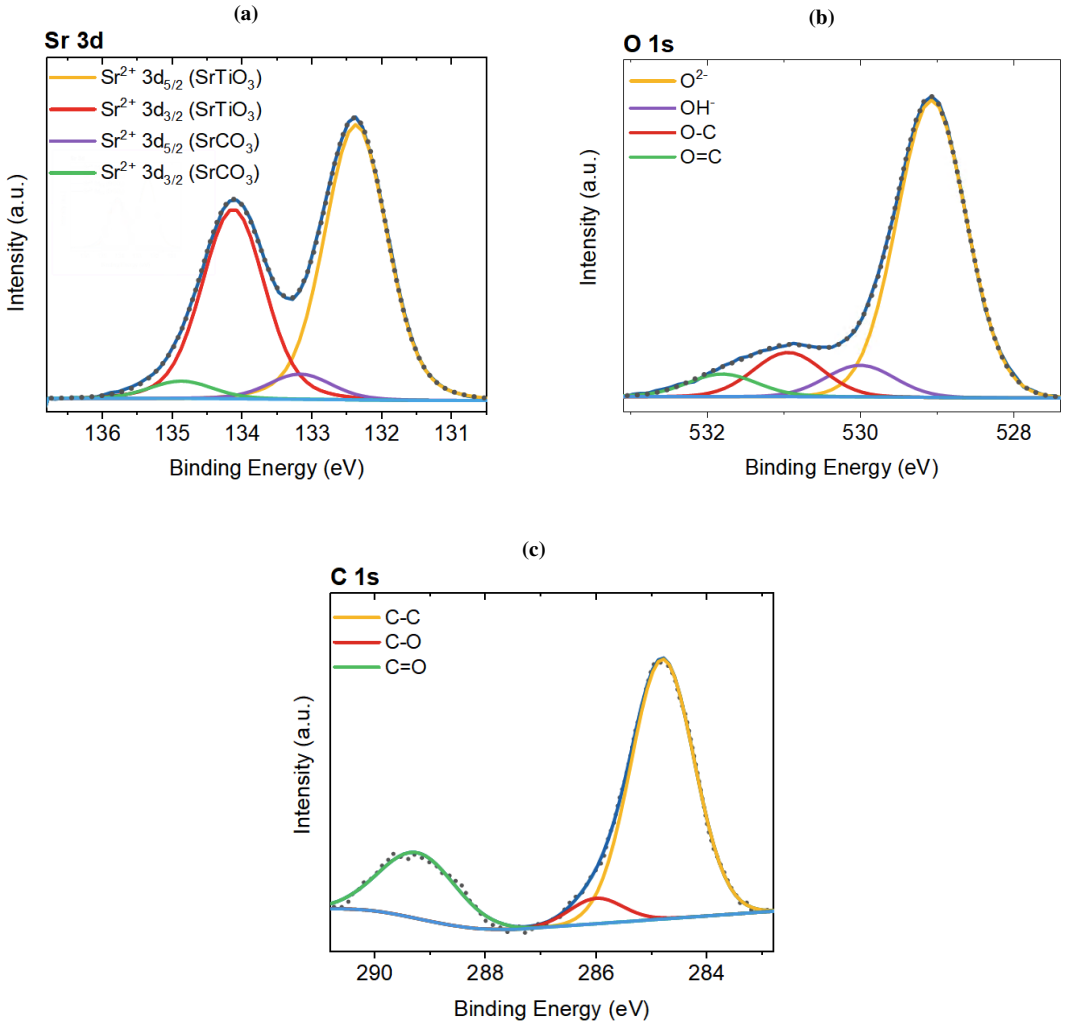

Figure A.8: XPS core line spectra corresponding to particulate $SrTiO_3$ for a) Sr 3d, b) O 1s and c) C 1s.

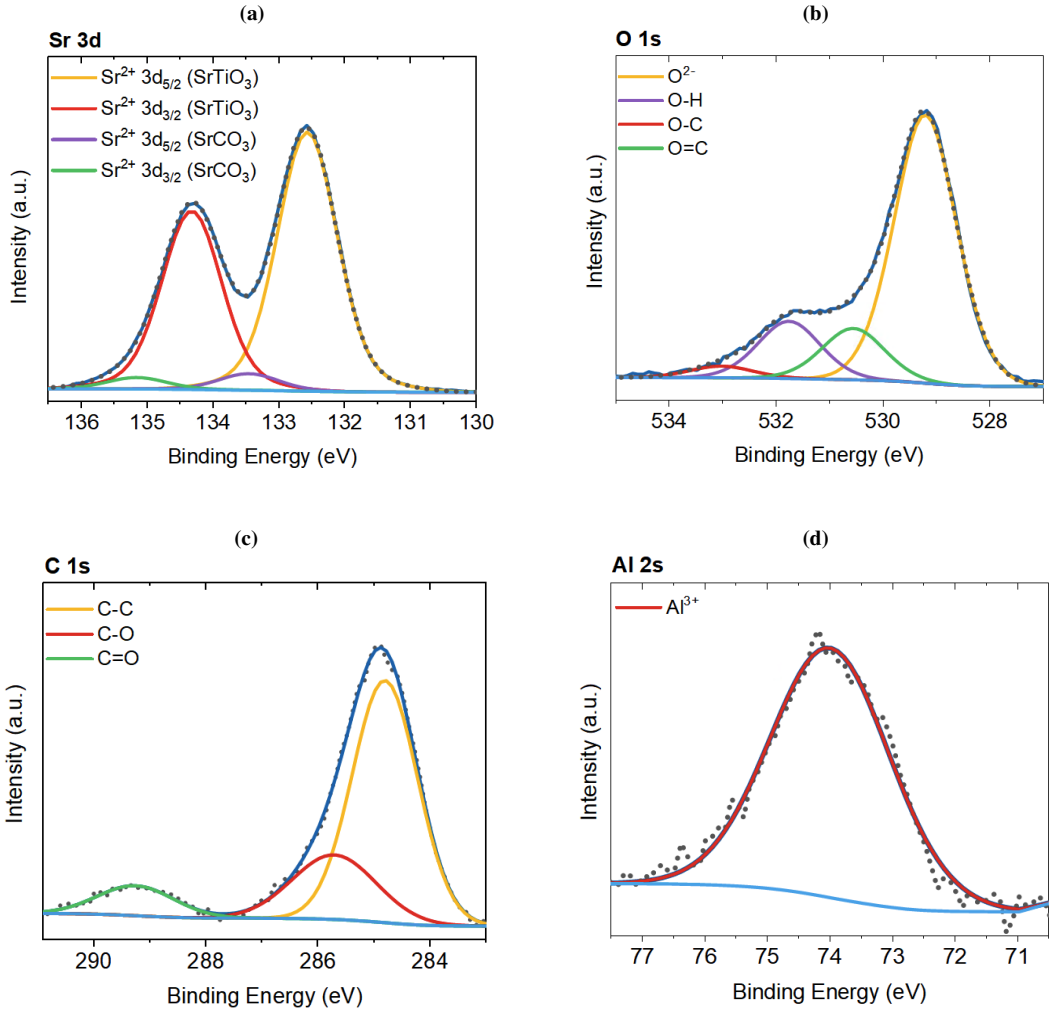

Figure A.9: XPS core line spectra corresponding to Al:$SrTiO_3$ for a) Sr 3d 1s, b) O 1s, c) C 1s, and d) Al 2s.

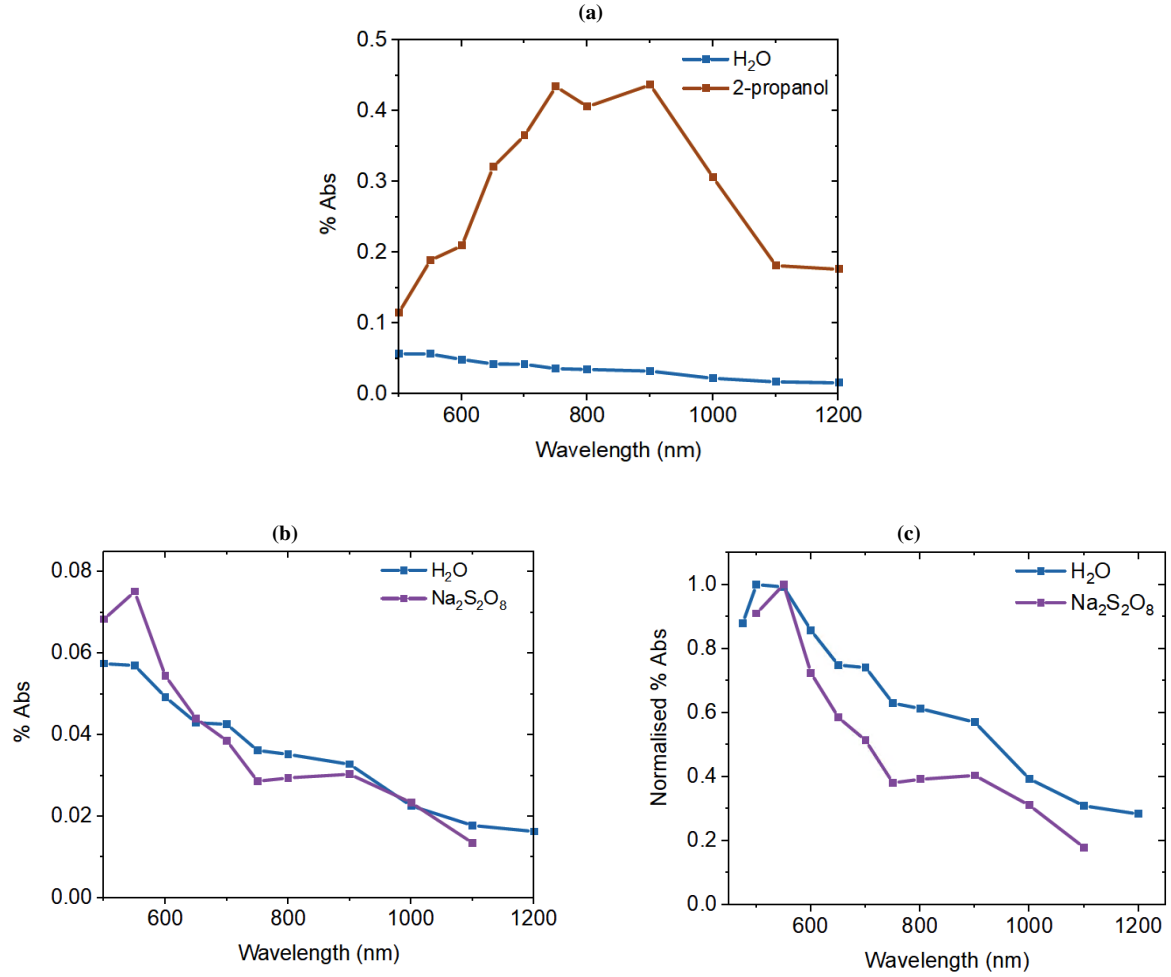

Figure A.10: Effects of scavengers on the $SrTiO_3$ PIAS spectrum compared to in H_2O. a) Effect of 2-propanol hole scavenger. Effect of $Na_2S_2O_8$ electron scavenger, c) as measured, and d) normalised.

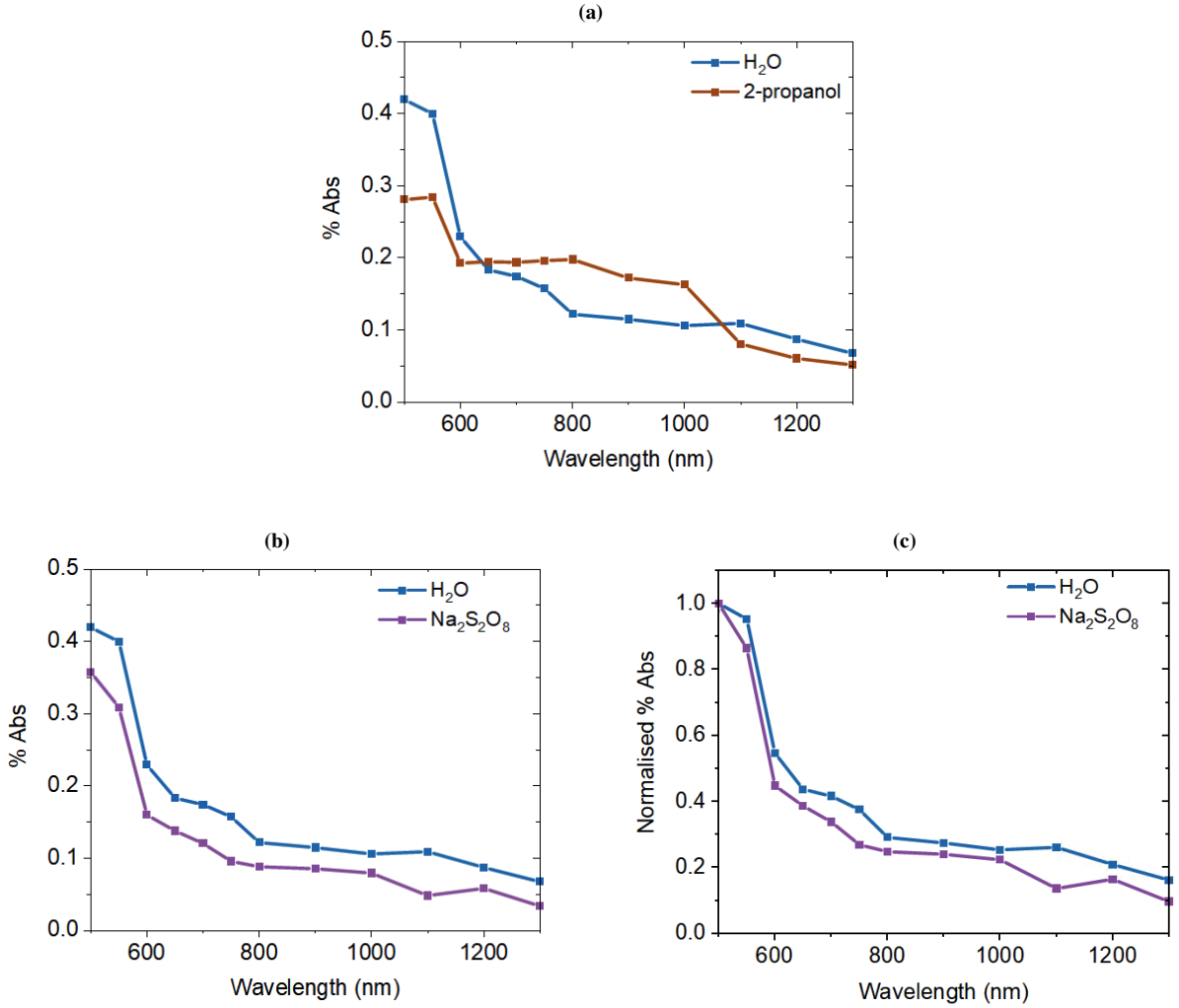

Figure A.11: Effects of scavengers on the Al:$SrTiO_3$ PIAS spectrum compared to in H_2O. a) Effect of 2-propanol hole scavenger. Effect of $Na_2S_2O_8$ electron scavenger, c) as measured, and d) normalised.

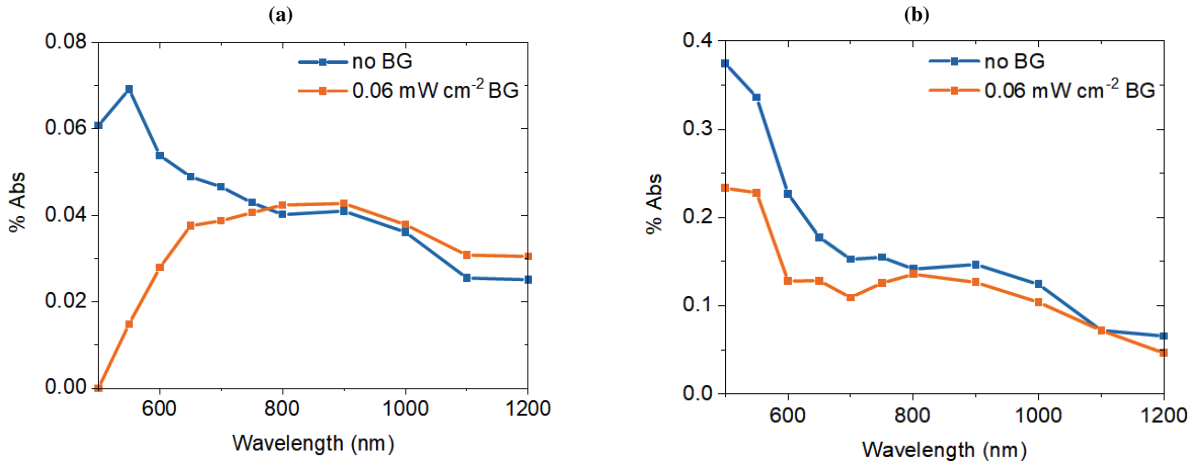

Figure A.12: Effect of continuous background illumination, using a 365 nm LED at an intensity of 0.06 mW cm^{-2}, on the PIAS spectrum in H_2O of a) $SrTiO_3$, and b) Al:$SrTiO_3$.

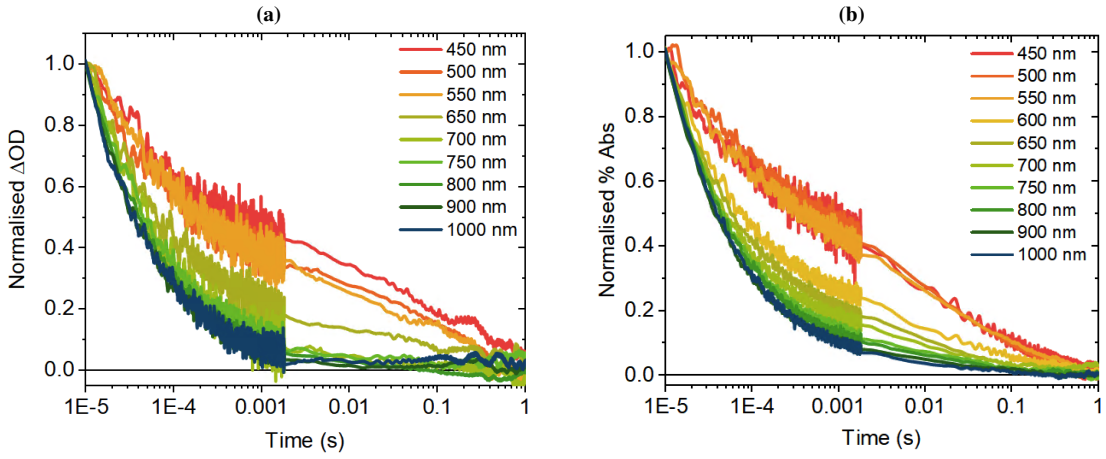

Figure A.13: Normalised DRTS kinetics in H_2O, for a) STO/FTO, and b) the $SrTiO_3$ films provided by Domen and co-workers.

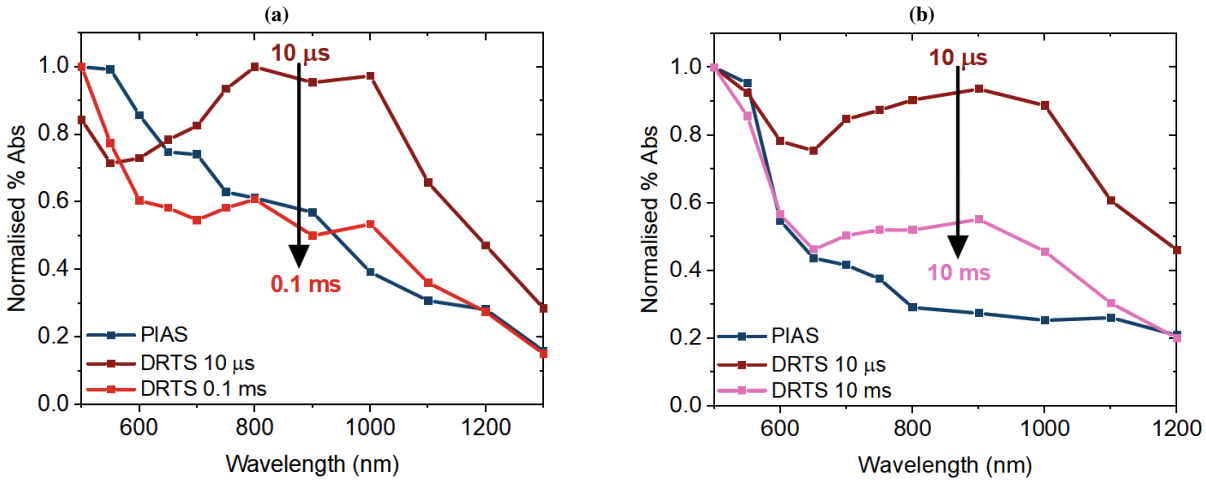

Figure A.14: Comparison of the PIAS spectral shape in H_2O, compared to that of DRTS at 10 μs and after it has evolved over time to resemble the PIAS spectral shape more closely (following the fast decay of the early NIR component), for a) $SrTiO_3$, and b) Al:$SrTiO_3$.

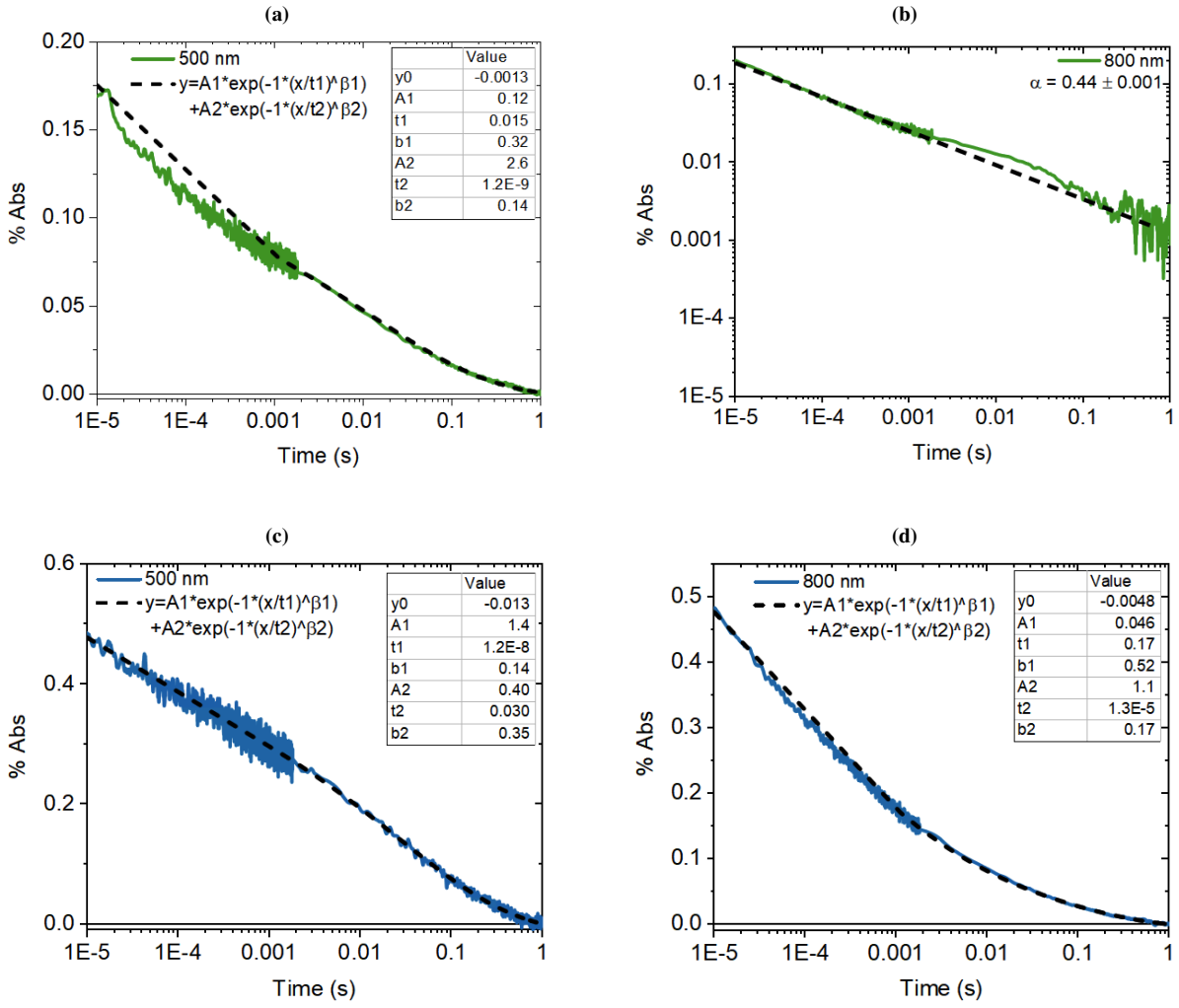

Figure A.15: Decay kinetics of $SrTiO_3$, probed at a) 500 nm fitted to two stretched exponentials ($\Delta OD(t) \propto e^{-(t/\tau)^{\beta}}$), and b) 800 nm fitted to a power law ($\Delta OD(t) \propto t^{-\alpha}$). Decay kinetics of Al:$SrTiO_3$ fitted to two stretched exponentials, probed at a) 500 nm, and b) 800 nm

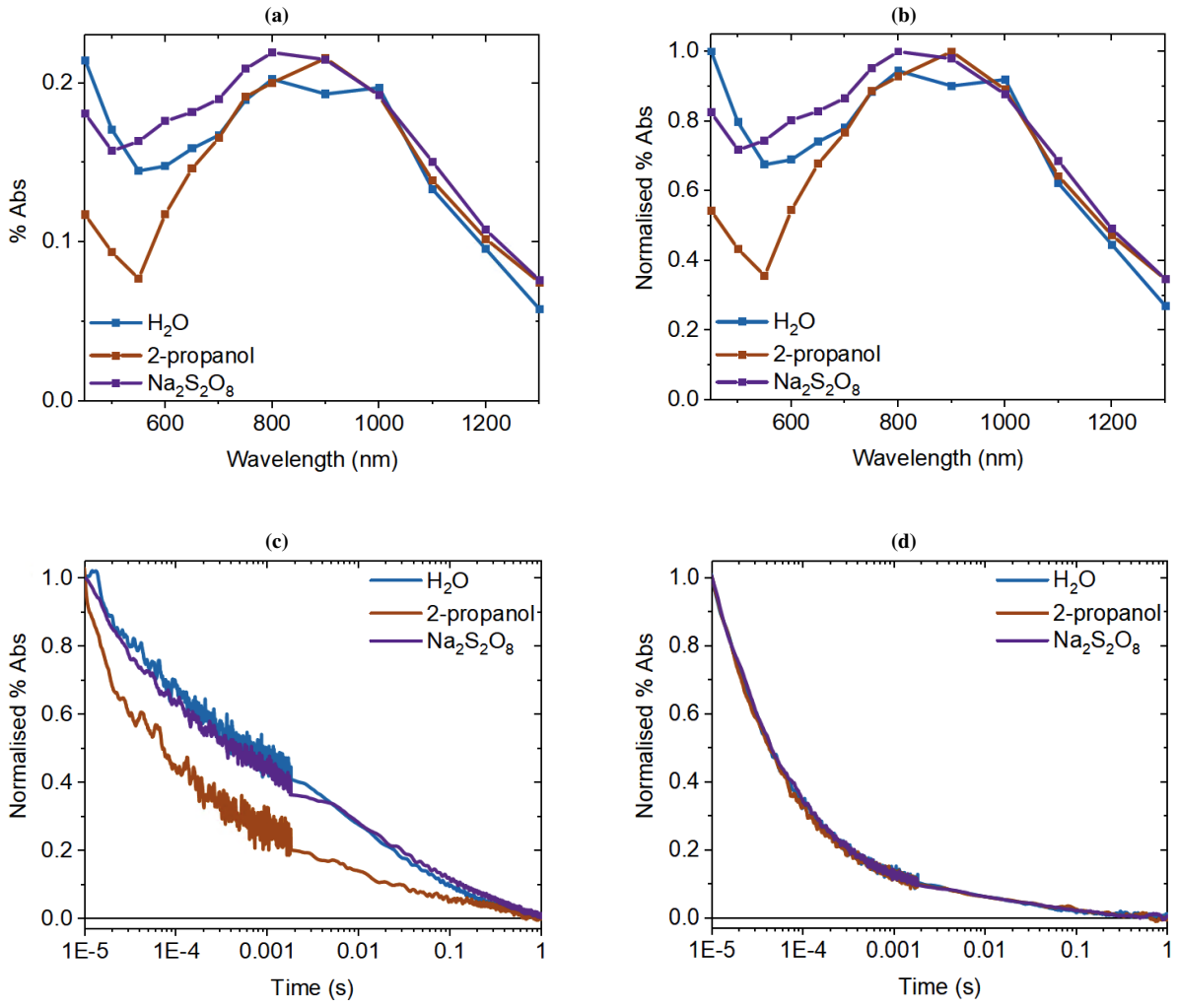

Figure A.16: The effect of hole (2-propanol) and electron ($Na_2S_2O_8$) scavengers on the DRTS of $SrTiO_3$, as shown by the a) spectrum as measured, b) spectrum normalised at 10 μs, c) decay kinetics probed at 500 nm, and d) decay kinetics probed at 800 nm. There is a suppression of the signals at low wavelengths and an acceleration of the decay kinetics at 500 nm, which is in agreement with the assignment of <600 nm signals to holes from PIAS studies. However, there is no effect of 2-propanol on the early NIR signals and no effect of $Na_2S_2O_8$.

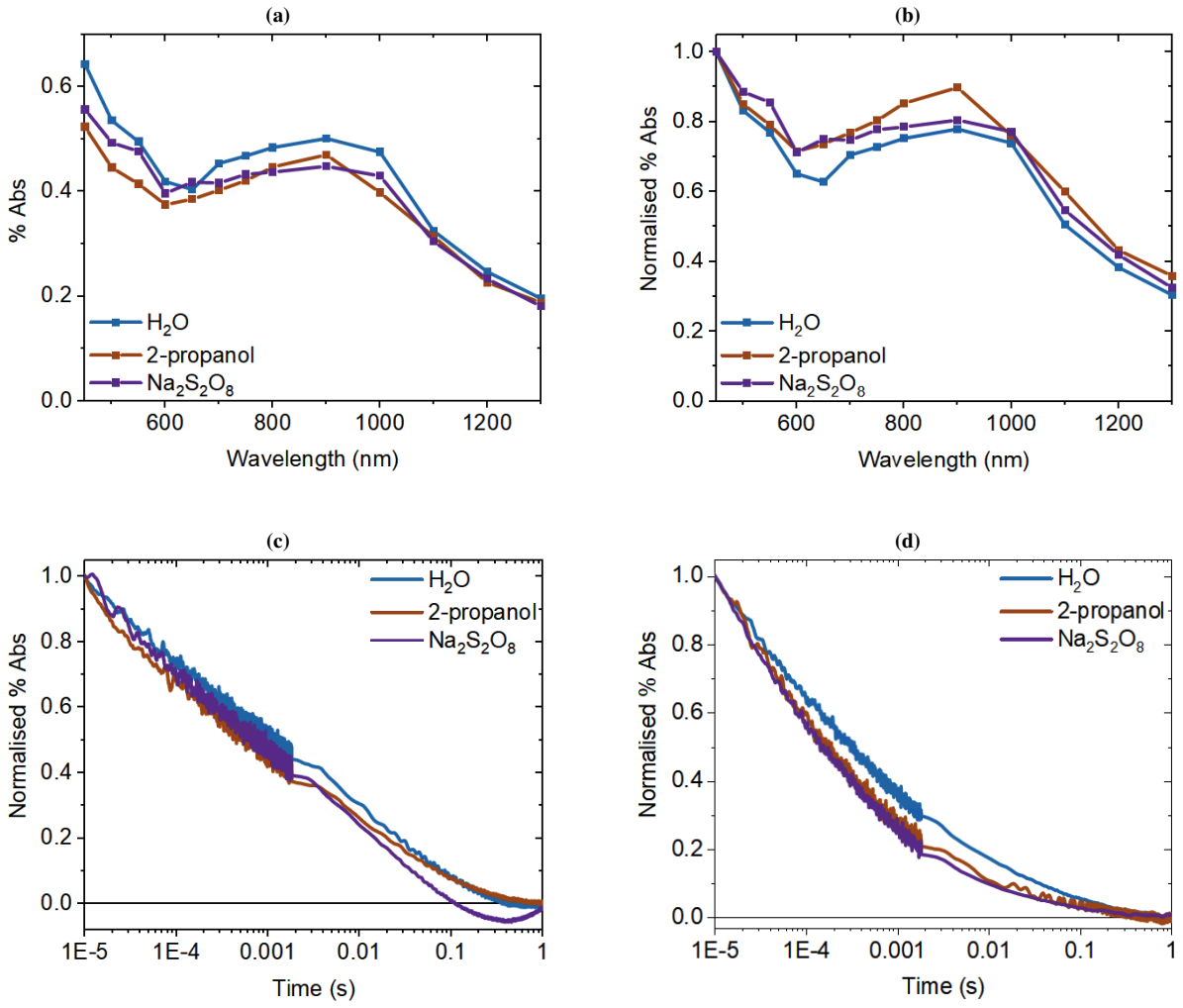

Figure A.17: The effect of hole (2-propanol) and electron ($Na_2S_2O_8$) scavengers on the DRTS of Al:$SrTiO_3$, as shown by the a) spectrum as measured, b) spectrum normalised at 10 μs, c) decay kinetics probed at 500 nm, and d) decay kinetics probed at 800 nm. Whereby, no clear spectral assignments result from the hole or electron scavengers.

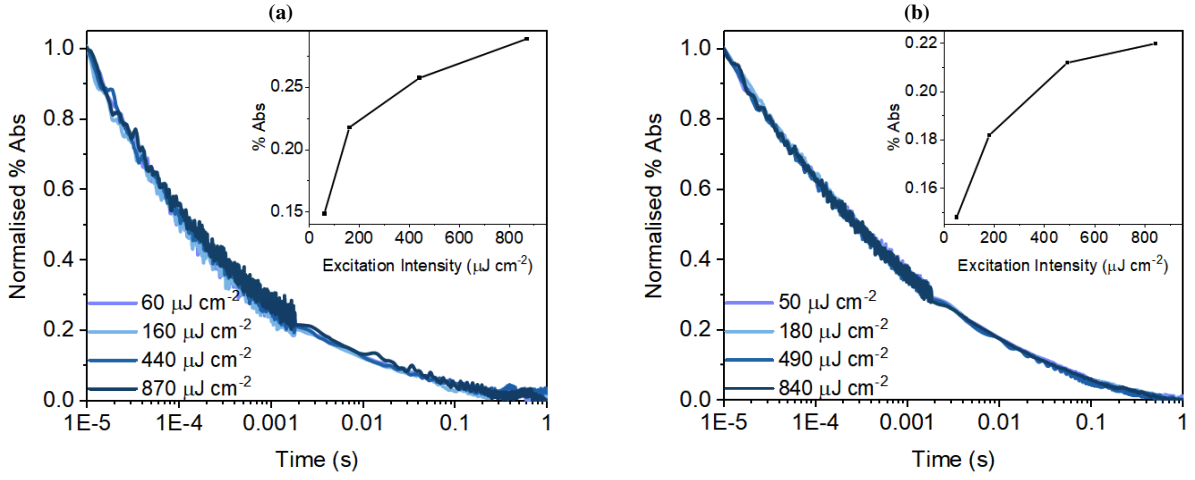

Figure A.18: Normalised intensity dependence of DRTS kinetics probed at 800 nm in H_2O, with as measured amplitudes as a function of excitation intensity in the insets, for a) $SrTiO_3$, and b) Al:$SrTiO_3$.

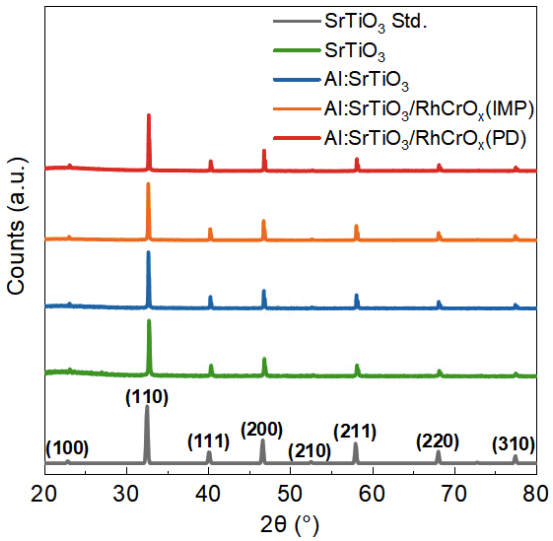

Figure A.19: X-Ray diffraction patterns of $SrTiO_3$, $Al:SrTiO_3$, $Al:SrTiO_3/RhCrO_x$(IMP) and $Al:SrTiO_3/RhCrO_x$(PD), compared to an $SrTiO_3$ standard pattern (ICDS collection no: 23076).

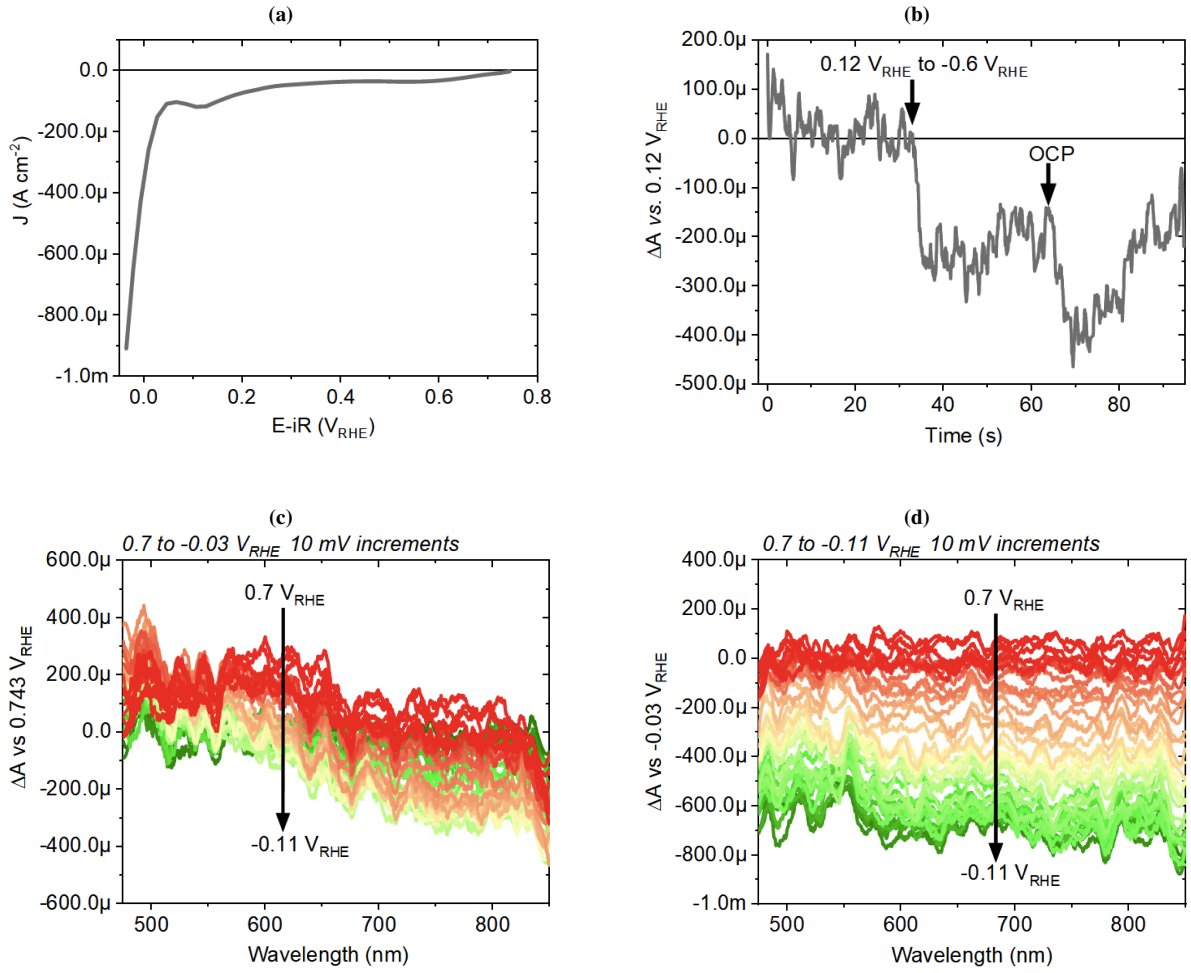

Figure A.20: SEC measurement of $RhCrO_x$ on FTO. A) J-V showing an onset potential at approximately -0.03 V_{RHE}. b) Transient measurement probed at 600 nm under different applied potentials, showing no clear effect of potential on optical signal. The differences that are observed are attributed to bubble formation on the surface, which was evident on the sample after the measurement. c) SEC spectrum measured prior to the onset from 0.7 V_{RHE} to -0.03 V_{RHE}, and d) SEC spectrum measured from 0.7 V_{RHE} to -0.11 V_{RHE}. The spectral shape is not reproducible and there is no obvious spectral shape, this is consistent with the features that are observed being due to bubble formation. With no evident spectral signal corresponding to the reduction of $RhCrO_x$, it is assumed that the electrons in $RhCrO_x$ are optically invisible under these conditions.

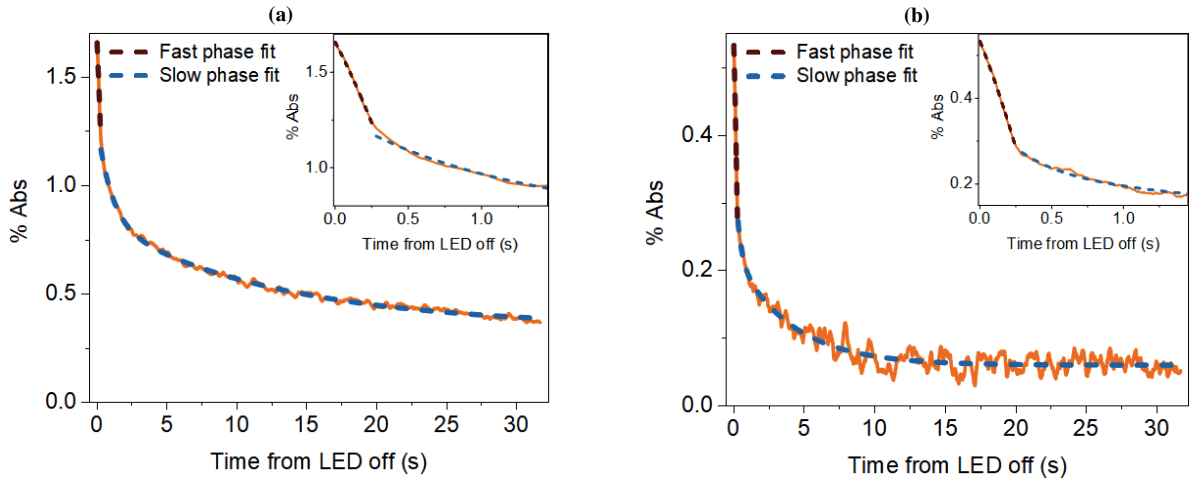

Figure A.21: PIAS decays of Al:$SrTiO_3$/$RhCrO_x$(IMP) and Al:$SrTiO_3$/$RhCrO_x$(PD) fitted as two distinct phases. The initial fast phase is fitted to a single exponential decay (%Abs = $y_0 + A_1 e^{-t/\tau_1}$), whilst the slower phase is fitted to two exponential decays (%Abs = $y_0 + A_1 e^{-t/\tau_1} + A_2 e^{-t/\tau_2}$).

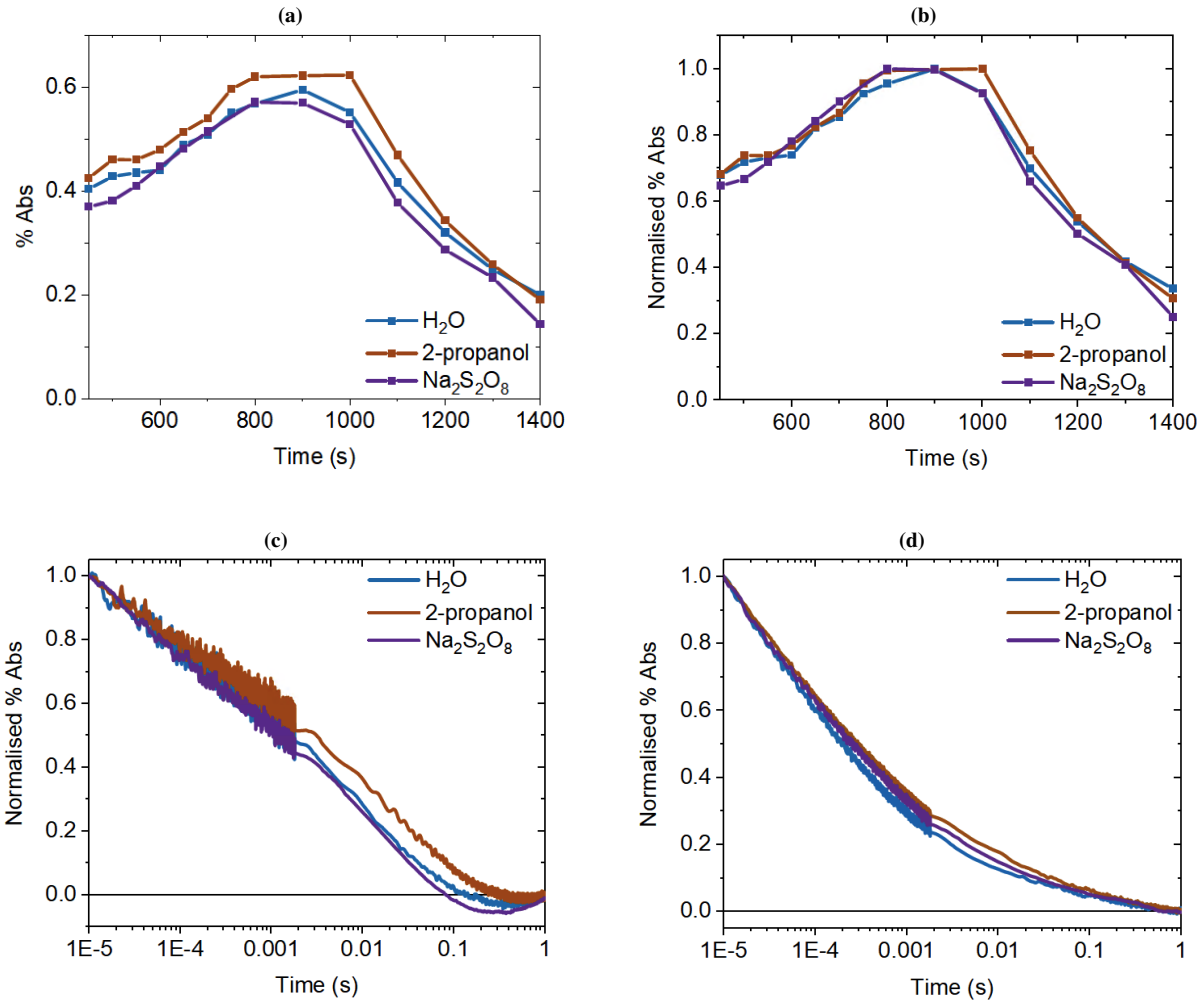

Figure A.22: The effect of hole (2-propanol) and electron ($Na_2S_2O_8$) scavengers on the DRTS of Al:$SrTiO_3$/-$RhCrO_x$(IMP), as shown by the a) spectrum as measured, b) spectrum normalised at 10 μs, c) decay kinetics probed at 500 nm, and d) decay kinetics probed at 800 nm. There is a small effect of hole scavenger on the 500 nm decay kinetics but the change is too small to be certain of a change here. Overall, there is no significant effect of scavengers observed.

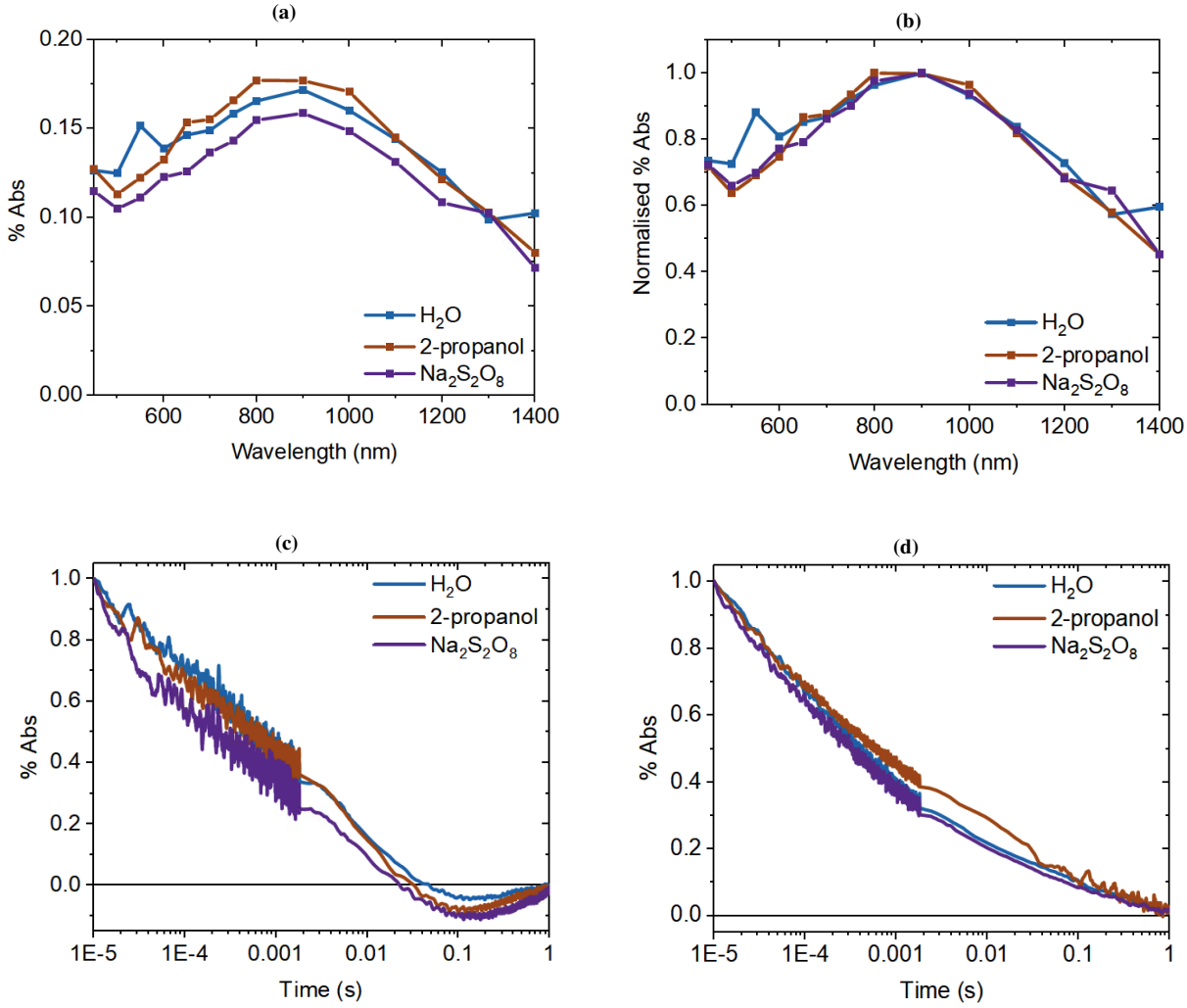

Figure A.23: The effect of hole (2-propanol) and electron ($Na_2S_2O_8$) scavengers on the DRTS of Al:$SrTiO_3$/-$RhCrO_x$(PD), as shown by the a) spectrum as measured, b) spectrum normalised at 10 μs, c) decay kinetics probed at 500 nm, and d) decay kinetics probed at 800 nm. The 550 nm peak in H_2O is suppressed by both hole and electron scavengers, so an assignment of species to this peak is not possible from these results. Overall, there is no significant effect of scavengers observed.

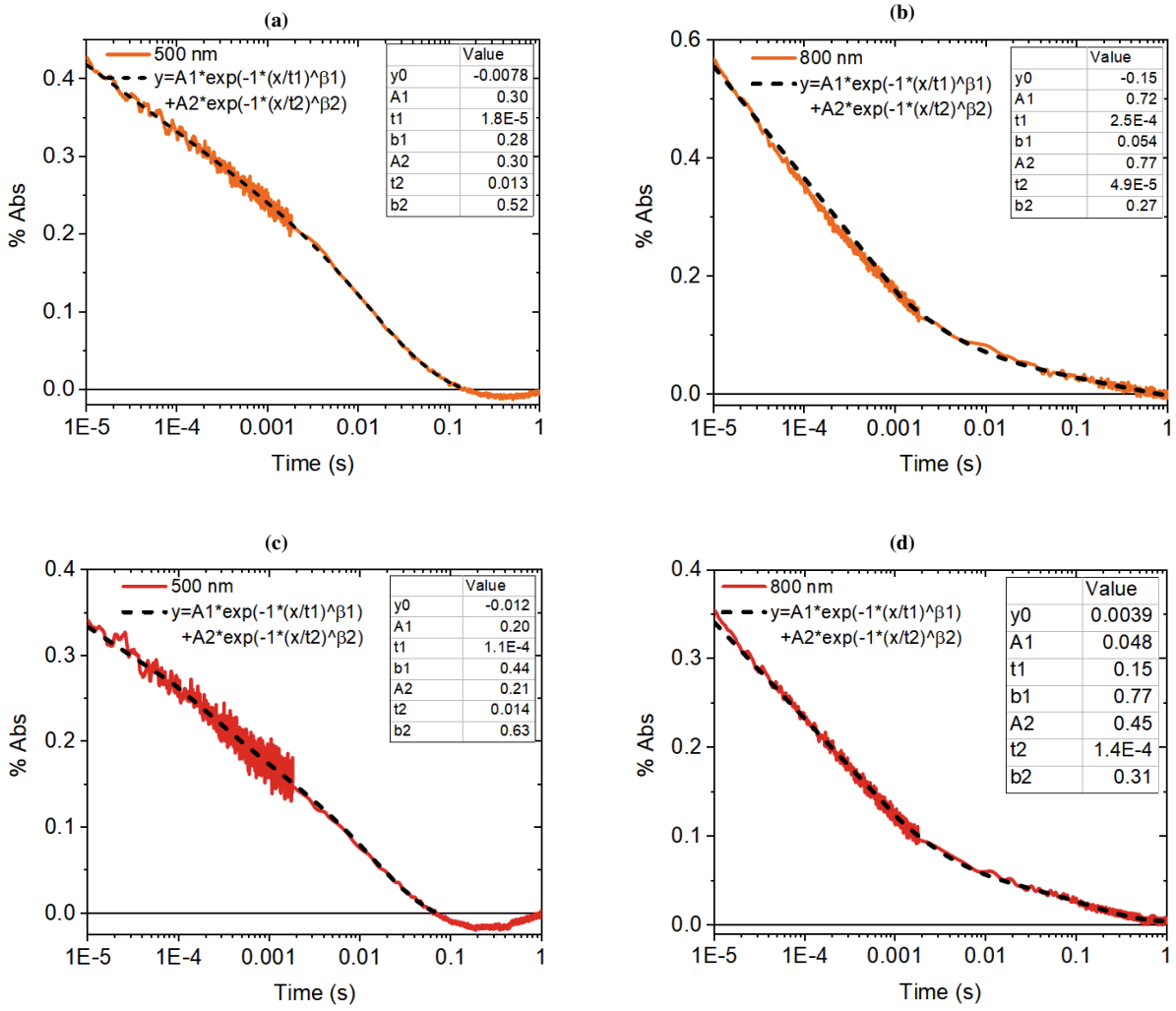

Figure A.24: Decay kinetics fitted to two stretched exponentials (ΔOD(t) $\propto e^{-(t/\tau)^{\beta}}$). For Al:$SrTiO_3$/$RhCrO_x$-(IMP), probed at a) 500 nm and b) 800 nm. For Al:$SrTiO_3$/$RhCrO_x$(PD), probed at a) 500 nm and b) 800 nm.

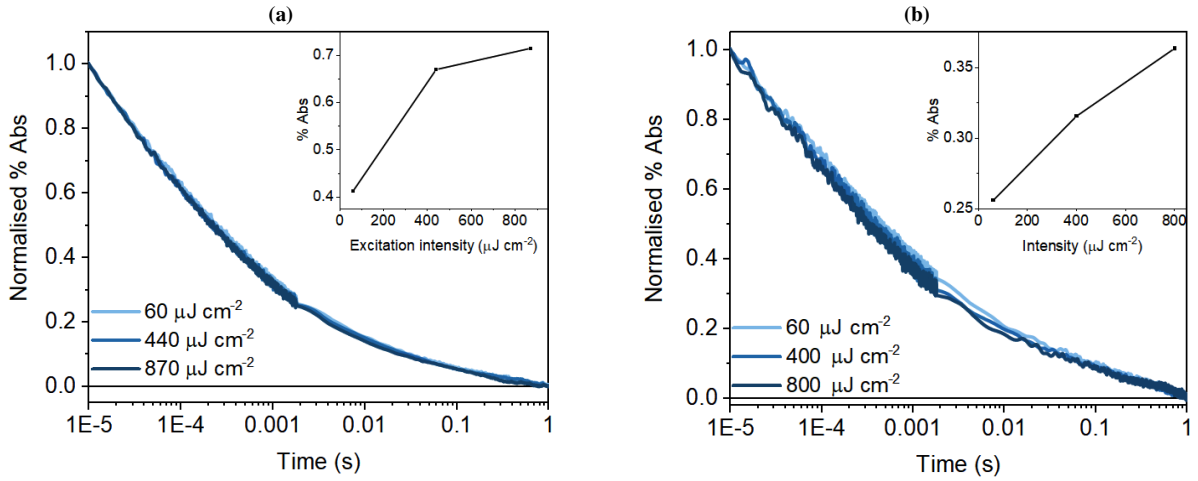

Figure A.25: Intensity dependant DRTS kinetics H_2O, with the dependence of the signal amplitude on intensity showed in the insets. Probed at 800 nm, for a) Al:$SrTiO_3$/$RhCrO_x$(IMP), and b) Al:$SrTiO_3$/$RhCrO_x$(PD). Whilst a small degree of intensity dependence was observed regarding an acceleration of decay kinetics with increasing excitation intensity at 500 nm, it is not observed at 800 nm. At both 500 nm and 800 nm the signal amplitude increases with increasing excitation intensity and begins to plateau at higher intensities.

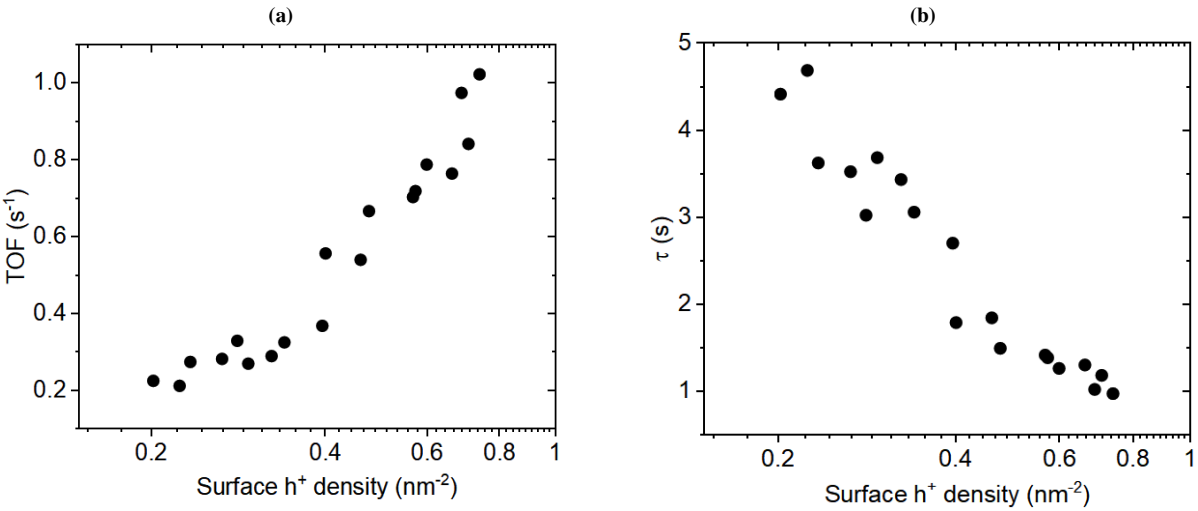

Figure A.26: Calculated a) TOF and b) τ of hole species in $SrTiO_3$ on FTO at a range of hole densities. Undertaken under an applied bias of 1.3 V_{RHE}.

Table A.1: Calculation of the bimolecular rate constant for $SrTiO_3$, TiO_2, $BiVO_4$ and α-Fe_2O_3, using the second order rate equation and the charge lifetime ($t_{50\%}$) at a given laser excitation intensity.

	Laser Energy (J cm^{-2})	Photon energy (J)	Abs at 355 nm	Photons absorbed (cm^{-2})	Thickness (cm)	Charge density (cm^{-3})	$t_{50\%}$ (s)	κ (cm^3 s^{-1})
$SrTiO_3$	8.5E-4	5.6E-19	0.33	5.0E14	7.0E-5	7.2E18	4.1E-9	3.4E-11
TiO_2 d^a	6.4E-4	5.6E-19	0.15	1.7E14	4.3E-5	9.3E18	9.6E-11	1.0E-9
TiO_2 m^b	6.4E-4	5.6E-19	0.15	1.7E14	4.3E-5	9.3E18	9.6E-11	1.0E-9
$BiVO_4$	1.2E-3	4.5E-19	0.21	5.6E14	1.0E-5	5.6E19	4.5E-12	3.9E-9
$BiVO_4$	5.3E-4	4.5E-19	0.21	2.5E14	1.0E-5	2.5E19	1.6E-11	2.5E-9
α-Fe_2O_3 ^{c}	7.5E-4	5.0E-19	0.70	1.1E15	1.0E-5	1.0E20	5.9E-13	1.6E-8
α-Fe_2O_3 ^{c}	3.6E-4	5.0E-19	0.70	5.1E14	1.0E-5	5.9E19	6.8E-13	2.9E-8
α-Fe_2O_3 ^{c}	7.5E-4	5.0E-19	0.70	1.1E15	1.0E-5	1.0E20	6.4E-13	1.6E-8

^{a}Dense anatase TiO_2, ^{b}Mesoporous anatase TiO_2, ^{c}The initial sub-ps decay in α-Fe_2O_3 has a non-bimolecular decay, however, even when measuring $t_{50\%}$ from 0.5 ps the bimolecular constant remains on the same order of magnitude.

Table A.2: Calculation of the intrinsic doping density of $SrTiO_3$, TiO_2, $BiVO_4$ and α-Fe_2O_3, using the excitation intensity from which intensity dependence of the decay kinetics is observed.

	Wavelength (nm)	Energy (eV)	Photon energy (J)	Laser Energy (J cm^{-2})	Abs at 355 nm	Photons absorbed (cm^{-2})	Thickness (cm)	Intrinsic doping density (cm^{-3})
$SrTiO_3$	355	3.49	5.6E-19	2.2E-4	0.33	1.3E14	7.0E-5	1.8E18
TiO_2 d^a	355	3.49	5.6E-19	1.3E-4	0.35	8.1E13	4.3E-5	1.9E18
$BiVO_4$	440	2.82	4.5E-19	9.0E-5	0.21	4.2E13	1.0E-5	4.2E18
α-Fe_2O_3	400	3.09	5.0E-19	2.0E-5	0.70	2.8E13	1.0E-5	2.8E18

^{a}Dense anatase TiO_2.